UNIVERSITÉ DE GENÈVE

Archive ouverte UNIGE
https://archive-ouverte.unige.ch

Thèse 2001

Open Access

This version of the publication is provided by the author(s) and made available in accordance with the copyright holder(s).

The volcanology, petrology and geochronology of the Fish canyon magmatic system, San Juan volcanic field, U.S.A

Bachmann, Olivier

How to cite

BACHMANN, Olivier. The volcanology, petrology and geochronology of the Fish canyon magmatic system, San Juan volcanic field, U.S.A. Doctoral Thesis, 2001. doi: 10.13097/archive-ouverte/unige:97988

This publication URL: https://archive-ouverte.unige.ch/unige:97988
Publication DOI: 10.13097/archive-ouverte/unige:97988

© This document is protected by copyright. Please refer to copyright holder(s) for terms of use.

UNIVERSITÉ DE GENÈVE
Département de minéralogie

FACULTÉ DES SCIENCES
Professeur M.A. Dungan

The Volcanology, Petrology, and Geochronology of the Fish Canyon Magmatic System, San Juan Volcanic Field, U.S.A.

THÈSE

présentée à la faculté des sciences de l'Université de Genève
pour obtenir le grade de Docteur ès sciences, mention sciences de la Terre

par

Olivier BACHMANN
de
Genève (GE)

Thèse N° 3213

Genève
2001

La Faculté des sciences, sur le préavis de Messieurs M. DUNGAN, professeur ordinaire et directeur de thèse (Département de minéralogie), T. DRUITT, professeur (Université Blaise Pascal - Clermont-Ferrand, France), P.W. LIPMAN, docteur (U.S. Geological Survey - Menlo Park, U.S.A.) et M. PICHAVANT, docteur (CNRS - Orléans, France), autorise l'impression de la présente thèse, sans exprimer d'opinion sur les propositions qui y sont énoncées.

Genève, le 16 novembre 2000

Thèse - 3213 -

Le Doyen, Jacques WEBER

O. Bachmann: The volcanology, petrology, and geochronology of the Fish Canyon magmatic system, San Juan volcanic field, U.S.A.
Terre & Environnement, vol. 28, 150 pp. (2001)

ISBN 2-940153-27-2
Section des Sciences de la Terre, Université de Genève, 13 rue des Maraîchers, CH-1211 Genève 4, Suisse
Téléphone ++41-22-702.61.11 - Fax ++41-22-320.57.32

Table des matières

Résumé: Le système magmatique de Fish Canyon, Colorado, Etats-Unis : évolution pétrologique et séquence éruptive d'un grand corps de magma acide

1. Introduction

La découverte de grandes nappes de ponces et de cendres, ayant des volumes estimés à plusieurs milliers de km^3, et leur lien avec de gigantesques éruptions explosives, ne remonte qu'à la fin des années 50 (Cook, 1959; Smith, 1960). Bien que ces dépôts, que l'on nomme " ignimbrites ", forment des couches évidentes dans les séries volcaniques anciennes, l'idée que de tels volumes de roches puissent être mis en place en une seule éruption explosive a pris un certain temps pour éclore. La compréhension de ces systèmes n'a cessé de progresser jusqu'à nos jours (Lipman, 1997a), mais un grand nombre de questions subsistent quant au déroulement de ces éruptions gigantesques ainsi qu'à l'existence possible de signes précurseurs. Les structures d'effondrement provoquées par l'évacuation rapide de ces énormes volumes de magma de la croûte supérieure, que l'on désigne par le terme " caldera ", restent également mal connues et controversées (Lipman, 1997b; McBirney, 1990). Cette relative ignorance, en comparaison de ce qui est connu sur les autres phénomènes volcaniques majeurs, découle principalement du fait qu'aucune observation directe n'a encore été possible. Ces énormes volumes de magma nécessitent un temps de gestation important, et les intervalles entre éruptions oscillent autour de 100'000 ans. La dernière de ces gigantesques ignimbrites s'est mise en place lors de l'éruption du Lac Toba, sur l'île de Sumatra il y a ~75'000 ans (Chesner, 1998), mais les hommes présents à cette époque sur les îles d'Asie du Sud-Est, pourtant déjà des Homo Sapiens Sapiens, n'avaient pas encore vraiment la tête à étudier la volcanologie. Des éruptions ignimbritiques de taille plus restreinte (quelques km^3) ont par contre eu lieu en des temps moins reculés, tels que Crater Lake (~6845 ans BP ; Bacon, 1983), Santorin (~3645 ans BP ; Bond and Sparks, 1976), et plus proche de nous Tambora (1815), lesquelles ont fourni quelques informations quant à leur impact sur l'environnement et les êtres vivants.

Les conséquences de telles éruptions dans le futur seraient désastreuses, non seulement pour les régions avoisinant les lieux de l'éruption, mais également pour la planète dans son ensemble. En plus des milliers de kilomètres carrés qui seraient recouverts par d'énormes quantités de dépôts incandescents, la dispersion de fines particules et de gaz dans l'atmosphère provoqueraient des changements climatiques durables (de Silva and Zielinski, 1998) mettant en danger la vie sur Terre. Des généticiens ont d'ailleurs proposé, d'après des études sur l'ADN mitochondrial permettant de déterminer le taux de peuplement humain à certaines époques du passé, que l'éruption du Lac Toba aurait provoqué la quasi-disparition de l'espèce humaine (Ambrose, 1998).

A l'heure actuelle, plusieurs zones de calderas potentielles montrent des signes d'activité. Des systèmes que l'on pensait endormis, comme la caldera de Valles au Nouveau Mexique, semblent sur la voie du réveil (Wolff and Gardner, 1995). La région de Yellowstone, dans l'état du Wyoming, qui a été le théâtre d'une des plus grandes éruptions connues il y a 600'000 ans, présente une intense activité géothermale, et est secouée par de nom-

breux tremblements de terre quotidiens. Ces tremblements de terre indiquent de fortes tensions et des mouvements de magma dans la croûte supérieure, qui se traduisent par un soulèvement de plus de 70 cm en 50 ans au centre de la caldera (Pelton and Smith, 1982). Les calderas de Long Valley, en Californie, et des Champs Phlégréens, dans la baie de Naples, potentiellement très dangereuses car proches de régions densément peuplées, montrent également de l'activité sismique et des mouvements de sol importants, avec des soulèvements atteignant par période 1 m par année (De Natale and Pingue, 1993). Sachant qu'une partie de ces calderas actives n'a pas encore été mise à jour, des recherches sont nécessaires pour déterminer ces zones à risques. De plus, des études détaillées sur d'anciennes calderas sont indispensables à la compréhension du déroulement de ces éruptions.

Ces grandes ignimbrites sont non seulement importantes du fait du danger qu'elles représentent, mais elles apportent également des informations précieuses quant aux processus magmatiques prenant place dans les enveloppes externes de la Terre. De par leur association spatiale et leur composition semblable, ces ignimbrites semblent être liées aux grands corps plutoniques, les " batholites ", qui constituent l'un des principaux composants de l'écorce terrestre. Le refroidissement rapide du magma induit par l'éruption permet d'obtenir une image littéralement figée de la chambre magmatique immédiatement avant l'éruption et d'accéder ainsi aux stades préliminaires de la cristallisation de ces grands corps. Les processus de différentiation magmatique peuvent donc être en partie explorés grâce à ces roches, menant à une meilleure compréhension des échanges entre le manteau et la croûte terrestre ainsi que de la croissance crustale.

Le cycle magmatique de Fish Canyon est remarquable à plusieurs points de vue. Ce cycle a donné naissance à la plus grande ignimbrite connue à l'heure actuelle, le Tuf de Fish Canyon, une unité sur laquelle de nombreuses informations ont déjà été récoltées lors d'études préalables, permettant ainsi de formuler des hypothèses de travail précises. Cette ignimbrite est entourée par deux éruptions satellites aux styles éruptifs très différents du Tuf de Fish Canyon ; une éruption précurseur, caractérisée par un style éruptif en fontaine de feu, et une petite coulée mise en place après l'éruption climactique. Ces trois unités, compositionnellement et minéralogiquement identiques, proviennent de la même chambre magmatique, et permettent de mettre en évidence la diversité des processus éruptifs pouvant être engendrés par un seul et même corps magmatique. Une autre particularité de ce cycle est que le sanidine du Tuf de Fish Canyon a été choisi comme minéral de référence (standard) pour la méthode géochronologique $^{40}Ar/^{39}Ar$. Il est, de ce fait, important de déterminer au mieux l'évolution du magma ainsi que l'âge absolu de l'éruption, afin de comprendre les caractéristiques isotopiques de ce minéral, sur lequel repose un nombre important de datations d'autres événements géologiques.

Cette thèse est divisée en trois chapitres. Ce premier chapitre est un résumé général en français, abordant tous les aspects de ce travail de manière succincte. Les deux prochains chapitres, en anglais, correspondent chacun à un aspect du titre; la volcanologie et la pétrologie du système magmatique de Fish Canyon. Chaque sujet est traité de manière largement indépendante, reprenant à chaque fois le contexte géologique et la séquence éruptive du cycle de Fish Canyon. Ceci est dû au fait que ces deux chapitres seront soumis à la publication sous forme d'articles autonomes, le chapitre 2 étant d'ailleurs déjà publié (Bachmann et al., 2000). La géochronologie est, quant à elle, à un stade préliminaire et nécessite un travail supplémentaire avant de pouvoir tirer des conclusions utiles. Cette partie est inclue sous forme d'annexe à la fin de la thèse.

2. Contexte géologique

Les montagnes de San Juan, au sud de l'actuel état du Colorado, sont formées par des restes érosifs d'une intense activité volcanique tertiaire. Après une période d'environ quatre millions d'années, de 33 à 29 Ma, principalement caractérisée par l'émission de coulées de laves andésitiques, de l'activité explosive a brutalement fait son apparition. Au moins 17 grandes ignimbrites, avec des volumes oscillant entre 100 et 5000 km^3 et des compositions chimiques plus évoluées (principalement dacitiques), ont été mises en place en moins de trois millions d'années (29-26 Ma). Ces éruptions ont provoqué l'effondrement d'immenses calderas, regroupées en trois amas bien distincts, à l'ouest, au centre et au sud-est des affleurements actuels (Figure 1). Le cycle magmatique de Fish Canyon s'est déroulé il y a environ 28 Ma, dans la partie centrale du champ, lors d'une crise d'activité magmatique, pendant laquelle plus de 8'000 km^3 de dépôts volcaniques se sont mis en place en environ 2 millions d'années (Lipman et al., 1996).

L'origine tectonique du magmatisme à San

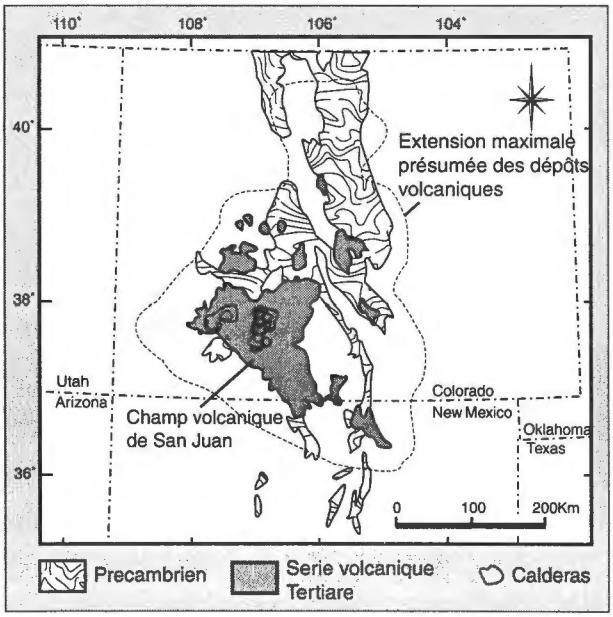

Figure 1: Localisation du champ volcanique de San Juan, ainsi que d'autres uintés extrusives et intrusives dans la région du Colorado et Nouveau Mexique (d'après Steven, 1975).

Juan reste controversée. Le champ volcanique se trouve à l'extrême nord d'une zone magmatique active liée à la subduction de la plaque de Farallon sous la plaque nord-américaine (Figure 2). Cette localisation le long d'une chaîne d'arc, soutenue par une signature géochimique des dépôts volcaniques généralement similaire aux magmas d'arc (Lipman et al., 1978) suggère que le magmatisme soit, à l'origine, lié à cette subduction. Toutefois, la position du champ est anormalement éloignée de la limite de plaque (>700 km), ce qui a poussé certains auteurs (Davis et al., 1993) à proposer comme alternative la refonte du manteau lithosphérique préalablement modifié par de la subduction lors d'une phase tectonique extensive.

L'apparition brutale des grandes éruptions explosives aux alentours de 29 Ma, mettant en place d'immenses nappes de ponce et de cendres chimiquement plus évoluées, indique une évolution dans le comportement des magmas de San Juan. Les signatures géochimiques et isotopiques de ces ignimbrites signalent une plus grande contribution crustale par rapport au magmas andésitiques antérieurs (Lipman et al., 1978; Riciputi et al., 1995) et la présence de calderas implique que les chambres magmatiques résidaient à faible profondeur. Cette différentiation progressive des magmas vers des compositions plus évoluées, ainsi que cette remontée des réservoirs de magma, a été interprétée comme la marque de la mise en place d'un batholite complexe dans la croûte supérieure (Lipman et al., 1978). Les résultats d'une campagne gravimétrique au début des années 1970 ont permis de mettre en évidence la plus importante anomalie négative de Bouguer d'Amérique du Nord dans la région des montagnes de San Juan (Plouff and Pakiser, 1972). Ces données requièrent la présence d'un corps de faible densité dans la partie supérieure de la croûte à l'aplomb du champ volcanique. L'association spatiale frappante entre l'anomalie de Bouguer et l'ex-

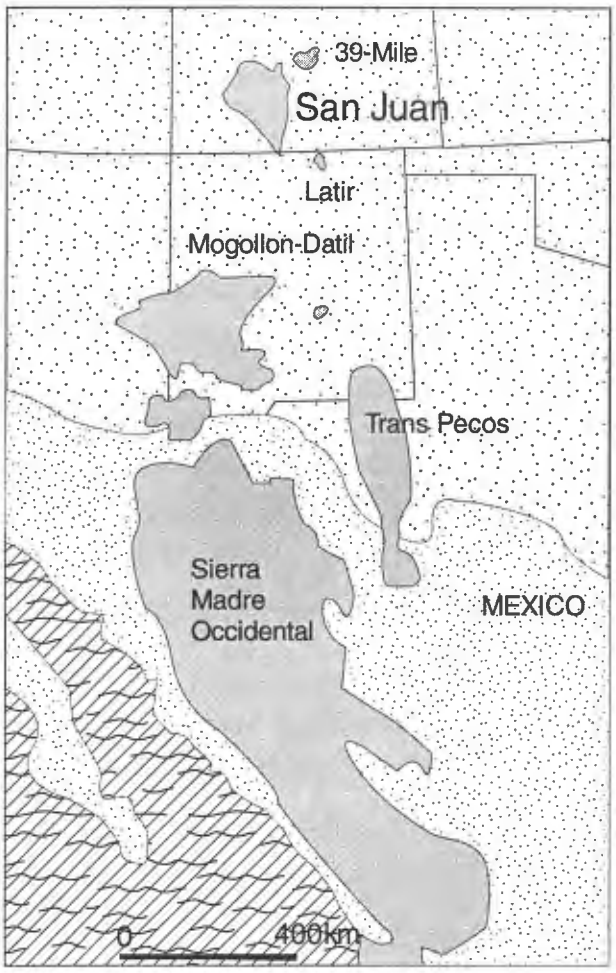

Figure 2: Alignements de champs volcaniques Tertiaires s'étirant de la Sierra Madre Occidental au Sud, montrant un volcanisme typique d'arc, jusqu'au champ volcanique de San Juan au Nord, montrant également des caractéristiques géochimiques de magmatisme lié à la subduction, mais se trouvant anormalement loin de la limite de plaque (<700 km). D'après Davis et al. (1993).

tension des produits volcaniques suggère que le corps provoquant l'anomalie soit génétiquement lié au magmatisme Tertiaire et corrobore donc l'interprétation de la synchronicité de l'activité volcanique et de la mise en place d'un batholite granitique dans la croûte supérieure.

Au début de cette étude, le cycle magmatique de Fish Canyon était supposé être constitué uniquement d'une grande ignimbrite, le Tuf de Fish Canyon, au volume estimé à plus de 3000 km^3. La caldera associée à cette éruption, la caldera de La Garita, était supposée être bien délimitée au nord, alors que sa partie sud avait apparemment été ensevelie par des cycles de calderas plus jeunes. Toutefois, une zone au sud de cet amas de calderas, montrant de nombreuses discordances géologiques, restait mal comprise. Des études de terrain détaillées, à partir de l'été 1995, ont permis de démontrer non seulement que la caldera de La Garita était plus grande qu'on ne le supposait (découverte de sa marge sud dans cette région), mais également qu'une unité précurseur de taille non négligeable (~200 km^3), que l'on a nommé la Dacite de Pagosa Peak, s'y était déposée (Figure 3). Complétant le cycle de Fish Canyon, une coulée de taille plus modeste (<1km^3), la Dacite de Nutras Creek, a été mise en évidence sur le flanc nord du dôme résurgent de la caldera de La Garita (Figure 3). Les âges de ces trois unités (c.f. chapitre 2 + annexe), obtenus par la méthode $^{40}Ar/^{39}Ar$, sont identiques, tenant compte de l'erreur analytique, et indiquent donc que cette séquence éruptive s'est mise en place rapidement.

Cette position du mur topographique de la caldera de La Garita a près de 30 km plus au sud que ce qui était cartographié auparavant double pratiquement sa surface, qui atteint maintenant plus de 2'500 km^2. Le volume du Tuf de Fish Canyon a donc été également revu à la hausse, réestimé à plus de 5000 km^3. La forme de la caldera, délimitée par le mur topographique, présente deux constrictions, suggérant un effondrement en trois segments (Figure 3). Ces trois segments ont des caractéristiques différentes. Le segment sud s'est effondré dans la région où l'éruption précurseur, la Dacite de Pagosa Peak, s'était mise en place, la tronquant en grande partie. Ce segment sud ne montre pas de résurgence ni d'activité éruptive post-caldera. Par contre, le segment nord présente une résurgence bien marquée, une coulée post-caldera, mais pas de dépôts précurseurs. Le segment central est, en majorité, enseveli par les calderas ultérieures, mais semble avoir suivi une évolution similaire au segment nord. Il est

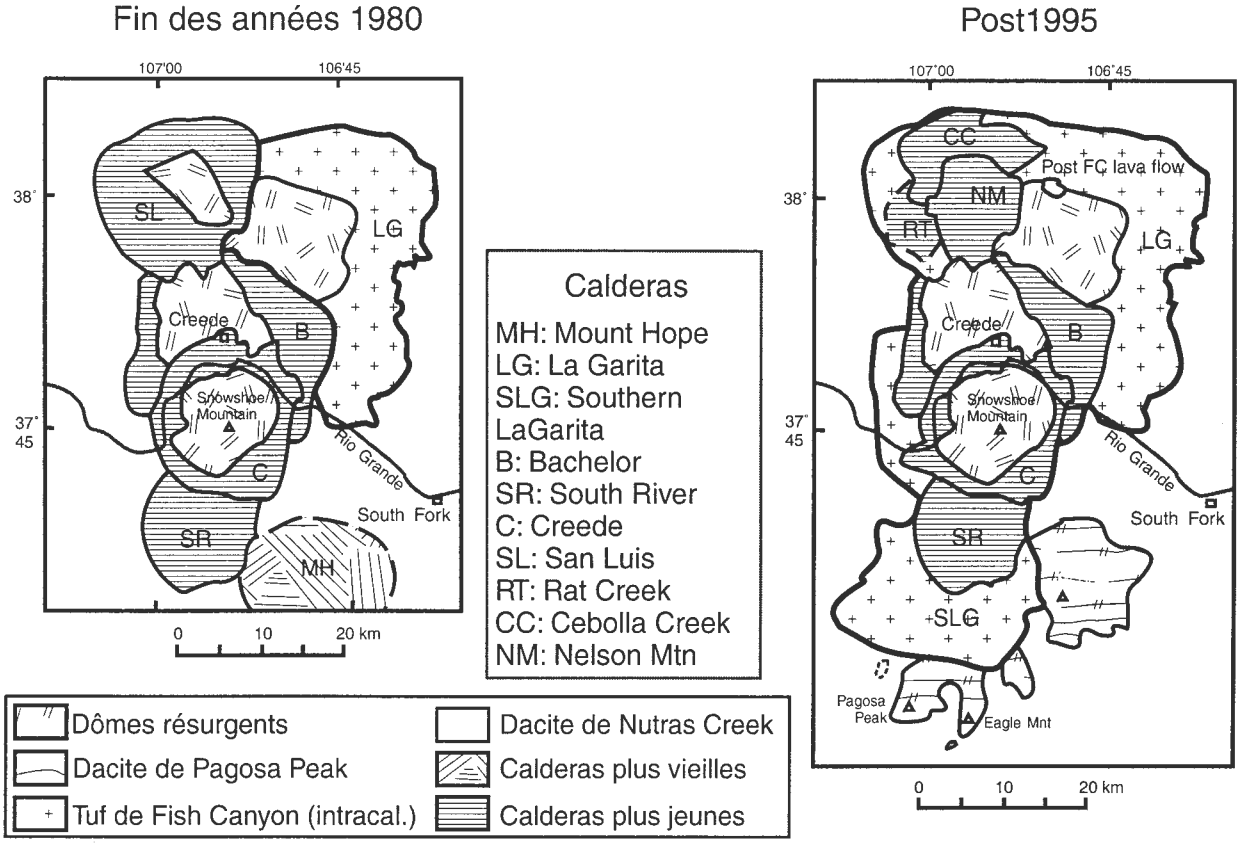

Figure 3: Distribution et limite des calderas de l'amas central du champ volcanique de San Juan à la fin des années 1980 et après l'été 1995. Sur la carte de droite. les unités du système de Fish Canyon, la Dacite de Pagosa Peak et la Dacite de Nutras Creek sont également représentées.

à noter également que des dépôts andésitiques importants, nommés Andésites de Huerto, se sont mis en place peu après la fin du cycle de Fish Canyon autour et dans le segment sud. Ils disparaissent assez rapidement en direction du nord, ne dépassant pas le segment central. Ces grandes coulées andésitiques sont probablement liées de près au cycle de Fish Canyon, étant donné que l'âge de ces dépôts est identique aux âges obtenus pour les trois unités du système magmatique de Fish Canyon (Parat et al., en prep.). Ce développement en segment ne semble pas être unique à la caldera de La Garita puisque d'autres grandes calderas, telle que celle de Yellowstone (Christiansen, 1984), montrent un découpage en plusieurs blocs à l'évolution post-effondrement largement indépendante.

L'évacuation de la chambre magmatique de Fish Canyon a donc suivi un cours totalement différent au sud et au nord. La Dacite de Pagosa Peak, au sud, représente la première manifestation volcanique de la chambre magmatique de Fish Canyon. Cette éruption précurseur a provoqué un réseau de failles syn-éruptives, déstabilisant le toit de toute la chambre, et a probablement déclenché l'éruption du Tuf de Fish Canyon. Des critères pétrographiques (Lipman et al., 1997) laissent supposer que l'effondrement de la caldera s'est ensuite propagé du sud au nord, en un temps relativement court, puisque tous les dépôts ne forment qu'une unité de refroidissement. La mise en place de la Dacite de Nutras Creek dans le segment nord, indique que la chambre magmatique était encore partiellement remplie à la suite de l'éruption du Tuf de Fish Canyon. Au contraire, dans la partie sud, la chambre était apparemment vide, puisque le magma andésitique de Huerto, pourtant plus dense que le magma dacitique de Fish Canyon, a pu atteindre la surface.

3. Volcanologie de la Dacite de Pagosa Peak

La Dacite de Pagosa Peak est constituée de dépôts pyroclastiques inhabituels. En effet, les textures, observées sur affleurement ou en lame mince, sont très différentes de celles de la majorité des dépôts pyroclastiques connus, et en particulier de celles du Tuf de Fish Canyon. Ce dernier peut-être considéré, outre son énorme volume, comme une ignimbrite typique. On y observe entre 10 et 20 % de fragments lithiques et de ponces, de taille centimétrique à décimétrique, prises dans une matrice constituée de fragments de cristaux et d'échardes de verre. La Dacite de Pagosa Peak, au contraire, est beaucoup moins fragmentée. Elle est constituée d'environ 50 % de blocs juvéniles, désignés par le terme " blob ", afin de les différencier des ponces et d'insister sur leurs formes sub-arrondies. Ces blobs sont en fait des ponces faiblement vésiculées (30-50 % de vésicules), en général de taille décimétrique, mais pouvant atteindre plusieurs mètres de diamètre. En lame mince, les échardes sont également beaucoup plus grandes et angulaires que les échardes habituellement observées dans les dépôt pyroclastiques. De plus, moins de 10 % des dépôts, à la base de l'unité, contiennent quelques rares fragments lithiques. Ceux-ci sont principalement arrachés aux conduits éruptifs et fournissent une indication sur la puissance explosive de l'éruption.

Ces dépôts se sont mis en place très rapidement, et se sont accumulés sur des épaisseurs dépassant 1 kilomètre par endroits. Une rétention de chaleur maximale a permis la soudure intense (" welding ") des dépôts, allant même jusqu'à permettre un écoulement post-emplacement (rhéomorphisme) dans les parties supérieures des sections les plus épaisses (Figure 4). Aucun centre éruptif de la Dacite de Pagosa Peak n'a pu être mis en évidence. Ces sources ont certainement été ensevelies par l'effondrement du segment sud de la caldera de La Garita. Toutefois, un réseau de failles spatialement relié aux dépôts de la Dacite de Pagosa Peak, montre des signes de mouvements syn-éruptifs (Figure 5). Ces failles sont tronquées par la caldera de la Garita, et s'étendaient certainement jusqu'à l'intérieur du segment sud. Nous pouvons donc conclure qu'elles ont probablement servi de conduit au magma lors de l'éruption, de ce fait largement fissurale. Ces failles ont formé une zone structurellement complexe, en horst et graben, dans le prolongement sud de la caldera de La Garita. Cet effondrement chaotique, désigné dans la littérature volcanologique par effondrement en piece-meal (par ex. Lipman, 1997b), est un phénomène rare et décrit uniquement pour des calderas anciennes (Branney and Kokelaar, 1994).

Les différences de textures entre les dépôts du Tuf de Fish Canyon et de la même chambre magmatique, permettent de conclure que les styles éruptifs ont été contrôlés principalement par des phénomènes syn-éruptifs, puisque les conditions initiales étaient identiques. Les observations effectuées sur les dépôts de la Dacite de Pagosa Peak, telles que l'absence de fragments lithiques, la faible fragmentation, la présence de ces grandes ponces faiblement vésiculées que sont les blobs et la rétention maximale de chaleur lors de la mise en place, indiquent que le style éruptif de la Dacite de Pagosa Peak était de faible énergie et que la fragmentation du magma s'est déclenchée à une vésicularité inférieure à celle observée dans la majorité des cas.

Le moteur d'une éruption explosive, sans participation d'eau externe au système, réside dans la quantité de gaz en solution dans le magma. Pour diminuer la puissance d'une éruption, il faut donc permettre un dégazage non-explosif au travers des murs fracturés, et donc perméables, des conduits magmatiques, lors de l'ascension du magma vers la surface. Ce phénomène est à l'origine de l'existence

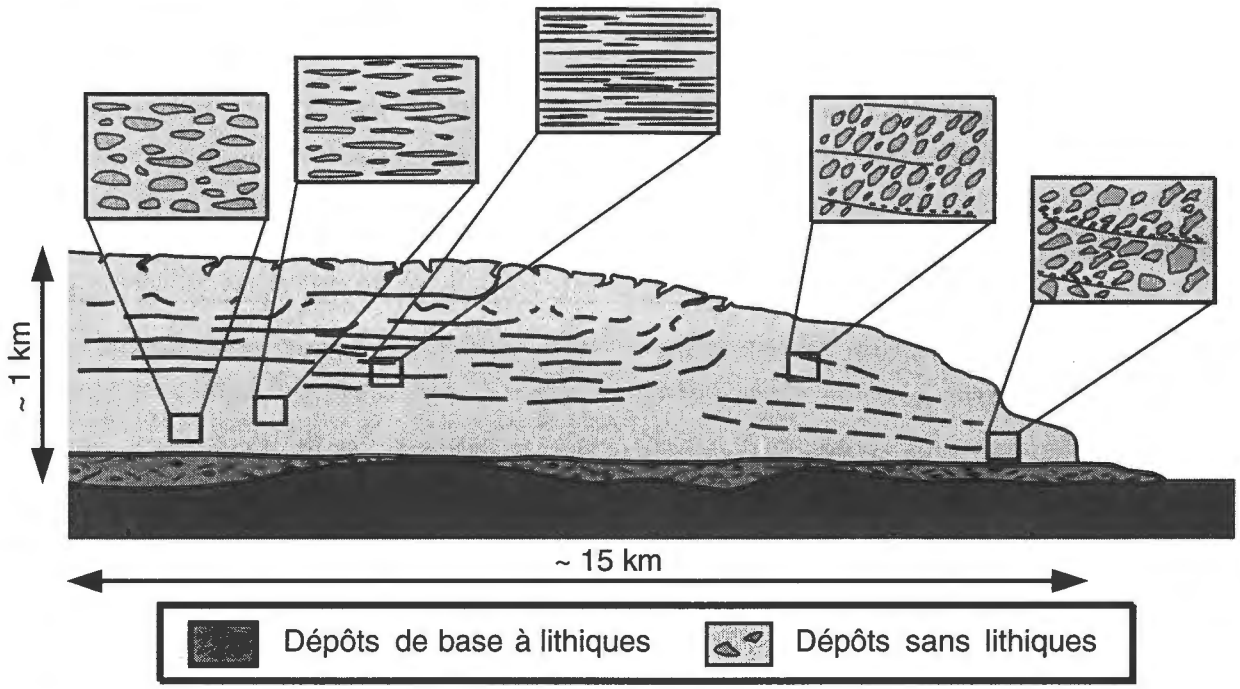

Figure 4: Coupe stratigraphique schématique de la Dacite de Pagosa Peak, montrant les proportions approximatives des dépôts avec et sans fragments lithiques. Les diagrammes rectangulaires représentent l'applatissement progressif des blobs dans la partie supérieure des dépôts proximaux.

de dômes de laves acides, pourtant riches en (Eichelberger et al., 1986; Sparks, 1997; Stasiuk et al., 1996) et semble inévitable pour expliquer le style éruptif de faible énergie de la Dacite de Dacite de Pagosa Peak, provenant de la Pagosa Peak, malgré un magma originellement très riche en gaz (~5%). Cependant, lors de ce dégazage passif syn-éruptif, des marques minéralogiques, telles que les bordures de réactions sur les hornblendes et la croissance de microlites dans le liquide interstitiel, se développent très rapidement à la suite des changements thermodynamiques provoqués par cette perte en gaz. En particulier, une étude sur le Pinatubo (Hammer et al., 1999) a pu démontrer que les microlites peuvent apparaître en moins d'une heure après le dégazage. Comme les dépôts de la Dacite de Pagosa Peak ne présentent aucun de ces signes minéralogiques, le dégazage a dû se faire rapidement et a probablement pu être aussi efficace grâce aux conduits fissuraux qui ont dirigé l'éruption. Ces conduits ont permis d'obtenir un rapport [surface de conduits/ volume de magma] élevé.

En résumé, les dépôts pyroclastiques du système de Fish Canyon suggèrent une séquence éruptive initiée par une phase explosive relativement puissante, durant laquelle s'est mise en place la partie basale de la Dacite de Pagosa Peak contenant des fragments lithiques. L'éruption a ensuite évolué vers un style en fontaine de feu produisant des coulées pyroclastiques de faible énergie. Ce style particulier a probablement été induit par l'ouverture de nombreuses bouches éruptives le long des failles syn-éruptives, permettant une diminution de l'explosivité de l'éruption grâce à un dégazage du magma au travers des murs des conduits. Les mouvements de sol importants liés à cette éruption ont probablement déstabilisé toute la chambre magmatique de Fish Canyon, et déclenché l'effondrement de la caldera de La Garita ainsi que l'évacuation rapide de plus de 5'000 km^3 de magma (Figure 6).

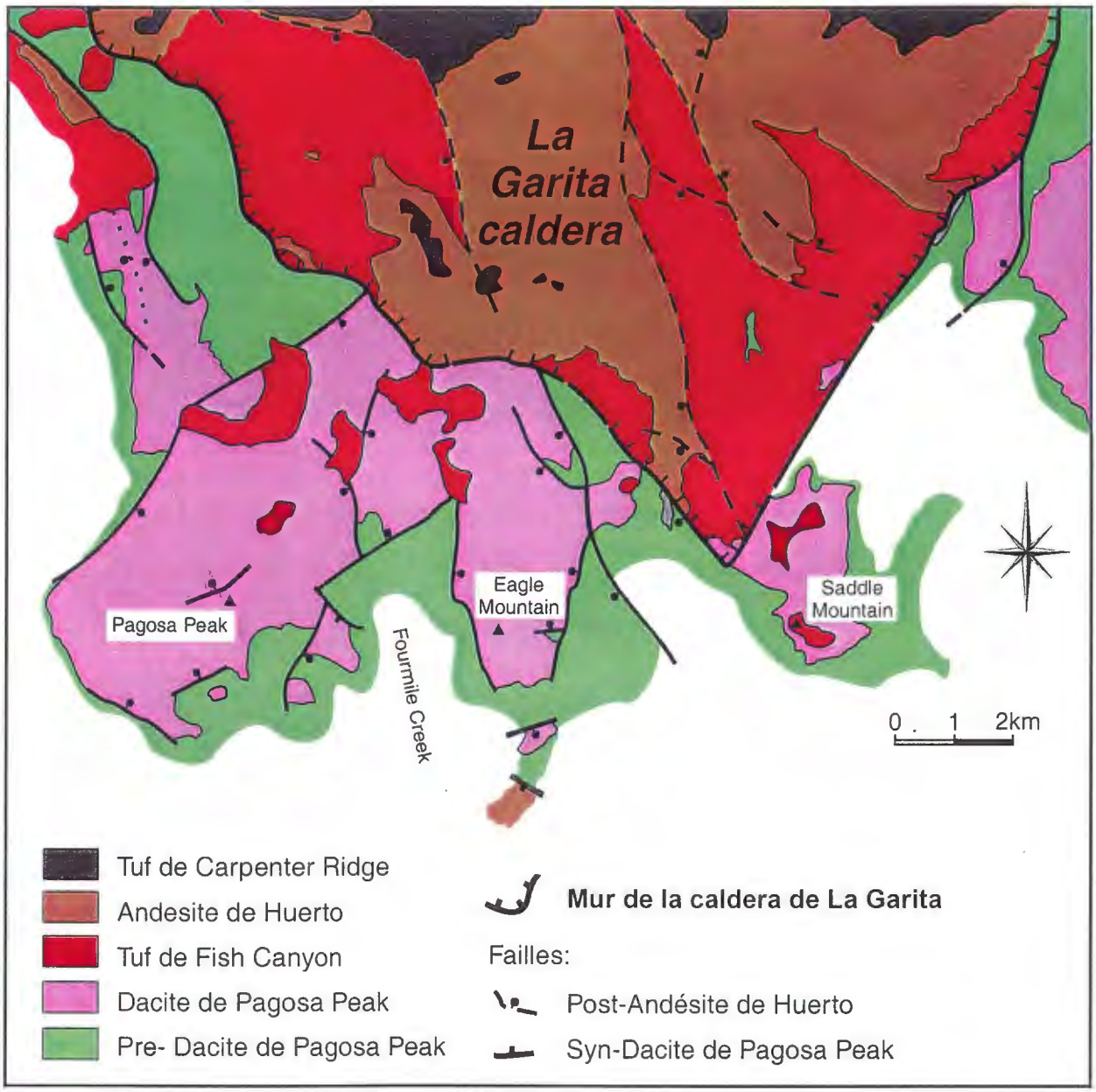

Figure 5: Carte géologique de la partie sud de la caldera de La Garita, montrant les failles actives lors de l'éruption de la Dacite de Pagosa Peak. Ces failles forment deux grabens principaux séparés par un horst, et sont recoupées au nord par la marge sud de la caldera de La Garita.

4. Evolution pétrologique du magma de Fish Canyon

Le magma de Fish Canyon a été le sujet de nombreuses recherches par le passé, le volume exceptionnel de l'éruption ayant attiré la curiosité des géologues dès les premières études (Lipman, 1975). Les observations effectuées lors de ces travaux préliminaires ont permis de dégager des caractéristiques inhabituelles pour une grande ignimbrite, telles que l'absence apparente de zonation chimique dans les dépôts et l'importante teneur en cristaux, s'élevant à près de 50 %. Ces particularités ont été également observées dans d'autres unités, et ont mené à la définition d'un groupe, désigné par le terme " Intermédiaires Monotones ", pour insister sur leur composition intermédiaire (dacitique) et homogène (Hildreth, 1981). Afin de mieux comprendre ces Intermédiaires Monotones, Whitney and Stormer (1985) ont conduit une étude détaillée axée principalement sur les textures, la géochimie et les conditions physico-chimiques qui régnaient dans la cham-

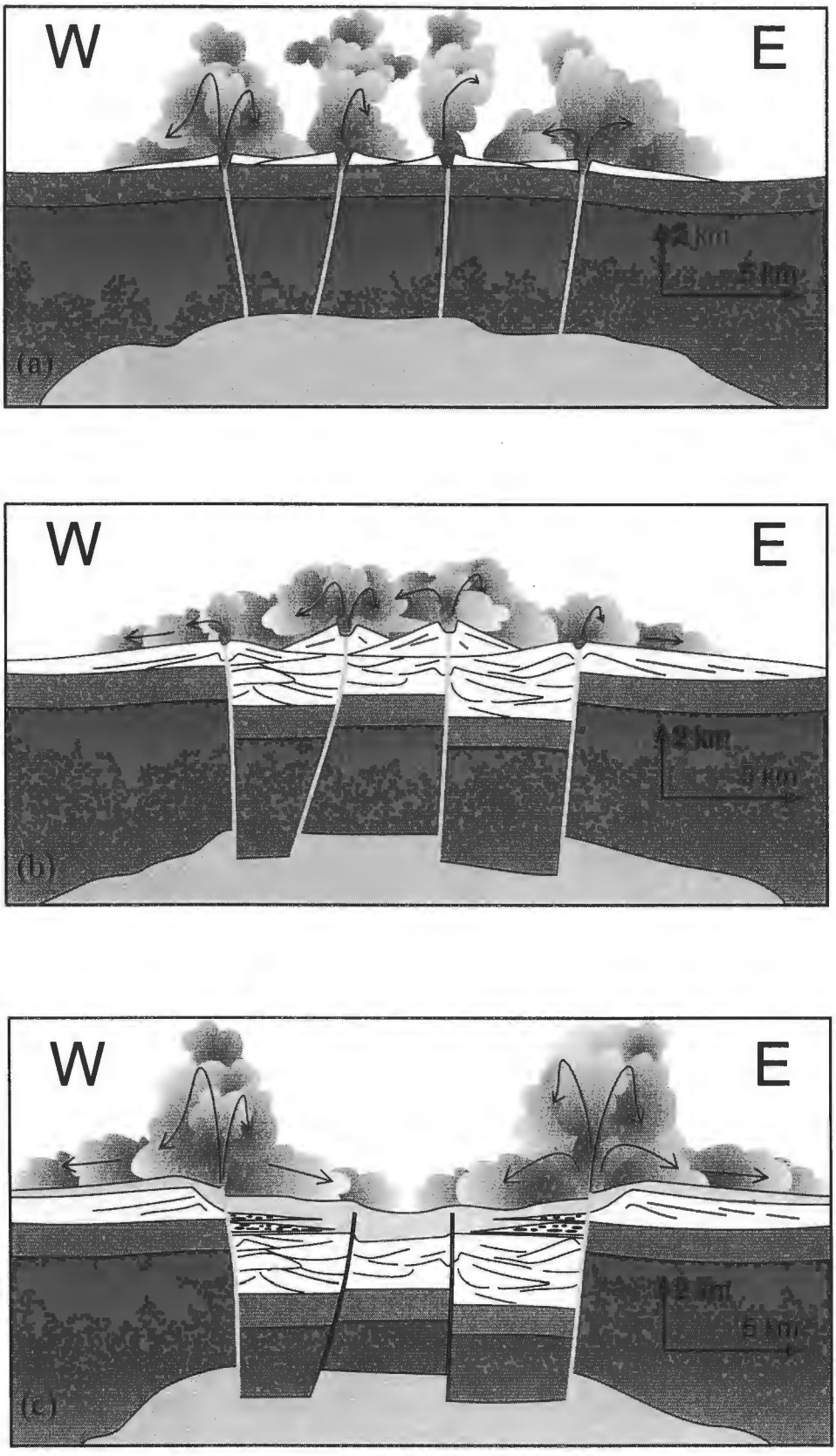

Fig. 12: Séquence éruptive du système magmatique de Fish Canyon. (a) Phase initiale de la Dacite de Peak Dacite: mise en place des dépôts contenant des fragments lithiques à la base de l'unité. (b) Phase principale de la Dacite de Pagosa Peak, montrant des colonnes de basse altitude et l'accumulation de dépôts très épais dans des grabens en formation. (c) Eruption du Tuf de Fish Canyon, déclenché par la dépressurisation de la chambre magmatique par l'éruption de la Dacite de Pagosa Peak.

bre avant l'éruption. Deux points controversés de leur étude, l'absence de gradients géochimiques dans la chambre magmatique et la forte pression de cristallisation enregistrée par les minéraux, ont motivé d'autres recherches (Johnson and Rutherford, 1989 ; Grunder and Boden, 1987) qui ont permis de préciser, et parfois corriger, certaines valeurs. En particulier, Johnson and Rutherford (1989) ont mis en évidence, grâce à un nouveau géobaromètre, que la pression à laquelle les minéraux avaient cristallisé était beaucoup moins élevée que celle déterminée par Whitney and Stormer (1985). La valeur fournie par le géobaromètre est compatible cette fois avec une chambre magmatique résidant dans la croûte supérieure (~6-8 km de prof.), une condition indispensable au développement d'une caldera. A ce stade, le magma de Fish Canyon était supposé avoir été généré dans la croûte inférieure, puis s'être mis en place dans la croûte supérieure, à moins de 10 km de profondeur, avant d'avoir été évacué vers la surface par l'éruption.

Les découvertes de la Dacite de Pagosa Peak et de la Dacite de Nutras Creek ont fondamentalement changé l'interprétation pétrologique du magma de Fish Canyon. La présence de faciès non fragmenté dans ces deux unités a donné accès à un magma n'ayant subi aucune transformation, permettant d'obtenir la composition réelle du magma et d'observer des textures magmatiques mieux conservées. Les analyses chimiques sur ces différentes unités ont confirmé l'homogénéité du magma de Fish Canyon, puisque aucune différence significative n'est décelable entre la Dacite de Pagosa Peak et la Dacite de Nutras Creek, pourtant séparées par l'évacuation de plus de 5000 km^3 de magma. L'observation des textures, au contraire, a mené à une réintreprétation de l'évolution du magma. Des textures de déséquilibre évidentes des feldspaths et quartz ont rapidement permis de conclure que le magma avait subi un réchauffement peu de temps avant son éruption (Figure 7). D'autres arguments, tel le comportement des éléments trace dans le liquide interstitiel et d'importantes zonations chimiques dans les minéraux (Figure 8), sont venus renforcer l'hypothèse d'un réchauffement pré-éruptif ayant mené à une refonte partielle d'un corps magmatique largement cristallisé. Plusieurs générations d'excroissances de plagioclase sur des feldspaths alcalins, textures que l'on nomme " Rapakivi " (Sederholm, 1891) et qui se forment principalement lors de fluctuations de la température dans des magmas dacitiques (Stimac and Wark, 1992), suggèrent que le magma a subi plusieurs périodes de réchauffement entrecoupés par des phases de cristallisation. Des fragments plutoniques du magma de Fish Canyon ont été entraînés par les diverses éruptions. On retrouve en effet dans le Tuf de Fish Canyon des xénolites holocristallines ayant la même minéralogie et des compositions similaires, tant au niveau roche totale qu'au niveau des phases minérales. Ces xénolites représentent des reliques d'un faciès complètement cristallisé, probablement situé sur les bordures de la chambre magmatique. Il existe également des agrégats polycristallins disséminés

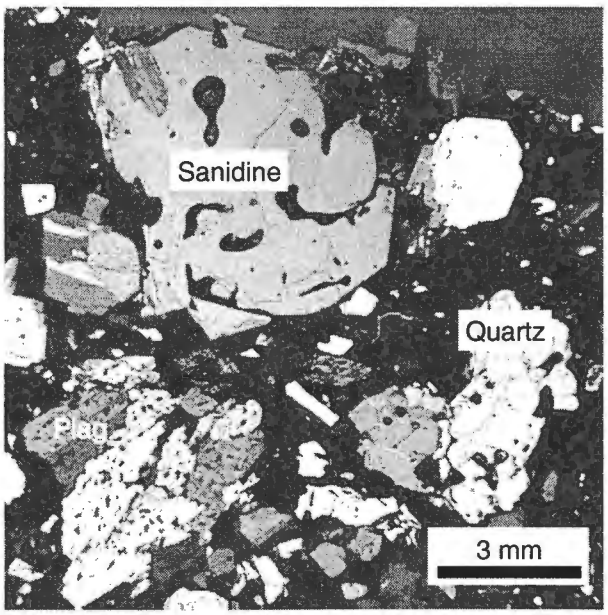

Figure 7: Photographie d'une lame mince de la Dacite de Nutras Creek, montrant des cristaux de quartz, sanidine et plagioclase résorbés.

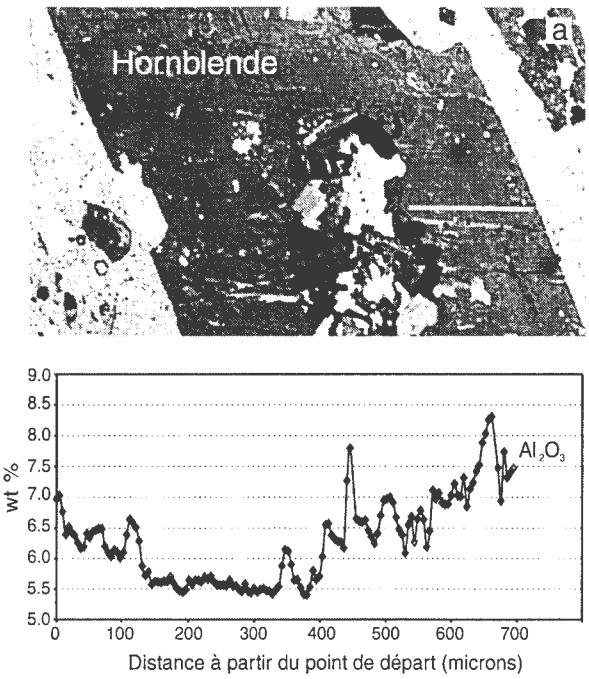

Figure 8: Zonation en aluminium dans une grande hornblende de la Dacite de Pagosa Peak. L'augmentation importante en Al_2O_3 vers la bordure est interprétée comme la marque d'une augmentation de la température peu de temps avant l'éruption.

dans le magma, présent dans les trois unités du système, qui ont conservé, malgré une refonte partielle, des contacts entre grains sans verre interstitiel (c.-à-d. plutoniques). La position de la norme du verre interstitiel proche du point eutectique à 2 kb dans le système haplogranitique (Qtz-Ab-Or), ainsi que la refonte n'affectant que le quartz et les deux feldspaths, suggèrent que la réaction responsable de la refonte soit une fusion à l'eutectique à faible pression.

Pour provoquer cette refonte partielle, un apport thermique important est nécessaire. Plusieurs marques d'interactions entre le magma de Fish Canyon et un magma plus primitif suggèrent que cette refonte a été provoquée par la réinjection de magma plus mafique, et donc plus chaud, à la base de la chambre magmatique de Fish Canyon. Des inclusions mafiques sont présentes dans la partie supérieure du faciès intracaldera du Tuf de Fish Canyon, qui représentent la partie profonde de la chambre. De plus, les texture Rapakivi semblent être une conséquence fréquente d'interactions entre magmas mafiques et magmas felsiques (Bussy, 1990; Hibbard, 1981; Wark and Stimac, 1992).

L'étude pétrologique du magma de Fish Canyon suggère donc une évolution par oscillations thermiques dans la croûte supérieure. Le magma s'est apparemment refroidi à une température proche de son solidus, comme l'indique l'assemblage minéralogique très varié et la présence de reliques plutoniques co-magmatiques. Il se serait ensuite réchauffé et aurait partiellement refondu lors d'arrivées de chaleur du manteau sous la forme de magma mafique. Ce processus de réactivation de plutons en formation peut donc, dans certains cas, mené à l'évacuation explosive de ces corps magmatiques. Ce modèle a déjà été invoqué par Mahood (1990) pour le système de Long Valley, afin de concilier des indices géochronologiques indiquant un temps de résidence de plusieurs centaines de milliers d'années dans la croûte supérieure (Halliday et al., 1989 ; van den Bogaard et Schirnick, 1995) avec la difficulté de maintenir des magmas au-dessus de leur solidus pendant une période prolongée dans les conditions relativement froides de la croûte supérieure (Sparks et al., 1990). Toutefois, les bases de l'argumentation de ce modèle sont largement spéculatives, le magma ne présentant aucune indication d'un processus de refonte. Le système de Fish Canyon apporte, par contre, des observations solides quant à l'existence de ces mécanismes dans la croûte supérieure.

5. Géochronologie du système de Fish Canyon

La motivation principale de l'étude géochronologique du système de Fish Canyon, par la méthode $^{40}Ar/^{39}Ar$, était d'essayer de différencier les âges éruptifs des trois unités, afin de mieux

contraindre la vitesse à laquelle ces grands cycles de calderas peuvent se développer. La question de l'âge absolu de l'éruption pour cette unité de référence largement utilisée en géochronologie $^{40}Ar/^{39}Ar$ reste sujet à discussion, mais ne sera pas abordé spécifiquement. La méthode appliquée dans le cas présent n'est pas apte à apporter une réponse précise et d'autres approches devront être tentées afin de résoudre cette question capitale.

Les résultats ont montré que la séquence éruptive s'est déroulée plus rapidement que la résolution pouvant être obtenue par la géochronologie. Un intervalle maximal de ~0.5 Ma a été défini sur la base de la méthode $^{40}Ar/^{39}Ar$, mais il est possible que des données supplémentaires par U-Pb sur les zircons permettent une réduction de cet intervalle. Cependant, la datation des différentes phases minérales contenues dans le même échantillon (Tuf de Fish Canyon) a soulevé des complications internes. Au lieu d'observer des âges concordants entre les différents minéraux, ceux-ci ont montré des disparités parfois importantes. Le minéral de référence, la sanidine, a été datée par plusieurs méthodes et semble converger vers un âge de 28 Ma (27.98, Villeneuve et al., 1998 ; 28.03 ± 0.18 Ma, Renne et al., 1994; 28.04 ± 0.45 Ma, Renne et Min, 1998). Par rapport à cette valeur, les zircons sont environ 400'000 ans plus vieux (~28.4 Ma; Oberli et al., 1990; Schmitz and Bowring, 1999), alors que les autres minéraux (hornblende, biotite, plagioclase) se regroupent aux alentours de 28.2 Ma (Figure 9). Dans le contexte d'oscillation thermique suggéré par l'étude pétrologique du magma de Fish Canyon, ces différences pourraient s'expliquer par un début d'accumulation des isotopes radiogéniques lors de la ou des périodes froides, suivi d'une réinitialisation partielle lors du réchauffement. Les différentes phases minérales, n'ayant pas les mêmes températures de fermeture, pourraient logiquement montrer des âges non concordants. Les zircons sont connus pour être très réfractaires et conserver des traces de composants hérités de stades de cristallisation antérieurs.

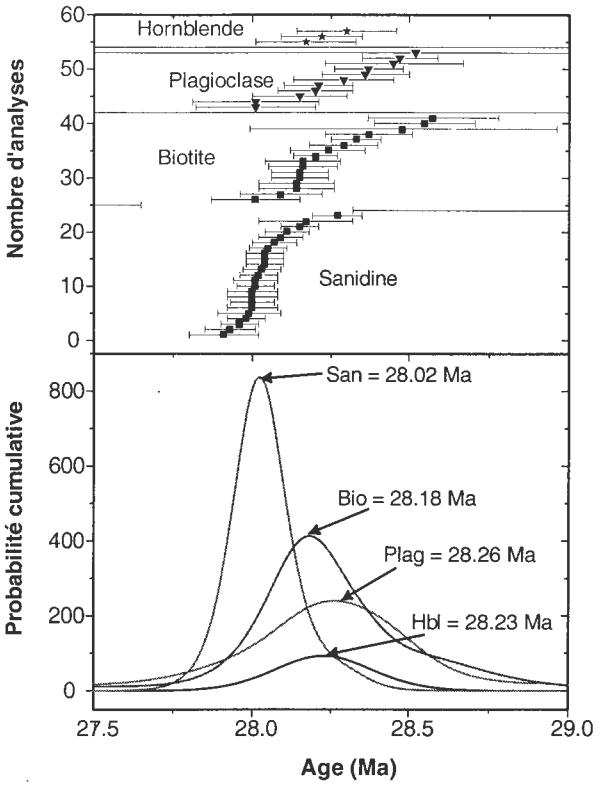

Figure 9: Idéogramme (Deino and Potts, 1992) montrant les différences d'âges entre les quatre principales phases minérales du Tuf de Fish Canyon.

Ce processus de réinitialisation partielle est soutenu par l'analyse $^{40}Ar/^{39}Ar$ par chauffage incrémental d'un mégacristal d'environ 2 cm de diamètre récolté dans une ponce du faciès intracaldera du Tuf de Fish Canyon. Les incréments de haute température montrent des âges légèrement plus vieux que ceux obtenus sur les incréments de basses et moyennes température (Figure 10). Ce type de résultat est typiquement observé lors d'analyses de xénolites partiellement réinitialisées par leur résidence dans le magma hôte (Gillespie et al., 1982; Gillespie et al., 1984) et ont donc été interprétée comme une indication d'argon radiogénique hérité (Singer et al., 1998). Ces diverses indications de réinitialisation partielle des systèmes isotopiques dans le magma de Fish Canyon restent au stade d'hypothèse et nécessite une documentation plus rigoureuse pour être confirmée. Des problèmes de fiabilité de

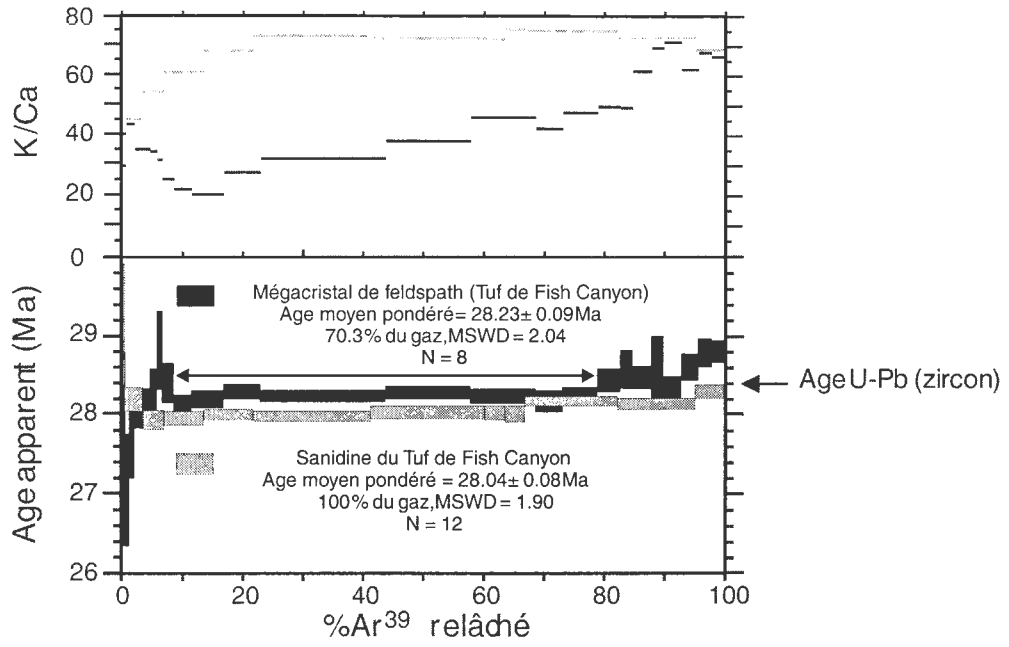

Figure 10: Analyse par chauffage incrémental d'un mégacristal de feldspath échantillonné dans une ponce du faciès intracaldera du Tuf de Fish Canyon, montrant une augmentation des âges dans les incréments à haute température, indiquant la présence d'argon hérité dans les parties les plus résistantes du minéral.

la méthode $^{40}Ar/^{39}Ar$, mis en exergue ces dernières années (Min et al., 2000; Renne et al., 1998) pourraient être à l'origine d'une partie de la différence d'âge entre les sanidines et les zircons. De plus, les disparités entre les âges des sanidines et ceux des hornblendes, biotites et plagioclases du Tuf de Fish Canyon sont de faible amplitude et le comportement de l'argon pendant les périodes de réchauffement est encore mal compris. Les températures de fermeture des systèmes isotopiques, seuil à partir duquel la diffusion s'est suffisamment ralentie pour empêcher la déperdition des isotopes radiogéniques produits et donc permettre un calcul d'âge, sont peu fiables (McDougall and Harrison, 1999), et l'efficacité de la rétention de composants hérités lors de réchauffement par les différentes phases minérales n'est pratiquement pas quantifiée. Beaucoup de travail reste donc à faire dans ce domaine avant de pouvoir tirer des conclusions rigoureuses sur cette étude géochronologique, tant sur les processus de réinitialisation des systèmes isotopiques que sur l'âge absolu de l'éruption.

6. Conclusions générales et directions futures

Le système magmatique de Fish Canyon est extrêmement riche en informations portant sur la volcanologie et la pétrologie des grands cycles de calderas. Le style éruptif inhabituel de la Dacite de Pagosa Peak, partant toutefois des mêmes conditions initiales que le Tuf de Fish Canyon, a confirmé que des phénomènes syn-éruptifs, en l'occurrence le dégazage non-explosif du magma lors de son ascension, peuvent avoir une importance capitale sur l'explosivité des éruptions, même pour des volumes aussi considérables que ceux mis en jeu dans ce système. La séquence éruptive du système de Fish Canyon, montrant une éruption précurseur de faible énergie et ne représentant qu'une infime partie du magma présent dans la chambre magmatique, indique que l'évacuation de ces chambres gigantesques peut commencer par une fuite relativement restreinte et que les phase initiales ne sont pas nécessairement les plus explosives.

L'analyse pétrogénétique a, quant à elle,

montré que ces plutons en devenir sont de véritable bombes à retardement. Des réinjections de magma mafique à la base de ces batholites peuvent partiellement refondre, ou réactiver, ces chambres magmatiques en grande partie solide et inverser l'évolution de ces plutons en formation pour engendrer d'immenses éruptions explosives. Ces épisodes de réinjections sont évidemment très difficilement décelables à la surface, et ces systèmes posent donc d'énormes problèmes quant à la prédiction de telles éruptions.

Le cycle magmatique de Fish Canyon va permettre d'aborder plusieurs autres questions importantes concernant les processus pétrologiques prenant place dans la croûte. Tout d'abord, une étude géochronologique détaillée sur les xénolites holocristallines contenues dans le Tuf de Fish Canyon ainsi que sur les zircons va peut-être apporter des contraintes de temps plus précises quant à la durée des processus de réactivation des chambres magmatiques dans la croûte supérieure. La datation des zircons a déjà été utilisée pour estimer le temps de résidence des magmas dans la croûte du fait de leur caractère très réfractaire (Brown and Fletcher, 1999; Reid et al., 1997). Les zircons du Fish Canyon, datés par deux laboratoires indépendants à ~28.4 (Oberli et al., 1990 ; Schmitz and Bowring, 1999) sont pourtant texturellement assez simples, ne présentant que très rarement des centres hérités (Schmitz and Bowring, 1999). Si la majorité des zircons du Fish Canyon ne montrent qu'une phase de croissance, ou que leurs bordures donnent des âges autour de 28.4 Ma, cette valeur pourrait être considérée comme une estimation de l'âge de cristallisation du batholite.

L'étude de feldspaths alcalins des xénolites par la méthode $^{40}Ar/^{39}Ar$ ouvre une seconde voie pour obtenir des informations sur la durée des processus de réactivation d'une chambre magmatique. Considérant que ces xénolites ont cristallisé pendant les périodes les plus froides du système, ces minéraux sont susceptibles de fournir un âge proche du début de la refonte si, toutefois, la réinitialisation due au réchauffement lors de la résidence dans le magma n'a pas été complète. La méthode $^{40}Ar/^{39}Ar$ permet de palier partiellement à ce problème en obtenant des âges à différentes températures sur le même échantillon. Les incréments de haute température permettent le dégazage des parties les plus résistantes des cristaux, et montrent souvent des âges plus élevés (Heizler et al., 1999), comme il a été observé avec le mégacristal (Figure 11). Cette caractéristique suggère que les parties les plus résistantes du cristal ont gardé en mémoire un âge qui s'approche de celui de la cristallisation des minéraux. Les 28 Ma du système de Fish Canyon pose une limite à la résolution atteignable pour différencier deux âges. L'erreur analytique des datations $^{40}Ar/^{39}Ar$ comportent sont de l'ordre de 0.3 à 0.5 % pour une roche de cet âge. Etant donné que la durée des phénomènes de réactivation des chambres magmatiques ne devrait pas dépasser le demi-million d'années, la probabilité d'obtenir une différence d'âge significative entre les xénolites et le Tuf de Fish Canyon est faible. Pour palier à ce problème, une unité plus jeune, l'ignimbrite de Kos (~160'000 ans ; Smith et al., 1996), qui contient également des xénolites co-magmatiques et qui est supposé avoir suivi une évolution similaire à celle du magma de Fish Canyon (Keller, 1969), est également datée en parallèle afin d'augmenter les chances du succès dans cette étude.

Le magma Fish Canyon offre d'autres directions d'étude susceptibles d'apporter des informations intéressantes sur certains processus magmatiques. La question de la chaleur nécessaire pour refondre une telle masse de magma dans la croûte supérieure revient de manière fréquente lorsque la formation du magma de Fish Canyon est discutée. En effet, il faut envisager un flux de chaleur extrê-

mement important, qui doit être transféré du manteau par le biais de magma basaltique, pour permettre la réactivation de plus de 5'000 km^3 de magma. Le cas du Fish Canyon est idéal pour tenter de mieux quantifier, au travers d'un modèle thermodynamique, les transferts de chaleur dans la croûte, grâce aux nombreuses données récoltées sur les conditions physico-chimiques du système ainsi que sur le magma mafique probablement à l'origine de cette refonte partielle (formation de Huerto ; Parat et al., en prep.). De plus, l'argument pétrogénétique portant sur les teneurs en Ba et Sr du verre interstitiel pourrait être développé dans l'espoir d'apporter un critère simple de distinction entre magmas rhyolitiques à l'évolution dominée par la cristallisation fractionnée et ceux dont l'origine est liée à la refonte de roches crustales riches en feldspaths. Une étude portant sur plusieurs champs volcaniques et de nombreuses unités pourrait définir plus précisément la validité de ce critère, et permettre, si les tests s'avèrent concluants, son utilisation sur des systèmes dont l'origine pétrogénétique est controversée. Finalement, le comportement de l'aluminium dans les hornblendes pourrait également être exploré plus en détail. Ce sujet, largement abordé dans plusieurs (Ague, 1997; Anderson and Smith, 1995; Hammarstrom and Zen, 1992; Poli and Schmidt, 1992; Rutherford and Johnson, 1992), a été testé spécifiquement sur les hornblendes du Fish Canyon par une étude expérimentale (Johnson and Rutherford, 1989). Les nouvelles données apportées par cette étude sont susceptibles d'apporter des moyens d'améliorer ce géothemobaromètre au potentiel indéniable.

References

Ague, J.J. (1997) Thermodynamic calculation of emplacement pressures for batholithic rocks, California; implications for the aluminum-in-hornblende barometer. Geology (Boulder), 25(6), 563-566.

Ambrose, S.H. (1998) Late Pleistocene human population bottlenecks, volcanic winter, and the differentiation of modern humans. Journal of Human Evolution, 34, 623-651.

Anderson, J.L., and Smith, D.R. (1995) The effects of temperature and f*O2* on the Al-in-hornblende barometer. American Mineralogist, 80, 549-559.

Bachmann, O., Dungan, M.A., and Lipman, P.W. (2000) Voluminous lava-like precursor to a major ash-flow tuff: low-column pyroclastic eruption of the Pagosa Peak Dacite, San Juan Volcanic field, Colorado. Journal of Volcanology and Geothermal Research, 98, 153-171.

Bacon, C.R. (1983) Eruptive history of Mount Mazama and Crater Lake caldera, Cascade Range, U.S.A. Journal of Volcanology and Geothermal Research, 18, 57-115.

Bond, A., and Sparks, R.S.J. (1976) The Minoan eruption of Santorini, Greece. Journal of the Geological Society of London, 132, 1-16.

Branney, M.J., and Kokelaar, P. (1994) Volcanoteconic faulting, soft-state deformation, and rheomorphism of tuffs during development of a piece-meal caldera, English Lake District. Geol Soc Amer Bull, 106, 507-530.

Brown, S.J.A., and Fletcher, I.R. (1999) SHRIMP U-Pb dating of hte preeruption growth history of zirconsfrom the 340 ka Whakamaru Ignimbrite, New Zealand: Evidence for >250 k.y. magma residence times. Geology, 27(11), 1035-1038.

Bussy, F. (1990) The rapakivi texture of feldspars in a plutonic mixing environment; a dissolution-recrystallization process? Granite; proceedings of the symposium celebrating the 70th birthday of W. S. Pitcher. Geological Journal, 25(3-4), 319-324.

Chesner, C.A. (1998) Petrogenesis of the Toba Tuffs, Sumatra, Indonesia. Journal of Petrology, 39(3), 397-438.

Christiansen, R.L. (1984) Yellowstone magmatic evolution: Its bearing on understanding large-volume explosive volcanism. Explosive Volcanism: Its

inception, evolution, and hazards. National Research Council Studies in Geophysics.National Academy Press, Washington D.C., 84-95.

Cook, E.F. (1959) Ignimbrite bibliography. Idaho Bureau of Mines and Geology Information Circular, 4, 30 p.

Davis, J.M., Elston, W.E., and Hawkesworth, C.J. (1993) Basic and intermediate volcanism of the Mogollon-Datil volcanic field: implications for mid-Tertiary tectonic transitions in southwestern New Mexico, USA. Geological Society Special Publications, 76, 469-488.

De Natale, G., and Pingue, F. (1993) Ground deformation in collapsed caldera structures. Journal of Volcanology and Geothermal Research, 57, 19-38.

de Silva, S.L., and Zielinski, G.A. (1998) Global influence of the AD 1600 eruption of Huayanaputina, Peru. Nature, 393(4), 455-457.

Eichelberger, J.C., Carrigan, C.R., Westrich, H.R., and Price, R.H. (1986) Non-explosive silicic volcanism. Nature, 323, 598-602.

Gillespie, A.R., Huneke, J.C., and Wasserburg, G.J. (1982) An assessment of ^{40}Ar-^{39}Ar dating of incompletely degassed xenoliths. JGR. Journal of Geophysical Research. B, 87, 9247-9257.

Gillespie, A.R., Huneke, J.C., and Wasserburg, G.J. (1984) Eruption age of a approximately 100,000-year-old basalt from ^{40}Ar-^{39}Ar analysis of partially degassed xenoliths. JGR. Journal of Geophysical Research. B, 89, 1033-1048.

Hammarstrom, J.M., and Zen, E.-a. (1992) Discussion of Blundy and Holland's (1990) "Calcic amphibole equilibria and a new amphibole-plagioclase geothermometer". Contributions to Mineralogy and Petrology, 111, 264-266.

Hammer, J.E., Cashman, K.V., Hoblitt, R.P., and Newman, S. (1999) Degassing and microlite crystallization during pre-climactic events of the 1991 eruption of Mt. Pinatubo, Phillipines. Bull Volcanol, 60, 355-380.

Heizler, M.T., Perry, F.V., Crowe, B.M., Peters, L., and Appelt, R. (1999) The age of the Lathrop Wells volcanic center: An $^{40}Ar/^{39}Ar$ dating investigation. Journal of Geophysical Research, 104(B1), 767-804.

Hibbard, M.J. (1981) The magma mixing origin of mantled feldspars. Contribution to Mineralogy and Petrology, 76, 158-170.

Hildreth, W. (1981) Gradients in silicic magma chambers: Implications for lithospheric magmatism. Journal of Geophysical Research, 86(B11), 10153-10192.

Johnson, M.C., and Rutherford, M.J. (1989) Experimental calibration of the aluminum-in-hornblende geobarometer with application to Long Valley Caldera (California) volcanic rocks. Geology (Boulder), 17, 837-841.

Lipman, P. (1997a) Chasing the volcano. Earth (Waukesha, Wis.), 6, 32-39.

Lipman, P.W. (1997b) Subsidence of ash-flow calderas: relation to caldera size and magma-chamber geometry. Bulletin of Volcanology, 59, 198-218.

Lipman, P.W., Doe, B., and Hedge, C. (1978) Petrologic evolution of the San Juan volcanic field, Southwestern Colorado: Pb and Sr isotope evidence. Geological Society of America Bulletin, 89, 59-82.

Lipman, P.W., Dungan, M.A., and Bachmann, O. (1997) Comagmatic granophyric granite in the Fish Canyon Tuff, Colorado: Implications for magma-chamber processes during a large ash-flow eruption. Geology, 25(10), 915-918.

Lipman, P.W., Dungan, M.A., Brown, L.L., and Deino, A.L. (1996) Recurrent eruption and subsidence at the Platoro Caldera complex, southeastern San Juan volcanic field, Colorado; new tales from old tuffs. Geological Society of America Bulletin, 108, 1039-1055.

McBirney, A.R. (1990) An historical note on the origin of calderas. Journal of Volcanology and Geothermal Research, 42, 303-306.

McDougall, I., and Harrison, T.M. (1999) Geochronology and Thermochronology by the $^{40}Ar/^{39}Ar$ method. Oxford University Press, 2nd ed., 269 p.

Min, K., Mundil, R., Renne, P.R., and Ludwig, K.R. (2000) A test for systematic errors in (super 40) Ar/ (super 39) Ar geochronology through comparison with U/Pb analysis of a 1.1-Ga rhyolite. Geochimica et Cosmochimica Acta, 64, 73-98.

Pelton, J.R., and Smith, R.B. (1982) Contemporary vertical surface displacements in Yellowstone National

Park. Journal of Geophysical Research, 91, 9488-9494.

Plouff, D., and Pakiser, L.C. (1972) Gravity study in the San Juan Mountains, Colorado. US Geological Survey Professional Paper, 800, B183-B190.

Poli, S., and Schmidt, M.W. (1992) A comment on Blundy and Holland's (1990) "Calcic amphibole equilibria and a new amphibole-plagioclase geothermometer" by J.D. Blundy and T.J.D. Holland. Contributions to Mineralogy and Petrology, 111, 273-278.

Reid, M.R., Coath, C.D., Harrison, T.M., and McKeegan, K.D. (1997) Prolongued residence times for the youngest rhyolites associated with Long Valley Caldera: ^{230}Th-^{238}U microprobe dating of young zircons. Earth and Planetary Science Letters, 150, 27-39.

Renne, P.R., Swisher, C.C., Deino, A.L., Karner, D.B., Owens, T.L., and DePaolo, D.J. (1998) Intercalibration of standards, absolute ages and uncertainties in (super 40) Ar/ (super 39) Ar dating. Chemical Geology, 145, 117-152.

Riciputi, L.R., Johnson, C.M., Sawyer, D.A., and Lipman, P.W. (1995) Crustal and magmatic evolution in a large multicyclic caldera complex: isotopic evidence from the central San Juan volcanic field. Journal of Volcanology and Geothermal Research, 67, 1-28.

Rutherford, M.J., and Johnson, M.C. (1992) Comment on Blundy and Holland's (1990) "Calcic amphibole equilibria and a new amphibole-plagioclase geothermometer". Contributions to Mineralogy and Petrology, 111, 266-268.

Sederholm, J.J. (1891) Uder die finnländischen Rapakivigesteine. Tschermak's Mineralogische und Petrographische Mitteilungen, 12, 1-31.

Singer, B.S., Wijbrans, J.R., Nelson, S.T., Pringle, M.S., Feeley, T.C., and Dungan, M.A. (1998) Inherited argon in a Pleistocene andesite lava; ^{40}Ar/^{39}Ar incremental-heating and laser-fusion analyses of plagioclase. Geology (Boulder), 26, 427-430.

Smith, R.L. (1960) Ash flows. Gological Society of America Bulletin, 71, 795-842.

Sparks, R.S.J. (1997) Causes and consequences of pressurization in lava dome eruptions. Earth and Planetary Science Letters, 150, 177-189.

Stasiuk, M.V., Barclay, J., Caroll, M.R., Jaupart, C., Ratté, J.C., Sparks, R.S.J., and Tait, S.R. (1996) Degassing during magma ascent in the Mule Creek vent (USA). Bulletin of Volcanology, 58, 117-130.

Stimac, J.A., and Wark, D.A. (1992) Plagioclase mantles on sanidine in silicic lavas, Clear Lake, California; implications for the origin of rapakivi texture. Geological Society of America Bulletin, 104(6), 728-744.

Wark, D.A., and Stimac, J.A. (1992) Origin and mantled (rapakivi) feldspars; experimental evidence of a dissolution- and diffusion-controlled mechanism. Contributions to Mineralogy and Petrology, 111(3), 345-361.

Wolff, J.A., and Gardner, J.N. (1995) Is the Valles Caldera entering a new cycle of activity? Geology (Boulder), 23(5), 411-414.

Fisher Mountain 12857 (3919)
12305 (3690)
10690 (3258)
Fisher Creek
11077 (3376)
11697 (3565)
11180 (3411)
12090 (3685)
11710 (3569)
11496 (3504)
Metroz Mountain
11892 (3625)
12013 (3662)
Ivy
12587 (3837)
11630 (3545)
12810 (3722)
12492 (3798)
Copper
12467 (3860)
11301 (3445)
12221 (3726)
11242 (3427)
13038 (3974)
Goose
South River Peak
13149 (4008)
11980 (3652)
12067 (3678)
12858 (3949)
11969 (3648)
12302 (3750)
Palomino Mountain
Creek
11833 (3607)
10377 (3163)
Mount Hope
12834 (3912)
Table Mountain
Tie Hill
11144 (3397)
Fox Mountain
11530 (3514)
11308 (3447)
12390 (3776)
11738 (3578)
Sheep Mountain
12369 (3770)
Spruce Mountain
11577 (3529)
Pagosa Peak
12640 (3853)
Black Mountain
Eagle Mountain
12007 (3660)
Saddle Mountain
9155 (2790)
Fourmile Creek
West Axis
8731 (2673)
East Fork
10287 (3135)
9978 (3041)
San Juan River
Wolf Creek
11580 (3530)
10400

LEGEND:

- Quaternary
- Carpenter Ridge Tuff
- Huerto Andesite
- Pagosa Peak Dacite
- Fish Canyon Tuff
- Older Units

0 1 2 3 miles
0 1 2 3 4 5 km
contour interval 400 feet

Chapitre 1: Voluminous lava-like precursor to a major ash-flow tuff: low-column pyroclastic eruption of the Pagosa Peak Dacite, San Juan volcanic field, Colorado

Article publié:

Bachmann, O., Dungan, M.A., and Lipman, P.W. (2000) Voluminous lava-like precursor to a major ash-flow tuff: low-column pyroclastic eruption of thePagosa Peak Dacite, San Juan Volcanic field, Colorado. Journal of Volcanology and Geothermal Research, 98, 153-171.

Abstract

The Pagosa Peak Dacite is an unusual pyroclastic deposit that immediately predated eruption of the enormous Fish Canyon Tuff (~5,000 km^3) from the La Garita caldera at 28 Ma. The Pagosa Peak Dacite is thick (to 1 km), voluminous (>200 km^3), and has a high aspect ratio (1:50) similar to those of silicic lava flows. It contains a high proportion (40-60 %) of juvenile clasts (to 3-4 m) emplaced as viscous magma that was less vesiculated than typical pumice. Accidental lithic fragments are absent above the basal 5-10% of the unit. Thick densely welded proximal deposits flowed rheomorphically due to gravitational spreading, despite the very high viscosity of the crystal-rich magma, resulting in a macroscopic appearance similar to flow-layered silicic lava. Although it is a separate depositional unit, the Pagosa Peak Dacite is indistinguishable from the overlying Fish Canyon Tuff in bulk-rock chemistry, phenocryst compositions, and $^{40}Ar/^{39}Ar$ age.

The unusual characteristics of this deposit are interpreted as consequences of eruption by low-column pyroclastic fountaining and lateral transport as dense, poorly inflated pyroclastic flows. The inferred eruptive style may be in part related to synchronous disruption of the southern margin of the Fish Canyon magma chamber by block faulting. The Pagosa Peak eruptive sources are apparently buried in the southern La Garita caldera, where northerly extensions of observed syneruptive faults served as fissure vents. Cumulative vent cross sections were large, leading to relatively low emission velocities for a given discharge rate. Many successive pyroclastic flows accumulated sufficiently rapidly to weld densely as a cooling unit up to 1,000 m thick and to retain heat adequately to permit rheomorphic flow. Explosive potential of the magma may have been reduced by degassing during ascent through fissure conduits, leading to fracture-dominated magma fragmentation at low vesicularity. Subsequent collapse of the 75 km x 35 km La Garita caldera and eruption of the Fish Canyon Tuff were probably triggered by destabilization of the chamber roof as magma was withdrawn during the Pagosa Peak eruption.

1. Introduction

Most eruptions of silicic magma involve either relatively quiet effusions of lava or high-energy plinian columns in which fragmentation of magma is efficient and the associated pyroclastic deposits consist mainly of fine ash and highly vesiculated pumice. Low-energy pyroclastic fountaining intermediate between these extremes has been inferred for a few eruptions that were characterized by unusual magmatic or eruptive conditions, such as low viscosity magmas (Duffield, 1990; Mahood, 1984; Turbeville, 1992) or syneruptive piecemeal collapse (Branney and Kokelaar, 1992). Where effusive and primary explosive activity occur during the same eruptive episode, effusion of lava commonly follows a more explosive initial phase (Eichelberger et al., 1986), although the reverse has been documented (Hildreth and Drake, 1992). Progressions from explosive to effusive activity are conventionally ascribed to vertical volatile gradients in stratified magma chambers, or alternatively to degassing of magma in a shallow magma reservoir or during ascent through permeable conduits (Fink et al., 1992).

This paper describes initial eruptions of homogeneous crystal-rich dacite from an enormous magma reservoir, which we refer to as the Fish Canyon magmatic system. Three distinct phases of activity differing in eruptive mechanism, volume, and vent geometry were produced from the same magma chamber, apparently in rapid succession at 28.0 Ma (Table 1). No important compositional distinctions (bulk composition, phenocryst modes, or mineral chemistry) have been detected among these three phases (Lipman et al., 1997). The second (main) eruptive phase is the Fish Canyon Tuff, a vast (~5,000 km^3) ignimbrite erupted during the formation of the La Garita caldera. The last phase is a post-resurgence lava-like unit of small-volume (<1km^3) within the caldera.

The Pagosa Peak Dacite, produced during the first phase of activity, is an unusual pyroclastic deposit. It has a volume of ~200 km^3, is locally >1 km thick, and is characterized by primary pyroclastic structures that differ vastly from the Fish Canyon Tuff. Although some basal flow units of the Pagosa Peak Dacite resemble typical pumiceous ignimbrite deposits, more than 90% of the deposit consists of a high proportion (40-60 %) of poorly vesiculated magmatic fragments in a fine-grained matrix that lacks bubble-wall shards. The flow units are densely welded in all but a few basal and distal localities, and welding breaks are rare. Much of the densely welded material is massive or flow layered, resembling lava, and these features are interpreted as the consequences of rheomorphic flow. Severe fluidal deformation has rarely been documented for such a viscous pyroclastic deposit containing abundant phenocrysts in a silicic matrix; heat must have been efficiently retained during emplacement. Magma ascent along syneruptive faults, as opposed

Table 1. Summary of total-fusion ages on sanidine phenocrysts, Fish Canyon magmatic system. All ages calculated relative to 28.34 Ma Taylor Creek sanidine (Renne et al., 1998). Analyses done in the Geneva $^{40}Ar/^{39}Ar$ laboratory.

Unit (in stratigraphic order)	Mean age (Ma)	Error (2σ)	Number of analysis
Nutras Creek Dacite	28.06	0.16	11
Fish Canyon Tuff	28.03	0.18	11
Pagosa Peak Dacite	27.93	0.18	11

to catastrophic escape along a caldera margin, may have been a critical factor in producing the unusual characteristics of the Pagosa Peak Dacite. Gas escape during ascent may have decreased the explosive potential of the magma, leading to low vesicularity and inefficient fracture-dominated fragmentation. The apparent absence of deposits analogous to the Pagosa Peak Dacite in the geological record may derive in part from the large volume of its magma reservoir, and perhaps from limited preservation of diagnostic features in units of similar origin but lower phenocryst content and magma viscosity.

2. Geological setting

2.1. San Juan volcanic field

The Oligocene San Juan volcanic field of southern Colorado (Fig. 1) is an erosional remnant of volcanism that covered much of the Southern Rocky Mountains during mid-Tertiary time (Larsen and Cross, 1956; Lipman et al., 1989). San Juan volcanic rocks now cover an area of about 25,000 km^2 and have a total volume close to 40,000 km^3. The eruptive products consist mainly of Oligocene calc-alkaline intermediate-composition lavas and silicic ash-flow tuffs, resulting from low-angle subduction under the North American plate (Lipman et al., 1978) or melting of lithospheric mantle previously modified by Proterozoic subduction (Davis et al., 1993). This sequence is locally overlain by thin Mio-Pliocene basaltic flows and minor rhyolite (mainly 26-20 Ma), related to the opening of the Rio Grande rift.

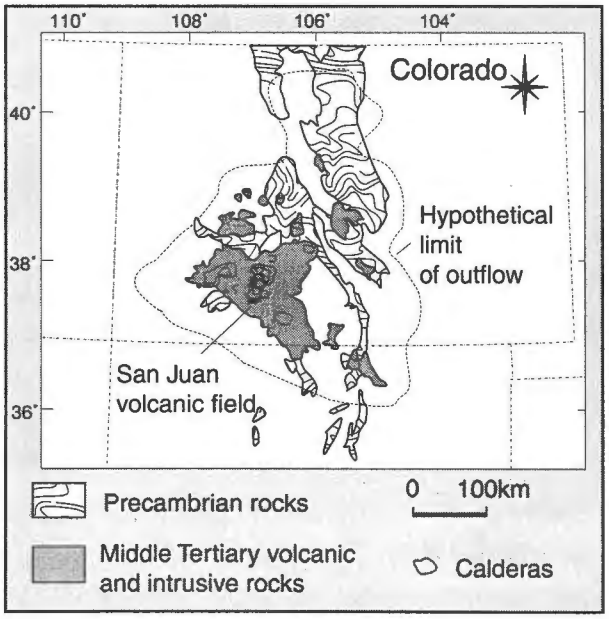

Fig. 1: Location of the San Juan volcanic field and related Tertiary extrusive and intrusive rocks in Colorado and New Mexico (Steven, 1975).

The Oligocene volcanism progressed from intermediate-composition calc-alkaline lavas and breccias to large silicic ash-flow sheets (Lipman et al., 1978). Eruptive activity began at approximately 35 Ma, as scattered stratovolcanoes produced large quantities of dominantly andesitic lavas and breccias. From 30 to 26 Ma, volcanism became more explosive, and at least 17 major silicic (~64-72 % SiO_2) ash-flow sheets (100-5,000 km^3) erupted from three caldera clusters. The western and southeastern (Platoro caldera complex) clusters were active concurrently from about 30 to 28 Ma. During the waning stages of ash-flow tuff volcanism in the Platoro complex (Lipman et al., 1996), caldera-related activity shifted to the center of the field at approximately 28.6 Ma, where it remained until dominantly calc-alkaline magmatism was succeeded by bimodal, dominantly basaltic rift-induced activity. The long-term evolution of the calc-alkaline volcanism is thought to record emplacement of a composite batholithic complex at shallow depth beneath the volcanic field, in accord with a large negative gravity anomaly centered on this region (Plouff and Pakiser, 1972; Lipman et al., 1978).

2.2. Fish Canyon magmatic system

The Fish Canyon Tuff, erupted from the La Garita caldera, is the second and largest of eight

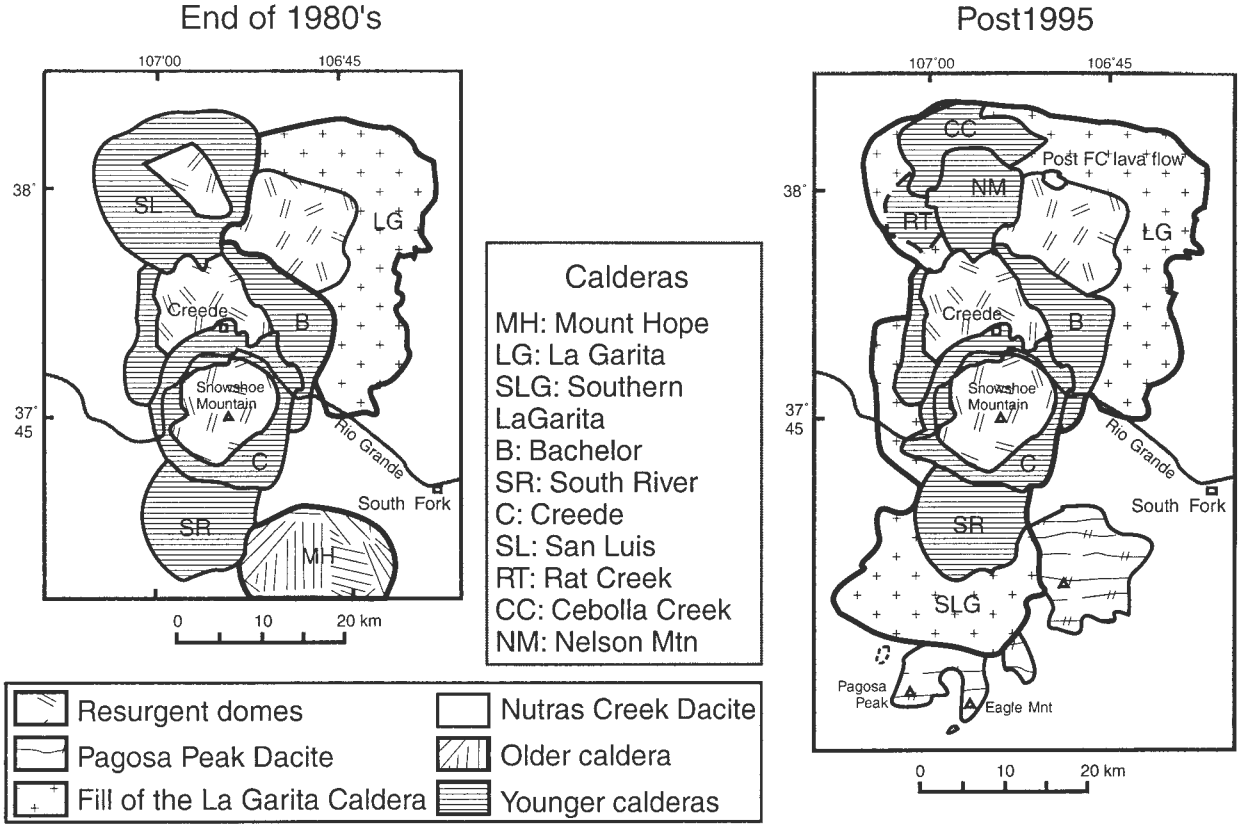

Fig. 2: Maps on the central caldera cluster of the San Juan volcanic field, as known at the end of the 1980's (Lipman et al., 1989) and after 1995 (Lipman, 2000).

major ash-flow sheets erupted from the productive central San Juan caldera cluster, which generated approximately 8,000 km^3 of silicic deposits through eight caldera-related eruptions during <2.5 million years (Lipman, 2000). Fish Canyon magma is compositionally unzoned crystal-rich dacite (35-45 % crystals; 68.5 % SiO_2) with a near-solidus mineral assemblage of two feldspars, hornblende, biotite, quartz, sphene, apatite, zircon and Fe-Ti oxides in silicic (~76 % SiO_2) matrix glass (Whitney and Stormer, 1985). Preceding and subsequent caldera eruptions of the central San Juan cluster are characterized by diverse magmas, distinct in bulk composition and mineralogy from the Fish Canyon magma (Lipman, 2000; Riciputi et al., 1995). In contrast, the distinctive Fish Canyon magma type was erupted as the Pagosa Peak and Nutras Creek Dacites both before and after subsidence of the La Garita caldera.

Reinvestigation of the eruptive products of the Fish Canyon magmatic system, in connection with an overall reassessment of the central San Juan caldera cluster (Lipman, 2000), has revealed several previously unrecognized features. Estimates of the dimensions of the La Garita caldera and the volume of the Fish Canyon Tuff have been revised upward (Lipman et al., 1997), in light of the fact that the southern margin of the caldera is 30 km further south than previously recognized (Fig. 2). This complex collapse feature comprises three overlapping depressions that form a composite caldera elongated north-south, with aggregate dimensions of 75 x 35 km (area >2,500 km^2). By assuming: (1) an average subsidence throughout the caldera of 1 km (variable but locally probably much greater), and (2) approximately co-equal proportions of intracaldera and outflow tuff (a large but unknown volume of the outflow tuff has been eroded), we arrive at a crude but conservative estimate of 5,000 km^3 for the volume of erupted Fish Canyon Tuff.

The non-resurgent southern depression is spatially associated with the precaldera Pagosa Peak Dacite, as well as voluminous intracaldera and extracaldera lavas and breccias of the postcollapse Huerto Andesite. By contrast, the northern segment, which is resurgent and lacks associated precursory eruptions of Fish Canyon magma or voluminous postcollapse andesitic volcanism, includes a post-resurgence lava flow of Fish Canyon type, the Nutras Creek Dacite (Fig. 2). The central depression is largely filled with and modified by younger nested calderas but may have been resurgent. No precursory activity has been identified in this sector that relates directly to the Fish Canyon magmatic system, but the northernmost vents for the postcollapse Huerto Formation are near its southwestern margin.

Although the mineralogy and mineral chemistry of the Pagosa Peak Dacite, Fish Canyon Tuff, and Nutras Creek Dacite are virtually identical, granophyric overgrowths form rim on shattered feldspars megacrysts in the last-erupted phases of the magmatic system (Lipman et al., 1997). These distinctive overgrowths occur only in intracaldera Fish Canyon Tuff of the northern depression and in Nutras Creek Dacite. This temporal and spatial zonation is ascribed to late syneruptive crystallization of granophyre during depressurization related to the precursory Pagosa Peak Dacite eruption and early collapse of the southern depression. On this basis, and the asymmetric distribution of the Pagosa Peak Dacite, eruption of the Fish Canyon Tuff is inferred to have progressed from south to north. This shift must have occurred rapidly, as the outflow Fish Canyon Tuff is a single compound cooling unit lacking granophyric overgrowths.

3. Pagosa Peak Dacite

The Pagosa Peak Dacite is preserved over an area of 350 to 400 km^2 around the southeastern margin of the La Garita caldera (Fig. 2). Distal nonwelded facies are rarely exposed, due to post-Oligocene erosion or burial by the Fish Canyon Tuff. Many features in the deposits suggest transport toward the south and southeast, and the initial depositional area may have exceeded 600 km^2. No eruptive sources for the Pagosa Peak Dacite are exposed; they are inferred to be buried within the southern La Garita caldera, along with as much as a third of the volume of the original deposit.

The Pagosa Peak Dacite is preserved primarily as two thick lobes (800 m to the south at Pagosa Peak, >1,000 m to the east at Mount Hope), separated by an intervening thinner zone (<100 m) centered on Saddle Mountain. Thickness tends to decrease away from the caldera, and the preserved lateral extent does not exceed 15 km beyond the caldera wall. Termination of the deposits tends to be abrupt, in part due to selective erosion of the weakly welded distal facies. Although many sections are not exposed to their base, thickness is widely >300 m, and accumulations may have been even greater near the vents, implying a total volume in excess of 200 km^3. Thus, the aspect ratio (average thickness/horizontal extent; Walker, 1983) of the preserved remnants of the unit is ~1:50, more similar to large silicic lava flows than typical ignimbrites (~1:500 to 1:1,000).

The Pagosa Peak Dacite was erupted prior to the Fish Canyon Tuff, but from the same magma chamber. Evidence for this relation includes: (1) indistinguishable mineralogy, mineral chemistry, and magma compositions of the two units, (2) truncation of the Pagosa Peak Dacite by the southern margin of the La Garita caldera, and (3) deposition of Fish Canyon Tuff directly on the Pagosa Peak. The time interval between these two units is inferred to have been brief. Where the contact is exposed, neither a soil horizon nor an erosional surface is present,

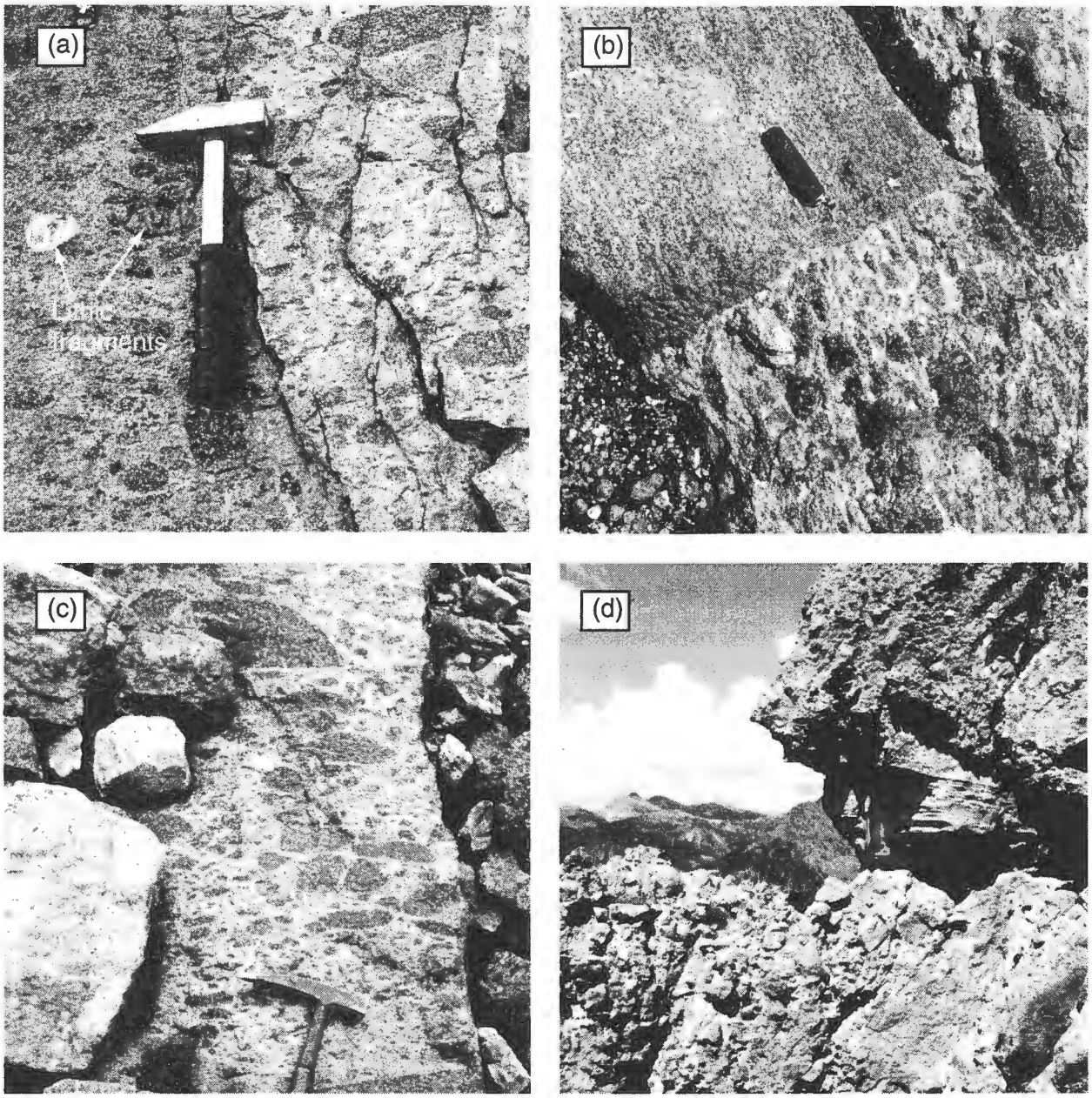

Figure 3: Blob textures in the Pagosa Peak Dacite: (a) densely welded lithic-bearing deposit: glassy blobs have lenticular shapes and limited flattening foliation (south part of the east lobe); (b) penetrative deformation in a densely welded outcrop: small lenticular blobs trend directly into a larger angular block, indicating absence of differential compaction between block and matrix (NE of Wolf Creek Pass)--Knife is approximately 10 cm long; (c) lithic-free vitrophyre: textures are similar to those in lithic-bearing deposits of fig. 3a (densely welded, limited compaction, glassy), although the blobs are larger, to 1.5 m (east lobe, at Camp Creek); (d) nonwelded flow units in distal lithic-free deposits, containing high proportion of blobs: surge-like interbeds at flow-unit break are 1.5 m thick (W side of Saddle Mountain).

suggesting emplacement in rapid succession. $^{40}Ar/^{39}Ar$ ages of the three eruptive phases of the Fish Canyon magmatic system are indistinguishable (Table 1).

3.1. Macroscopic textures and structures

The Pagosa Peak Dacite differs from other eruptive phases of the Fish Canyon magmatic system, and from other eruptive products of the San Juan volcanic field, by the presence of unusual

juvenile pyroclasts. These magmatic fragments are dense, subrounded to elliptical in shape, and are inferred to have been viscous at the time of emplacement (Fig. 3). They constitute high proportions of the rock relative to matrix (~50%). The typical size range for the Pagosa Peak pyroclasts is 20-60 cm; many exceed 1 m, and some are 3-4 m in diameter. We refer informally to these pyroclasts as *magma blobs*, to distinguish them from the rigid juvenile blocks characteristic of block-and-ash flows. The blobs are morphologically different from pumices in most silicic pyroclastic rocks, although similar lenticular fragments have been described in the Taylor Creek Rhyolite (Duffield, 1990). They have no relation to mafic enclaves resulting from magma mixing, for which the term "blob" is also sometimes applied; the Pagosa Peak blobs are fragments of dacitic Fish Canyon magma that are chemically indistinguishable from the matrix.

Flattening ratios of densely welded Pagosa Peak blobs <1:5 are rare, except where they are modified by rheomorphic flow. Even densely welded blobs commonly are subequant, although many are weakly elongate. Neither composite blobs nor evidence for incorporation of previously fragmented and welded material has been recognized. Blob morphologies are subrounded to angular, contacts

Fig. 4: Flow-layered blob in distal, non-welded Pagosa Peak Dacite, probably reflecting shearing during magma ascent. (E side of Saddle Mountain).

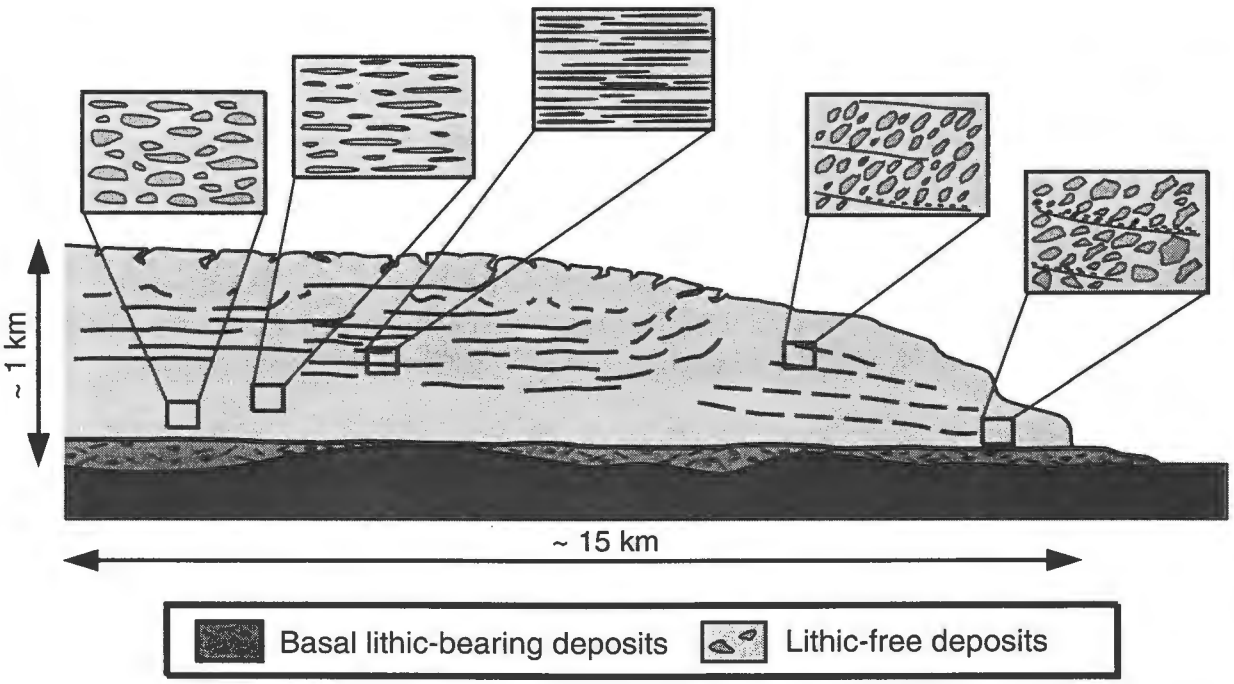

Fig. 5: Schematic stratigraphy of the Pagosa Peak Dacite, showing rough proportions between basal lithic-bearing and overlying lithic-free deposits. Inset boxes diagrammatically show progressive flattening of the blobs in proximal, upper part of the lithic-free deposits.

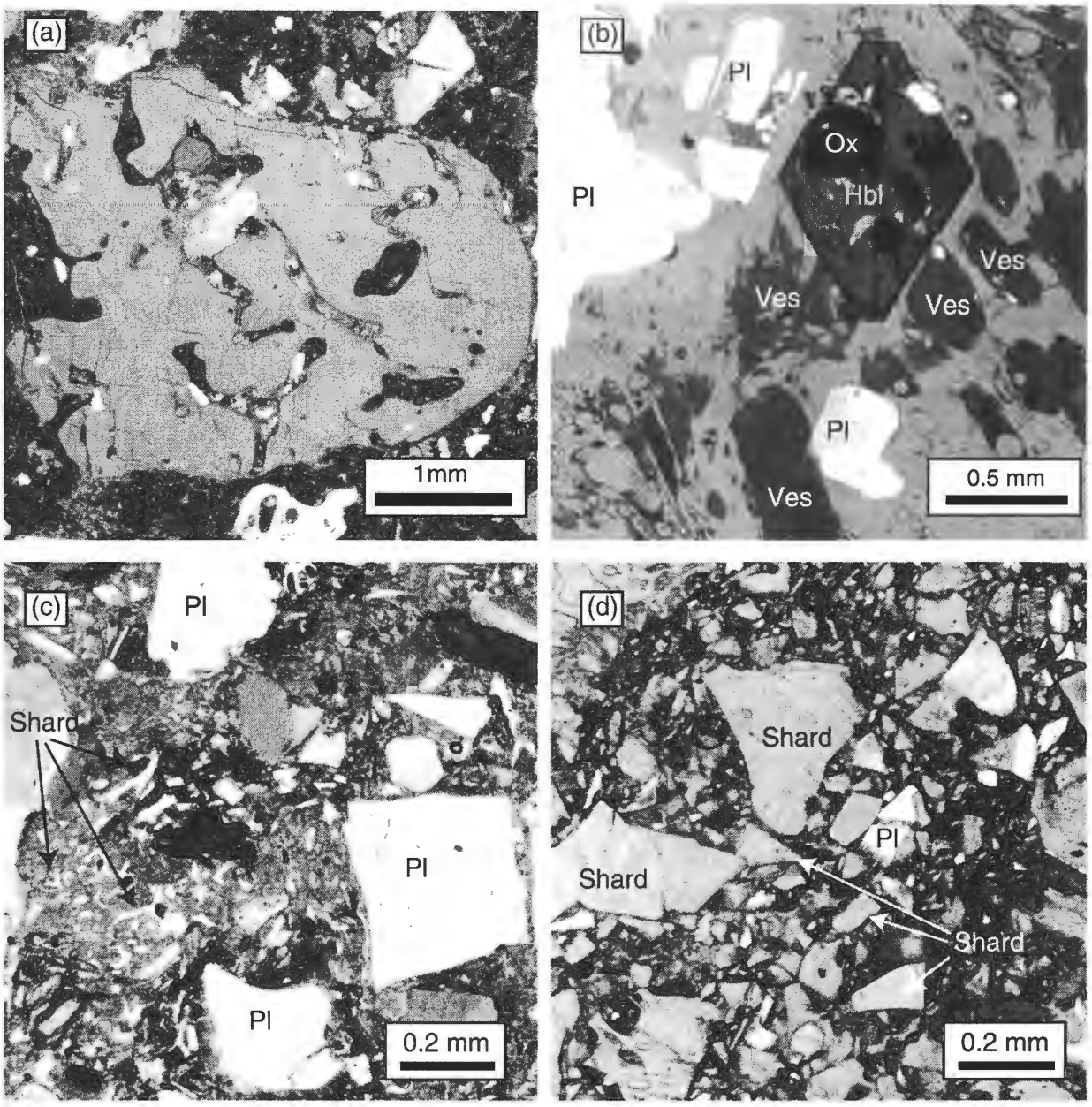

Fig. 6: Microscopic textures in rocks of the Fish Canyon magmatic system: (a) large (~5 mm) resorbed sanidine containing melt pockets and channels, in Pagosa Peak Dacite; (b) heterogeneously distributed vesicles in a nonwelded blob: most are elongated and show coalescence to form small clusters- vesicularity is ~25 %; (c) matrix texture in nonwelded Fish Canyon Tuff: glass shards have the typical cuspate morphology of bubble walls; (d) matrix texture in a nonwelded blob- glass shards in the matrix are blocky, differing from the cuspate shapes of bubble-wall shards.

with the matrix are everywhere sharp, and fiamme-like interdigitations with matrix are absent. The subequant shapes of many blobs suggest limited compaction during welding, denoting relatively low vesicularity at the time of emplacement. The matrix (plus small blobs) does not compact differentially around larger blobs (Fig. 3b), even in densely welded units, indicating that primary porosity was comparable in both matrix and blobs.

Many blobs have internal mineral lineations or flow layering (Fig. 4), both in densely welded and nonwelded facies. Such fabrics within blobs are randomly oriented relative to depositional bedding, and some internal flow layering or mineral lineations are at high angles to the elongation of the blob. These relations indicate that the internal fabrics formed prior

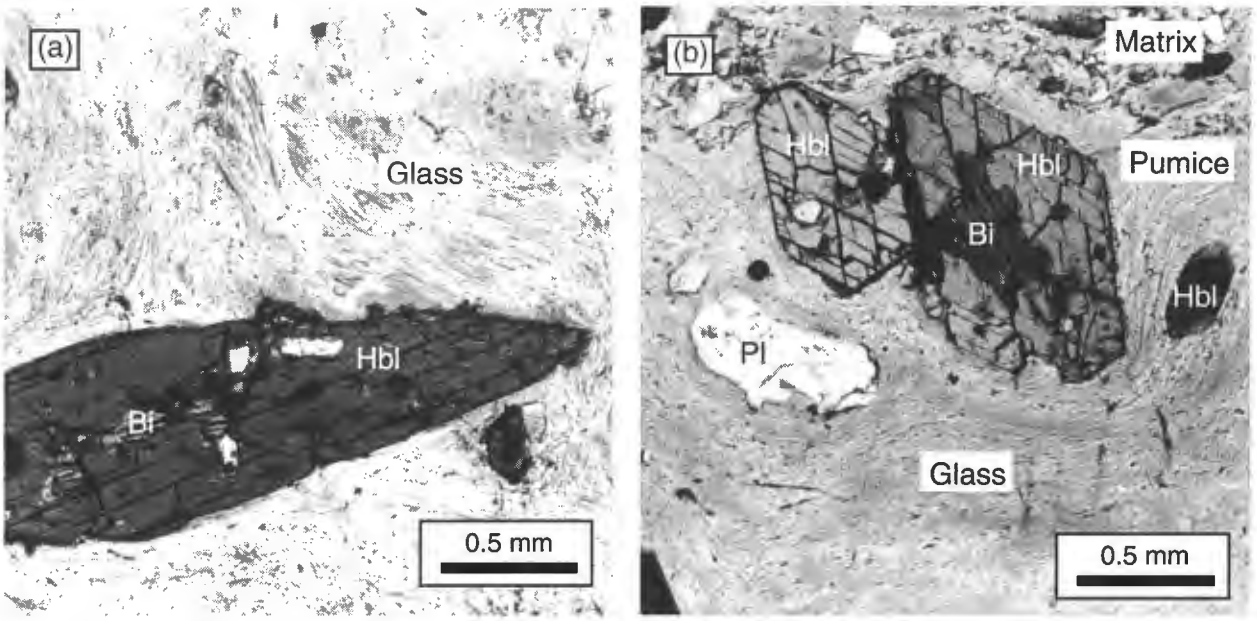

Fig. 7: Matrix flowage textures: (a) fluidal texture, surrounding euhedral hornblende in glassy matrix of Pagosa Peak Dacite, is enhanced by preferred orientation of small oxide filaments; (b) texture of welded pumice lens (bottom) in intracaldera Fisn Canyon Tuff, containing euhedral hornblendes and a small corroded plagioclase. Flowage fabric is similar to that in Pagosa Peak Dacite blobs, due to annealing of vesicles upon welding.

to fragmentation.

Two subunits of the Pagosa Peak Dacite are distinguished on the basis of accidental lithic fragments (Fig. 5). Lithic-bearing deposits are confined to basal units and form less than 5-10% of the total volume. Most are blob-bearing pyroclastic-flow deposits, but minor pumiceous pyroclastic-flow, fallout, and surge deposits are also present. The distribution of lithic-bearing flow and surge deposits was controlled by pre-existing low-relief topography, and thickness ranges from a few meters to ~80 m. Accidental lithic fragments rarely exceed more than a few volume percent. Most are small andesitic fragments (to 15-20 cm; Fig. 3a) that were probably incorporated in the flows during conduit erosion in the initial stage of activity.

The overlying lithic-free deposits are thick accumulations (averaging 300 m) of pyroclastic-flow deposits containing high proportions of blobs (Fig 3c). Thickness of individual pyroclastic-flow units commonly is a few meters to >30 m. Such flow units apparently do not become finer-grained distally and are poorly sorted internally, although faint inverse grading can be present. Subhorizontal bedding is locally defined by the presence of multiple pyroclastic flows, especially in weakly welded distal sections, where surge-like interbeds separate flow units (Fig. 3d). Most proximal sections are massive, and flow-unit boundaries are obscure. Except for distal sections on Saddle Mountain, the lithic-free deposits are densely welded without breaks, even where >500-1,000 m thick; rapid accumulation of many successive flow units is implied.

The base of the Pagosa Peak Dacite is everywhere vitrophyric, and glassy material is locally >200 m thick. In contrast, basal vitrophyres are rare in the Fish Canyon Tuff, and generally <5 m where present.

3.2. Microscopic textures

Fish Canyon magma contained about 40 % phenocrysts, with diameters to 5 mm (~1-2 mm average), in a matrix of silicic rhyolite glass. In glassy samples the matrix is free of feldspar microlites. Most glasses contain minute filamental oxide grains

Table 2: Vesicularities of silicic pumices in comparison to the Pagosa Peak Dacite and Fish Canyon Tuff. The Fish Canyon value is approximate, due to lack of fresh, nonwelded pumices.

Unit	Mean bulk vesicularity (%)	Bulk vesicularity (range in %)
Pagosa Peak Dacite	~25	18-35*
Fish Canyon Tuff	>60	-
Bishop Tuff (Houghton and Wilson, 1989)	71	64-78
Taupo Ignimbrite (Houghton and Wilson, 1989)	73	70-77
Average silicic pumices (Cashman and Mangan, 1994)	~75	70 to 80

*: This range of bulk vesicularity translates into 30-50 % matrix vesicularity if the magma averaged 40 % phenocrysts

resulting from incipient devitrification, not magmatic crystallization. Devitrified samples contain spherulites and crystallites similar to welded and devitrified ignimbrites.

Phenocrysts of feldspar (especially sanidine) and quartz are intricately corroded, and they contain numerous melt pockets (Fig. 6a). In large sanidine grains these pockets commonly contain inclusions of plagioclase, or more rarely of other phases. We interpret these resorption textures as consequences of the magma-generation process, not as melting related to eruption. Although these melt-laden crystals are potentially fragile during explosive volcanism due to internal expansion of exsolved vapor (Best and Christiansen, 1997), few crystals in the Pagosa Peak blobs are extensively broken. Many large feldspars in pumices of the northern intracaldera Fish Canyon Tuff are shattered and rimmed by granophyric overgrowths (Lipman et al., 1997), whereas "phenocrysts" in typical outflow Fish Canyon Tuff matrix are predominantly smaller, angular, fragments of broken crystals without granophyric overgrowths. Neither biotite nor hornblende exhibit the marginal breakdown textures documented in many calc-alkaline magmas (e.g., Devine et al., 1998; Rutherford and Hill, 1993). Both are typically euhedral and lack evidence for the mineral-melt disequilibrium typical of quartz and sanidine (Fig. 7a and b).

Most blobs are dense and lack porosity as a consequence of welding. Glassy samples preserve fluidal textures, highlighted by minute oxide filaments that are locally aligned and wrap around phenocrysts (Fig. 7a), similar fiamme in the intracaldera Fish Canyon Tuff (Fig. 7b), and the Badland lava flow (Manley, 1996). This similarity probably reflects the former presence of vesicles in blobs that were subsequently annealed during welding.

In rare non- to weakly-welded flow units, elliptical to highly irregular vesicles are preserved in blobs (Fig. 6b). They are mostly <10-30 μm, although the size distribution is irregular and some are large (~500 microns). Due in part to high crystal contents, the vesicles are heterogeneously distributed as local clusters separated by dense zones. All vesicles are somewhat deformed, as indicated by

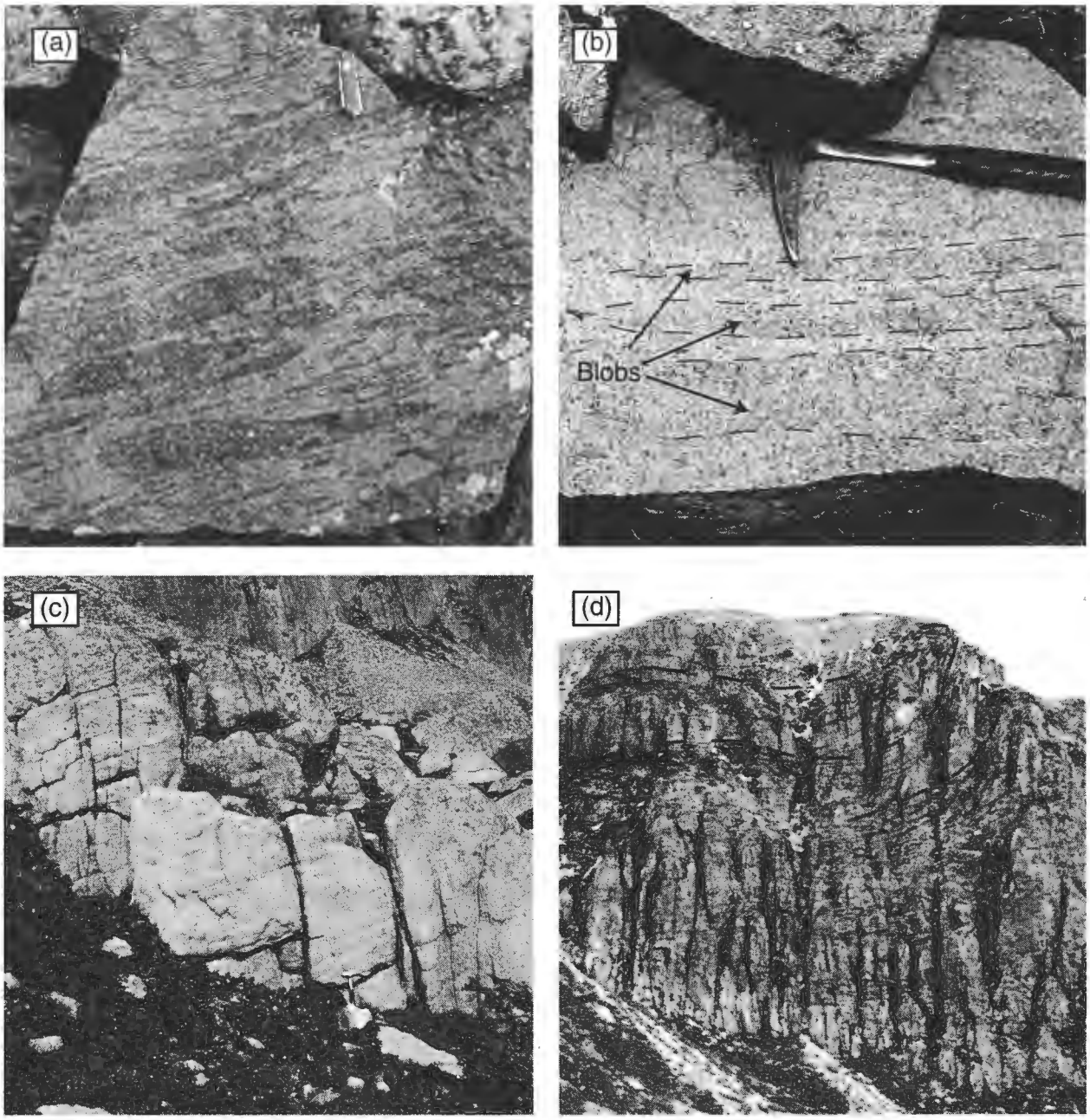

Fig. 8: Progressive upward flattening of primary pyroclastic fragments (blobs) until the rock resembles lava. (a) Elongated lenticular blobs in basal vitrophyre (west part of south lobe). (b) Devitrified interior of deposit, having elongated blobs with aspect ratios to 1:15 (Camp Creek); blob boundaries enhanced by dashed lines. (c) Foliated texture in devitrified rock, resembling flow-layered silicic lavas due to the elongation of blobs (Camp Creek). (d) Ramp structure, indicating flowage in upper parts the deposit (head of Camp Creek); foliation trends enhanced by dashed lines.

elliptical to highly elongated shapes, suggesting vesicle collapse or a small component of shear.

Bulk-rock and glass vesicle contents were measured in thin sections impregnated with colored epoxy (Cashman and Mangan, 1994), assuming that vesicle orientation is quasi-random in two dimensions at thin-section scale. Although limited in scope by the rarity of nonwelded samples and the heterogeneous distribution of vesicles, measured vesicularity is lower in the Pagosa Peak Dacite (Table 2) than in most pyroclastic deposits (Houghton and Wilson, 1989). Such low vesicularity is in accord with the limited flattening upon welding and lack of macroscopic interdigitations with matrix at the terminations of blobs. Reliable estimates of vesicularity in the Fish Canyon Tuff are more difficult

Table 3. Compositions of two representative magmatic fragments in the Pagosa Peak Dacite (XRF) and interstitial glass (electron microprobe).

	Bfc 83	Bfc 91	Glass (Bfc 83)
SiO_2	68.26	67.94	76.05
Al_2O_3	15.38	15.29	12.37
FeO_t	3.55	3.79	0.26
MgO	0.92	1.09	0.05
CaO	2.91	2.95	0.60
Na_2O	3.92	3.94	2.66
K_2O	4.35	4.16	5.42
TiO_2	0.44	0.46	0.13
MnO	0.09	0.10	0.04
P_2O_5	0.18	0.19	0.02
Total	99.99	99.91	97.77

to obtain, due to the small size of pumices, widespread dense welding, and spherulite growth in the glass.

The fine-grained matrix of non-devitrified Pagosa Peak Dacite consists mostly of smaller, broken phenocrysts, glass shards, and fine crystal and glass dust. Preserved glass shards in these deposits are angular and equant (Fig. 6d) in contrast to the cuspate shapes of bubble-wall shards in the Fish Canyon Tuff (Fig. 6c) and other ignimbrites. Because vesicularity may be underestimated due to incipient collapse of vesicles following emplacement, the unusual shapes of glass shards in the Pagosa Peak Dacite are important evidence that vesicularity was comparatively low at the time of fragmentation. An origin for the ashy matrix of the Pagosa Peak Dacite by comminution during eruption and emplacement, rather than bubble-wall rupture due to high vesicularity, is consistent with the large dimensions of blobs, the lack of differential compaction during welding, and the heterogeneous distributions of irregularly shaped vesicles in Pagosa Peak blobs.

3.3. Rheomorphic flow

Pyroclastic textures, everywhere well preserved in the distal and lower parts of the lithic-free deposits, are partly to completely obliterated in the upper parts of thick proximal sections by extreme welding, rheomorphic flow, and devitrification. At a few tens to 150 m above the base, distinctions between increasingly flattened blobs and matrix become gradually obscure, and outcrop surfaces resemble weakly foliated lava (Fig. 8a to c). The foliation is defined by differences in crystal size between layers of similar thickness (a few cm), reflecting the larger size of non-broken phenocrysts

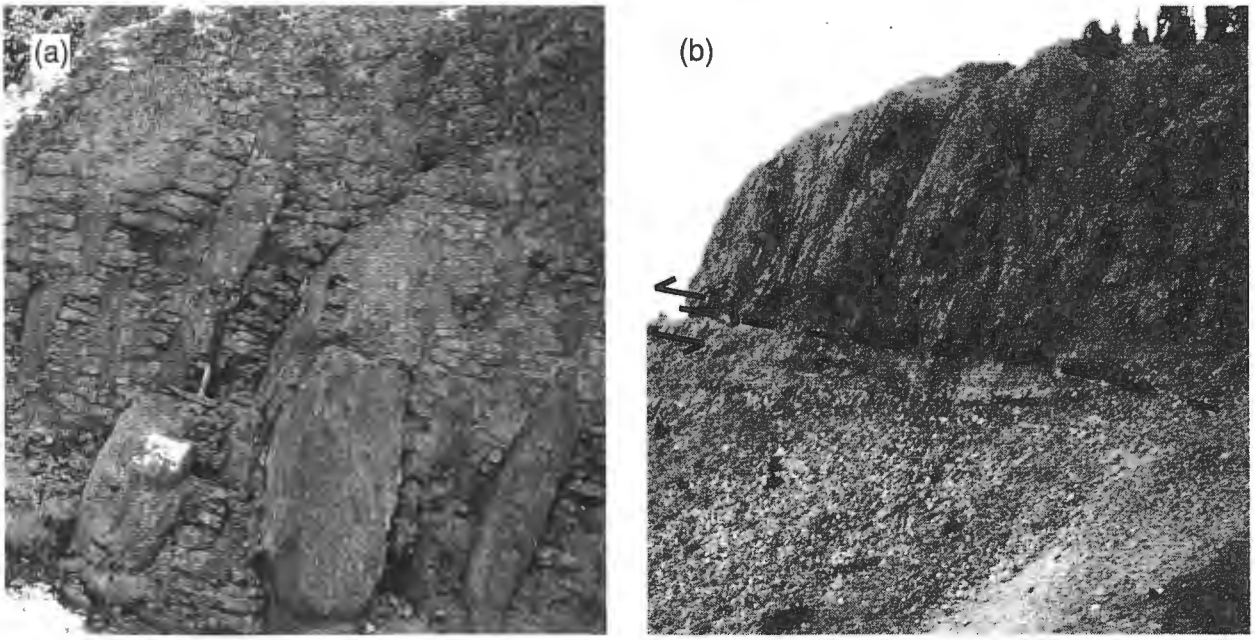

Fig. 9: Textures related to secondary brittle deformation. (a) Steeply dipping elongated blobs (to 1.5 m in long axis) south of Mount Hope; brittle pull-apart fractures cut matrix but not the blobs. (b) Subhorizontal thrust fault in a cliff face west of Wolf Creek Pass.

in flattened blobs relative to matrix.

The blobs are elongate parallel to the transport direction and flattened in the plane of the foliation, which is generally subparallel to the regional dip (~5-10° to NE). Gentle undulations in orientation are common, and foliations locally dip steeply in upper parts of several thick sections. Small-scale tight folds are rare, but the role of plastic flow is confirmed by ramp structures at two localities in the eastern lobe that resemble those in upper parts of large silicic lava flows (Fig. 8d). Orientations of the ramps are consistent with directions of flow away from the inferred vent region.

At the tops of some thick sections, the Pagosa Peak Dacite is brecciated where depositionally overlain by Fish Canyon Tuff. Such breccias are several meters thick, massive, and dense; they are characterized by coarse (<1 m) angular dacite blocks in a reddish oxidized matrix. Interpreted as carapace breccias, these provide further support for the inferred post-depositional flow.

Distal blob deposits near Wolf Creek Pass were deformed differently from the more widespread features just described. Large stretched and slightly flattened blobs (elongation ratios to 20:1, surfboard shapes in 3D) are spectacularly inclined to the northwest; dips, increase upward, to 70° at high stratigraphic levels (Fig. 9a). The matrix was more brittle, at least during late stages of deformation, as it contains well-developed pull-apart fractures. The only well exposed contact between blobs and overlying foliated rock in this area (a few km NE of Wolf Creek Pass) is abrupt. Within <2 m, well-developed blob-bearing material changes abruptly into weakly foliated massive rock, a discontinuity which suggests subhorizontal shear motion. The highest recognizable blobs are cut by vertical pull-apart fractures, and the presence of low-angle thrust faults (NW-SE) lower in this area (Fig. 9b) also attests to a component of late brittle deformation.

Rheomorphic flow has been recognized elsewhere in a few calc-alkaline tuffs (Chapin and Lowell, 1979; Smith and Cole, 1997), but is more common in low-viscosity peralkaline deposits (Mahood, 1984; Mahood and Hildreth, 1986;

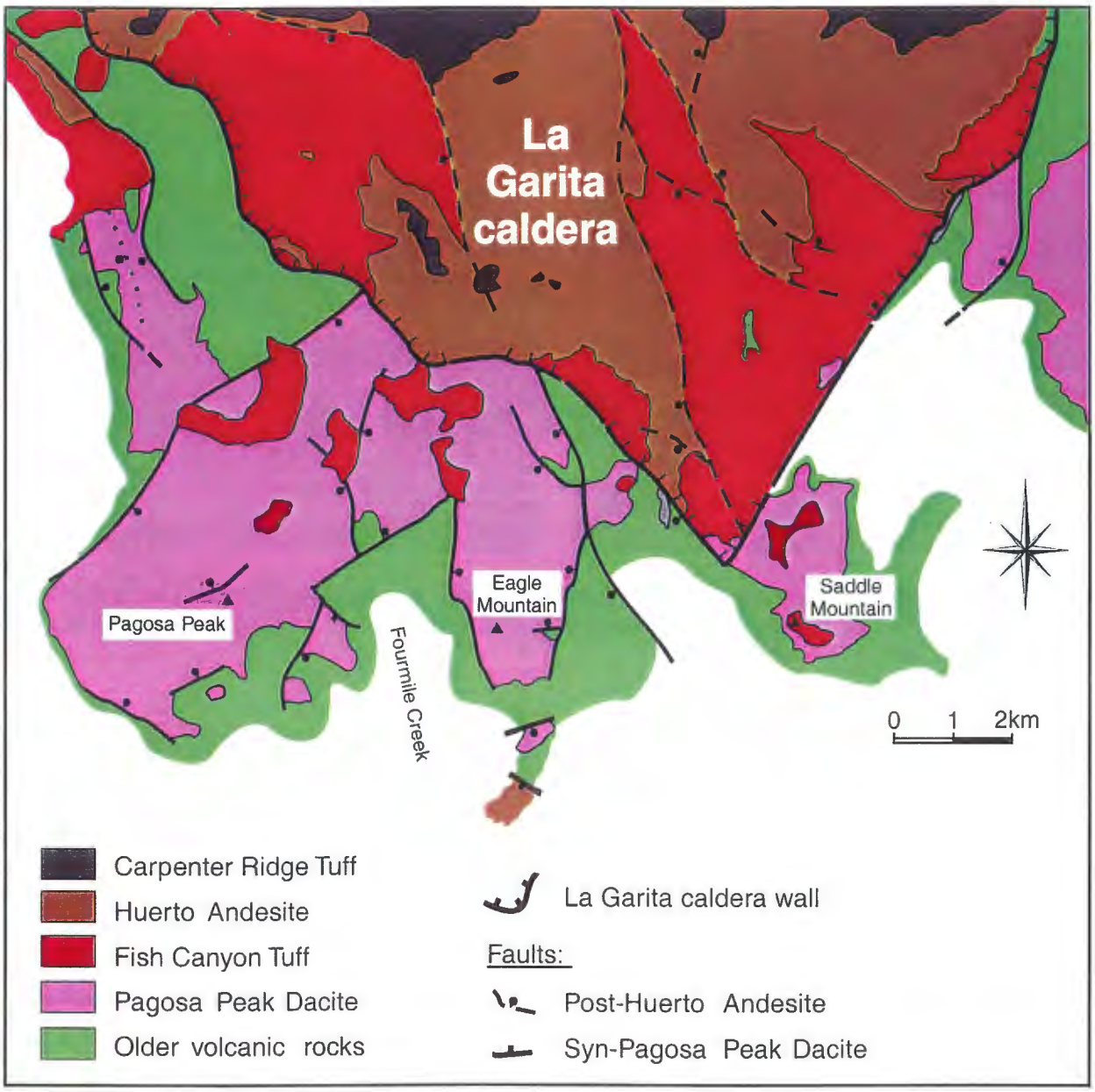

Figure 10: Map of the southern part of the La Garita caldera, showing faults active during eruption of the Pagosa Peak Dacite. These faults form a complex graben aligned with the N-S axis of the La Garita caldera, having two deep segments separated by a horst. Units predating the Pagosa Peak Dacite include older tuffs (Masonic Park and Chiquito Peak Tuffs) and andesites (Conejos Formation and Sheep Mountain Andesite).

Schmincke and Swanson, 1967) and high-temperature crystal-poor units (Milner et al., 1992; Twist and Elston, 1989). The Pagosa Peak Dacite, with its near-solidus mineral assemblage in a rhyolitic matrix and relatively low magmatic temperature, was more viscous than most pyroclastic rocks that display fluidal deformation. Rapid deposition and exceptionally efficient heat retention seem required.

3.4. Magma water content and viscosity

Fish Canyon magma was homogeneous, crystal-rich dacite (Table 3), reflecting near-solidus conditions, in agreement with the inferred magmatic temperature of 760 ± 30 °C (Johnson and Rutherford, 1989). This temperature and the presence of biotite and hornblende at 2.5 kbar suggest a high water content, estimated at 5 wt. % (Johnson and Rutherford, 1989).

Calculated magma viscosities of extrusive silicic magma are 10^4 to 10^6 Pa s (Scaillet et al., 1998). Fish Canyon magma viscosity is near the upper end of this range, both matrix melt viscosity (~$10^{5.2}$ Pa s) calculated by the method of Hess and Dingwell, (1996) at 5 wt % H_2O, and bulk viscosity (~10^6 Pa s) calculated using their equation 2.

4. Syneruptive subsidence structures

Subsidence during eruption of the Pagosa Peak Dacite is characterized by block faulting that produced a broad zone of grabens and horsts, similar to that described as piecemeal subsidence (Branney and Kokelaar, 1994; Moore and Kokelaar, 1998), rather than collapse of a piston-like caldera. The faulted area is within the southern lobe of the Pagosa Peak Dacite, immediately south of the La Garita caldera (Fig. 10). Subvertical normal faults trending NE and NW, some with displacements >500 m, form two grabens 3-4 km wide. They are separated by a horst to the south but merge northward near the southern topographic wall of the caldera. The La Garita wall truncates these faults, indicating that they extended into the region that collapsed during eruption of the Fish Canyon Tuff.

No significant fault movement has been recognized prior to eruption of the Pagosa Peak Dacite, but major faulting was concurrent with its eruption. Landslide blocks derived from underlying footwall units are locally intercalated with Pagosa Peak pyroclastic flows adjacent to fault scarps, and drastic changes in thickness of the Pagosa Peak Dacite across such faults indicate that large displacements were contemporaneous with its emplacement. Deformation of Pagosa Peak Dacite adjacent to a fault scarp at Eagle Mountain was apparently related to fault movement prior to complete solidification (Fig. 11).

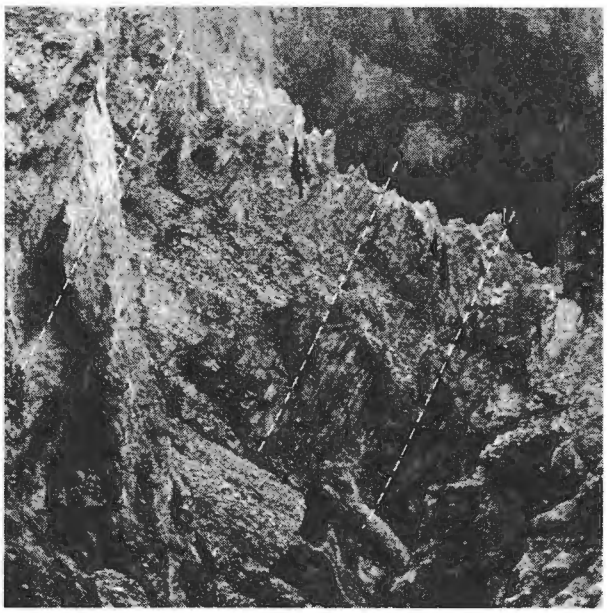

Fig. 11: Steep flow layering in brecciated Pagosa Peak Dacite; adjacent to fault at Eagle Mountain); foliation trends enhanced by dashed lines.

Faulting outside the caldera ceased at the onset of caldera collapse; Fish Canyon Tuff overlaps these faults without offset. In contrast, extensional faulting continued inside the caldera during and slightly after the emplacement of the postcaldera Huerto Andesite (Fig. 10). Several northwest-trending faults with vertical displacements of 50-250 m cut the Huerto Andesite but are covered without offset by the younger Carpenter Ridge Tuff.

The southern La Garita wall is locally faulted, and two linear segments of the caldera margin that are subparallel to trends of Pagosa Peak-related faults intersect at an acute angle northwest of Saddle Mountain (Fig. 10). These faults appear to have formed in part during the collapse of the caldera, and in part during a younger Huerto-related episode. The subparallelism of La Garita caldera margins to syn-Pagosa Peak faults trends suggests that these pre-existing faults played a role in localizing the southern caldera structures.

Vents for the Pagosa Peak Dacite are probably buried within the southern segment of the La Garita caldera. Syneruptive extensional faults that project into the caldera area may have served as magma conduits, as indicated by general parallelism

with post-Huerto faults within the caldera that suggest sustained influence by early structures.

5. Eruptive mechanisms

Many observations indicate that pyroclastic flows were the primary emplacement mechanism for the Pagosa Peak Dacite, but this exceptionally thick composite unit differs from typical ignimbrites, including the Fish Canyon Tuff. It is characterized by high aspect ratios, a near absence of accidental lithic fragments, and a high proportion of large subequant blobs that are distinct in size, shape, and vesicle content from typical pumices. These features resemble those of block-and-ash flows related to dome collapse (e.g., Ui et al., 1999; Rodriguez-Elizarras et al., 1991), but such an emplacement mechanism seems improbable for the Pagosa Peak Dacite.

5.1. Dome collapse or low-column fountaining of silicic magma?

Formation of the Pagosa Peak Dacite by dome collapse would require the extrusion of an immense lava-dome complex that shed block-and-ash flows in rapid succession as the flanks of active domes became gravitationally unsTable. The Pagosa Peak deposits are extraordinarily voluminous and thick in comparison to well-documented dome-related block-and-ash flows. These are typically small volume (<0.01 km^3), represent only a fraction of the parental-dome volume, and have runout distances of only a few kilometers (Cole et al., 1998). The near-vent topographic relief needed to deposit the Pagosa Peak as an accumulation of gravitationally-emplaced block-and-ash flows more than 1 km thick would require the growth of domes to extraordinary heights. Such a dome complex would have been entirely inboard of the topographic rim of the La Garita caldera, as no remnants are preserved.

Additional features of the Pagosa Peak Dacite require rapid emplacement and efficient heat retention during deposition. It is uniformly glassy near the base, becomes thoroughly devitrified upward, largely lacks welding breaks, and was deformed by post-emplacement flow. Clasts in block-and-ash flows are typically variably devitrified, in contrast to the absence of devitrified clasts in the glassy basal Pagosa Peak Dacite. Block-and-ash flow deposits are also nonwelded or at most weakly cintered (Boudon et al., 1993), in contrast to the unified welding-crystallization zonation that encompasses multiple flow units in the Pagosa Peak Dacite. The extrusion of lava, followed by gravitational collapse on the flanks of immense domes, is an inefficient heat-retentive mechanism, not compatible with the high emplacement rate indicated by the simple welding zonation of the Pagosa Peak Dacite. Intense post-emplacement viscous flow is also more difficult to reconcile with initial emplacement as block-and-ash flows than with magma fragmentation in the eruptive conduit and primary pyroclastic eruption.

A sustained low-column eruption from fissures, and lateral transport in poorly-inflated, low-momentum pyroclastic flows, is our favored model for the rapid emplacement and efficient heat retention that these deposits appear to require. Many characteristics of the deposits (high aspect ratio, near absence of lithic fragments, high proportion of poorly vesiculated blobs, absence of shattered crystals) suggest lower emission velocities than typical ignimbritic eruptions (Best and Christiansen, 1997; Wilson et al., 1995; Wilson et al., 1980). A fracture-dominated magma fragmentation mechanism is apparently required by the large sizes and the angular shapes of magmatic blobs, as well as by the near absence of typical bubble-wall shards in the ashy matrix of these deposits. These unusual

characteristics may reflect high viscosity at fragmentation, induced by gas escape during magma ascent, and high strain rate in the conduits as recorded by the flow layering in many blobs (Fig. 4).

Measured vesicularity in pyroclasts of high-viscosity magmas, such as the Fish Canyon, are effective recorders of vesicularity at fragmentation (Gardner et al., 1996; Klug and Cashman, 1996). The bulk vesicularity of Pagosa Peak magmatic blobs is lower than that in typical silicic pumices (Cashman and Mangan, 1994). Even the vesicle content in matrix glass is much lower than the 60-70 % threshold (Table 2) that is commonly cited for in-conduit fragmentation induced by bubble-wall rupture (Gardner et al., 1996; Sparks, 1978). The limited welding-related flattening of blobs in glassy Pagosa Peak Dacite is consistent with the low vesicle contents of nonwelded samples, implying fragmentation at vesicularity levels well below the typical threshold. A phreatomagmatic component to the eruption might contribute to fragmentation at low vesicularity (Houghton and Wilson, 1989), but the coarse clast size, large total volume, and absence of accidental lithic fragments in most of the deposit are inconsistent with such a mechanism.

5.2. Syneruptive degassing?

The eruption of the Pagosa Peak Dacite, the Fish Canyon Tuff, and the postcaldera lava-like Nutras Creek Dacite from the same homogeneous magma chamber suggests that differences in eruptive style were independent of pre-eruptive magma characteristics, and that these differences arose from syneruptive processes in magmatic conduits. The diversity of such processes is also emphasized by apparently quiescent eruption of the Chao dacite (Chile; de Silva et al., 1994), the largest known Quaternary eruption of silicic lava (24 km^3), which is compositionally similar to units of the Fish Canyon magmatic system. Factors influencing the unusual eruptive and deposition features of the Pagosa Peak Dacite seem to include a delicate balance between gas loss in the conduit and rate of magma ascent.

Gas loss through conduit walls from magma ascending as a permeable foam has been widely recognized as an important control on eruptive styles of silicic magmas (Eichelberger et al., 1986; Jaupart and Allègre, 1991; Stasiuk et al., 1996; Woods and Koyagushi, 1994). Protracted syneruptive degassing and attendant viscosity increase (Dingwell et al., 1996; Sparks, 1997) during rise of the Pagosa Peak magma may have contributed to its low vesicularity at fragmentation and the difference between this eruption and the Fish Canyon Tuff. Magma fragmentation during sustained silicic eruptions is thought to occur when the strain rate overcomes magma relaxation time, a parameter inversely proportional to viscosity (Dingwell and Webb, 1989). This process implies a correlation between void fraction and viscosity at fragmentation, observed both in natural pumices (Thomas et al., 1994) and by numerical simulations (Papale, 1999). Efficient degassing coupled with high shear stress during ascent, as suggested by the ubiquitous inherited flow layering in blobs, could thus have provoked brittle fracturing of the magma at a low vesicularity and the low inferred explosivity of the Pagosa Peak eruption may be a direct consequence of inefficient fragmentation, as the amount of exsolved gas available to expand explosively at fragmentation was limited.

Two indicators of extensive degassing of initially water-rich magmas are reaction rims on amphibole phenocrysts (Rutherford and Hill, 1993) and nucleation of plagioclase microlites in matrix liquid due to elevation of the solidus temperature (Geschwind and Rutherford, 1995; Hort, 1998). The absence of such textures in all eruptive phases

of the Fish Canyon magmatic system suggests that degassing during the Pagosa Peak eruption occurred under a restricted range of conditions. Required are ascent rates that permitted vesiculation, efficient degassing, fragmentation, and eruption without amphibole breakdown or microlite nucleation.

Studies of recent eruptions of magmas close in bulk composition and mineralogy to the Fish Canyon magma, in part calibrated by experimental studies, provide limits on the rates of these two processes. Hornblende breakdown occurs within days or hours of magma ascent. Dacite erupted at Mount St. Helens (~930° C) is less evolved than the Fish Canyon magma, but crystal-rich andesite forming the active dome on the Island of Montserrat (~830° C) is characterized by interstitial liquid compositions like the Fish Canyon magma. For both eruptions, hornblende phenocrysts have well-developed reaction rims and the matrix contains microlites, interpreted as resulting from pre-eruptive vapor loss (Devine et al., 1998; Rutherford and Hill, 1993; Sparks, 1997). The rhyolitic Inyo Domes, for which the permeable-foam hypothesis was first proposed (Eichelberger et al., 1986), and the Chao Dacite both contain well-developed matrix microlites (de Silva et al., 1994; Swanson et al., 1989). Presence of microlites in rhyolite matrix (76 % SiO_2) of Pinatubo dacite, erupted after repose periods >40 minutes, also suggests rapid degassing-induced nucleation (Hammer et al., 1999). The Pinatubo dacite, which is similar to the Fish Canyon magma in temperature and glass composition, lacks hornblende breakdown textures; microlite nucleation may be the more sensitive indicator of degassing.

These examples provide useful analogues for the Fish Canyon magma, although eruption temperatures of the Mt. St. Helens and Montserrat magmas were as much as 70-170° C higher. The low temperature of Fish Canyon magma (~760° C) may have retarded the kinetics of hornblende breakdown, but the appearance of microlites in the Pinatubo magma after short periods of degassing would appear to be an applicable constraint. Thus, if fracture-dominated fragmentation of the Fish Canyon magma during the Pagosa Peak eruption operated primarily due to low gas contents, degassing must have occurred shortly before fragmentation.

A major distinction between the Pagosa Peak Dacite and typical ignimbrite eruptions may be the rate of roof-rock subsidence. Slow foundering of fault blocks and the development of fissures, without catastrophic caldera collapse and accompanying sudden depressurization of the magma reservoir, may have permitted magma ascent rates higher than the 65-70 m/hr needed to avoid hornblende breakdown (Rutherford and Hill, 1993), but slow enough to permit fissure-wall degassing due to the large surface area of such conduits. The large cross-sectional area of fissure vents would facilitate the high discharge rates needed to explain rapid emplacement of the deposit, without requiring the vent-emission velocities associated with plinian eruptions. The formation of many simultaneously active vents, thereby decreasing the initial emission velocity for a given discharge rate, has also been invoked for ignimbrite eruptions related to low-column pyroclastic fountaining (Branney and Kokelaar, 1992; Branney and Kokelaar, 1994).

5.3. Post-emplacement viscous flow

Two contrasted styles of viscous deformation apparently affected the Pagosa Peak deposits. Widespread rheomorphic flow flattened and stretched the pyroclastic fragments at high temperature, soon after emplacement. The horizontal fabric of most flow layering and the absence of complex folding in the deposits exclude large transport distances. This suggests that the driving force was gravitational spreading of the thickest

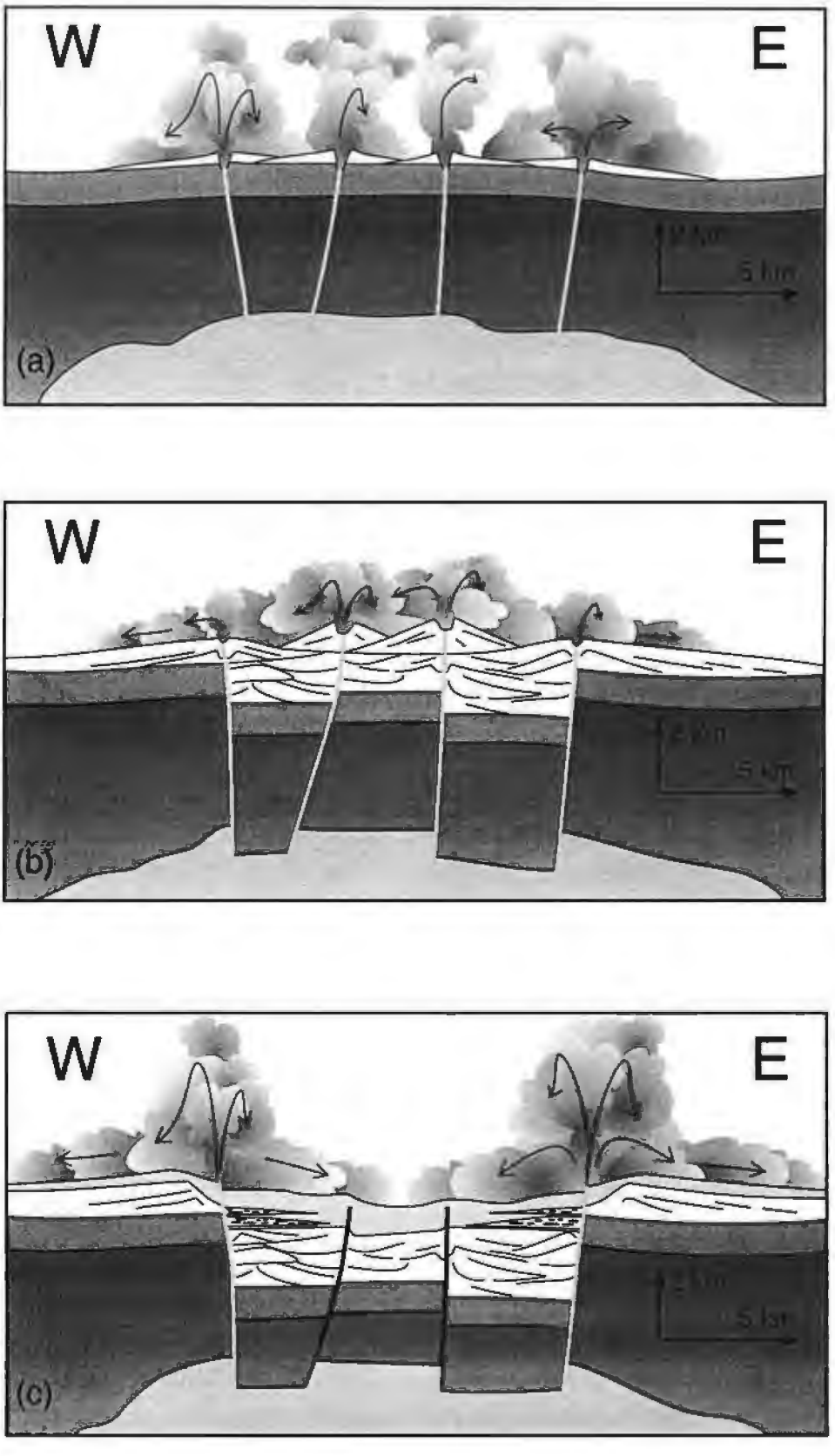

Fig. 12: Schematic processes during eruption of the Pagosa Peak Dacite and Fish Canyon Tuff. (a) Early eruption of Pagosa Peak Dacite: emplacement of lithic-bearing deposits from multiple vents. (b) Main stage of this eruption: low-column pyroclastic fountaining from fissure vents along syneruptive faults. (c) Eruption of the Fish Canyon Tuff and collapse of the La Garita caldera, triggered by magma-chamber depressurization induced by eruption of the Pagosa Peak Dacite. More explosive eruptive style results from catastrophic magma escape along ring-fault vents.

accumulations, rather than wholesale mobilization leading to advancing flow fronts.

Distal sections southeast of Mount Hope deformed in a more brittle and kinematically complex style (Fig. 9). This deformation most likely accompanied the horizontal spreading of proximal sections, which pushed outward and ramped the less mobile distal rocks, deforming them by penetrative shear.

6. Conclusions

The Pagosa Peak Dacite is an atypical pyroclastic deposit. The observed characteristics are consistent with lateral transport as dense, poorly inflated pyroclastic flows, which accumulated locally to >1 km thick. Widespread rheomorphic flow of this viscous deposit, presumably due to gravitational spreading, required efficient heat retention and rapid emplacement. Although an origin as block-and-ash flows emplaced by collapse of enormous lava domes is possible, the deposit is more likely to have resulted from a low-column pyroclastic eruption (Fig. 12).

New field evidence and $^{40}Ar/^{39}Ar$ ages demonstrate that the Pagosa Peak Dacite is a less explosive precursor to eruption of the Fish Canyon Tuff (Fig. 12). Differences in eruptive mechanisms between these two units are probably unrelated to primary magmatic properties, as both were erupted in rapid succession from the same unzoned magma chamber. Varied rates of magma discharge versus degassing in the eruption conduit, influenced by different structures in the magma-chamber roof, may have been critical. The opening of multiple vents during fault-block subsidence may have allowed efficient degassing and low-column fountaining during the Pagosa Peak eruption. The absence of microlites or hornblende reaction rims constrains the timing of degassing to shortly before or during eruption. Depressurization of the enormous magma chamber during the proportionally smaller Pagosa Peak event may have led to instability of the magma chamber roof, thereby triggering eruption of the enormous Fish Canyon Tuff and formation of the La Garita caldera.

Acknowledgements

Many thanks to Christian Huber and Olivier Roche for strong-legged support during strenuous field seasons, to Jenni Barclay, Fidel Costa, Thao Ton-That, and Fleurice Parat for their advice, and to Jacques Metzger for his support on computer-aided drafting. We are grateful to participants of the 1997 informal San Juan workshop for helpful comments. Reviews by Jake Lowenstern, Tim Druitt, and Wendell Duffield considerably improved the manuscript. Costs of fieldwork were supported by the USGS Volunteer Program and by Swiss FNRS grant # 20-49730.96, which also provided funding for laboratory analyses.

References

Best, M.G. and Christiansen, E.H., 1997. Origin of broken crystals in ash-flow tuffs. Geol Soc Amer Bull, 109: 63-73.

Boudon, G., Camus, G., Gourgaud, A. and Lajoie, J., 1993. The 1984 nuée ardente deposits of Merapi volcano, central Java, Indonesia: stratigraphy, textural characteristics, and transport mechanisms. Bull Volcanol, 54: 327-342.

Branney, M.J. and Kokelaar, P., 1992. A reappraisal of ignimbrite emplacement: progressive aggradation and changes from particulate to non-particulate flow during emplacement of high-grade ignimbrite. Bull Volcanol, 54: 504-520.

Branney, M.J. and Kokelaar, P., 1994. Volcanoteconic faulting, soft-state deformation, and rheomorphism of tuffs during development of a

piece-meal caldera, English Lake District. Geol Soc Amer Bull, 106: 507-530.

Cashman, K.V. and Mangan, M.T., 1994. Physical aspects of magma degassing II. Constraints on vesiculation processes from textural studies or eruptive products. Rev Mineral, 30: 447-478.

Chapin, C.E. and Lowell, G.R., 1979. Primary and secondary low structures in ash-flow tuffs of the Gribbles Run Paleovalley, central Colorado. Geol Soc Am Spec Pap, 180: 137-154.

Cole, P.D., Calder, E.S., Druitt, T.H., Hoblitt, R., Robertson, R. and Sparks, R.S.J., 1998. Pyroclastic flows generated by gravitational instability of the 1996-7 lava dome of Soufrière Hills Volcano, Montserrat. Geophys Res Lett, 25 (18): 3425-3428.

Davis, J.M., Elston, W.E. and Hawkesworth, C.J., 1993. Basic and intermediate volcanism of the Mogollon-Datil volcanic field: implications for mid-Tertiary tectonic transitions in southwestern New Mexico, USA. Geol Soc Spec Publ, 76: 469-488.

de Silva, S.L., Self, S., Francis, P.W., Drake, R.E. and Carlos Ramirez, R., 1994. Effusive silicic volcanism in the Central Andes: The Chao dacite and other lavas of the Altiplano-Puna Volcanic Complex. J Geophys Res, 99(9): 17805-17825.

Devine, J.D., Rutherford, M.J. and Gardner, J.E., 1998. Petrologic determination of ascent rate for the 1995-1997 Soufrière Hills Volcano andesitic magma. Geophys Res Lett, 25 (19): 3673-3676.

Dingwell, D.B., Romano, C. and Hess, K.-U., 1996. The effect of water on the viscosity of haplogranitic melt under P-T-X conditions relevant to silicic volcanism. Contrib Mineral Petrol, 124: 19-28.

Dingwell, D.B. and Webb, S.L., 1989. Structural relaxation in silicate melts and non-Newtonian melt rheology in geologic processes. Physics and Chemistry of Minerals, 16: 4351-4366.

Duffield, W.A., 1990. Eruptive fountains of silicic magmas and their possible effects on the Tin content of fountain-fed lavas, Taylor Creek Rhyolite, New Mexico. Geol Soc Amer Spec Pap, 246: 251-262.

Eichelberger, J.C., Carrigan, C.R., Westrich, H.R. and Price, R.H., 1986. Non-explosive silicic volcanism. Nature, 323: 598-602.

Fink, J.H., Anderson, S.W. and Manley, C.R., 1992. Textural constraints on effusive silicic volcanism : beyond the permeable foam model. J Geophys Res, 97(B6): 9073-9083.

Gardner, J.E., Thomas, R.M.E., Jaupart, C. and Tait, S., 1996. Fragmentation of magma during Plinian volcanic eruptions. Bull Volcanol, 58: 144-162.

Geschwind, C.H. and Rutherford, M.J., 1995. Crystallization of microlites during magma ascent: the fluid mechanics of the 1980-1986 eruptions at Mount St-Helens. Bull Volcanol, 57: 356-370.

Hammer, J.E., Cashman, K.V., Hoblitt, R.P. and Newman, S., 1999. Degassing and microlite crystallization during pre-climactic events of the 1991 eruption of Mt. Pinatubo, Phillipines. Bull Volcanol, 60: 355-380.

Hess, K.U. and Dingwell, D.B., 1996. Viscosities of hydrous leucogranite melts: A non-arrhenian model. Am Mineral, 81: 1297-1300.

Hildreth, W. and Drake, R.E., 1992. Volcán Quizapu, Chilean Andes. Bull Volcanol, 54: 93-125.

Hort, M., 1998. Abrupt change in magma liquidus temperature due to volatile loss or magma mixing: effects on nucleation, crystal growth, and thermal history of the magma. J Petrol, 39: 1063-1076.

Houghton, B.F. and Wilson, C.J.N., 1989. A vesicularity index for pyroclastic deposits. Bull Volcanol, 51: 451-462.

Jaupart, C. and Allègre, C., 1991. Gas content, eruption rate, and instabilities of eruption regime in silicic volcanoes. Earth Planet Sci Lett, 102: 413-429.

Johnson, M. and Rutherford, M., 1989. Experimentally determined conditions in the Fish Canyon Tuff, Colorado, magma chamber. J Petrol, 30: 711-737.

Klug, C. and Cashman, K.V., 1996. Permeability development in vesiculating magmas: implications for fragmentation. Bull Volcanol, 58: 87-100.

Larsen, E.S.J. and Cross, W., 1956. Geology and petrology of the San Juan region, Southwestern Colorado. US Geol Surv Prof Pap, 258: 303 p.

Lipman, P.W. (2000) The central San Juan caldera cluster: Regional volcanic framework. *in* P.M. Bethke and

R.L. Hay, eds., Ancient Lake Creede: Its Volcano-Tectonic Setting, History of Sedimentation, and Relation of Mineralization in the Creede Mining District: Geological Society of America Special Paper, 346, 9-69.

Lipman, P.W., Doe, B. and Hedge, C., 1978. Petrologic evolution of the San Juan volcanic field, Southwestern Colorado: Pb and Sr isotope evidence. Geol Soc Am Bull, 89: 59-82.

Lipman, P.W., Dungan, M.A. and Bachmann, O., 1997. Comagmatic granophyric granite in the Fish Canyon Tuff, Colorado: Implications for magma-chamber processes during a large ash-flow eruption. Geology, 25(10): 915-918.

Lipman, P.W., Dungan, M.A., Brown, L. and others, 1996. Ash-flow sheets and calderas of the southeastern San Juan volcanic field, Colorado: New tales from old tuffs. Geol Soc Am Bull, 108(8): 1039-1055.

Lipman, P.W., Sawyer, D.A. and Hon, K., 1989. Central San Juan caldera cluster: Field guide 3, South Fork to Lake City. in Lipman, PW, ed., IAVCEI fieldtrip guide: Oligocene-Miocene San Juan volcanic field, Colorado. New Mex Bur of Mines and Miner Resour Mem, 46: 330-350.

Mahood, G., 1984. Pyroclastic rocks and calderas associated with strongly peralkaline magmatism. J Geophys Res, 89: 8540-8553.

Mahood, G.A. and Hildreth, W., 1986. Geology of the alkalic volcano at Pantellaria, Straits of Sicily. Bull of Volcanol, 48: 143-172.

Manley, C.R., 1996. In situ formation of welded tuff-like textures in the carapace of a voluminous silicic lava flow, Owyhee County, SW Idaho. Bull Volcanol, 57: 672-686.

Milner, S.C., Duncan, A.R. and Ewart, A., 1992. Quartz-latite rheoignimbrite flows of the Etendeka Formation, north-western Namibia. Bull Volcanol, 54: 200-219.

Moore, I. and Kokelaar, P., 1998. Tectonically-controlled piecemeal caldera collapse: a case study of Glencoe volcano, Scotland. Geol Soc Am Bull, 110: 1448-1466.

Papale, P., 1999. Strain-induced magma fragmentation in explosive eruptions. Nature, 397: 425-428.

Plouff, D. and Pakiser, L.C., 1972. Gravity study in the San Juan Mountains, Colorado. US Geol Surv Prof Pap, 800: B183-B190.

Renne, P.R. et al., 1998. Intercalibration of standards, absolute ages and uncertainties in 40Ar/39Ar dating. Chem Geol, 145: 117-152.

Riciputi, L.R., Johnson, C.M., Sawyer, D.A. and Lipman, P.W., 1995. Crustal and magmatic evolution in a large multicyclic caldera complex: isotopic evidence from the central San Juan volcanic field. J Volcanol Geotherm Res, 67: 1-28.

Rodriguez-Elizarras, S., Siebe, C., Komorowski, J.C., Espindola, J.M. and Saucedo, R., 1991. Field observations of pristine block-and-ash-flow deposits emplaced April 16-17, 1991 at Volcan de Colima, Mexico. J Volcanol Geotherm Res, 48: 399-412.

Rutherford, M.J. and Hill, P.M., 1993. Magma ascent rate from amphibole breakdown: an experimental study applied to the 1980-1986 Mount St-Helens eruptions. J Geophys Res, 98 (B11): 19667-19685.

Scaillet, B., Holtz, F. and Pichavant, M., 1998. Phase equilibrium constraints on the viscosity of silicic magmas 1. Volcanic-plutonic comparison. J Geophys Res, 103 (B11): 27257-27266.

Schmincke, H.U. and Swanson, D.A., 1967. Laminar viscous flowage structures in ash-flow tuffs from Gran Canaria, Canary Islands. J of Geology, 75: 641-664.

Smith, T.R. and Cole, J.W., 1997. Somers Ignimbrite Formation: Cretaceous high-grade ignimbrites from South Island, New Zealand. J Volcanol Geotherm Res, 75: 39-57.

Sparks, R.S.J., 1978. The dynamics of bubble formation and growth in magmas: a review and analysis. J Volcanol Geotherm Res, 3: 1-37.

Sparks, R.S.J., 1997. Causes and consequences of pressurization in lava dome eruptions. Earth Planet Sci Lett, 150: 177-189.

Stasiuk, M.V. et al., 1996. Degassing during magma ascent in the Mule Creek vent (USA). Bull Volcanol, 58: 117-130.

Steven, T.A., 1975. Mid-Tertiary volcanic field in the southern Rocky Mountains. Geol Soc Am Mem,

144: 75-94.

Swanson, S.E., Namey, M.T., Westrich, H.R. and Eichelberger, J.C., 1989. Crystallization history of Obsidian Dome, Inyo Domes, California. Bull Volcanol, 51: 161-176.

Thomas, N., Jaupart, C. and Vergniolle, S., 1994. On the vesicularity of pumice. J Geophys Res, 99 (B8): 15633-15644.

Turbeville, B.N., 1992. Tephra fountaining, rheomorphism, and spatter flow during emplacement of the Pitigliano Tuffs, Latera caldera, Italy. J Volcanol Geotherm Res, 53: 309-327.

Twist, D. and Elston, W.E., 1989. The Rooiberg felsite (Bushveld complex): textural evidence pertaining to emplacement mechanisms for high-temperature siliceous flows. New Mex Bur Mines Res Bull, 131: 274.

Ui, T., Matsuwo, N., Sumita, M. and Fujinawa, A., 1999. Generation of block and ash flows during the 1990-1995 eruption of Unzen Volcano, Japan. J Volcanol Geotherm Res, 89: 123-137.

Walker, G.P.L., 1983. Ignimbrite types and ignimbrite problems. J Volcanol Geotherm Res, 17: 65-88.

Whitney, J.A. and Stormer, J.C., 1985. Mineralogy, petrology and magmatic conditions from the Fish Canyon Tuff, Colorado. J Petrol, 26 (3): 726-762.

Wilson, C.J.N., Houghton, B.F., Kamp, P.J. and McWilliams, M.O., 1995. An exceptionally widespread ignimbrite with implications for pyroclastic flow emplacement. Nature, 378: 605-607.

Wilson, L., Sparks, R.S.J. and Walker, G.P.L., 1980. Explosive volcanic eruptions-IV. The control of magma properties and conduit geometry on eruption column behavior. Geophys J Res Astr Soc, 63: 117-148.

Woods, A.W. and Koyagushi, T., 1994. Transitions between explosive and effusive eruptions of silicic magmas. Nature, 370: 641-644.

Chapitre 2: The Fish Canyon magma body, San Juan volcanic field, Colorado: rejuvenation and eruption of an upper crustal batholithic magma chamber

Abstract

More than 5,000 km^3 of nearly compositionally homogeneous crystal-rich dacite (~68 wt.% SiO_2: ~45% plag+san+qtz+hbl+biot+sphn+ox+zirc+ap) erupted from the Fish Canyon magma body during three phases: (1) the pre-caldera Pagosa Peak Dacite (an unusual poorly-fragmented pyroclastic deposit, ~200 km^3), (2) the syn-collapse Fish Canyon Tuff (one of the largest known ignimbrites, ~5,000 km^3), and (3) the post-collapse Nutras Creek Dacite (a volumetrically minor lava). The Fish Canyon magma formed by remobilisation of a near-solidus upper crustal intrusive body of batholithic dimensions, not by progressive differentiation of a more mafic parental magma. The necessary thermal input was supplied by an upper crustal intrusion of mafic magma represented at the surface by sparse mafic enclaves in late-erupted Fish Canyon Tuff and by the post-caldera Huerto Andesite. Silicic magma regeneration occurred by eutectic melting in the quartz-feldspar system and may have been promoted by fluid-flux from the mafic magma. Manifestations of this up-temperature magmatic evolution are: (1) extensively resorbed feldspars and quartz, with textures resembling those in partially melted granitoid xenoliths entrained in mafic magmas, but without hydrous phase breakdown; (2) major and trace element compositions of the high-SiO_2 rhyolite matrix glasses, which are consistent with remelting but not with extreme crystal fractionation; (3) rimward increase in Al_2O_3 (> 2.5 wt. %) in hornblende phenocrysts, and An content in plagioclase; (4) multi-generation epitaxial nucleation and growth of plagioclase on partly resorbed K-feldspar crystals (Rapakivi-like textures), which records thermal oscillations; and (5) holocrystalline granodioritic xenoliths in late-erupted tuff, which are interpreted as fragments of the protolith intrusion. Textural and chemical similarities among typical "Monotonous Intermediates", a group of voluminous dacitic ignimbrites lacking obvious chemical zonation, for which the Fish Canyon Tuff is an archetype, suggest that rejuvenation and eruption of young, partly solidified subcaldera plutons in response to voluminous intrusive events may be a common process in the evolution of large pyroclastic units.

Keywords: Monotonous Intermediates, ash-flow eruption, magma rejuvenation by mafic intrusion, large-volume silicic magma systems

1. Introduction

The Fish Canyon Tuff is the largest documented ash-flow tuff (Lipman *et al.*, 1970; Whitney & Stormer, 1985; Lipman, 2000) and the archetypal example of a group of voluminous silicic ignimbrites defined by Hildreth (1981) as the "Monotonous Intermediates". These dominantly dacitic magmas are important for the understanding of crustal magmatism, not only because they are the largest known manifestations of explosive volcanism on Earth (a few hundreds of km^3 to more than 5000 km^3 for a single eruption), but also because these ash-flow sheets provide a link between the plutonic and volcanic realms. Indeed, they resemble erupted batholiths in the sense that they have comparable volumes, occur in the same tectonic settings, and are characterized by a high crystal contents (>40 %), near-solidus mineral assemblages, and lack of evidence for compositional zoning in pre-eruptive magma chambers (de Silva, 1991; Francis *et al.*, 1989).

Some of the most controversial issues in the study of silicic magmatism are the thermal evolution and residence time of large upper crustal magma bodies and whether silicic magmas are generated dominantly by crystal fractionation or by melting of pre-existing crustal material (*e.g.*, Knesel & Davidson, 1997). In particular, the question of residence time of magmas in the upper crust has been debated (see Halliday, 1990; Sparks *et al.*, 1990; Mahood, 1990; Reid *et al.*, 1997; Brown & Fletcher, 1999; Reid & Coath, 2000), following the inference, based on Rb-Sr and $^{40}Ar/^{39}Ar$ data from the Long Valley system (Halliday *et al.*, 1989; van den Bogaard & Schirnick, 1995), that upper crustal silicic magma bodies may remain partly molten for periods > 1 m.y. In acknowledgement of the difficulty of maintaining a large magma body above its solidus in the upper crust for such a long period, an alternative model was proposed in which the magma chamber is episodically reheated, with periods of crystallization alternating with periods of partial remelting following new magma inputs; *i.e.*, "defrosting" of a crystal mush (Mahood, 1990).

The present reinvestigation of the Fish Canyon magmatic system, which has been extensively studied in the past (Lipman *et al.*, 1970; Whitney & Stormer, 1985; Johnson & Rutherford, 1989a; Riciputi *et al.*, 1995), has led to a new model of its petrologic evolution. A rich catalogue of previously unrecognized textural and geochemical features which are well preserved in the recently identified lava-like facies of Fish Canyon magma (Pagosa Peak Dacite and Nutras Creek Dacite; Bachmann *et al.*, 2000), serve as the basis for inferring that the Fish Canyon magma body has been remobilized following a voluminous injection of mafic magma, which reheated and partially remelted an upper crustal near-solidus magma chamber of batholithic dimensions. Similar models have been proposed for the Kos ignimbrite (Keller, 1970), the Long Valley system (Mahood, 1990), the southwest moat rhyolites of the Valles caldera (Wolff & Gardner, 1995) and the ongoing Soufrière Hills eruption on Montserrat (Murphy et al., 2000). The fact that these units, with vastly different volumes, seem to originate by the same mechanism may indicate that thermal rejuvenation of near-solidus upper crustal intrusions shortly prior to eruption is a fairly common process in silicic systems, and offers a plausible alternative to derivation of these crystal-rich magmas by fractional crystallization from a more mafic parent. Moreover, this model does not necessarily require long magma residence time in the upper crust.

2. Geological setting

The San Juan volcanic field, located on the

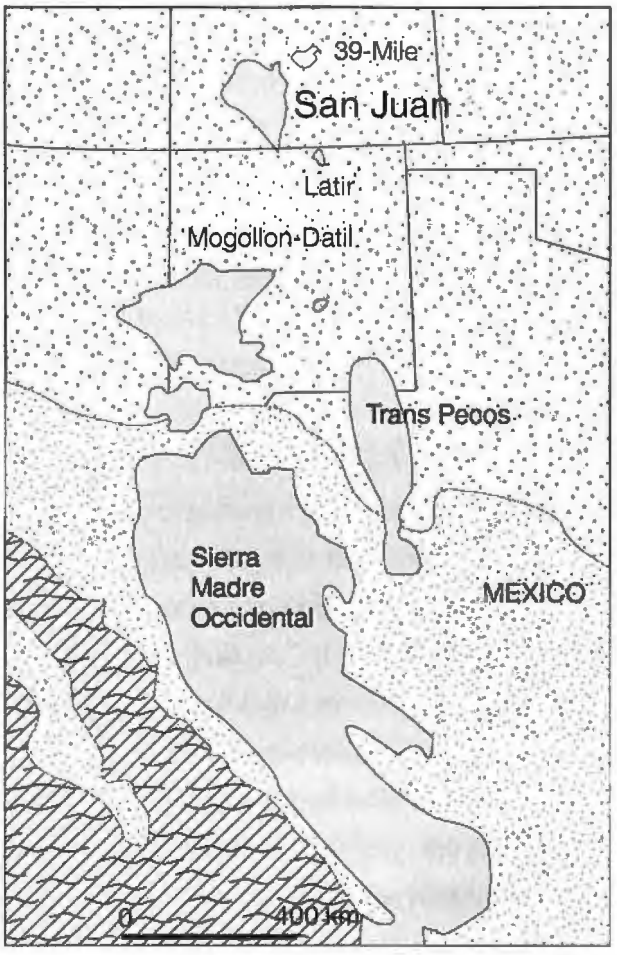

Figure 1: Map of the southwestern U.S.A., emphasizing the alignment of mid-Tertiary volcanic fields extending from the apparently subduction-related magmatism of the Sierra Madre Occidental to the San Juan volcanic field, which is characterized by high-K calc-alkaline eruptive products with arc-like geochemical affinities, despite its unusually large distance from the plate margin (>700 km). Modified from Davis et al. (1993).

eastern margin of the Colorado plateau, in southwest Colorado covers an area of ~25,000 km^2 with a total volume of ~40,000 km^3 of intermediate to silicic volcanic rocks. The San Juan volcanic field is the largest erosional remnant of a nearly continuous igneous province that extended over much of the southern Rocky Mountains during mid-Tertiary time (Steven, 1975). It lies at the northern tip of a succession of Tertiary volcanic fields extending south to the Sierra Madre Occidental, in present-day Mexico (Fig. 1). Although magmatic activity in the Sierra Madre Occidental is plausibly related to Oligocene subduction of the Pacific plate beneath North America, the tectonic setting of the volcanic fields which are located further to the north, several hundreds of kilometers inboard from the plate margin, is more controversial. The arc-like geochemical signature of San Juan magmas (*e.g.*, high-K calc-alkaline series with high La/Nb and Ba/La) has led to the interpretation that low-angle subduction was associated with this magmatic activity (Lipman *et al.*, 1972, 1978), but magma generation from lithospheric mantle previously modified by subduction has been proposed as an alternative (Davis et al., 1993).

Tertiary activity in the San Juan volcanic field began with a period of more than four m.y. of andesitic magmatism (~33-29 Ma) in the form of large stratovolcanoes (Lipman *et al.*, 1970), which accumulated to thicknesses of 1 to 2 km across the entire area of the volcanic field. Voluminous explosive activity began at ~29 Ma, and at least 17 large silicic ash-flow sheets (100-5,000 km^3) and related post-collapse lavas were erupted during ~3 m.y. from three nested caldera clusters in the west, central, and southeast part of the field (Fig. 2; Steven & Lipman, 1976). Caldera-forming eruptions started in the west and southeast caldera clusters and then converged on the central part of the field at ~28.5 Ma. The Fish Canyon magmatic system belongs to a sequence of nine major ash-flow tuffs and related lavas erupted in approximately 2.5 m.y. (28.5 to 26 Ma) from the extremely productive central San Juan cluster, reaching a magma production rate of more than 4,000 km^3 per m.y. (Lipman et al., 1996). Andesitic activity was generally prevalent between caldera-related volcanism, as intermediate composition lavas and clast-rich laharic breccias are interlayered with the ignimbrites. San Juan magmatism ended with a Mio-Pliocene bimodal suite, the Hinsdale Formation, which was associated with crustal extension of the Rio Grande Rift (Lipman

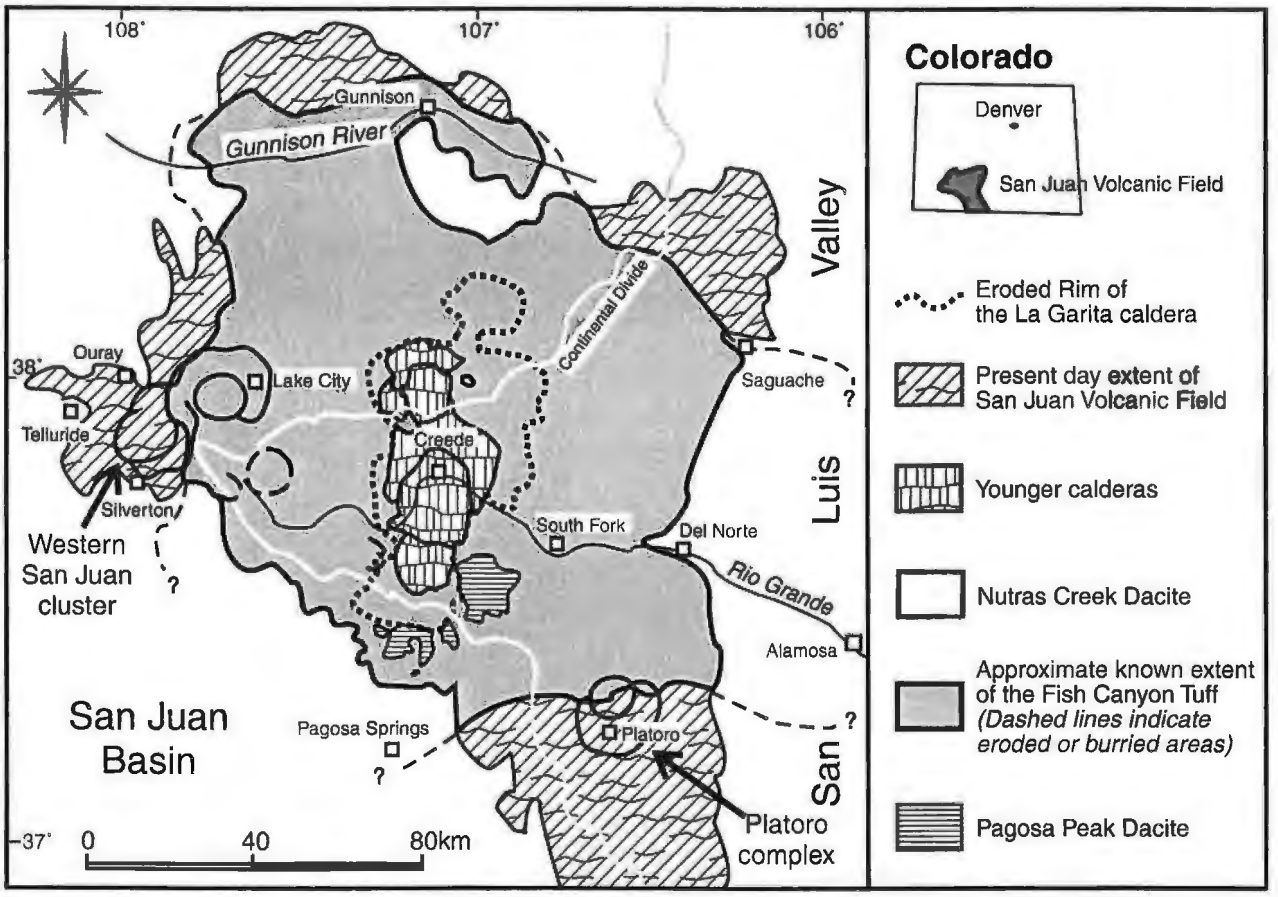

Figure 2: Location map showing the preserved extent of the San Juan volcanic field and the approximate distribution of the outflow facies of the Fish Canyon Tuff (modified from Steven & Lipman, 1976). Ash-flow tuff volcanism in the San Juan volcanic field was concentrated in three caldera clusters. The source of the Fish Canyon eruptions is the La Garita caldera, the second (after buried source of Masonic Park Tuff) and largest of a series of eight calderas which comprise the central San Juan caldera cluster. The northernmost segment of the La Garita caldera was formerly referred to as the Cochetopa Park caldera (CP), but recent field work (Lipman, 1999-2001) has shown that this is a subsidiary collapse structure associated with the Fish Canyon Tuff eruption.

et al., 1970, 1978).

The changes in eruptive style and chemical composition recorded by the products of San Juan volcanic field reflect progressive crustal hybridization and emplacement of a composite high-level batholith during long-term intracontinental magmatism. During the early stages, the eruptive products consisted mainly of andesitic lava flows, produced by differentiation of mantle-derived basalts, combining fractional crystallization and crustal assimilation (Colucci *et al.*, 1991; Riciputi *et al.*, 1995). Volumetrically-minor units with more evolved compositions appear in some sections, but basaltic magma apparently did not reach the surface during Oligocene magmatism. The relatively abrupt appearance of silicic ash-flow sheets at ~29 Ma, emplaced during large caldera-forming eruptions, marks the ascent of magma bodies to shallow levels and increased chemical contributions from the lower and upper crust after several millions of years of crustal heating by injection of mantle-derived magmas. During the period dominated by explosive silicic volcanism, mantle input continued, as indicated by the andesitic units interlayered with the ignimbrites. This led to progressive hybridization of the crustal column within the main zone of magma transport and injection (Lipman *et al.*, 1978; Riciputi *et al.*, 1995). This long-term progression toward more evolved magma compositions and shallower magma storage has been interpreted as representing

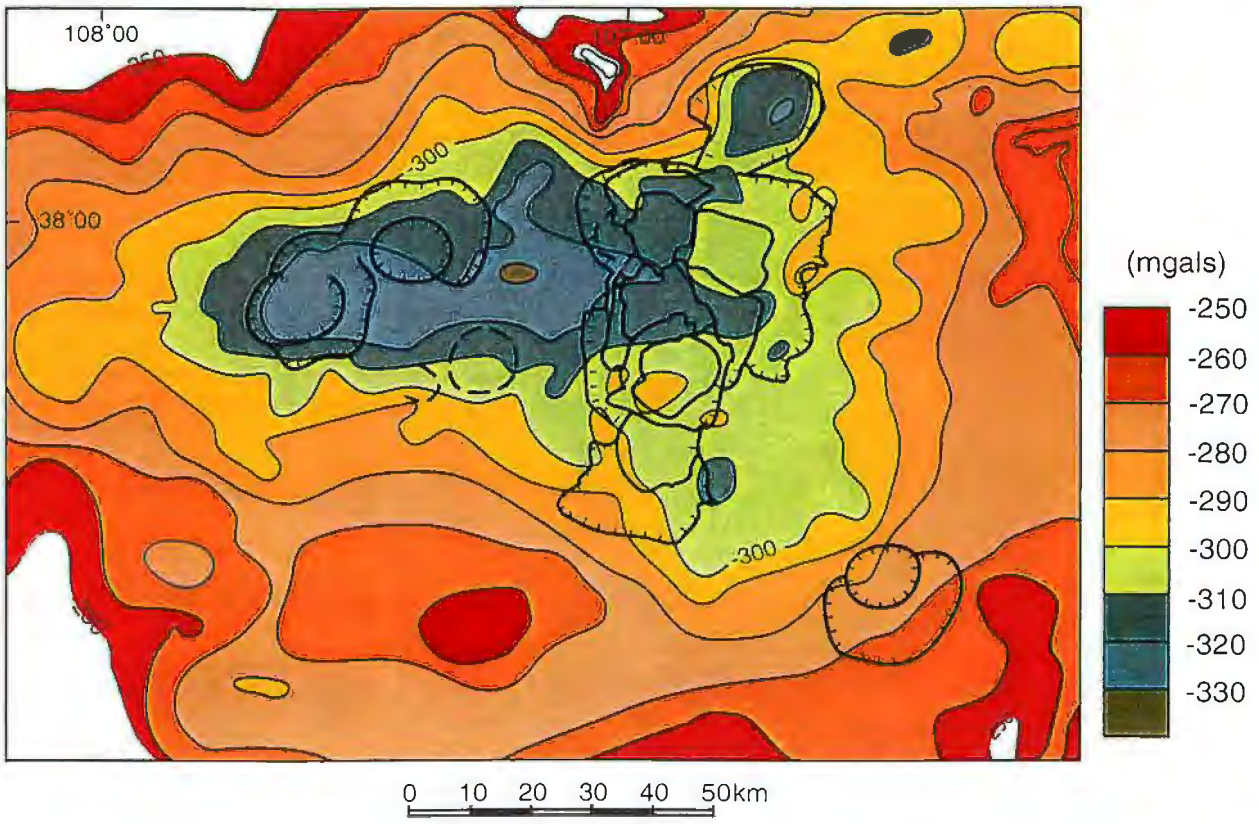

Figure 3: Bouguer gravity field for the San Juan volcanic field (modified from Plouff & Pakiser, 1972). The entire volcanic field is associated with a negative anomaly that is most pronounced in the region encompassing the western caldera cluster and the northern La Garita caldera (hachured lines mark the topographic margins of calderas).

the emplacement and differentiation of a large composite batholith in the upper crust. This interpretation is corroborated by the presence of a large negative Bouguer gravity anomaly (down to –330 mgals) in the San Juan region (Fig. 3; Plouff & Pakiser, 1972).

The eruptive history of the Fish Canyon magmatic system is more complex than previously thought. The Fish Canyon magma chamber produced three separate but compositionally identical units with different eruptive styles in rapid succession about 28 m.y. ago (Lipman *et al.*, 1997; Bachmann *et al.*, 2000). The Fish Canyon Tuff, with a total volume of ~5000 km^3, was erupted during the collapse of the ~100x35 km La Garita caldera as a highly fragmented crystal-rich deposit containing only scarce small pumices. In contrast, the precursory Pagosa Peak Dacite eruption produced ~200 km^3 of poorly fragmented pyroclastic deposits, which are preserved around the southeastern edge of the La Garita caldera (Fig. 2). This unit, which was first recognized as a separate eruptive phase in 1995, and which is interpreted as the product of a low-energy fire-fountain eruption (Bachmann et al., 2000), contains large low-vesicularity pumices, up to 4 m in diameter, referred to as magma "blobs". Unlike bulk Fish Canyon Tuff, the Pagosa Peak Dacite blobs closely approximate Fish Canyon magma compositions. Furthermore, they preserve magmatic textures which have been largely destroyed in the Fish Canyon Tuff by shattering of phenocrysts (particularly feldspars) and dispersal of crystal fragments. The Nutras Creek Dacite is a small post-Fish Canyon lava flow (<1 km^3) on the north flank of the resurgent dome (Fig. 2), which has also yielded non-fragmented samples of Fish Canyon magma.

3. Previous investigations of the Fish Canyon magmatic system

The regional extent of the Fish Canyon Tuff, its large volume, distinctive petrologic character with respect to most ash-flow sheets (uniform dacitic composition, high phenocryst content, near-solidus mineral assemblage), and relation to large-scale caldera collapse were initially recognized more than 30 years ago (Lipman *et al.*, 1970; Lipman, 1975; Steven & Lipman, 1976). Hildreth (1981) called attention to the anomalous character of voluminous compositionally silicic units which lack compositional zoning (Monotonous Intermediates) in light of the prevailing view that most such magmas were derived by differentiation from subjacent mafic parental magmas commonly by crystal fractionation. Such an origin was, and still is, thought to inevitably produce chemical and thermal gradients or discontinuities in shallow magma chambers. Moreover, erupted volumes of homogeneous silicic magma greater than a few thousand km^3 require prohibitively large volumes of parental mafic magma. In effect, the question of how Monotonous Intermediate tuffs originate raises the same issues as does the origin of batholithic granitoid intrusions.

The origin of the Fish Canyon magma was examined by Whitney & Stormer (1985) and Stormer & Whitney (1985) who derived estimates of the intensive parameters associated with magma formation (P, T, volatile fugacities) and addressed the question of thermal and chemical gradients in the pre-eruptive magma chamber. We stress that both goals were pursued on the basis of whole-rock and coexisting phase compositions in bulk samples of the Fish Canyon Tuff *sensu stricto*, which is notable for: (1) an extreme scarcity of pumices (fiamme) sufficiently large to permit direct determinations of magma composition, (2) shattering and dispersion of phenocrysts and glassy matrix during eruption and emplacement, and (3) nearly pervasive devitrification of the matrix. Bulk analyses of non-fragmented magma samples, such as those obtainable from the unit now designated as the Pagosa Peak Dacite were not presented, although these had been previously inferred to be part of the Fish Canyon magmatic assemblage (Lipman, 1975; p. 42, table 6, sample # 10). These authors ascribed minor whole-rock variations among tuff samples to ash elutriation (syn-eruptive crystal-ash fractionation; Lipman, 1967; Walker, 1972), and concluded, on the basis of uniform mineralogy and apparently indistinguishable mineral compositions throughout the tuff, that the pre-eruptive magma body was essentially homogeneous, probably due to convective stirring.

With regard to how estimates of the conditions under which the phenocryst assemblage equilibrated were obtained, Whitney & Stormer (1985) emphasized the presence of resorbed quartz, previously noted by Lipman *et al.* (1978), but described all other mineral phases as euhedral crystals, with little optical zoning, apart from plagioclase which displays oscillatory zoning and occasional more calcic core (p. 729 of Whitney & Stormer, 1985). A temperature estimate (800°C ± 30 °C) was obtained by Fe-Ti oxide thermometry and the mineral equilibration pressure was inferred from the contrasting temperatures determined from the relatively pressure-insensitive Fe-Ti oxide geothermometer and the pressure-dependant two-feldspar geothermometer (Stormer & Whitney, 1985). Based on an apparent need for a large pressure correction, they concluded that the phenocrysts had equilibrated at depths of 25-30 km (~7-9 kb; their Table 8). They estimated a similarly elevated pressure from the high normative anorthite content from the tuff "matrix" (glass+microlites+fine fragments; their Table 6), analyzed with the electron microprobe using broad-beam averaging, when

compared to experimentally determined cotectic compositions in the plagioclase-alkali feldspar-quartz-water system. To account for the syn-eruptive collapse of a caldera, they proposed a two-chamber model, specifying a sufficiently rapid ascent and emplacement, such that the phenocryst assemblage did not equilibrate at low pressure conditions prior to eruption. Magma genesis was not discussed in detail; both crustal melting and fractional crystallization from a more mafic end-member were cited as possible mechanisms.

The data and interpretations of Whitney & Stormer (1985) were criticized on a number of grounds by Grunder & Boden (1987), including the suggestion that the unit was insufficiently sampled to support the contention that no compositional gradient was present in the pre-eruptive magma chamber. Whereas previous studies probably lacked adequate material to evaluate magma homogeneity, our more comprehensive sampling from all three eruptive phases of the Fish Canyon magmatic cycle provides no evidence for pre-eruptive chemical gradients in the magma chamber. A more contentious point pertains to the high pressure of mineral equilibration obtained by Whitney & Stormer (1985), as both lines of evidence advanced by Whitney & Stormer (1985) were disputed. The pressure correction applied to the feldspar geothermometer was inferred to be inaccurate due to incomplete knowledge of the ternary feldspar equilibria, and the argument of a high anorthite content of their matrix analysis, defined as a mixture of glass, microlites and fine fragments, was refuted on the basis of contamination by finely pulverized phenocrysts and lithic fragments in the matrix.

This controversy led to a direct test of the Whitney & Stormer (1985) pressure value by Johnson & Rutherford (1989a), who used the Fish Canyon Tuff as an experimental starting material in order to obtain estimates of P, T, X_{H2O}, and f_{O2} of equilibration for the Fish Canyon phenocryst assemblage and coexisting melt. Johnson & Rutherford (1989a) reproduced the Fish Canyon mineral assemblage and glass chemistry at 2.4 kb, $X_{H2O} = 0.5$, and log f_{O2} = NNO+2 log units at 760°C, the magmatic temperature derived from a reassessment of Fe-Ti oxides thermometry in the Fish Canyon magma. To further establish the pressure at which minerals equilibrated, Johnson & Rutherford (1989b) reported a new experimental calibration of the geobarometer utilizing total Al (Al^T) in hornblende in equilibrium with two feldspars, quartz, biotite, sphene, ilmenite or magnetite, and melt (Hammarstrom & Zen, 1986). Applying this new calibration, which is in broad agreement with the original formulation, to the Fish Canyon hornblendes, Johnson & Rutherford (1989a) determined a pressure of ~2.4 ± 0.5 kb, further strengthening arguments for upper crustal residence and low-pressure equilibration of the Fish Canyon mineral assemblage.

The large, easily extracted blobs of Fish Canyon magma in the Pagosa Peak Dacite and the recognition of the effusive origin of the Nutras Creek Dacite (Bachmann *et al.*, 2000) provide samples of unmodified magma composition, which have allowed us to test the assertion that the pre-eruptive Fish Canyon magma chamber lacked thermal and chemical gradients (Whitney & Stormer, 1985). These samples preserve textural information critical to the formulation of our new model for the genesis and evolution of the Fish Canyon magma body. Because crystals were less broken during the relatively low-energy eruptions, numerous textural relationships that were not previously appreciated are evident (Figs. 4-9). In particular, resorption textures are not limited to quartz, but also are widespread in feldspar phenocrysts, and evidence of grain boundary melting is preserved when the two feldspar phases are in contact (Figs. 7-9). These observations have led to a new working hypothesis

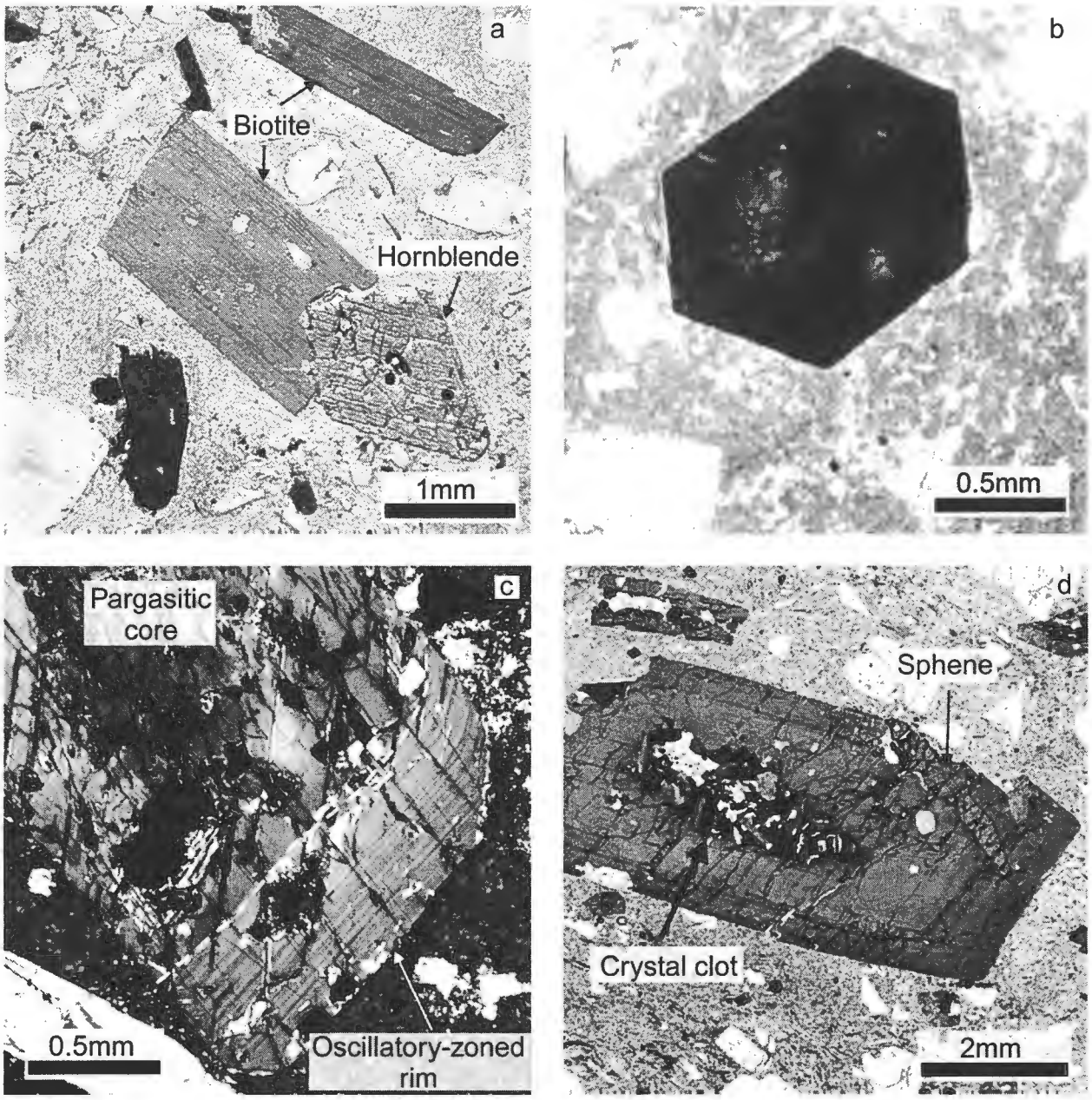

Figure 4: Hornblende and biotite phenocrysts in Fish Canyon magma. (a) Euhedral hornblende and biotite phenocrysts in the Pagosa Peak Dacite (Bfc 171; plain polarized light). (b) Large euhedral biotite in the Pagosa Peak Dacite (PCB1; plain polarized light). (c) Large hornblende phenocryst showing an oscillatory zoned rim and an inherited pargasitic core (PCB1; partially crossed polars). (d) Large hornblende containing a complex core composed of an intergrowth of plagioclase, biotite, and oxides, as well as smaller hornblendes which are compositionally identical to the rim. A large euhedral sphene is also included in the hornblende rim (Bfc 68; plain polarized light).

for the origin of the Fish Canyon magma body, in which a pre-existing near-solidus intrusive body was partly melted immediately prior to large-scale eruption from a caldera.

4. modal abundances and phenocryst textures

The Fish Canyon magma is a crystal-rich (>40%) dacite characterized by a near-solidus mineral assemblage, consisting of two feldspars, quartz, hornblende, biotite, Fe-Ti oxides, apatite, sphene, zircon, and rare pyrrhotite, in a microlite-free interstitial melt of high-silica rhyolite (75-77 wt.

Table 1: Modal analyses of samples from different parts of the Fish Canyon magmatic system.

Sample	Bfc 59	Bfc 83	Bfc 13	Bfc 12	Bfc 115	Average	Range
Description	PPD	PPD	PPD	PPD	NCD	Unfrag. W&S (1985)	
Plagioclase	28.1	23.9	26.4	26.0	26.6	26.2	20 to 30
K-feldspar	5.7	9.6	4.3	4.3	6.5	6.1	6 to 13
Quartz	3.9	4.3	1.2	2.2	3.6	3.0	1 to 8
Hornblende	1.8	3.7	6.8	4.3	2.4	3.8	1 to 4.5
Biotite	3.4	2.8	5.3	3.5	3.2	3.6	2.5 to 7
Sphene	0.2	0.2	0.3	1.3	1.3	0.7	0.1 to 0.5
Opaques	0.0	0.7	1.3	0.2	0.1	0.5	1 to 3
Matrix	57.0	54.9	54.4	58.2	56.3	56.2	50 to 60
% pheno.	43.0	45.1	45.6	41.8	43.7	43.8	40 to 50
Sample	Bfc 49	Elep.	Bfc 134	Bfc 187	MLX Big	CsGr10	Bfc 138
Description	FCT (prox.)	FCT (dist.)	Gran. xeno.	Gran. xeno.	Porph. xeno.	Gran. xeno.	Xtal-rich inc.
Plagioclase	26.8	31.4	32.4	34.7	21.5	~40	48.7
K-feldspar	4.7	7.5	30.8	28.8			-
Quartz	3.7	4.7	21.9	24.6	{ 74.1*	{ ~50*	-
Hornblende	3.2	4.5	3.5	3.8	-	4.4	10.9
Biotite	3.6	4.8	8.4	5.0	3.3	3.7	9.1
Sphene	0.3	0.7	0.5	0.7	-	0.5	-
Opaques	1.4	1.3	2.6	2.4	1.1	1.4	3.5
Matrix	56.3	45.4	-	-	-	-	27.8
% pheno.	43.7	54.6	-	-	-	-	72.2

Representative modal calculations for the Fish Canyon magmatic system. Measurements for the Fish Canyon magma done on Pagosa Peak Dacite blobs and Nutras Creek Dacite, to avoid biased results due to crystal-ash fractionation. Total number of points: 2000. Sample Bfc 49 and Elep are respectively proximal and distal outflow facies of the Fish Canyon Tuff. They were measured to estimate the impact of elutriation on modal abundances. Measurements of Whitney and Stormer (1985) done uniquely on Fish Canyon Tuff samples (Agua Ramon section, Goodrich Creek section, Beaver Creek section).*= sum of K-feldpar and quartz. Abundances of sanidine and quartz in xenoliths are relatively inaccurate due to similar appearance in thin sections. Gran. xeno. refers to the granodioritic xenoliths, Porph. xeno. to the porphiritic granitic xenoliths and Xtal-rich inc. to the crystal-rich inclusions. CsGr10 contains interstitial granophyre.

% SiO_2). These attributes characterize all three stratigraphic units that comprise the Fish Canyon magmatic system. Modal abundances of phenocrysts are similar among Pagosa Peak Dacite blobs and Nutras Creek Dacite samples (non-fragmented Fish Canyon magma) and overlap with the modal data reported by Whitney & Stormer (1985; Table 1). Apparent modal variations in feldspars, quartz, and hornblende among Pagosa Peak Dacite samples (Table 1) probably lack geological significance, but are a consequence of the size of Fish Canyon phenocrysts (0.5 to 5 mm), which are too large to provide highly reproducible modal analyses at thin section scale. Sanidine and quartz abundances also have large uncertainties due to difficulties in distinguishing them in thin section. Despite these obstacles, the impact of glass winnowing during ash-flow emplacement is perceptible (Table 1). One outflow Fish Canyon Tuff sample ("Elep") is ~ 11 % more crystal-rich than any magma blobs from the Pagosa Peak Dacite, or the other outflow Fish Canyon Tuff sample (49), for which we have modal

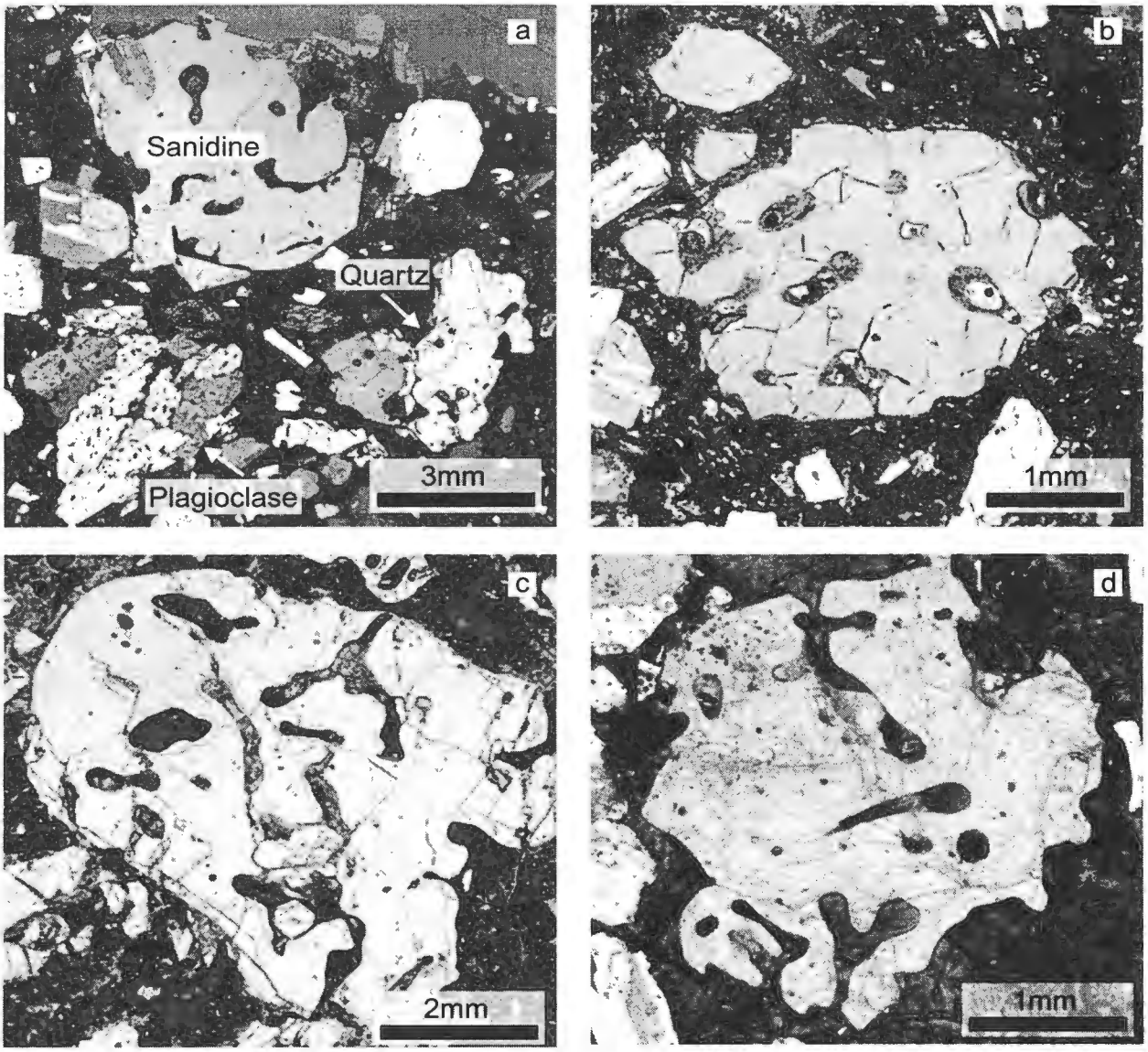

Figure 5: Resorption textures in feldspars and quartz in non-fragmented Fish Canyon magma. (a) Sanidine, plagioclase and quartz in the Nutras Creek Dacite (Bfc 115c; crossed polars). (b) Quartz in the Pagosa Peak Dacite (Bfc 68; crossed polars). (c) Sanidine in the Pagosa Peak Dacite (PCB1; partially crossed polars). (d) Sanidine in the Nutras Creek Dacite (Bfc 115a; crossed polars). Note that both sanidine and quartz are riddled with long melt channels connected to the matrix. Euhedral terminations on these phases are rarely observed, and we interpret these textures as indications of partial melting, not skeletal growth.

data. The interstitial glass is, in most cases, devitrified, but is preserved in basal vitrophyres of the Pagosa Peak Dacite and Fish Canyon Tuff.

Hornblende and biotite, 0.5 to 5 mm in size, as well as the largest accessory minerals (apatite and sphene), are essentially euhedral in all three Fish Canyon units and show little evidence of reaction with the surrounding melt (Fig. 4). In contrast, sanidine and quartz tend to occur as large (to 5-6 mm) complexly resorbed grains, deeply dissected by melt channels (Fig. 5). All three Fish Canyon units exhibit these corrosion textures, although efficient crystal shattering and dispersal related to magma fragmentation and high-energy emplacement has rendered them obscure in the Fish Canyon Tuff. Some sanidines are overgrown in late-erupted units (intracaldera Fish Canyon Tuff and Nutras Creek Dacite) by euhedral granophyric rims (see later section and Lipman *et al.*, 1997). Plagioclase displays diverse textures, showing both internal and marginal resorption as well as oscillatory-zoned euhedral overgrowths on volumetrically minor partially

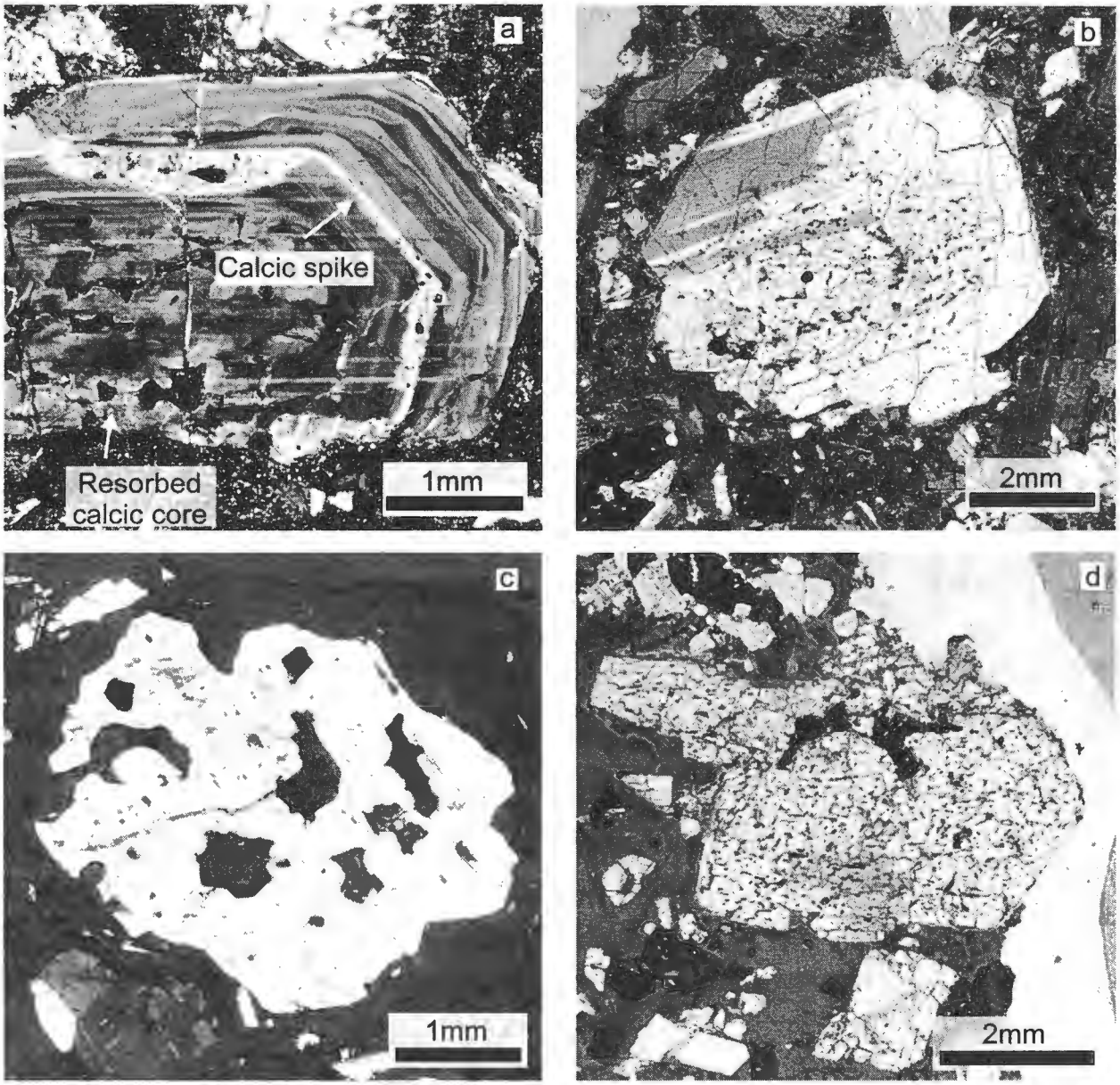

Figure 6: Plagioclase phenocrysts in the Fish Canyon magma. (a) Complexly zoned plagioclase in the Pagosa Peak Dacite, wherein a euhedral mantle displaying oscillatory growth zoning has overgrown a partly resorbed core (Bfc 12; crossed polars). Note the prominent 'calcic spike' immediately outboard of the resorption surface that marks the boundary between the core and the overgrowth. (b) Large plagioclase in the Nutras Creek Dacite, with a faceted outline (Bfc 115c; partially crossed polars). (c) Corroded plagioclase grain in the Pagosa Peak Dacite (Bfc 171; partially crossed polars). (d) Large corroded phenocryst in a Fish Canyon pumice (Bfc 191a; plain polarized light).

resorbed cores (Fig. 6).

Many of the extensively resorbed sanidine grains contain inclusions of other mineral phases. Plagioclase is by far the most abundant, but hornblende, biotite, Fe-Ti oxides, apatite, and sphene are also present in minor quantities. Plagioclase inclusions in these poikilitic sanidines are of two types (Fig. 7). The first consists of irregularly shaped grains, which are in optical continuity despite being physically isolated (Fig. 7a, b and c); the second are subhedral-euhedral laths up to 1 mm long (Fig 7c and d). Both types of plagioclase inclusions in sanidine are instructive with regard to the origin and evolution of the Fish Canyon magma.

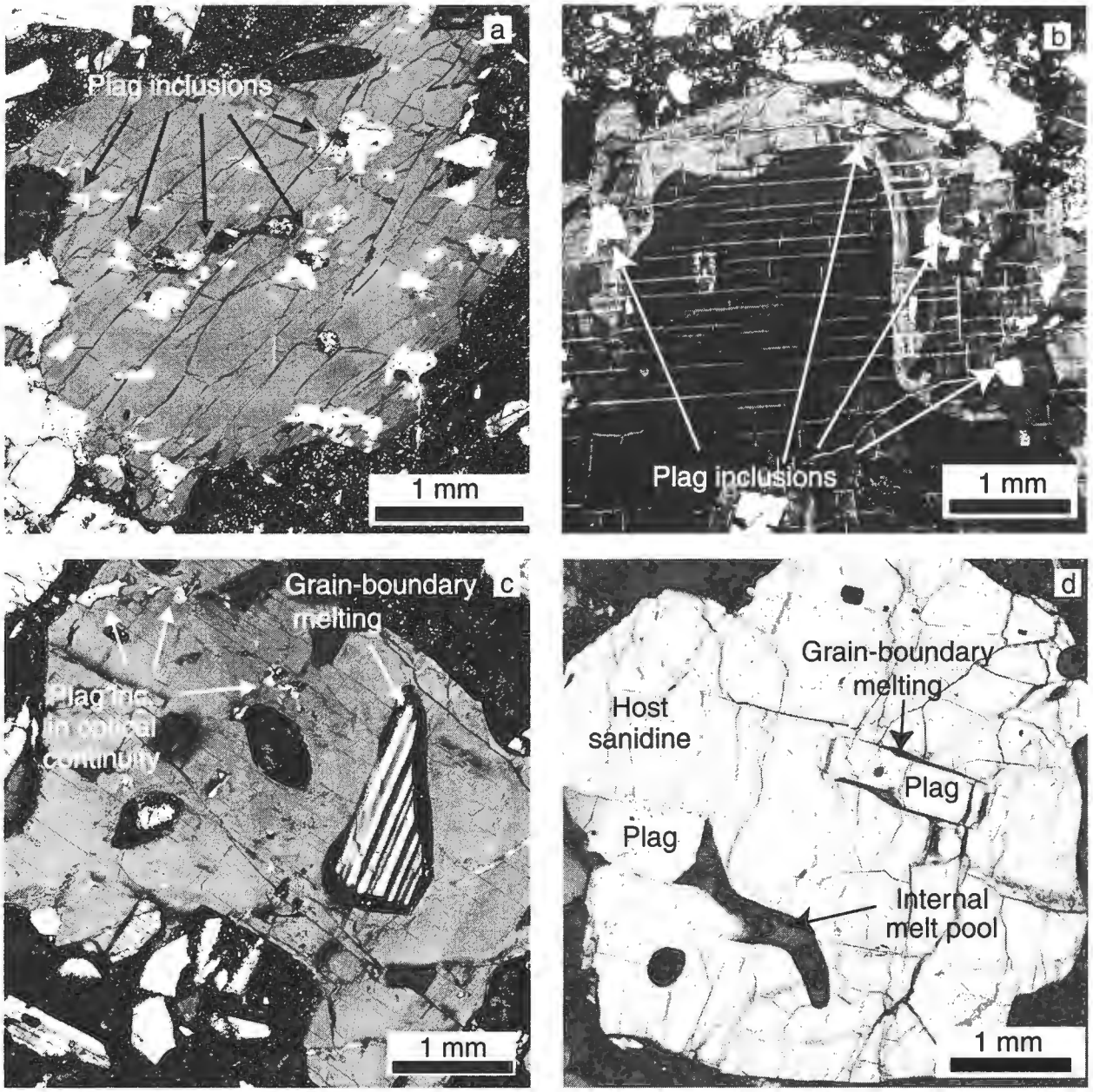

Figure 7: Two types of plagioclase inclusions in Fish Canyon sanidines. (a) and (b) Isolated, anhedral inclusions in optical continuity, showing variable sizes (PCB1 and Bfc 174). (c) and (d) Larger plagioclase inclusions, often subhedral-euhedral, displaying incipient dissolution at the grain contact with the host sanidine (Bfc 12 and Bfc91). Picture (c) shows both populations.

1.1. Plagioclase inclusions in optical continuity

Isolated plagioclase inclusions in optical continuity display a wide diversity of size (a few microns to ~1 mm) and generally have subequant shapes with irregular contours. In favorable sections, where large poikilitic sanidine phenocrysts are transected (Fig. 7b), inclusions are preferentially concentrated near the rims of the host crystal and complex Ba zoning in the sanidine is everywhere spatially associated with these inclusions (and section 6.4.).

One process capable of generating these textures is phase unmixing at the solvus (exsolution). However, diversity of sizes and the irregular subequant shapes of the inclusions set them apart from any exsolution textures described in the literature (*e.g.,* Smith, 1974). An alternative hypothesis, proposed by (Stimac & Wark, 1992) to explain similar textures in silicic lavas of Clear Lake,

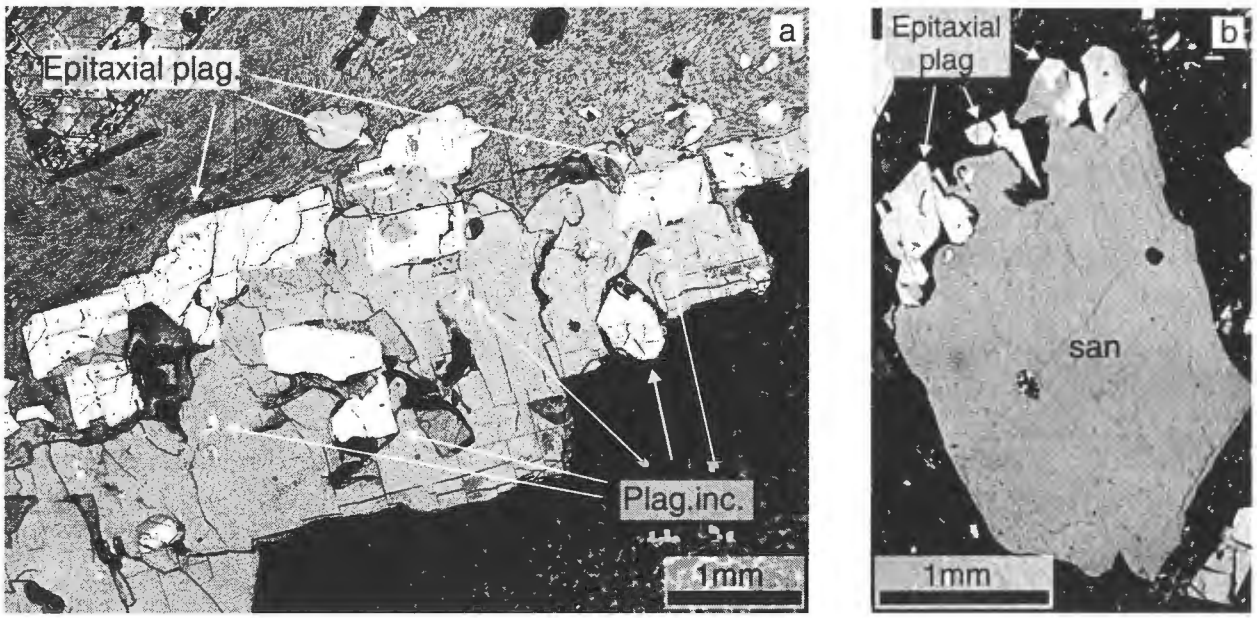

Figure 8: Discontinuous plagioclase mantles on sanidines in the Pagosa Peak Dacite. (a) The multiple grains of plagioclase intergrown with the outer margin of the associated sanidine are all in optical continuity with each other and with the plagioclase crystals located within this sanidine (Bfc 171; plain polarized light; lower right margin of the sanidine crystal is truncated at the edge of the thin section). (b) Large grain of resorbed sanidine rimmed on one end by multiple grains of plagioclase, all in optical continuity. We interpret the attachment sites of these grains on sanidine as nucleation sites. Plagioclase grains which are not in contact with sanidine in the plane of this thin section are still likely to have attained their orientation by epitaxial nucleation. We interpret this grain as an example of the initial stages of formation of Rapakivi-like texture wherein plagioclase mantles form during sanidine dissolution.

California, is epitaxial nucleation (*i.e.*, nucleation with a fixed crystallographic orientation; Bernal & Mackay, 1965) and growth of plagioclase at many points on the periphery of sanidine, followed by regrowth of sanidine in the interstitices between plagioclase grains. The Clear Lake silicic lavas show multiple examples of well-developed plagioclase mantles on sanidine (*i.e.*, Rapakivi textures; Sederholm, 1891), into which these poikilitic zones grade, and the conclusion that these inclusions are related to plagioclase mantling is straightforward. Although plagioclase mantles are rare in the Fish Canyon magma, patches of plagioclase with the same optical orientation attached at the rims of large sanidine crystals are preserved in a few samples (Fig. 8), hinting at remnants of discontinuous plagioclase mantles. Regrowth of sanidine in the interstices is supported by Ba zoning in the sanidine, which is spatially associated with these plagioclase inclusions. As demonstrated by the experimental study of Wark & Stimac (1992), which was designed to trigger plagioclase mantling on sanidine, development of Ba zoning, observed in both Fish Canyon and Clear Lake examples, is consistent with cycles of resorption and growth of sanidine (see section 6.4.).

1.2. Plagioclase laths and grain-boundary melting

The second type of plagioclase inclusion in sanidine consists of subhedral-euhedral laths, up to several millimeters in length, characterized by thin melt zones at the contact with sanidine (Fig. 7c-d). These textural relations are in sharp contrast with the other type of plagioclase inclusions, implying a different origin. These inclusions were most likely free phenocrysts that were engulfed by sanidine, not the products of epitaxial nucleation. The preservation of thin melt zones at the contact between the two phases and the absence of Ba zoning associated with

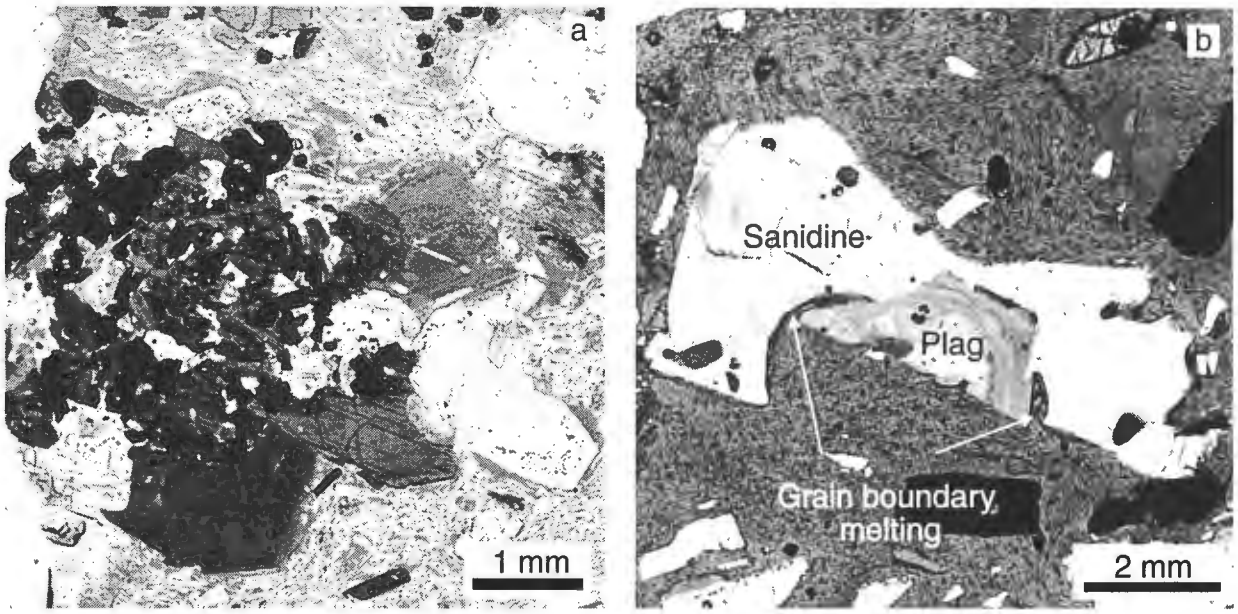

Figure 9: Polycrystalline aggregates in the Fish Canyon magma. (a) Glomerocryst in the Pagosa Peak Dacite characterized by an intimate intergowth of plag+hbl+biot+ox in which preservation of solid-solid grain contacts suggest that this may be a microxenolithic fragment (Bfc 196a; plain polarized light). Euhedral overgrowths on plagioclase and hornblende were precipitated from Fish Canyon magma, and even the mineral composition in the intergrowth are indistinguishable from Fish Canyon phenocrysts. (b) Incipient grain boundary melting along the contact between plagioclase and sanidine in a plutonic microfragment (Pagosa Peak Dacite; Bfc 59; partially crossed polars). Note also that the sanidine contains internal melt pools.

these inclusions (see section 6.4) suggest that grain boundary melting occurred after the establishment of solid-solid contacts following egulfment and that sanidine did not regrow subsequently.

Multi-phase mineral clots, comprising variable amounts of intergrown feldspars, hornblende, biotite and oxides (Fig. 9a) are found in the Fish Canyon magma. These clots are inferred to represent fragments of plutonic material, as they commonly retain solid-solid grain contacts. However, whenever two feldspar phases are in contact, thin melt zones are common along grain boundaries (Figs. 7c, 7d, 9b). These textures resemble those in partially melted granitoid xenoliths entrained in mafic to intermediate lavas (*e.g.,* Grove *et al.*, 1988; Kaczor *et al.*, 1988; Gardner & McPhie, 1999), and are consistent with an up-temperature evolution shortly prior to eruption.

Evidence of partial remelting of inclusions is also present where quartz was included in feldspar. Secondary SiO_2 reprecipitation in internal melt channels within sanidine, and an inclusion of pure SiO_2 glass in a plagioclase phenocryst, suggests extensive dissolution of quartz inclusions in contact with both plagioclase and sanidine (Figs. 10a-b). Disequilibrium affecting quartz and both feldspars supports the inference of a pre-eruptive temperature increase. Dissolution of quartz alone can result from magma depressurization as the quartz stability field contracts relative to feldspars in the Qz-Ab-Or ternary phase diagram with decreasing pressure (*e.g.,* Tuttle & Bowen, 1958), but volumetrically important dissolution affecting all three phases is incompatible with adiabatic ascent of water-rich magmas.

5. Whole-rock chemistry

Whitney & Stormer (1985) report whole-rock major element compositions for Fish Canyon Tuff (outflow tuff facies from the region south-

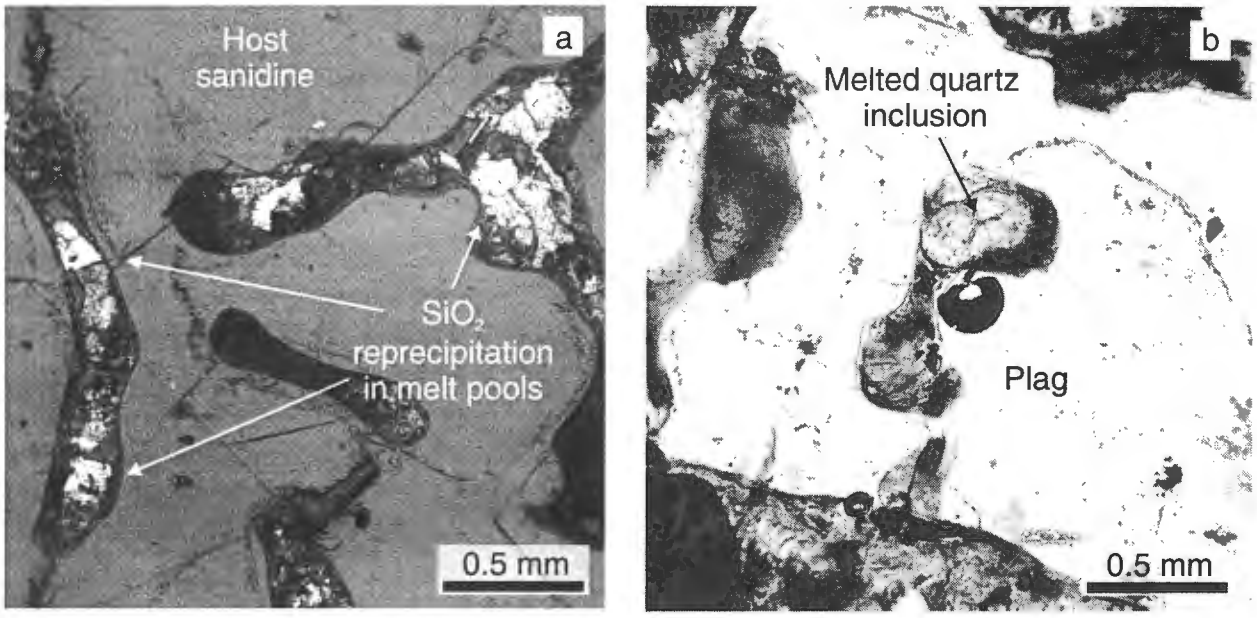

Figure 10: Evidence for melting of quartz inclusions in feldspar hosts. (a) High magnification view of the melt channels of the large Pagosa Peak Dacite sanidine shown on Fig. 5c (PCB1). Birefringent multigrain aggregates within melt channels are SiO2 which we interpret as the product of reprecipitation from extremely SiO_2-rich liquid after melting of quartz inclusions. (b) Complex melt inclusion in a Pagosa Peak Dacite plagioclase. The inner glassy zone marked by the arrow has the composition of 100% SiO2 whereas the surrounding darker glass has the same composition as typical matrix (Bfc 59; plain polarized light). We interpret this occurrence as melting of a quartz inclusion and host plagioclase within a melt channel that was connected in three dimensions to the surrounding melt.

southeast of the La Garita caldera) ranging in SiO_2 wt. % from ~62.5 to 67.5. On the basis of mass-balance calculations tied to glass compositions and crystal contents, they concluded that the Fish Canyon magma is a high-SiO_2 dacite (quartz latite in their nomenclature) with ~67-68 wt. % SiO_2, and that the compositions with lower SiO_2 are the products of variable syn-eruptive crystal-ash fractionation (glass elutriation). We have analyzed 17 bulk Fish Canyon Tuff samples (16 outflow and 1 intracaldera) with widespread geographic coverage (65.4-68 wt. % SiO_2), including one with an extremely high crystal content (~55 %; Elep in Table 2), but we have not reproduced the wide range of SiO2 values that Whitney & Stormer (1985) reported. For most major elements (Fig. 11), our Fish Canyon samples define linear correlations with SiO_2 (compare with Fig. 3 of Whitney and Stormer, 1985), and these data fall on extrapolation of lines connecting glass compositions (electron microprobe analyses) with the average composition of Pagosa Peak Dacite magma blobs (*cf* sample 1, 83, 55, 34 of Table 2 and analysis #10 in Table 6 of Lipman, 1975), which we infer to be representative of bulk magma compositions. The three least crystal-rich tuff samples fall close in major element composition to the average Pagosa Peak Dacite, as do a large pumice from the northern intracaldera facies of the Fish Canyon Tuff (#129 of Table 2) and the post-collapse Nutras Creek Dacite (#115 of Table 2).

On the basis of these data, we infer that the major element range of Fish Canyon magma compositions was narrowly restricted (~67.5-68.5 wt. % SiO_2), but not homogeneous within the limits of analytical precision. As both early-erupted and late-erupted magma compositions are closely similar, and there are few systematic variations in mineral chemistry among the different eruptive phases (see section 6), our data confirm the inference that the Fish Canyon magma chamber was not characterized

Table 2: Whole-rock analyses of representative samples of the Fish Canyon magmatic system

Label	BLOB1	83	55	129	124	49	ELEP	115	csgr16	138	QMI 2	BIG
Description	PPD	PPD	PPD	FCT pum (I)	FCT vitr. (O)	FCT Prox. (O)	FCT Dist. (O)	NCD	Gran. Xeno.	X-rich inc. Hybr. And. inc.		Porph. Xeno.
SiO_2	68.79	68.26	68.51	67.82	67.47	68.00	65.37	67.93	67.16	58.31	57.92	76.13
Al_2O_3	15.16	15.38	15.48	15.25	15.89	15.63	16.32	15.23	14.30	16.98	16.55	12.59
Fe_2O_3	3.40	3.55	3.45	3.97	3.73	3.70	4.85	4.14	3.05	8.05	7.44	1.50
MgO	0.98	0.92	0.93	1.23	0.92	0.93	1.13	0.85	0.84	2.79	2.94	0.34
CaO	2.83	2.91	2.92	3.05	3.06	2.98	3.47	2.79	4.31	4.94	5.84	1.02
Na_2O	3.70	3.92	3.90	3.79	3.91	3.78	3.85	3.66	3.53	3.87	3.29	3.14
K_2O	4.189	4.349	4.119	3.943	4.099	4.101	4.149	4.421	4.366	3.271	3.423	5.062
TiO_2	0.441	0.437	0.413	0.468	0.458	0.453	0.579	0.485	0.383	0.887	1.012	0.200
MnO	0.067	0.089	0.077	0.073	0.076	0.072	0.112	0.101	0.186	0.146	0.159	0.030
P_2O_5	0.180	0.176	0.175	0.197	0.184	0.187	0.235	0.200	0.167	0.577	0.417	0.060
Total	99.73	99.99	99.98	99.82	99.8	99.83	100.06	99.81		99.82	99.78	100.23
Total w/ traces	99.85	100.28	100.11	100.04	100.06	99.96	100.18	100.07	100.17	100.09		
Mg#	0.36	0.34	0.35	0.38	0.33	0.33	0.32	0.29	0.22	0.41	0.28	0.18
LOI	0.21	1.72	0.34	0.70	0.90	0.88	0.40	0.94	1.88	1.12	0.77	0.16
Ni	6.1	5.3	5.8	5.7	5.9	6.8	6.7	6.8		6.5		
Cr	5.0	8.0	5.0	5.0	5.0	7.0	7.0	6.0	4.0	6.0	58.0	7.0
Co	5.4	6.1	7.4	7.1	6.5	7.5	9.2	7.1		15.7	19.3	2.1
V	48.4	48.9	44.2	51.3	52.5	53.3	64.7	56.3	42.0	99.6		
Sc	5.3	6.6	6.0	6.57	6.3	6.5	8.1	6.0		12.8	16.5	2.5
Cu	7.1	8.3	7.4	10.6	10.0	8.3	12.4	10.9		19.4		
Zn	46.0	92.0	67.0	55.7	58.0	58.0	68.0	63.5	34.0	100.3	100.0	34.0
Cl	242	657	336	102	235	249	44	218		502		
Ga	16.8	17.6	18.5	17.8	17.6	17.6	18.8	18.2	17.0	21.5		
Pb	15.9	17.3	17.4	17.1	16.6	18.3	13.1	17.1	11.0	13.3		
Sr	438.2	439.2	454.2	456.0	486.9	452.7	570.3	436.4	384.0	541.9		
Rb	116.8	119.8	112.2	117.2	109.6	114.7	96.0	122.8	123.4	100.6	98.0	162.0
Ba	864.6	834.9	879.7	638.0	891.0	809.7	1035.2	849.4	933.0	488.9		
Zr	182.0	186.5	172.3	180.0	174.0	180.6	194.7	191.7	172.0	198.9		
Nb	17.8	17.1	15.5	16.9	16.0	16.6	15.9	17.3		15.5		
Th	13.9	13.6	13.8	13.8	12.4	13.2	9.8	12.9	11.0	9.1	5.8	22.7
U	5.6	6.0	5.1	4.3	3.9	4.4	2.3	4.5		3.3	2.1	5.1
Y	21.4	22.1	18.9	21.4	21.9	23.8	24.5	26.4	19.5	23.4		
Ta	1.2	1.2	1.1	1.1	1.1	1.1	1.0	1.1		0.7	0.7	1.2
Hf	4.9	5.4	4.9	5.0	4.7	5.1	5.3	5.0		5.0	5.2	3.9
Cs	3.2	2.9	2.9	2.4	2.4	2.4	1.0	3.3		1.4	1.7	1.2
La	43.7	43.3	42.6	43.6	40.2	45.0	40.6	45.4	41.0	48.3	41.9	39.5
Ce	85.3	84.8	81.5	82.0	81.0	86.0	83.0	81.1	75.0	90.5	84.7	59.2
Nd	33.8	33.4	30.2	31.1	31.5	32.9	35.6	32.1	15.6	36.1	39.8	16.2
Sm	5.73	5.75	5.24	5.40	5.42	5.91	6.29	5.44		6.3	7.59	2.7
Eu	1.16	1.22	1.10	1.17	1.24	1.24	1.46	1.22		1.4	1.87	0.5
Tb	0.62	0.64	0.54	0.65	0.63	0.68	0.70	0.67		0.8	0.79	0.3
Yb	2.38	2.39	2.07	2.26	2.21	2.59	2.45	2.32		2.3	2.04	1.3
Lu	0.37	0.36	0.32	0.33	0.34	0.41	0.43	0.36		0.4	0.33	0.3

Note: Major and trace elements on all samples but Csgr16, Big, and QMI done by XRF in University of London at Royal Holloway and Bedford New College (O.Bachmann analysist, helped by G.F. Marriner and M.F. Thirlwall. Samples Csgr16, Big and MLX QMI were analysed by XRF at the University of Lausanne (F. Capponi analysist). On sample Blob1, 83, 55, 34, 124, 49, ELEP, 115, 138, QMI and Big, all the REE and Th, U, Ta, Hf, Cs, Zn, Co, Cr, and Sc were analysed by INAA at the Open University (N. Rodgers analysist). PPD = Pagosa Peak Dacite. FCT = Fish Canyon Tuff. NCD = Nutras Creek Dacite. I = Intracaldera. O = outflow. Dist. = distal. Prox. = proximal. Vitr. = vitrophyre. Inc. = inclusion. Hybr. And. inc. = Hybrid Andesite inclusion. Gran. xeno. = granodioritic xenolith. Porph. xeno. = porphyritic granitic xenolith. Pum. = pumice. Analytical errors estimated with reproducibility and analytical precision.

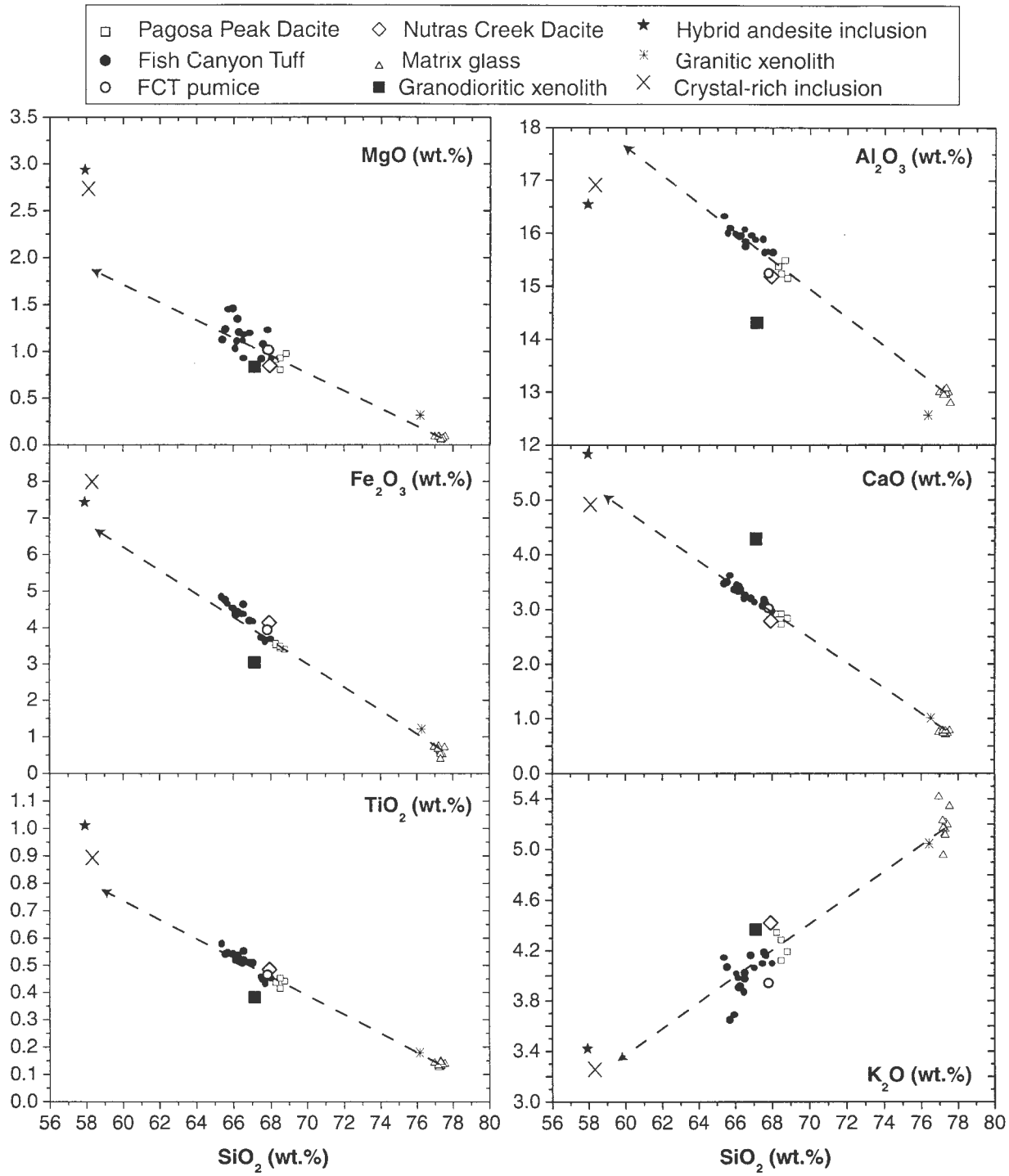

Figure 11: Major element Harker variation diagrams for the Fish Canyon magmatic system. Note that all major elements in the Fish Canyon tuff samples are correlated with SiO_2 and that they lie along extrapolations of lines connecting the Fish Canyon glass composition with the average Pagosa Peak Dacite blob compositions, thought to accurately represent Fish Canyon magma compositions. This relationship is consistent with different degrees of crystal accumulation in the Fish Canyon Tuff samples resulting from crystal-ash fractionation during transport. The hybrid andesite enclave does not fall on this extrapolation, in accord with the absence of evidence for chemical mixing between the Fish Canyon magma and a more mafic component. The data plotted in these diagrams are those reported in Table 2 (Pagosa Peak Dacite, Nutras Creek Dacite, granodioritic xenolith, crystal-rich inclusion, and porphyric granitic xenolith) plus additional Fish Canyon Tuff samples for which we do not have the complete range of trace element data. Major element broad-beam glass compositions were analyzed with the Cameca SX50 electron microprobe at the University of Lausanne (Table 9). The relatively large scatter of K_2O for glass, Pagosa Peak Dacite, and Fish Canyon Tuff probably reflects minor alkali mobility during post-emplacement dehydration, but this may also be due to real variations in matrix liquid compositions.

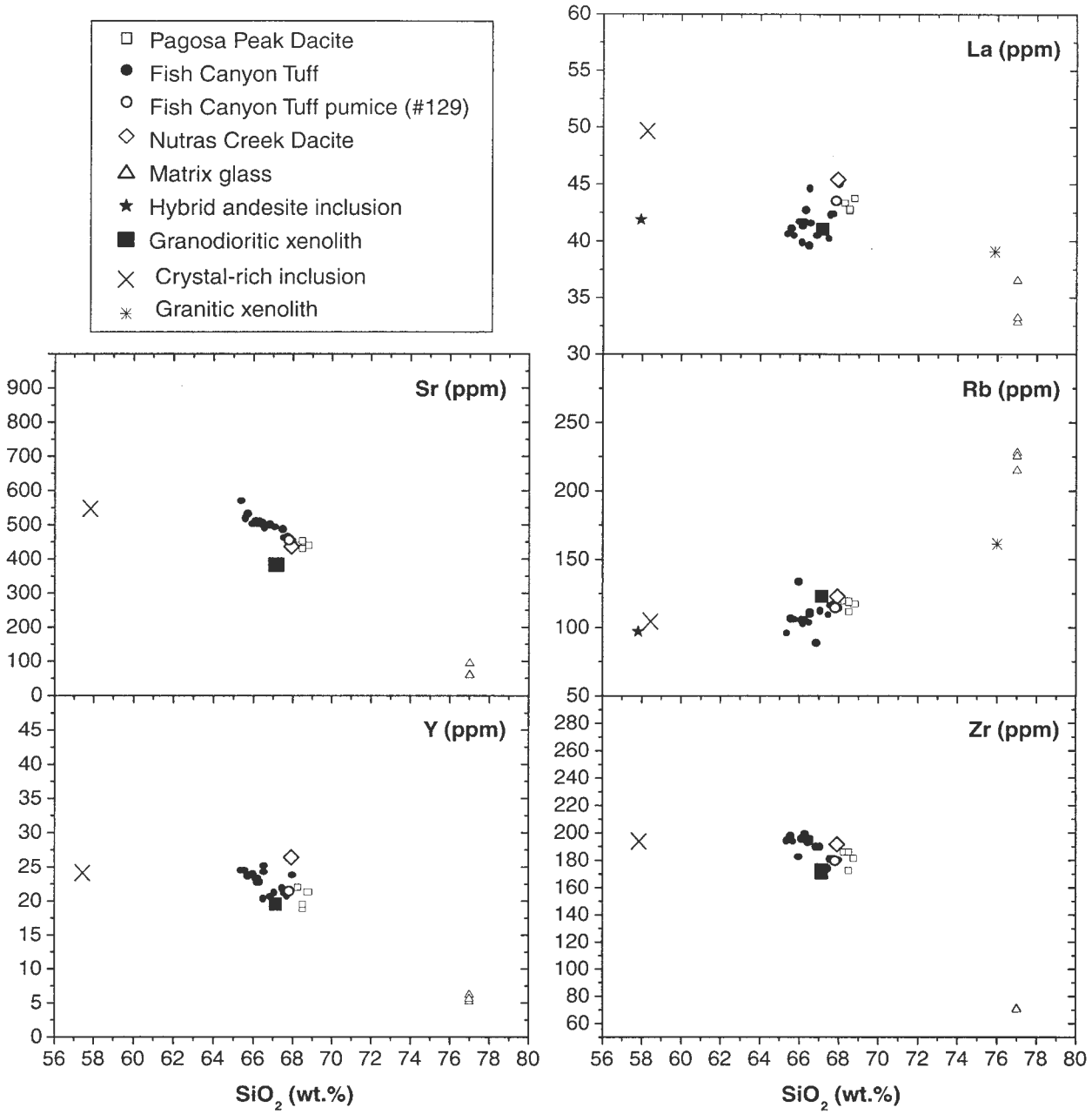

Figure 12: Trace element Harker variation diagrams for the Fish Canyon magmatic system. Sub-linear relationships similar to those observed in major element variation diagrams are present for Sr, Y, Rb and Zr. The hybrid andesite inclusion sample is not plotted for Y and Zr because we lack data for these two elements. Trace element concentrations in glass were analyzed with the Cameca IMS-4f ion microprobe of the University of Edinburgh (Table 5). Note that the andesitic inclusion has a much lower La concentration than the extrapolation of a line from glass through Pagosa Peak Dacite analyses.

by strong compositional and thermal gradients (large variations in Cl are due to degree of devitrification). In fact, an equally plausible explanation for such a narrow range of compositions is minor heterogeneities in phenocryst abundances. Small, fine-grained mafic magmatic inclusions are found in the late-erupted intracaldera facies of the northern collapse depression (QMI 2 of Table 2; see section 7.2). Although these inclusions are hybridized (mixing with Fish Canyon magma), the linear trends defined by glass and whole-rock compositions of Fish Canyon material do not project toward the analyzed inclusion for most elements, in accord with the virtual absence of finely dispersed andesitic fragments in

more than 250 Fish Canyon samples that we have examined.

Variations of some trace elements in non-fragmented samples (*i.e.*, magmatic compositions) span wider ranges than do major elements in the same samples (Fig. 12). Although the Nutras Creek Dacite and pumice from the intracaldera Fish Canyon Tuff are indistinguishable from the average Pagosa Peak Dacite blobs in terms of almost all trace elements (Ba alone is low in pumice), there are differences among Pagosa Peak Dacite blob samples on the order of 15 % relative for Y and HREE (La/Yb ~18-21) and 10 % for Zr and Hf. Given the presence of several accessory phases (apatite, zircon, sphene), it is difficult to assess the role of modal differences among analyzed splits of material versus first order magmatic processes in generating these variations.

Based on the linear trends defined by the Fish Canyon Tuff samples and glass on major element variation diagrams (Fig.11) and the enrichment–depletion diagram (Fig. 13) featuring trace-element ratios of the most crystal-rich Fish Canyon Tuff (Elep) relative to the Pagosa Peak Dacite (#55), we concur with Whitney & Stormer (1985) that most of the compositional variability among Fish Canyon Tuff samples is likely to be the result of syn-eruptive crystal-ash fractionation, not the presence of substantial pre-eruptive compositional gradients in the magma chamber. In addition, although there are previously unrecognized quenched andesite inclusions in the intracaldera facies, volumetrically important mingling or mixing with a more mafic component does not appear to be a factor. In light of the probability that the magma chamber was weakly heterogeneous, such heterogeneities do not appear to have been erupted in a systematic fashion, with the possible exception of the preferential occurrence of andesitic inclusions in late-erupted intracaldera tuff. We emphasize that the sampling of multiple eruptive phases of the Fish Canyon magmatic system in this study provides a more solid basis than previous data sets for documenting variations in magma composition and interpreting them.

As noted by Whitney & Stormer (1985), the Fish Canyon magma for most major elements to average granodiorite (Nockolds et al., 1978). Moreover, the products of the Fish Canyon magmatic system rather closely approximate the average composition of the upper continental crust proposed by Taylor & McLennan (1985; Fig. 14). In comparison to the latter, the Fish Canyon magma is higher in Ba, Th, K_2O (and total alkalies), and

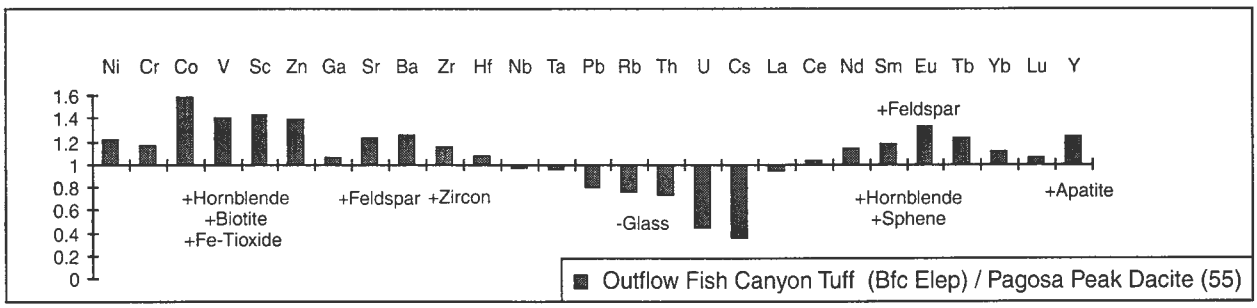

Figure 13: Trace element enrichment-depletion diagram comparing Fish Canyon magma wherein the most crystal-rich Fish Canyon Tuff sample that we have analyzed (Elep) is normalized to a Pagosa Peak Dacite blob sample (55) which is representative of non-fragmented Fish Canyon magma. This diagram illustrates general consequences of crystal-ash fractionation during pyroclastic flow transport and emplacement. Fine particles of ash are preferentially lost during transport, and tuff samples are enriched in crystals with respect to non-fragmented magma. Elements concentrated in one or more of the nine solid phases are enriched (>1) by as much as 30-40% relative to the magma composition, whereas those few elements which are incompatible with respect to all the mineral phases are depleted (<1) in the tuff.

LREE in accord with the relatively high-K nature of San Juan volcanism. The Fish Canyon magma is also notable in having a more pronounced negative Nb-Ta anomaly, and therefore an apparent arc-like signature (Ba/Nb ~50 vs. 22 for the crust; La/Nb ~2.5 vs. 1.2), but we emphasize that the Fish Canyon dacitic composition is 1.5-3 times higher in Nb and Ta than comparable magmas from modern continental margin arcs. We concur with Whitney & Stormer (1985) that the similarity of the Fish Canyon magma to average granodiorite (and average upper crust) implies that the processes involved in the generation of the Fish Canyon magma were similar to those which are typically responsible for the generation of batholithic intrusions.

6. Phase chemistry

The four main mineral phases (biotite, hornblende, plagioclase, sanidine) of the Fish Canyon magma were analyzed by Whitney & Stormer (1985). Hornblende, due to its potential for geobarometry, was reexamined by Johnson & Rutherford (1989a). Both studies concluded that the mineral phases lacked significant internal compositional variability. However, complex textures and optical zoning in thin section led us to analyze by electron microprobe hornblende, biotite, sanidine and plagioclase in the three stratigraphic units of the Fish Canyon magmatic system with special attention to textural relations. The results document greater compositional variability and more systematic chemical zonations for all these phases than previous studies had reported. However, apart from Al, Mg, and Fe in biotite, phenocryst compositions overlap among the three units, consistent with limited thermal and chemical gradients in the magma chamber.

6.1. Biotite

Biotite in Fish Canyon magma has compositions typical of large dacitic crystal-rich ash-flow sheets, such as the Atana ignimbrite (Lindsay et al., 2001) and Cerro Galan ignimbrite (Francis et al., 1989). Grain-to-grain variations in major elements are up to 5 wt. % absolute for FeO and MgO, but few inter-element correlations are apparent in the data set as a whole, nor are there systematic zoning profiles (Table 3; Fig. 15). Biotite is the only phase for which average compositions are systematically offset among the three eruptive units of the Fish Canyon magmatic system. Biotites in Fish Canyon Tuff and Nutras Creek Dacite overlap for all elements, but are higher (1-2 wt. % absolute) in FeO_{tot} and Al_2O_3, and lower in MgO, with respect to those in the Pagosa Peak Dacite. Other elements such as K_2O and TiO_2 are not systematically different. Analogous variations in FeO_{tot}, MgO, and Al_2O_3 between biotite crystals from the same magma have also been detected in the Cerro Galan ignimbrite (Francis *et al.*, 1989), where biotite from the intracaldera facies is slightly lower in Al and has consistently higher Fe/(Fe + Mg) than in the outflow facies. These slight chemical variations are the only signs of gradients between different parts of the magma chamber.

6.2. Hornblende

The new data on Fish Canyon amphiboles show that they are not restricted to the hornblende composition documented by earlier work, although the vast majority (>99%) of the analyses done in this study are indeed hornblende *s.s.*, extending into the edenite field for the most alkali-rich analyses (Table 4; Fig. 16). A second population, corresponding to a pargasitic composition (Fig. 16),

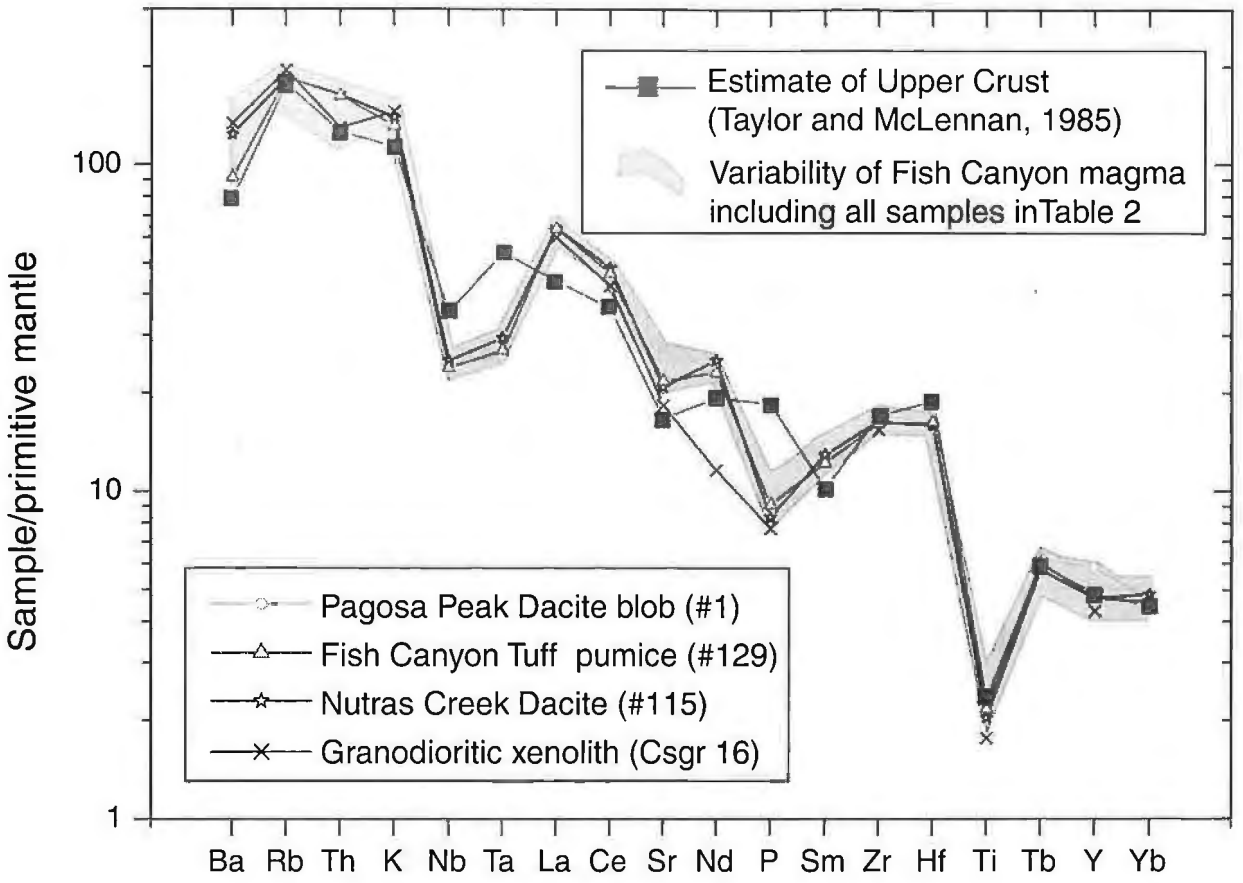

Figure 14: Mantle-normalized multi-element diagram comparing the compositions of the eruptive products of the Fish Canyon magmatic system to: (1) an estimate of the composition of the upper crust by Taylor and McLennan (1985), and (2) to a granodioritic xenolith with Fish Canyon mineralogy and mineral chemistry (collected from intracaldera Fish Canyon Tuff; Figs. 11, 12, 23, 33-36). Concentrations are normalized to the primitive mantle composition of Sun and McDonough (1989). The shaded field encompasses all the analyses listed Table 2, and these account for the total variability of the Fish Canyon magma, as well as modifications due to crystal-ash-fractionation during transport (Fig. 13). Representative non-fragmented samples from the Pagosa Peak Dacite, Fish Canyon Tuff, and Nutras Creek Dacite, as well as the analysis of the granodioritic xenolith are plotted to illustrate to absence of large systematic differences between the early- and late-erupted products of the Fish Canyon magmatic system. No INAA data are available for the granodioritic xenolith. Thus, the low Nd concentration (XRF) determined for this sample may be an analytical artifact.

has been documented in the cores (Fig. 4c) of a few large hornblende phenocrysts. These pargasites are enriched in Al_2O_3, TiO_2, Na_2O, and K_2O by up to 50 % relative, mainly balanced by depletion in MgO and SiO_2 in comparison to typical Fish Canyon hornblendes (Fig. 17). An ion microprobe analysis in one of these cores shows enrichment in Rb, Sr, Y, Zr, Ba, and all REE in comparison to the rim population, with the exception of Li and Nb, for which concentrations are similar (Table 5). Certain elements, such as Ba, Zr, and Sr are 5 to 10 times more abundant in these pargasitic cores, whereas enrichment factors are between 1.3 and 1.9 for the REE.

Apart from volumetrically minor pargasitic cores, hornblende analyses vary widely, in contrast to data reported by Whitney and Stormer (1985) and by Johnson and Rutherford (1989a). Compositions vary 2.5-3 wt. % absolute for Al_2O_3, MgO, and SiO_2, but remain nearly constant for CaO. When plotted against SiO_2, Al_2O_3, FeO_{tot}, MgO, TiO_2, Na_2O, and K_2O form linear trends, all with negative slopes but MgO. The natural hornblende analysis listed by Johnson and Rutherford (1989a)

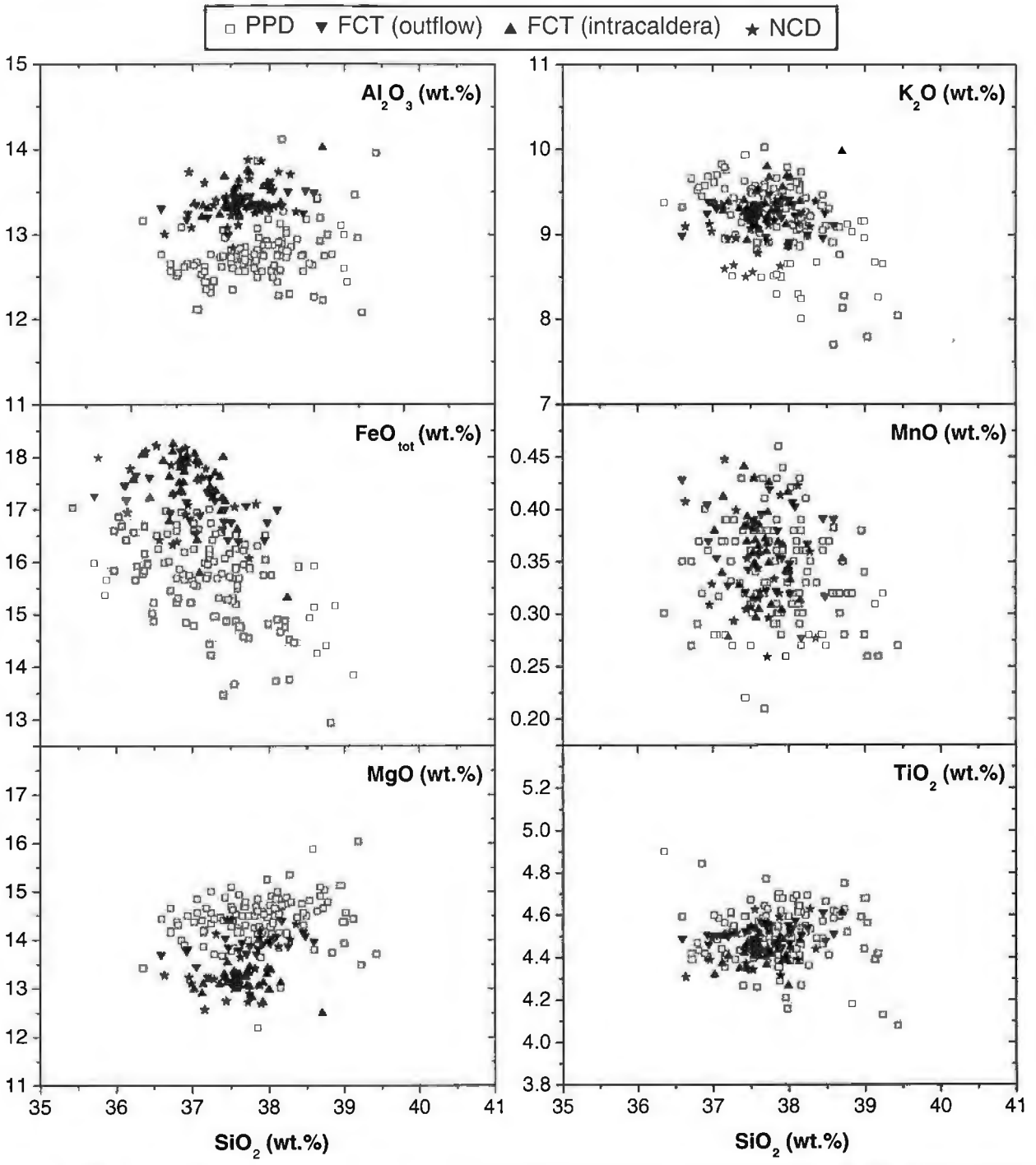

Figure 15: Major element variation diagrams for biotite (electron microprobe) of each of the stratigraphic units of the Fish Canyon magmatic system. Although fields overlap for MnO, K_2O and TiO_2, FeO_{tot} and Al_2O_3, biotite compositions in Pagosa Peak Dacite blobs are slightly offset to higher MgO concentrations and lower Fe_2O_3 and Al_2O3 with respect to Fish Canyon Tuff and Nutras Creek Dacite samples.

plots at the extremities of these linear trends (Fig. 17) for Al_2O_3, MgO and FeO_{tot}, whereas the composition of the hornblende obtained in 2 kb experiments plots near the average of the new data set.

The complete range of major element compositions shown in Fig. 17 is present within single crystals. High resolution (5-10 mm point spacing) microprobe traverses across large hornblende grains record significant variations in major elements, with rimward increases in Al_2O_3, FeO_{tot}, TiO_2, Na_2O, and K_2O, which are compensated by decreases in MgO and SiO_2. In particular, Al_2O_3 first decreases from ~6.5-7 wt. % to a minimum of 5.5 wt. %, then

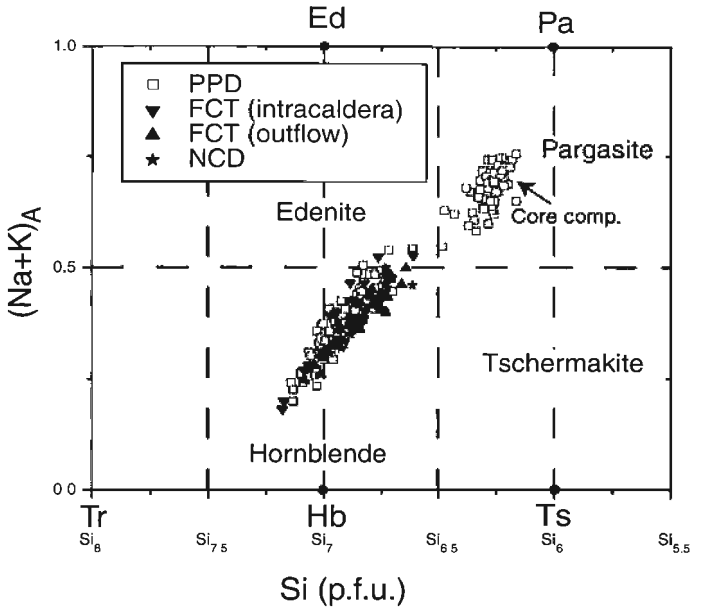

Figure 16: Fish Canyon amphibole compositions (electron microprobe) expressed as Na+K in A sites and Si atoms per formula unit (p.f.u.). Tr: Tremolite; Hb: Hornblende (sensu stricto); Ts: Tschermakite; Ed: Edenite; Pa: Pargasite; Fields from Deer et al. (1992). Note that except for rare pargasitic cores in a few Pagosa Peak Dacite samples, Fish Canyon amphiboles define a narrow linear array and there is no systematic difference among amphiboles from different stratigraphic units.

rises to maximum values at the rim (~7.5-8.3 wt. %; Figs. 18a and b), which overlap with the 8.0 ± 0.5 wt. % Al_2O_3 reported by Johnson & Rutherford (1989a). Fine-scale oscillatory zoning (~10-20 mm) is superimposed on the rimward zoning. The fine-scale variations define strong correlations between all major elements: the zoning profiles of Al_2O_3, FeO_{tot}, TiO_2, Na_2O, and K_2O are perfectly parallel, whereas the profiles of MgO and SiO_2 are mirror images. This striking interdependence indicates that the same coupled substitutions are responsible for these chemical changes from core to rim.

If Al content in Fish Canyon hornblende were primarily controlled by pressure, as suggested by Johnson and Rutherford (1989a), an increase toward the crystal rim would translate dynamically into a foundering magma chamber. The minimum depth implied by hornblende with 5.4 wt. % Al_2O_3 would have been as shallow as ~1.5 km (~0.4 kb), using the recalibration of Anderson and Smith (1995; Table 6) at 760 °C. This scenario seems geologically unrealistic, strongly implying that Al-in-hornblende is at least in part controlled by parameters other than pressure.

It is now firmly established that temperature has an important effect on the Al^{iv} content of hornblende (Blundy and Holland, 1990; Holland and Blundy, 1994; Anderson and Smith, 1995), and that Al-in-hornblende barometry should only be attempted if temperature is known. Initially, the Fish Canyon magma seemed a perfect case for the barometer, as the temperature of equilibration of the Fe-Ti oxides is well constrained (760 ± 30 °C; Johnson and Rutherford, 1989a) and was inferred to be stable prior to eruption. However, our new findings suggest that the temperature of the magma body was increasing toward the end of the evolution of the Fish Canyon magma. The significant change in Al content observed on microprobe profiles in large hornblendes phenocrysts is thus more plausibly explained by a dominant thermal control on Al distribution. The influence of fO_2, also known to affect the concentration of Al in hornblende (Anderson and Smith, 1995), was apparently minor as the $Fe^{3+}/(Fe^{3+}+Fe^{2+})$ ratios in hornblende, determined from

Table 3: Average biotite composition s from the Fish Canyon magma.

	Average PPD N=45	Average FCT (O) N=25	Average FCT (I) N=41	Average NCD N=23	Average Xtal-rich inc. N=41	Average Gran. xeno. N=86	Average Proph. xeno. N=34
SiO_2	37.80	37.74	37.65	37.58	38.03	38.41	38.63
TiO_2	4.47	4.50	4.44	4.47	4.42	4.22	4.30
Al_2O_3	12.70	13.36	13.40	13.40	13.41	13.07	13.21
FeO_{tot}	15.21	17.05	17.50	17.36	16.20	15.30	14.81
MnO	0.33	0.36	0.36	0.34	0.37	0.49	0.54
MgO	14.39	13.85	13.13	13.46	13.88	14.95	15.35
CaO	0.09	0.02	0.01	0.04	0.01	0.01	0.00
Na_2O	0.37	0.38	0.34	0.47	0.40	0.45	0.63
K_2O	8.89	9.20	9.33	9.01	9.16	9.35	9.26
F	1.11	0.56	0.64	0.83	0.73	1.33	1.63
Cl	0.03	0.16	0.17	0.16	0.15	0.20	0.12
Sum Oxides	98.64	97.46	97.21	97.36	97.03	97.98	98.76
Mg #	0.63	0.59	0.57	0.58	0.60	0.64	0.65
Si(T)	2.82	2.77	2.79	2.77	2.80	2.81	2.81
Al^{IV}(T)	1.12	1.15	1.17	1.16	1.16	1.13	1.13
$Fe^{3+}c$	0.07	0.08	0.05	0.07	0.03	0.06	0.06
Σ(T)	4.00	4.00	4.00	4.00	4.00	4.00	4.00
Al^{VI}(M2)	0.00	0.00	0.00	0.00	0.00	0.00	0.00
Ti(M2)	0.25	0.25	0.25	0.25	0.24	0.23	0.23
Mg	1.60	1.51	1.45	1.48	1.52	1.63	1.66
Fe^{2+}(M2)	0.61	0.65	0.75	0.69	0.69	0.62	0.59
Fe^{3+}(M2)	0.27	0.32	0.29	0.31	0.28	0.25	0.25
Mn	0.02	0.02	0.02	0.02	0.02	0.03	0.03
Σ(T+M2)	6.75	6.75	6.75	6.75	6.76	6.77	6.77
Ca(M4)	0.01	0.00	0.00	0.00	0.00	0.00	0.00
Na(M4)	0.05	0.05	0.05	0.07	0.06	0.06	0.09
K(M4)	0.84	0.86	0.88	0.85	0.86	0.87	0.86
Σ(cations)	7.66	7.67	7.68	7.67	7.67	7.71	7.71

All Fe as Fe^{2+}. Mineral formulas calculated as Dymek (1983)(11 Oxygen, OH+F+Cl=2, cations-(Ca+Na+K) + Ti =7. Octaheral Al is always low). Averages were calculated based on all analyses included in Fig. 15 and 34. Mg # was calculated using FeOtot. Note: Electron microprobe analyses done at the University of Lausanne (O. Bachmann analysist, helped by F. Bussy). Biotite and hornblende: 15 kV, 15 nA, magnification 200'000. Feldspars: 15 kV, 15 nA, magnification 100'000. Glass: 15kV, 10nA, magnification 50'000. PPD = Pagosa Peak Dacite. FCT = Fish Canyon Tuff. NCD = Nutras Creek Dacite. I = Intracaldera. O = outflow. Xtal-rich inc. = Crystal-rich inclusion. Porph. = porphiritic granitic xenolith. Gran. = granodioritic xenolith. Glass analyses recalculated to 100. Standards used were all mineral standards. For Al in hornblende, an orthoclase (ort2) standard was used.

Table 4: Representative hornblende analyses from the Fish Canyon magmatic system

	Average PPD rim	Average PPD core	Average FCT (O)	Average FCT (I)	Average NCD	Average Gran. xeno.	Average Xtal-rich inc.	Lowest Al Fig.18a	Highest Al Fig.18a
	N=116	N=78	N=24	N=20	N=27	N=42	N=56		
SiO_2	47.55	42.70	47.40	47.52	46.78	48.65	47.06	49.83	45.78
TiO_2	1.39	2.40	1.37	1.31	1.39	1.15	1.40	1.01	1.58
Al_2O_3	6.73	11.42	7.11	6.88	7.35	6.08	7.20	5.41	8.31
FeOtot	14.14	14.00	14.24	14.30	14.35	13.10	14.07	12.65	15.11
MnO	0.77	0.49	0.76	0.76	0.75	0.96	0.73	1.10	0.71
MgO	13.73	12.31	13.81	13.57	13.47	14.36	13.35	15.43	12.96
CaO	11.74	11.92	11.78	11.64	11.78	11.63	11.65	11.78	12.01
Na_2O	1.41	2.13	1.46	1.50	1.46	1.77	1.49	1.22	1.76
K_2O	0.82	1.05	0.82	0.79	0.83	0.69	0.83	0.61	1.03
F	0.37	0.31	0.27	0.24	0.24	0.58	0.26	0.31	0.22
Cl	0.11	0.06	0.10	0.10	0.11	0.10	0.11	0.09	0.16
Sum Oxides	98.76	98.80	99.13	98.59	98.51	99.07	98.16	99.44	99.62
Si(T)	6.91	6.28	6.85	6.91	6.82	7.04	6.88	7.08	6.66
Al^{IV}(T)	1.09	1.72	1.15	1.09	1.18	0.96	1.12	0.92	1.34
Σ(T)	8.00	8.00	8.00	8.00	8.00	8.00	8.00	8.00	8.00
Al^{VI}(M2)	0.06	0.26	0.06	0.08	0.08	0.08	0.12	-0.01	0.09
Ti(M2)	0.15	0.27	0.15	0.14	0.15	0.12	0.15	0.11	0.17
Mg	2.97	2.70	2.98	2.94	2.93	3.10	2.91	3.27	2.81
Fe^{2+}(M2)	1.20	1.34	1.14	1.21	1.19	1.18	1.27	0.82	1.37
Fe^{3+}(M2)	0.52	0.38	0.58	0.53	0.55	0.41	0.46	0.68	0.47
Mn	0.10	0.06	0.09	0.09	0.09	0.12	0.09	0.13	0.09
Σ(M2)	13.00	13.00	13.00	13.00	13.00	13.00	13.00	13.00	13.00
Ca(M4)	1.83	1.88	1.82	1.81	1.84	1.80	1.83	1.79	1.87
Na(M4)	0.17	0.12	0.18	0.19	0.16	0.20	0.17	0.21	0.13
S(M4)	15.00	15.00	15.00	15.00	15.00	15.00	15.00	15.00	15.00
Na(A)	0.23	0.48	0.23	0.24	0.25	0.30	0.25	0.13	0.37
K(A)	0.15	0.20	0.15	0.15	0.15	0.13	0.16	0.11	0.19
Σ(cations)	15.38	15.68	15.38	15.38	15.41	15.43	15.40	15.24	15.56

All Fe as FeO. Structural formulas (13 cations-Ca-Na-K) as in Leake et al. (1997). Average compositions were calculated on all analyses included in Fig. 17 and 34. Complete analyses of both electron microprobe traverses displayed on figure 18 are given in annexe 3.

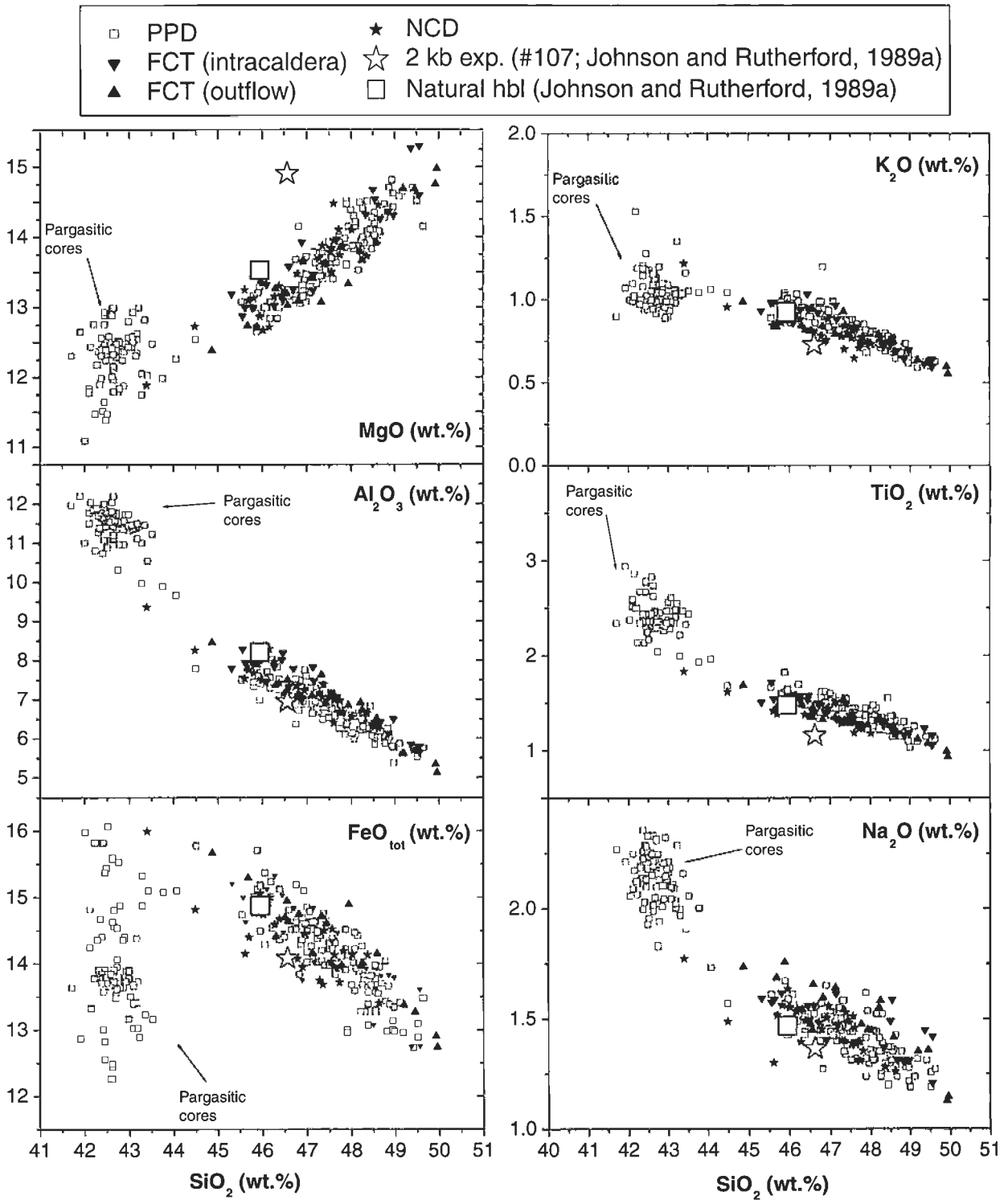

Figure 17: Major element variation diagrams for hornblendes from each stratigraphic unit of the Fish Canyon magmatic system. The natural and experimental hornblendes reported by Johnson & Rutherford (1989a) are plotted for comparison. Note the overlap between amphibole compositions from the various Fish Canyon stratigraphic units, except for the distinctive pargasitic cores which we interpret as relics inherited from an earlier event.

electron microprobe analyses (recalculated using 13 cations excluding Ca, Na and K; Leake et al., 1997), are relatively constant for the three Fish Canyon eruptive units (Fig. 19). Temperatures calculated using the Blundy and Holland (1990) geothermometer and An_{30} plagioclase at 2 kb pressure (Table 6) rise from ~719°C for the lowest Al content (5.4 wt. %) to 775°C for the outermost rim

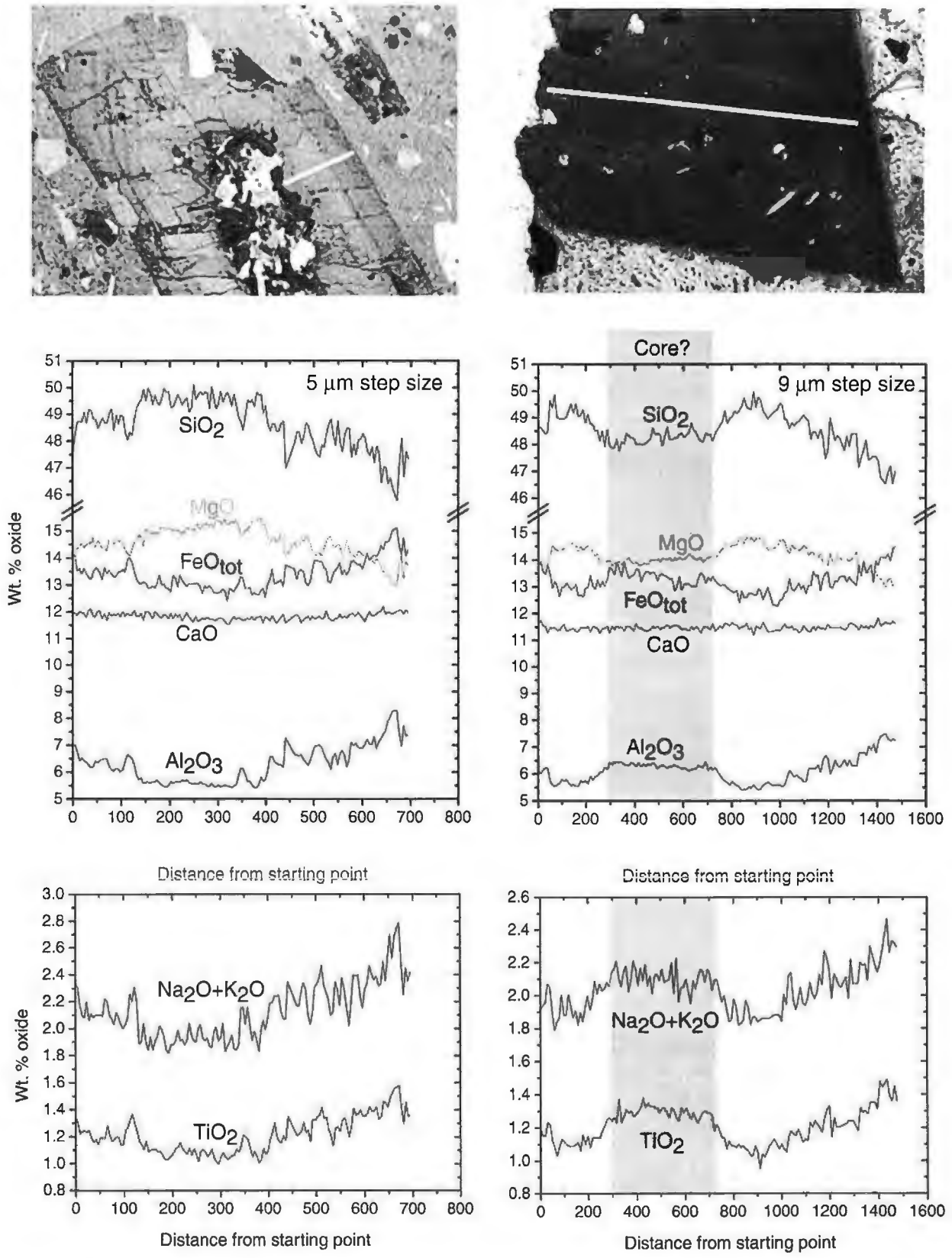

Figure 18: Microprobe profiles in Pagosa Peak Dacite hornblendes, showing internal variations in Al_2O_3, MgO, FeO_{tot} and SiO_2 (Bfc 68 and 196a). (a) The variations in the sevenoxides shown in this Figure form two groups with parallel profiles (1. Al_2O_3-FeO_{tot}-Na_2O+K_2O-TiO_2 and 2. MgO-SiO_2). These two groups are nearly perfect mirror image of each other, suggesting coupled cation exchange in the hornblende. This particular phenocryst contains a polycrystalline core. (b) Same zoning profiles in another phenocryst. The relatively flat area between 200 and 600 microns probably represents the core of this crystal.

composition (average calculated on the last 6 analyses of the traverse on Fig. 18a), which is indistinguishable within error from the value obtained by the Fe-Ti oxide geothermometer (Johnson and Rutherford, 1989a). The Blundy and Holland (1990) calibration was preferred over the Holland and Blundy (1994), which has been demonstrated to be too sensitive to Na^A content (Anderson and Smith, 1995). Using the well-constrained temperature of 760°C and the Al_2O_3 rim composition (~7.4 wt. %), the Al-in-hornblende barometer can be applied and yields an estimate of ~2 kb, differing from Johnson and Rutherford (1989a) value only because of the slightly lower Al_2O_3 content used.

Determining the dominant substitutions responsible for the cations variations in these hornblendes provide further evidence of temperature-dependant chemical exchanges. Experimental work on amphiboles at different pressure and temperature (Spear, 1981; Blundy and Holland, 1990; Johnson and Rutherford, 1989b; Schmidt, 1992) has allowed to assign a temperature or pressure dependance for the different substitutions occurring in amphiboles. In particular, of the two linearly independent substitutions involving Al (edenite exchange: $Si + vac.^A = Al^{iv} + (Na + K)^A$ and Tschermak exchange: $Si + R^{2+} = Al^{iv} + (Al^{vi}; Fe^{3+})$), the edenite is temperature-dependent (Blundy and Holland, 1990) and the Tschermak is pressure-dependent [Johnson and Rutherford 1989b; Schmidt, 1992). Ti content was also demonstrated to be a reliable criteria of temperature variations (Spear, 1981). Based on a robust correlation on Fig. 20 (correlation coefficient R>0.98) and the slope of 0.6 on the Al^{iv} vs. $(Na + K)^A$ diagram (Fig. 21a), the dominating substitution responsible for the Al variations in the Fish Canyon hornblendes is the temperature-sensitive, accounting for ~60 % of the Al increase. The rest of the Al was added in a coupled substitution with Ti ($Si^{4+} = Ti^{4+} + Al^{3+}$), as indicated by the slope of ~1 on Fig. 21c. In contrast, the pressure-sensitive Tschermak exchange ($Si + R^{2+} = Al^{iv} + (Al^{vi}; Fe^{3+})$) was limited, as Al^{vi}, Fe^{3+}, and R^{2+} (Mg+Fe^{2+}+Mn) remain nearly constant (Fig. 22 a to c). Thus, apart from the variations in Fe^{2+} and Mg, which apparently occurred as a simple

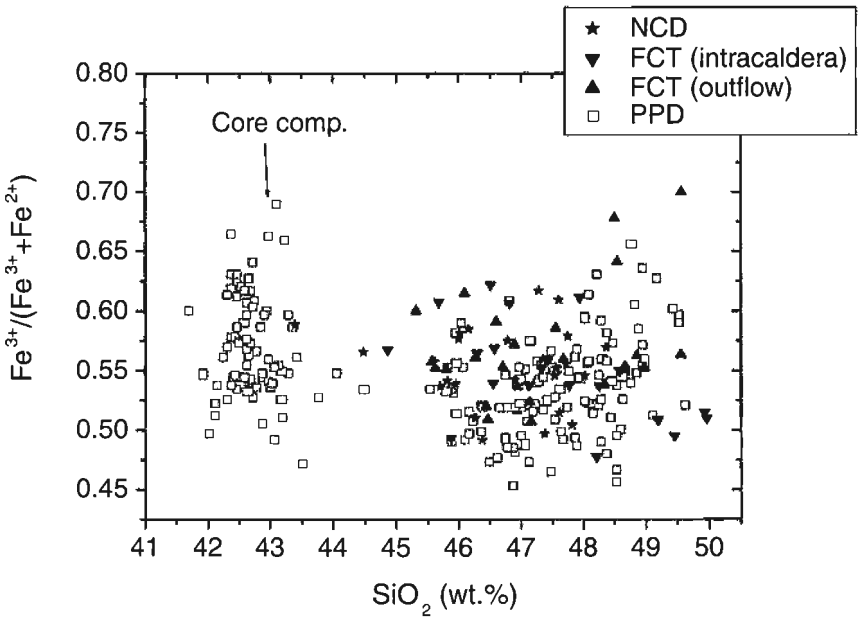

Figure 19: $Fe^{3+}/(Fe^{3+}+Fe^{2+})$ in hornblendes for the different units of the Fish Canyon magma suggest that the f_{O2} remained fairly constant throughout the late evolution of the Fish Canyon magma body. Fe^{3+} and Fe^{2+} were calculated on the basis of electron microprobe analyses using the method of Leake et al., 1997 (13 cations -Ca-Na-K).

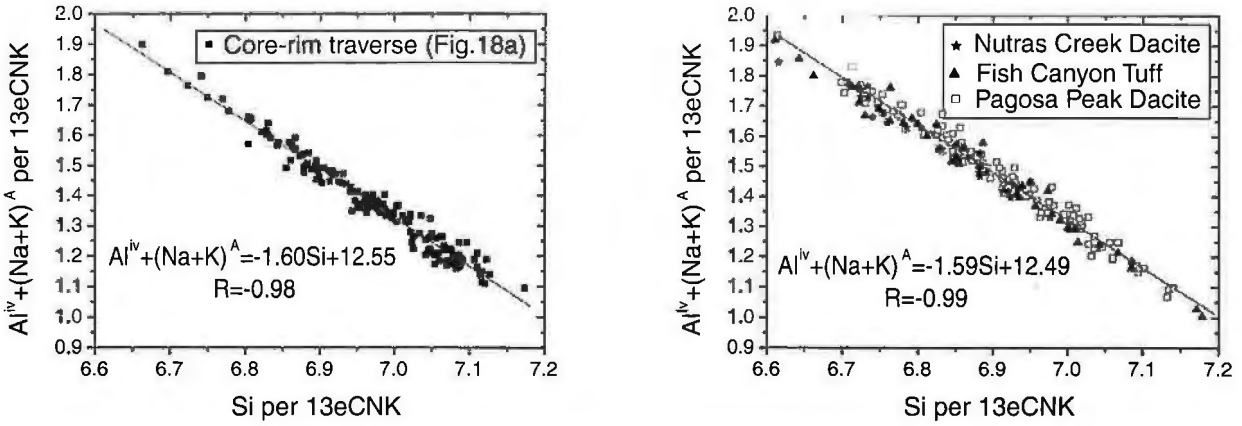

Figure 20: Variation plots illustrating the edenite exchange (Si + vac. => Al^{iv} + $(Na+K)^{A}$) for both the microprobe traverse and the Fish Canyon magmatic system, with analyses obtained from numerous phenocrysts from the three units of the system. Note the remarkable correlation and the fact that the internal variation of a single phenocryst corresponds essentially to variations measured in the whole magma body.

Table 5: Ion probe analyses of Fish Canyon hornblendes and glass.

	59hb3p-1 PPD, core	59hb3p-2 PPD, rim	59hb3-1 PPD, rim	59hb3-2 PPD, rim	59MT-1 Glass (PPD)	59MT-2 Glass (PPD)	59MT-3 Glass (PPD)
SiO_2	44.5	47.0	47.0	47.0	76.0	76.0	76.0
CaO	12.8	11.6	11.8	11.8	0.5	0.6	0.5
K_2O	1.2	0.8	0.8	0.7	6.8	6.7	6.7
TiO_2	2.2	1.3	1.2	1.2	0.1	0.1	0.1
Li	3.8	4.6	5.2	5.2	28.3	29.3	50.3
Rb	18.2	15.6	16.6	14.4	227.9	225.3	214.8
Sr	114.0	38.3	40.3	37.8	60.2	58.4	93.6
Y	120.0	83.9	73.8	84.2	6.2	5.2	5.6
Zr	153.0	50.0	45.0	49.1	71.1	70.9	70.3
Nb	36.8	37.4	30.3	35.3	13.1	12.5	12.4
Ba	306.0	23.7	32.1	30.8	542.0	503.2	562.7
La	77.6	58.0	52.9	56.1	36.5	32.8	33.2
Ce	229.0	175.0	154.0	169.0	49.0	43.9	43.7
Pr	32.7	24.4	21.4	23.2	3.4	2.9	2.8
Nd	150.0	99.6	95.1	102.0	9.5	7.8	7.9
Sm	30.3	19.0	17.9	21.1	1.1	1.0	0.9
Eu	6.0	3.3	3.3	3.5	Interf.	Interf.	Interf.
Gd	24.4	15.1	14.3	14.2	Interf.	Interf.	Interf.
Tb	4.3	3.0	3.0	3.1	0.2	0.1	0.1
Dy	25.1	17.2	15.3	16.7	0.8	0.5	0.8
Ho	5.0	3.2	3.1	3.4	0.3	0.2	0.2
Er	15.4	9.8	9.1	10.8	0.6	0.8	0.6
Yb	14.8	11.7	9.9	11.4	0.9	1.0	0.8

Ion microprobe analyses were performed at the University of Edinburgh, with the assistance of R. Hinton, using a cameca IMS-4fion microprobe with an O-primary beam of net impact energy of 15 keV and an operating current of 5-8 nA. Beam diameter ranged between 15 and 30 mm. The concentrations were obtained by normalizations of mass 30Si to the silica values obtained by electron microprobe analyses. The SRM-610 glass standard was used to monitor day to day changes in experimental conditions. The ion yields relative to SRM-610 were calculated using Lake Country plagioclase for plagioclase, SHF1 alkali feldspar for sanidine, and Courning glass for the glass. Hornblendes ion yields were close enough to the standard to avoid correction (R. Hinton, pers. communication). The 2-s precision for most elements is under 5 % relative. Error of more than 10 % relative can occur only in La, Ce, Y and Rb.

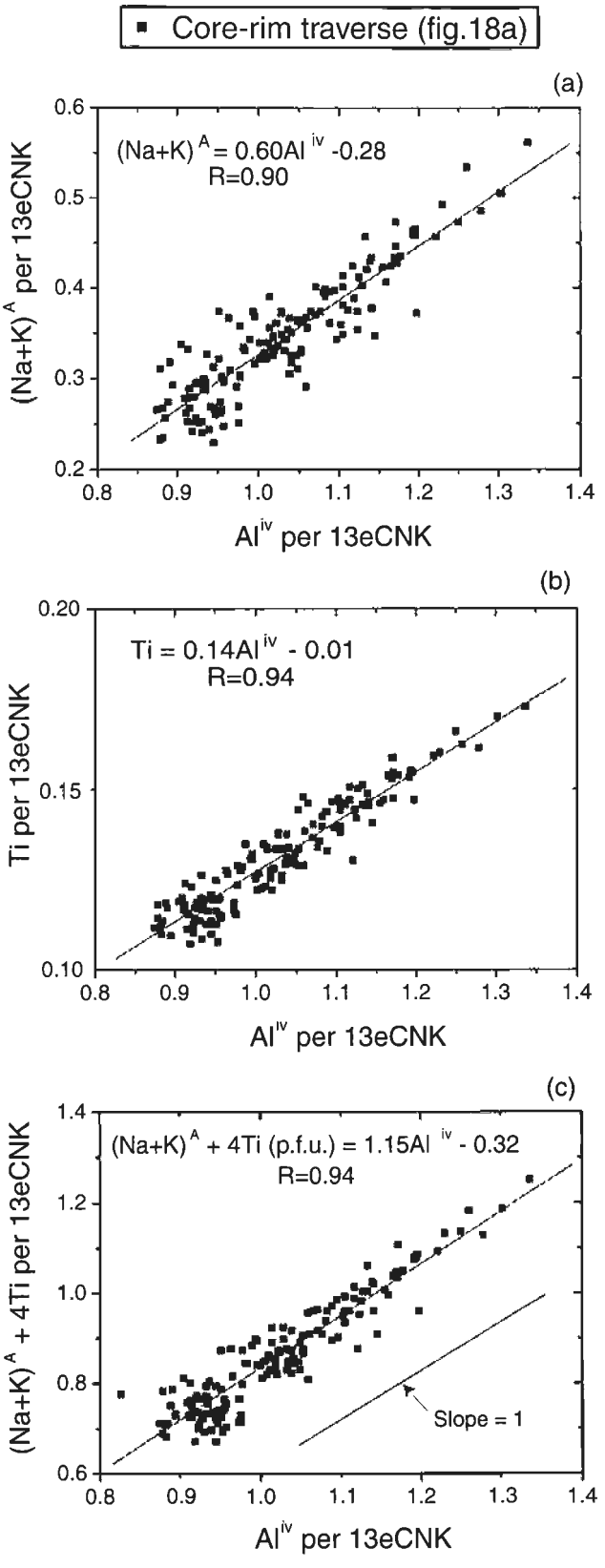

Figure 21: (a) and (b) Variations plots of A-site occupancy and Ti versus Al^{iv} in the microprobe traverse of fig. 18(a). Correlations are obvious in these plots, with correlation factors of 0.90 and 0.94, indicating that the A-site occupancy (i.e. edenite substitution) and Ti increased with Al^{IV}. (c) Variation plot of the A-site occupancy + 4Ti versus Al^{IV} in the microprobe traverse of fig 18(a). A slope of approximately 1 suggest that essentially all the Al^{IV} variations can be explained by the edenite exchange (Si + vac. => Al^{IV} + $(Na+K)^A$) and 4Si + vac. => Ti + $4Al^{IV}$.

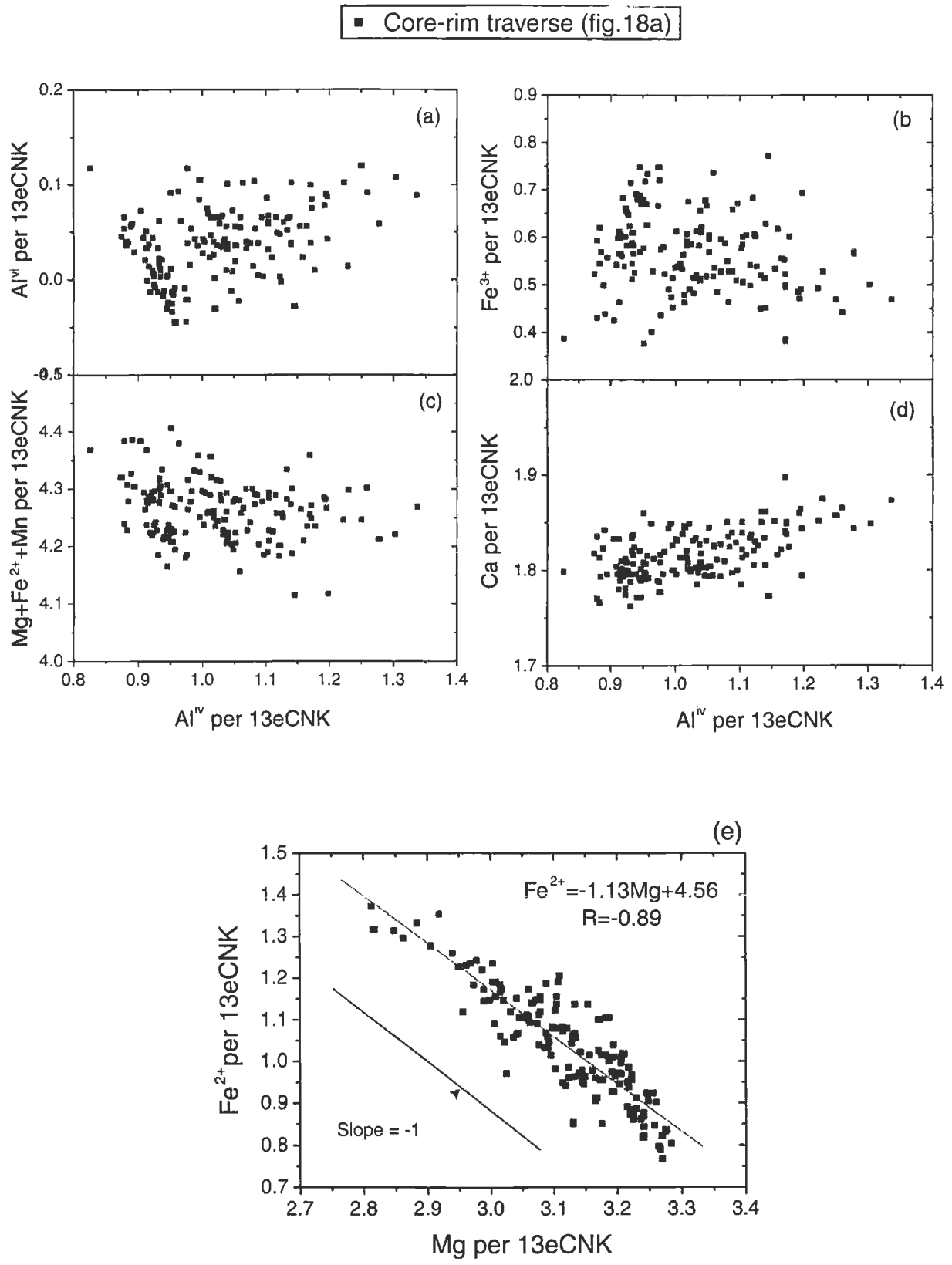

Figure 22: (a) to (d): Variations plots of different cations versus Al^{iv} in the microprobe traverse on fig. 18a. No obvious correlation appear in these diagramms, indicating that substitutions involving these cations were not active. (e) Fe^{2+}-Mg variations in the microprobe traverse on fig. 18a. The slope close to 1 suggests a simple Fe^{2+}=>Mg substitution in these hornblendes, with a $Fe^{2+}/(Fe^{2+}+Mg)$ increasing rimward.

Table 6: Variations in aluminium in a hornblende phenocryst from the Pagosa Peak Dacite (Fig. 18a) and their implications for temperature and pressure.

	Al_2O_3 (%wt)	Sum Ox%	Al_{tot}	T (°C)		P (kbar)
				B&H (90)	H&B (94)	A&S (95)
Lowest	5.4	99.44	0.905	719	722	0.37
Outermost rim (average of 6)	7.4	99.44	1.256	775	804	1.85
Highest	8.3	99.62	1.425	813	846	2.57

Al_{tot} calculated using the method described in Leake et al. (1997). Temperature and pressure were calculated with Blundy and Holland (1990; B&H, 90) and Holland and Blundy (1994; H&B, 94) plagioclase-horblende geothermometer at 2 kb and Anderson and Smith (1995) Al-in-horblende geobarometer at 760 °C, respectively. Expected uncertainties are approximately ± 75°C for the thermometers and ± 0.5 kb for the barometer. Plagioclase composition of An_{30} was used for the temperature calculations.

exchange (Fig. 22e, Bachmann et al., in prep.), essentially all the internal chemical variability in the Fish Canyon hornblendes is achieved through the two temperature-sensitive Ti and edenite substitutions.

Pargasitic cores of a few large crystals probably represent inherited relicts of earlier stages of differentiation, perhaps deeper in the crust. The pargasitic exchange is a combination of the T-sensitive edenite and the P-sensitive Tschermak substitution. The fact that Al content is higher in these cores, due to both the edenite and the Tschermak exchange, suggests that they formed at higher temperatures and pressures. Melt composition may have also played a role, as there is no indication that the buffering near-solidus mineral assemblage, limiting the degrees of freedom, was present at the time these pargasites crystallized. However, the low MgO content of the cores, in comparison to the hornblende rims, is inconsistent with crystallization from a more mafic precursory magma.

6.3. Plagioclase

Fish Canyon plagioclase crystals, as described by Whitney & Stormer (1985), are mainly oscillatory zoned, with compositions from An_{25} to An_{35}, although a few volumetrically minor more calcic cores have compositions up to An_{75} (Table 7; Fig. 23). The oscillatory-zoned rims have, however, two important chemical characteristics that were not noted previously (Fig. 24). First, narrow (~10 mm wide) excursions to more calcic compositions (up to An_{40}) following dissolution surfaces periodically interrupt the typical background trend. Second, the background trend progressively rises to more calcic average compositions, from ~An_{28} in the interior to An_{33} at the rim.

The major element composition of plagioclase is controlled by parameters such as pressure, temperature, and melt composition, including a major effect of H_2O content (Rutherford & Devine, 1988; Housh & Luhr, 1991). The reverse compositional trend in the plagioclase rims requires a gradual change in one or more of these parameters. As a temperature increase at the end of the Fish Canyon magmatic evolution is indicated by several other observations, heating likely played a role in the development of the zoning profile. However, changes in the melt chemistry (increased Ca and H_2O due to interactions with more mafic magma) may have also contributed to the overall reverse trend and calcic spikes.

Plagioclase compositions span similar ranges in both Pagosa Peak Dacite and Fish Canyon Tuff. High-anorthite cores were not analyzed in the Nutras Creek Dacite (Fig. 23), but fewer analyses of plagioclase were obtained in this unit. Complexly-

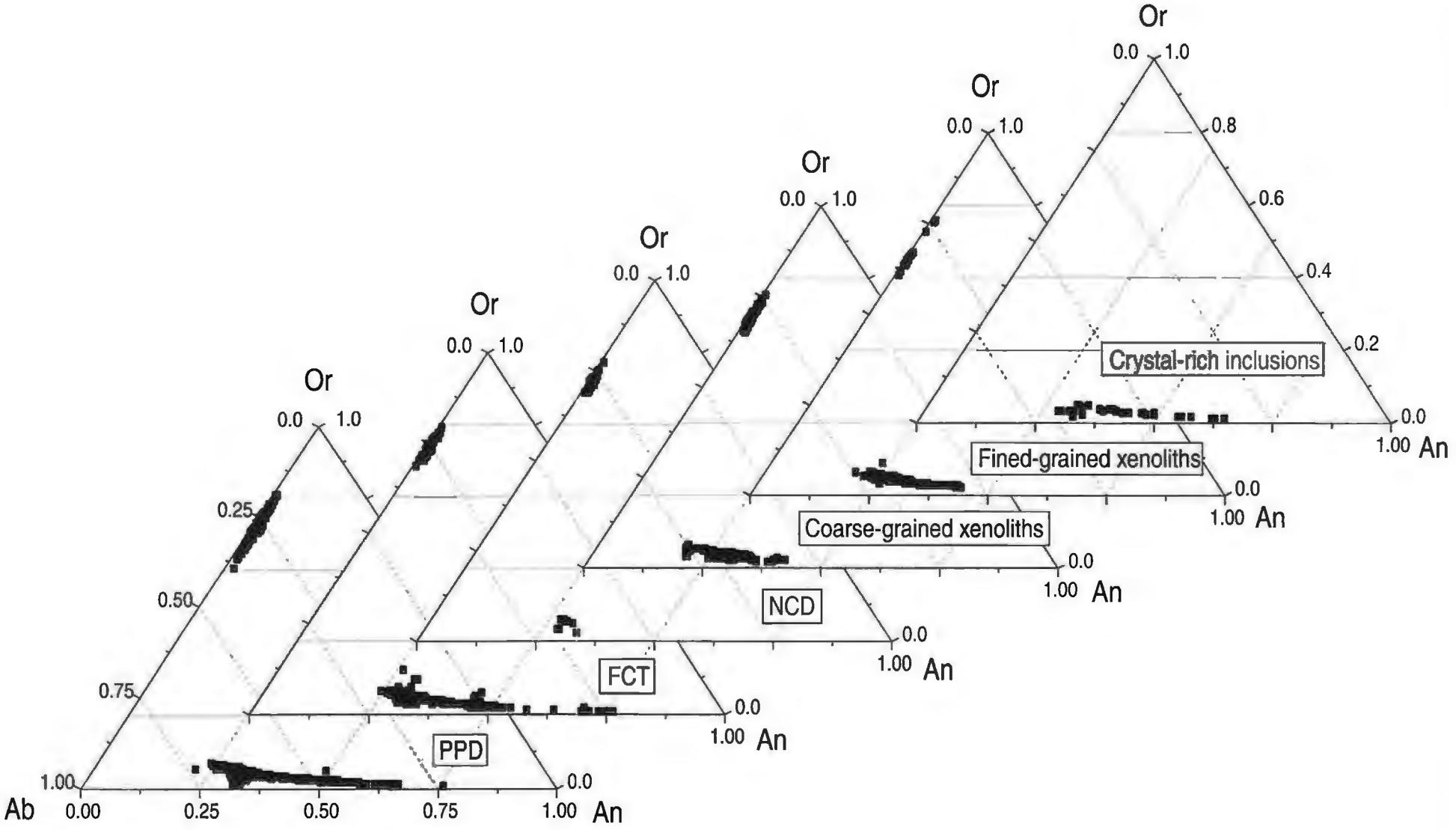

Figure 23: Feldspar ternary diagrams for the different units of the Fish Canyon magmatic system. The crystal-rich inclusions do not contain alkali feldspar.

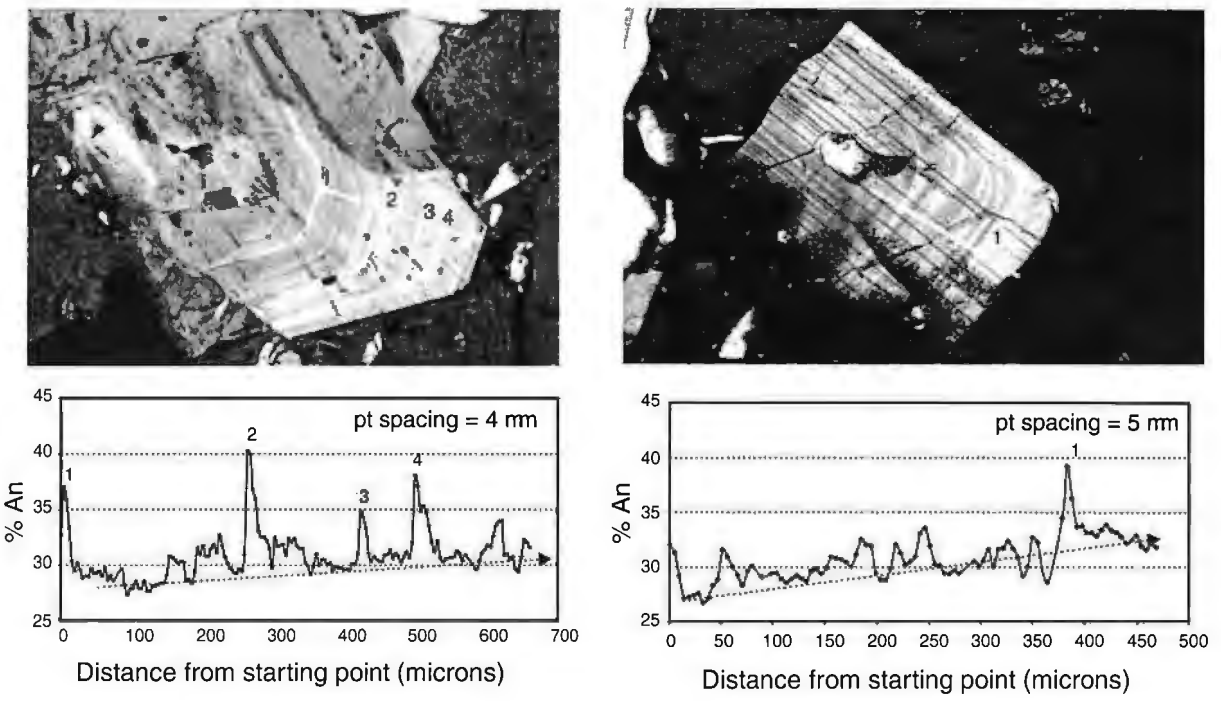

Figure 24: High resolution electron microprobe traverses across two plagioclase phenocrysts with euhedral, oscillatory zoned mantles. (a) Pagosa Peak Dacite; Bfc 59, and (b) Fish Canyon Tuff; Bfc Fv (both in crossed polars). Both compositional profiles shown here are typical of euhedral plagioclase in Fish Canyon magma. In both cases, the main features are oscillatory zoning marked by abrupt 'calcic spikes' up to An_{40} which is superimposed on an increase in the baseline level from ~An_{27} to ~An_{32}.

Nutras Creek Dacite (Fig. 23), but fewer analyses of plagioclase were obtained in this unit. Complexly-zoned phenocryst cores, some showing sieve textures, are observed in thin sections of Nutras Creek Dacite, suggesting that more calcic material is also present.

6.4. Sanidine

In addition to the complex resorption textures and multiple types of mineral and glass inclusions, most Fish Canyon alkali feldspars are conspicuously zoned, mainly in the outer parts of crystals (Fig. 25). Optical zoning is manifested as 0.1 to 1 mm wide bands with slightly different extinction angles than the unzoned part of the crystals. Whereas these bands are generally subparallel to grain boundaries, their morphology is more complex than euhedral growth zoning. Extinction angles generally change gradually across individual bands (Fig. 25b-d), although internal convolutions and patchy zoning occur (Fig. 25a). Where banding is repeated, an undulating surface truncates earlier bands, suggesting dissolution events (Fig. 25b-d). Celsian (Cn) increases abruptly, up to 4 mol. % absolute—a factor of two for this component—immediately outside the zoning boundaries, balanced mainly by decreases in Or and increases in Ab (Fig. 26). Within each zone, Cn then decreases progressively to its background value (~2 mol %), accompanied by a decrease in Or and an increase in Ab (Fig. 26a; Table 8). In phenocrysts containing multiple juxtaposed zones, Cn variations define saw-tooth profiles, with abrupt reestablishments of high Cn content across zoning boundaries, followed by linear decrease (Fig. 26b; Fig. 5 of Lipman *et al.*, 1997).

Barium zoning in sanidine is everywhere spatially associated with swarms of isolated plagio-

clase inclusions in optical continuity (section 4.1; Figs. 8c, 25, 26a). The spatial association of these plagioclase inclusions, which have the same compositions as the euhedral overgrowths on plagioclase phenocrysts (An_{28} to An_{33}), with large variations in Ba/K in the host sanidine was noted as well by Stimac & Wark (1992) in the Clear Lake lavas and strongly supports the interpretation that the patchy plagioclase was engulfed during renewed growth of K-feldspar. As demonstrated experimentally by Wark & Stimac (1992) in a companion paper, Ba zoning is intrinsic to the development of Rapakivi texture if thermal fluctuations remain in the range of 700° to 850°C. A similar Ba-rich zone outboard of a dissolution surface was produced during an experiment where a K-feldspar was heated to 850 °C, then cooled 1 °C/hour to 700 °C and held at this temperature for five days (Wark & Stimac, 1992). They proposed the following model to explain this zoning pattern. When a K-feldspar is heated above its stability range, a thin film of melt is produced around the crystal. This melt, of feldspathic composition, is inferred to maintain stoichiometry, and remain physically stable around the dissolving feldspar (Watson, 1982). If sufficient Ca is present in this dissolution boundary layer, and the intensive parameters are such that plagioclase is stable, plagioclase will nucleate epitaxially on the surface of resorbing K-feldspar grains and grow inward as the other phase retreats. Barium, due to its strong partitioning into K-feldspar, will be progressively enriched in the dissolution boundary layer during K-feldspar resorption and plagioclase growth, whereas Na and Ca will become gradually depleted. If this boundary layer of feldspathic composition remains isolated from the main magma body for a sufficiently long period, the combination of cooling and progressive enrichment of K, coupled with depletions of Ca and Na in the interstitial melt, will restore the stability of K-feldspar, which will then grow outwards, incorporating Ba in the enriched boundary layer melt. In the Fish Canyon magma, sanidine is inferred to have regrown within melt pockets between the discontinuous plagioclase grains, which originated by epitaxial nucleation, resulting in the poikilitic texture associated with Ba zoning. Barium is expected to be highest just outboard of the reprecipitation surface and to decrease as Na content increases away from this surface, reflecting the enrichment of Na and the depletion of K and Ba in the interstitial melt during renewed growth of K-feldspar (Figs. 4g and 4h of Wark & Stimac, 1992). This pattern is observed in a microprobe profile across a Fish Canyon sanidine (Fig. 22).

To explain cycles of Ba zoning associated with dissolution surfaces in zoned sanidines, invoking several generations of sanidine growth seems more likely than the development of oscillatory zoning following repeated mixing with a more Ba-rich andesitic magma, as proposed by Lipman *et al.* (1997). Evidence of physical mixing between silicic and mafic magmas is scarce in the Fish Canyon magmatic system, and the spatial association of this zoning with the optically continuous plagioclase inclusions is more readily explained by repeated episodes of plagioclase mantling, each time followed by sanidine reprecipitation. However, the possibility of some addition of Ba from a more mafic magma cannot be ruled out. Mass-balance considerations, based on the volume ratio of zoned sanidine versus plagioclase inclusions (>5:1), tend to suggest that some Ba was contributed from a more mafic magma, an alternative consistent with the presence of calcic spikes in the euhedral plagioclase overgrowths. Although the Clear lake lavas have abundant evidence of magma mixing, Stimac & Wark (1992) do not mention the possibility of an addition of Ba from a mafic component and concluded that the observed Ba zoning in sanidine was due to K-

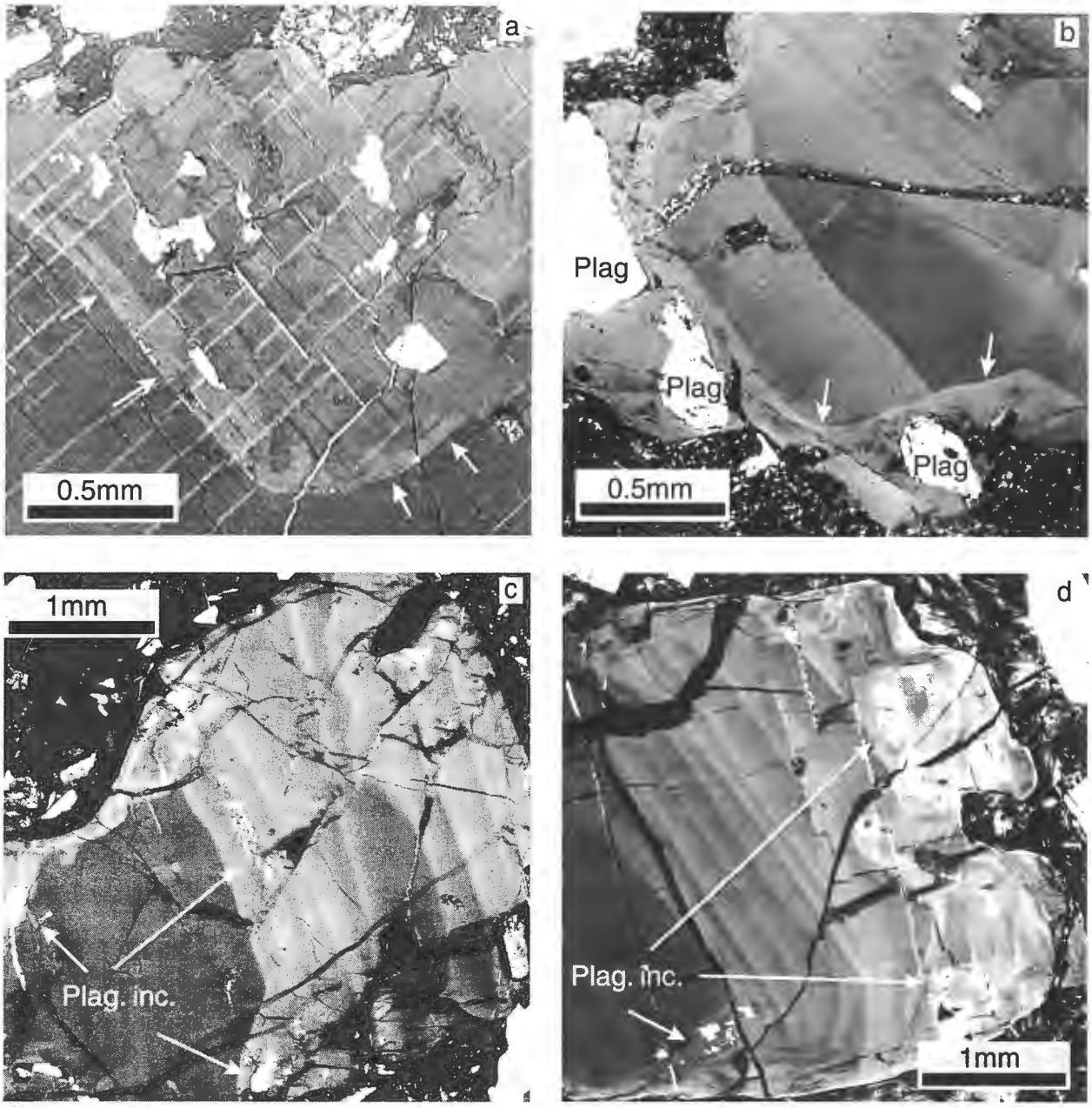

Figure 25: Fish Canyon sanidine showing compositional zoning associated with plagioclase inclusions in optical continuity (all pictures with crossed polars). (a) Plagioclase inclusions in optical continuity enclosed in the zoned outer part of a large sanidine (inclusions are absent in the homogeneous core - boundary marked by arrows). (b) Truncation of earlier bands by an undulatory surface (arrows) suggesting a dissolution event (Bfc 41). Three optically continuous plagioclase inclusions are preserved in the outermost rim. (c) and (d) Two sanidines showing numerous bands in association with plagioclase inclusions in optical continuity (Bfc 31 and 100a). Minerals were partly fractured during polishing.

feldspar regrowth from the previously established Ba-rich boundary layer. This inference may hold in the case of the Clear Lake lavas, as the volume of plagioclase mantles is much larger than in the Fish Canyon system.

Another alternative to explain the large volume ratio of zoned sanidine versus plagioclase inclusions in the Fish Canyon magma is partial dissolution of the plagioclase mantles before sanidine regrowth. This mechanism could also explain the highly irregular contours of the plagioclase inclusions, and is suggested by the partly corroded and discontinuous plagioclase mantles shown in Fig. 8. Ultimately, a detailed isotopic study sampling the

Table 7: Representative plagioclase analyses from the different units of the Fish Canyon magmatic system.

	Core PPD	Core FCT	Rim PPD	Rim FCT	Rim NCD	Rim Gran. xeno.	Outermost rim Gran. xeno.	Matrix plag Porph. xeno.
SiO_2	48.23	49.00	59.98	61.35	60.09	59.64	63.12	65.35
Al_2O_3	32.11	32.41	24.74	23.36	25.31	25.24	22.46	21.72
FeO	0.27	0.37	0.20	0.24	0.00	0.00	0.00	0.00
CaO	15.63	15.70	6.69	5.68	6.72	6.64	3.87	3.18
BaO	0.01	0.00	0.05	0.00	0.02	0.07	0.00	0.00
Na_2O	2.71	2.65	7.51	7.60	7.52	7.52	8.62	8.91
K_2O	0.14	0.10	0.74	1.10	0.44	0.54	0.95	1.46
Sum Ox%	99.10	100.23	99.90	99.33	100.36	99.89	99.20	100.89
Ab	23.65	23.29	64.19	66.29	65.24	65.04	75.72	76.62
An	75.53	76.16	31.60	27.39	32.21	31.75	18.76	15.11
Or	0.80	0.55	4.13	6.31	2.52	3.08	5.51	8.27
Cn	0.02	0.00	0.08	0.00	0.03	0.13	0.00	0.00

Table 8: Sanidine analyses from microprobe traverse illustrated in Fig. 26b.

	*~100 µ	~120µ (point #1)	~370µ (point #2)	~500 µ	~670 µ	~690µ (point #3)
SiO_2	64.02	63.66	63.41	64.60	65.35	64.84
Al_2O_3	18.72	18.79	18.92	18.97	18.75	18.90
FeO	0.00	0.06	0.09	0.05	0.07	0.18
CaO	0.17	0.22	0.25	0.16	0.12	0.18
BaO	1.14	1.47	1.76	1.33	1.05	1.56
Na_2O	2.77	2.74	2.81	2.81	2.90	2.89
K_2O	12.46	11.98	12.05	12.25	12.44	12.04
Sum Ox%	99.28	98.92	99.28	100.18	100.69	100.59
Ab	24.50	24.81	24.99	25.01	25.52	25.73
An	0.82	1.08	1.24	0.77	0.59	0.87
Or	72.64	71.42	70.61	71.82	72.02	70.59
Cn	2.05	2.68	3.17	2.40	1.87	2.81

*: approximate distance from starting point on traverse from Fig. 26b

outer parts of sanidine, plagioclase, and hornblende might be the best tool to constrain the amount of mixing that occurred during interaction between the Fish Canyon magma and a more mafic component.

6.4.1. Granophyre overgrowths

Fine-scale granophyric intergrowths of quartz and K-feldspar with planar terminations against adjacent melt, formed as overgrowths around preexisting feldspar crystals in the late-erupted material of the Fish Canyon magmatic system (northern and central intracaldera Fish Canyon Tuff, and Nutras Creek Dacite; Lipman *et al.*, 1997). Granophyre is a late magmatic feature, as it has faceted outer margins and fills open fractures in broken host crystals, thought to have been partly disrupted by expansion of melt inclusions during rapid decompression related to the early Fish Canyon eruptions (Fig. 27; Best & Christiansen, 1997; Lipman *et al.*, 1997). An important feature, not reported by Lipman *et al.* (1997), is that granophyre seems to have preferentially nucleated on sanidines containing plagioclase inclusions in optical continuity (*i.e.*, "Rapakivi" feldspars). Granophyre is

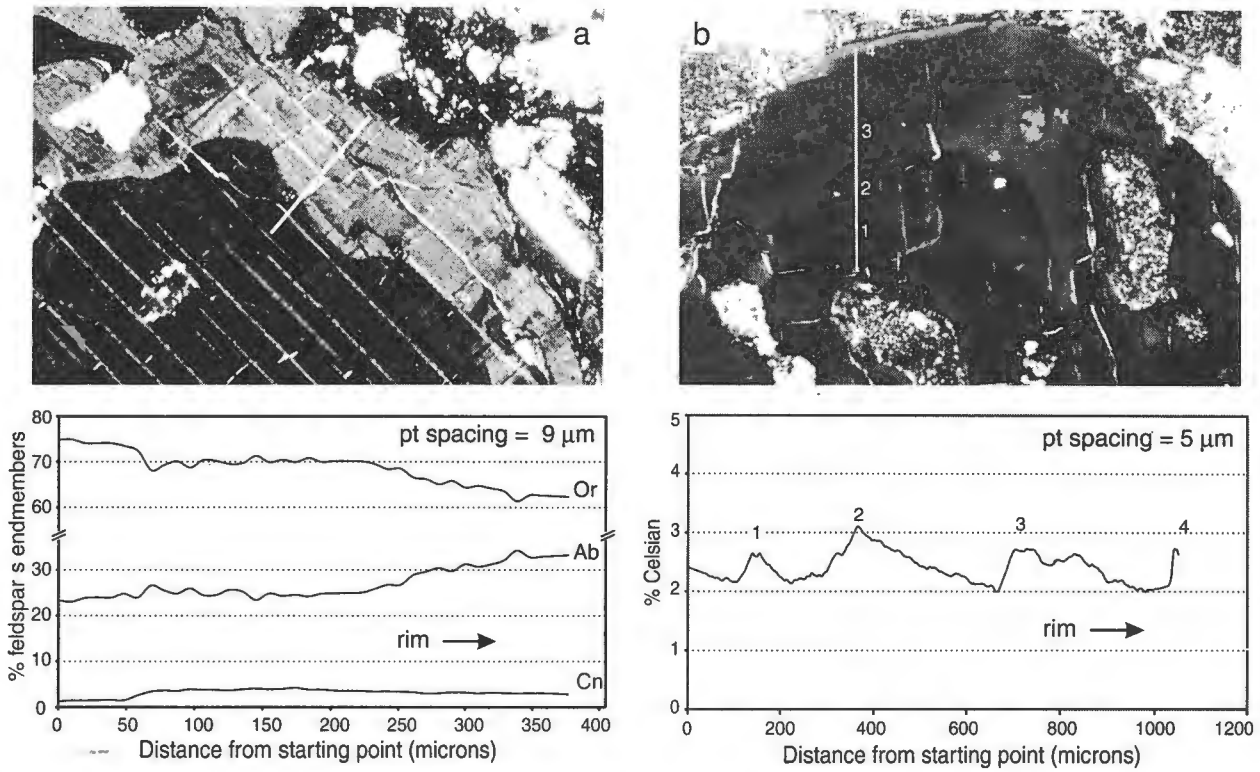

Figure 26: (a) Electron microprobe traverse across a zoning boundary in a large Pagosa Peak Dacite sanidine (Bfc 171, same as Fig. 8b), showing a sharp increase in Cn (Ba) just outboard the undulating surface resorption, correlated with a limited decrease in Or (K) and increase in Ab (Na). The trends then define a progressive increase in Na, correlated with a decrease in Ba and K away from this surface. This Ba-rich outer zone is thought to represent a second generation of sanidine, which grew from a melt enriched in Ba. The origin of this Ba enrichment in the melt is thought to result directly from the development of Rapakivi textures (see Wark & Stimac, 1992 and text for details), as Ba released by sanidine dissolution is not incorporated in the plagioclase structure. Limited addition of Ba from a more mafic magma may also have played a role in the development of this zoning.(b) Electron microprobe traverse in a large sanidine (PCB1; crossed polars) showing abrupt increases in Cn, by up to 1 mol %, across optical zoning boundaries (numbered 1 to 4). The profile displayed here was slightly smoothed using a running average.

associated with Rapakivi texture elsewhere (Wahl, 1925; Backlund, 1938; Vorma, 1971), in particular in granites of the Wiborg Massif, Finland, the type locality of Rapakivi granite. The textures in these plutonic examples are similar to those in the Fish Canyon magmatic system, consistent with a genetic relationship between Rapakivi and granophyre formation. In the Fish Canyon magmatic system, a related crystallization history for both phases of alkali feldspar growth is strengthened by the optical continuity and compositional similarity (~Or_{70-75}) of granophyric overgrowths and host crystals (Lipman *et al.*, 1997).

To explain occurrences of granophyre uniquely in the late-erupted units of the Fish Canyon magmatic system, Lipman *et al.* (1997) proposed that granophyre crystallization was induced by the early eruptions from the Fish Canyon magmatic system. Rapid decompression and devolatilization of the remaining magma upon eruption of the upper part of the chamber produced near-instantaneous, isothermal undercooling, which triggered this distinctive type of crystallization. The same mechanism has also been proposed for the formation of granophyre-bearing xenoliths in the Alid volcanic field (Lowenstern *et al.*, 1997), and provides a satisfactory explanation for the observed characteristics of the Fish Canyon granophyre. The association of granophyre with Rapakivi textures may be a consequence of preferential crystallization

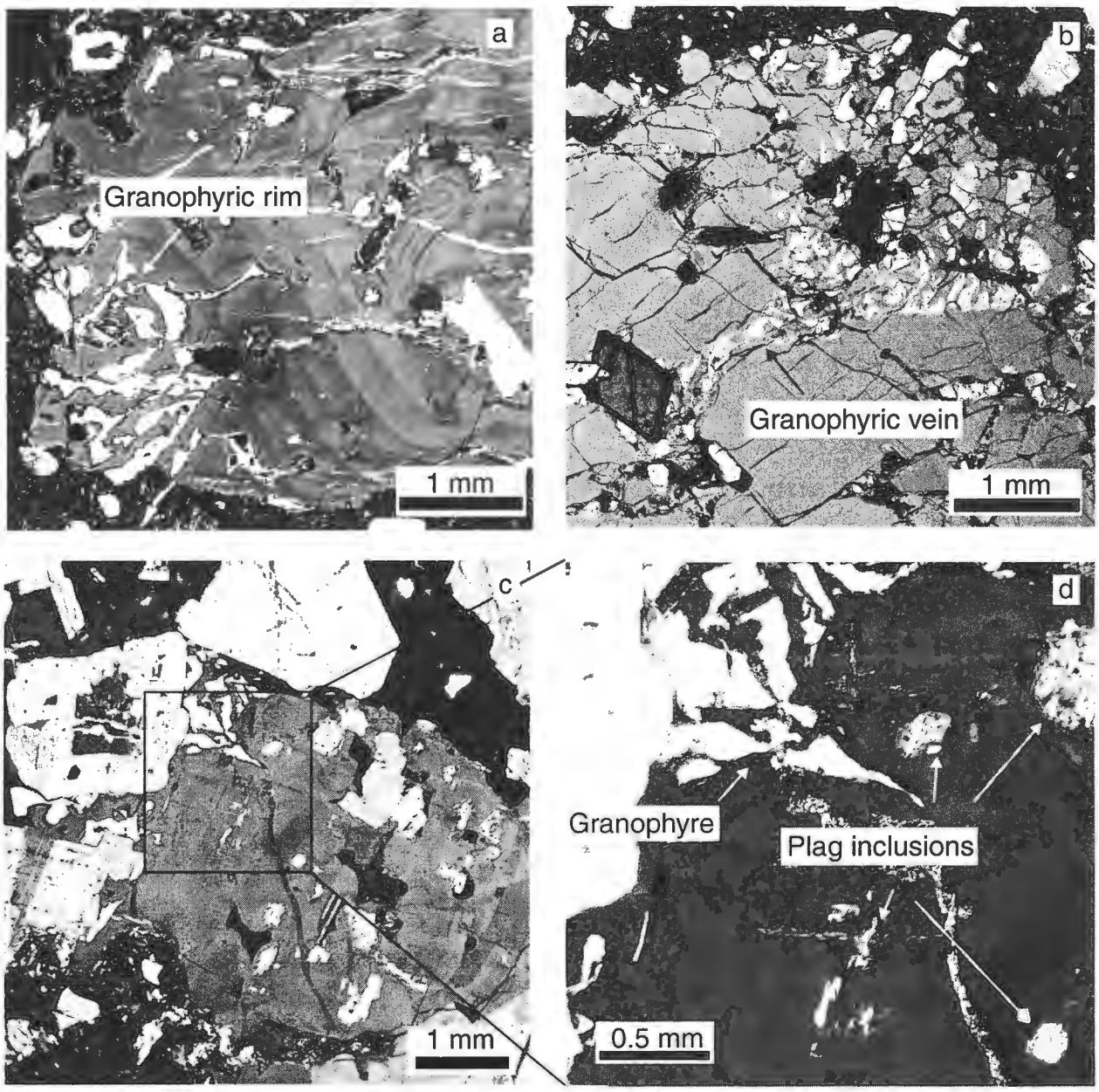

Figure 27: Granophyric overgrowths on Fish Canyon feldspars (all pictures with crossed polars). (a) Granophyric rim on a large crystal in the Nutras Creek Dacite associated with multiple broad oscillatory zones which are spatially associated with plagioclase inclusions in optical continuity and numerous melt pockets (Bfc 115). (b) Granophyre filling a fracture in a sanidine from the late-erupted intracaldera Fish Canyon Tuff. These fractures are thought to result from crystal shattering during decompression of the magma chamber due to early eruptions of the Fish Canyon magmatic system (c.f. main text; Bfc 191). (c) Granophyre overgrowths on a large sanidine (Bfc 115) filling a crack within a large sanidine grain. This sanidine is riddled with plagioclase inclusions and melt pockets, and displays oscillatory Ba zoning. (d) Enlargement of the granophyre-sanidine transition in the sanidine of picture (c), showing no textural evidence for a discontinuity between the K-feldspar in the granophyre and the sanidine. Note the small plagioclase inclusions in optical continuity.

of granophyre in the vicinity of Rapakivi crystals, due to local enrichment of silica and K-feldspar component in the melt as K-feldspar dissolves and plagioclase crystallizes from this feldspathic melt (Watson, 1982; Stimac & Wark, 1992).

6.4.2. Diffusive re-equilibration?

The preservation of solid-solid contacts between sanidine and plagioclase in many multi-grain aggregates that appear to be plutonic fragments has led us to test whether the complex thermal history that we have inferred is recorded in diffusion-controlled compositional profiles near these grain boundaries. In most grain boundaries that are oriented sub-vertically, the width of the affected zone is so narrow (<10 μm) that useful information cannot be obtained. An exception is a plagioclase-sanidine contact which has a subhorizontal orientation (~5-10° inclination) relative to the plane of the thin section. This geometry provides a lateral expansion of the gradients so that they can be resolved analytically, but it also limits quantitative treatment. A traverse from a plagioclase characterized by oscillatory magmatic zoning, without apparent subsolidus equilibration, across the grain boundary into sanidine (Fig. 28a) shows compositional variations consistent with diffusive exchange of Na and K during both cooling and subsequent reheating. This interpretation is consistent with evidence, already summarized, for grain-boundary melting along previously solid-solid contacts.

The primary magmatic and diffusion-controlled zoning profiles are distinguished by different co-variations in Ab-An-Or (Fig. 28b; Table 9). A prominent 'magmatic spike' in the plagioclase profile at ~200 microns from the grain boundary shows the expected troughs in Ab and Or associated with a peak in An component. In contrast, the Ab peak located ~70 microns from the grain boundary is not associated with any decrease in An, but it is mirrored by a trough in Or. Significantly, corresponding peaks in Or and Ab have opposite polarity in the adjacent sanidine (*i.e.*, high Or in sanidine mirrors low Or in plagioclase, as well as high Ab in sanidine), again at ~70 microns from the grain boundary and without a complementary change in An. These complex profiles are nearly impossible to explain as the products of magmatic crystallization, but a two-stage diffusive exchange in response first to subsolidus cooling and then to reheating is plausible. During cooling the plagioclase and sanidine exchanged Na and K, whereas divalent Ca remained nearly unchanged, such that the sanidine became more potassic and less sodic (and vice versa for plagioclase). This trend was reversed during a short heating event, and the cooling profiles within ~70 microns of the grain boundary were overprinted

Table 9: Feldspar analyses used to calculate temperatures in Fig. 28.

	T1 plag	T1 san	T2 plag	T2 san	T3 plag	T3 san
SiO_2	60.21	64.27	60.31	63.64	59.31	64.35
Al_2O_3	24.13	18.71	24.41	18.31	24.30	18.76
FeO	0.23	0.12	0.28	0.18	0.24	0.22
CaO	6.79	0.29	6.56	0.15	6.86	0.20
BaO	0.06	1.61	0.00	1.13	0.05	1.08
Na_2O	7.33	2.88	7.46	1.81	7.89	2.72
K_2O	0.84	11.71	0.22	13.42	0.42	12.08
Sum Ox%	99.59	99.59	99.25	98.66	99.09	99.39
Ab	62.96	25.98	66.42	16.56	65.93	24.76
An	32.21	1.45	32.30	0.78	31.67	0.99
Or	4.73	69.64	1.29	80.58	2.33	72.27
Cn	0.10	2.93	0.00	2.09	0.08	1.98

Temperatures calculated with the feldspar thermometer program Solvcalc (Wen and Nekvasil), using the Elkins and Grove (1990) calibration. Input parameters: 2 kb and precision of 0.02 on mole fraction.

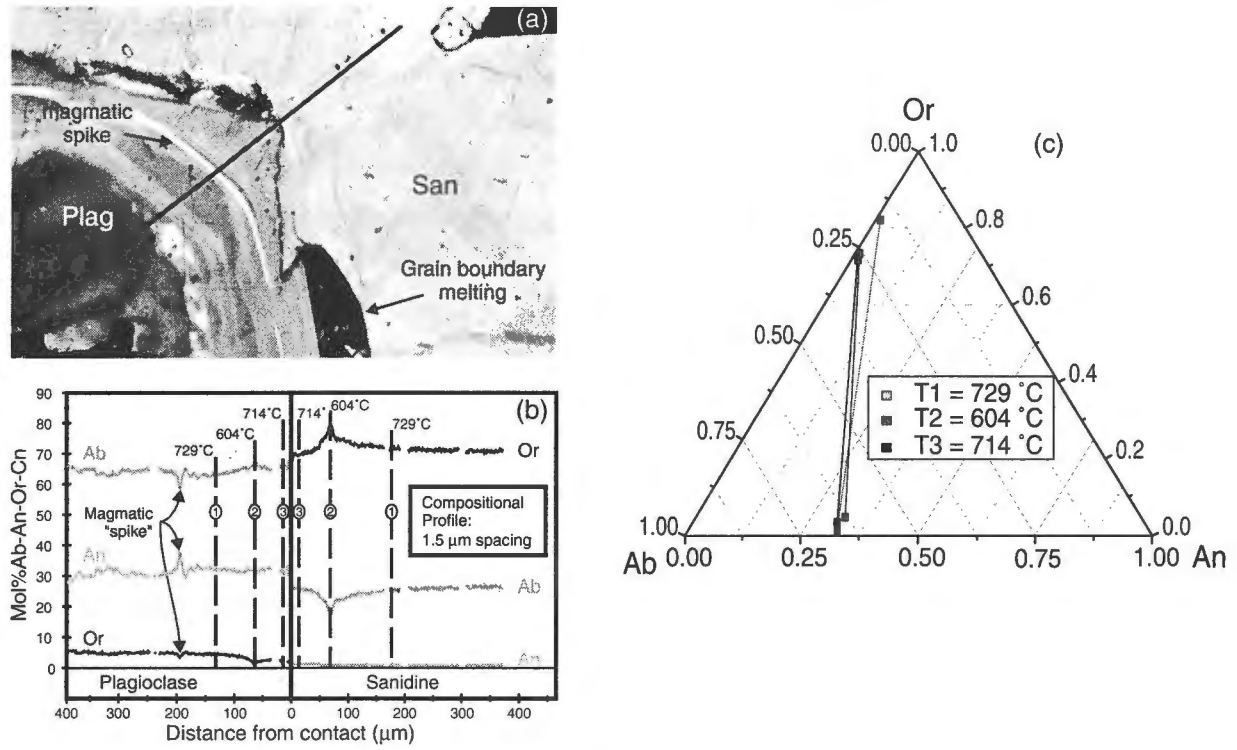

Figure 28: (a) and (b) Electron microprobe traverse across a plagioclase-sanidine grain boundary (Fig. 9b), designated by the line on the photomicrograph above. This profile shows wave-like compositional zoning on both sides of the contact, interpreted as diffusive Na-K exchange across the grain boundary induced by a thermal fluctuation. Note the irregular contact, highlighted by the dashed line, suggesting a nearly horizontal interface between the two phases. (c) Ternary diagram showing the three feldspar pairs chosen on the microprobe profile for the thermometry exercise. T1 and T3 have essentially the same compositions and overlap on this diagram. T2 is shifted toward higher Or in sanidine and lower An in plagioclase, inducing a clockwise rotation of the tie line, which crosses the other two. Temperatures are calculated using the Solvcalc program of Wen & Nekvasil and the calibration of (Elkins & Grove, 1990).

by diffusive exchange in the opposite sense, leading to mineral compositions not too different from those in the interiors of the grains.

In order to provide a qualitative thermal framework for this discussion, we calculated nominal temperatures of coexisting plagioclase-sanidine pairs along this profile. The first pair (1: 729 °C) is at the inferred limit of diffusive exchange, and therefore approximates late-stage magmatic crystallization; the second pair (2: 604 °C) is situated at the complimentary Or-Ab peaks ~70 microns from the grain boundary, and therefore records the impact of subsolidus cooling; and the third pair (3: 714 °C) records reheating near the grain boundary. In the feldspar ternary (Fig. 28c, Table 9), the rotation of the low temperature tie line shows the proportionally larger impact of temperature on the alkali feldspar relative to plagioclase. Although these temperatures are only a qualitative record of thermal changes in the Fish Canyon magma chamber, the apparently diffusion-related profiles signal the difficulty of documenting coexisting equilibrium feldspars in a magma that shows feldspar resorption textures as complex as these, and illustrates the problem of uncritical applications of feldspar compositions from such grain boundaries.

6.5. Glass

Apart from four analyses listed in Table6 of Whitney & Stormer (1985), microprobe analyses

of glass in Fish Canyon Tuff samples reported by Whitney & Stormer (1985) and by Johnson & Rutherford (1989a) were obtained from devitrified material, and they appear not to be entirely accurate measures of melt composition. The interstitial melt in large magmatic blobs from the Pagosa Peak Dacite is preserved mainly of colorless glass containing minute filamental oxide grains (1-2 mm diam.), but isolated pools (200-500 mm) of brownish glass lacking crystallization or devitrification products were also found (Figs. 29 a-b). Rare pools of similarly homogeneous brown glass are present in a few vitrophyre samples from the outflow and intracaldera facies of the Fish Canyon Tuff (Figs. 29 c-d). We infer that these homogeneous areas (hereafter "glass") approximate liquid compositions, even though they almost certainly have undergone post-emplacement hydration.

Glasses in both Pagosa Peak Dacite and Fish Canyon Tuff are high-SiO_2 rhyolite (75-76 wt. % SiO_2; Table 10) with high K_2O (5.0-5.6 wt. %), and correspondingly low CaO (0.6 to 0.8 wt. %), FeO_{tot} (0.3-0.8 wt.%) and MgO (<0.1 wt. %, close to detection limit). Na content is also relatively low (2.0-3.1 wt. %) in comparison to other rhyolites (3-4 wt. %: Bishop Tuff, Anderson *et al.*, 2000; Glass Mountain lavas, Metz & Mahood, 1991). Some Na loss during secondary hydration could be in part responsible for these low values, although the sum of the oxides of the analyses are high for hydrated glasses (97-98) and Na/K ratios do not vary widely. The colorless Pagosa Peak Dacite glass and the glass in the outflow Fish Canyon Tuff vitrophyre span the same range of composition as the Pagosa Peak Dacite homogeneous brown glass, although the colorless glass is slightly depleted in FeO. The sample from the intracaldera Fish Canyon Tuff is slightly lower in SiO_2 and higher in Al_2O_3 and Na_2O (Table10). The four fresh glass analyses reported by Whitney & Stormer (1985) in their Table 6 and the matrix analysis reported by Johnson & Rutherford (1989a) in their Table 1 have slightly lower CaO and Al_2O_3 contents with correspondingly higher K_2O and Na_2O.

As expected for a high-SiO_2 rhyolite melt, the normative mineralogy of the Fish Canyon glass

Table 10: Representative glass analyses from the Fish Canyon magma.

	83gl5.pt1	83gl4.pt2	83gl4.pt8	91glm.pt1	196agl3	113gl1	191agl4
	PPD (brown)	PPD (brown)	PPD (white)	PPD (brown)	PPD (brown)	FCT (O)	FCT (I)
SiO_2	75.95	76.34	76.68	76.40	75.66	76.48	75.41
TiO_2	0.13	0.14	0.09	0.11	0.16	0.13	0.12
Al_2O_3	12.43	12.43	12.32	12.32	12.26	12.78	13.07
FeO	0.58	0.68	0.20	0.25	0.57	0.57	0.26
MnO	0.02	0.08	0.02	0.05	0.06	0.03	0.01
MgO	0.05	0.07	0.04	0.02	0.08	0.02	0.04
CaO	0.67	0.74	0.72	0.64	0.78	0.70	0.64
Na_2O	2.35	2.59	2.65	2.65	1.95	2.53	3.13
K_2O	5.52	5.26	4.99	5.37	5.48	5.53	4.97
P_2O_5	0.01	0.00	0.00	0.00	0.00	0.01	0.06
Sum Ox%	97.88	98.30	97.90	97.97	96.99	98.79	97.71
Na_2O/K_2O	0.43	0.49	0.53	0.49	0.36	0.46	0.63

For PPD samples, four analyses are from the undevitrified, brown pools, and one from a white zone containing minute oxide filaments.

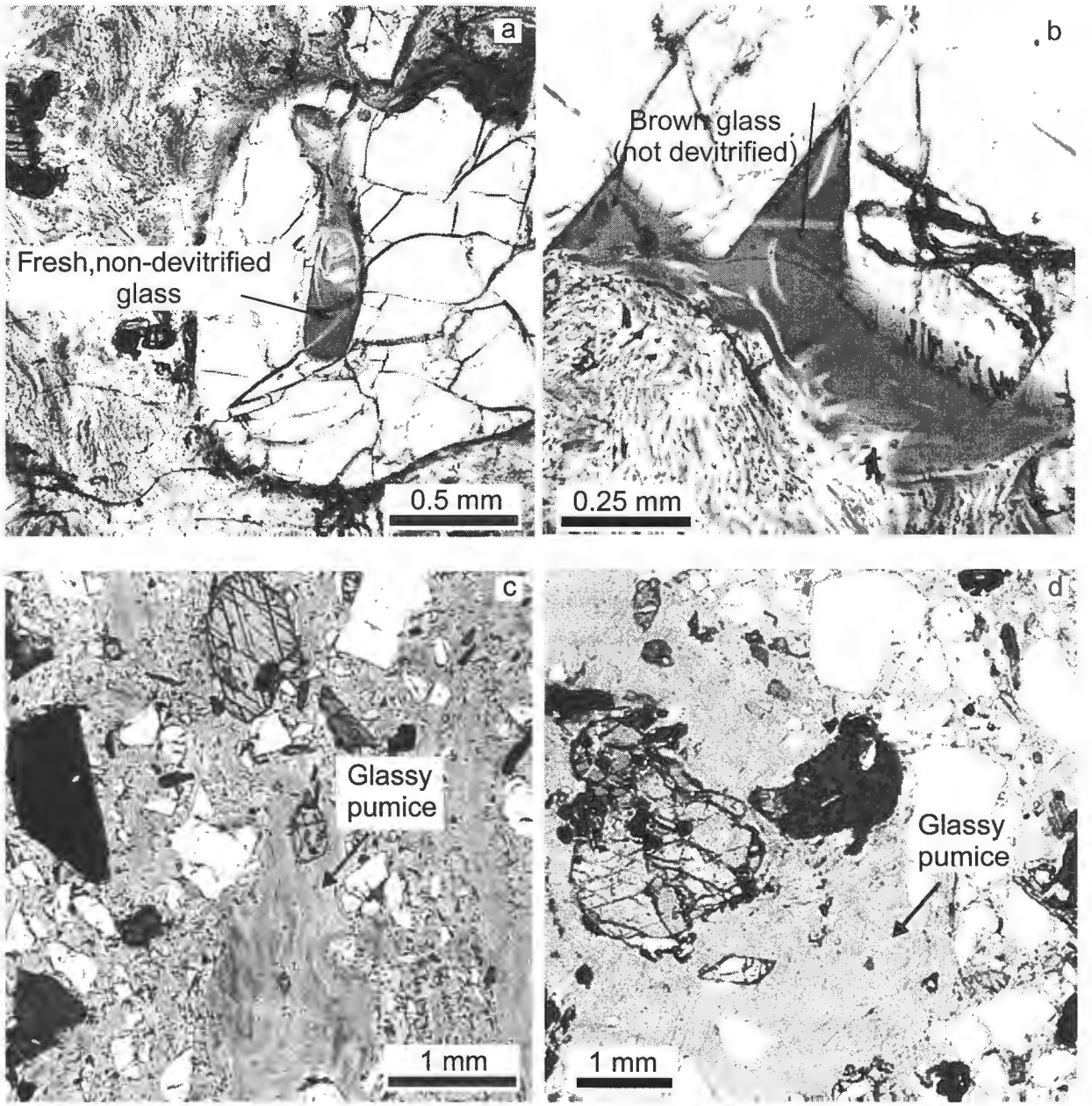

Figure 29: Interstitial glass in Fish Canyon magma (all pictures in plain polarized light). (a) and (b) are both from Pagosa Peak Dacite blobs (Bfc 83). Although the matrix remains glassy, the formation of minute oxide filaments during incipient devitrification has rendered the glass around it colorless (iron loss). However, in areas bordering phenocrysts and in large melt pools inside remelted crystals, glass remained free of even the oxide filaments and has retained its brown coloration. Microprobe analyses in these zones are inferred to provide reliable compositions of the Fish Canyon melt immediately prior to eruption. (c) Small glassy pumices from an outflow Fish Canyon Tuff vitrophyre (Bfc 113). (d) Glassy pumice from an intracaldera Fish Canyon Tuff vitrophyre (Bfc 191a). In rare Fish Canyon Tuff vitrophyres, glass is generally free of oxide filaments.

is mainly quartz, K-feldspar, and albite (>95 %) and can, therefore, be evaluated in the ternary Qz-Ab-Or haplogranite system (Fig. 30). The position of this glass, taking into account the role of Ca in expanding the volume of plagioclase (normative An_{12-20}), suggests a near-eutectic composition equilibrated at a pressure close to 2 kb. The most evolved experimental glass composition obtained by Johnson & Rutherford (1989a; experimental conditions: P = 2.5 kb, T = 760 °C, X_{H2O} = 0.5 and AMQH f_{O2} buffer) plots toward a slightly higher pressure eutectic. Accordingly, the Fish Canyon

magma body is confirmed to have resided in a shallow environment, in agreement with eruption during caldera collapse and Al barometry for hornblende rims at 760°C, most likely in the range of 5-7 km depth (~2 ± 0.5 kb).

To assess whether the interstitial liquid in the Fish Canyon magma was mainly produced by crystallization (*i.e.*, residual melt) or by melting (*i.e.*, anatectic melt), Sr and Ba contents in the Fish Canyon glass have been compared to other high-SiO_2 rhyolites. Sr and Ba have high partition coefficients for plagioclase and sanidine, respectively. The model of Blundy & Wood (1991) yields a partition coefficient of approximately 20 for Sr in An_{30} plagioclase at 760 °C, and the Ba partition coefficient in K-feldspar (Or_{70}) is thought to exceed 10 (Icenhower & London, 1996; Nash & Crecraft, 1985). In magmas where feldspars dominate the mineral assemblage, such as in the Fish Canyon, Sr and Ba contents in the interstitial melt should differ markedly, depending on whether the system is crystallizing or melting. Liquids (glass) produced by melting are predicted to have high Sr and Ba contents (Knesel & Davidson, 1999). In contrast, fractional crystallization should produce residual melts highly depleted in these elements (Halliday et al., 1991). High-SiO_2 rhyolites such as the Glass Mountain lavas (Metz & Mahood, 1991; Halliday *et al.*, 1989), the Bishop Tuff (Anderson et al., 2000), and the Bandelier Tuff (Dunbar & Hervig, 1992), in which fractional crystallization is thought to have played a major role, have low Sr (0.1-5 ppm) and Ba (1-80 ppm) contents. Conversely, silicic xenolith suites from Tatara-San Pedro (Costa, 2001) and Crater Lake (Bacon, 1992), which partially remelted during residence in the host magma, have interstitial glass

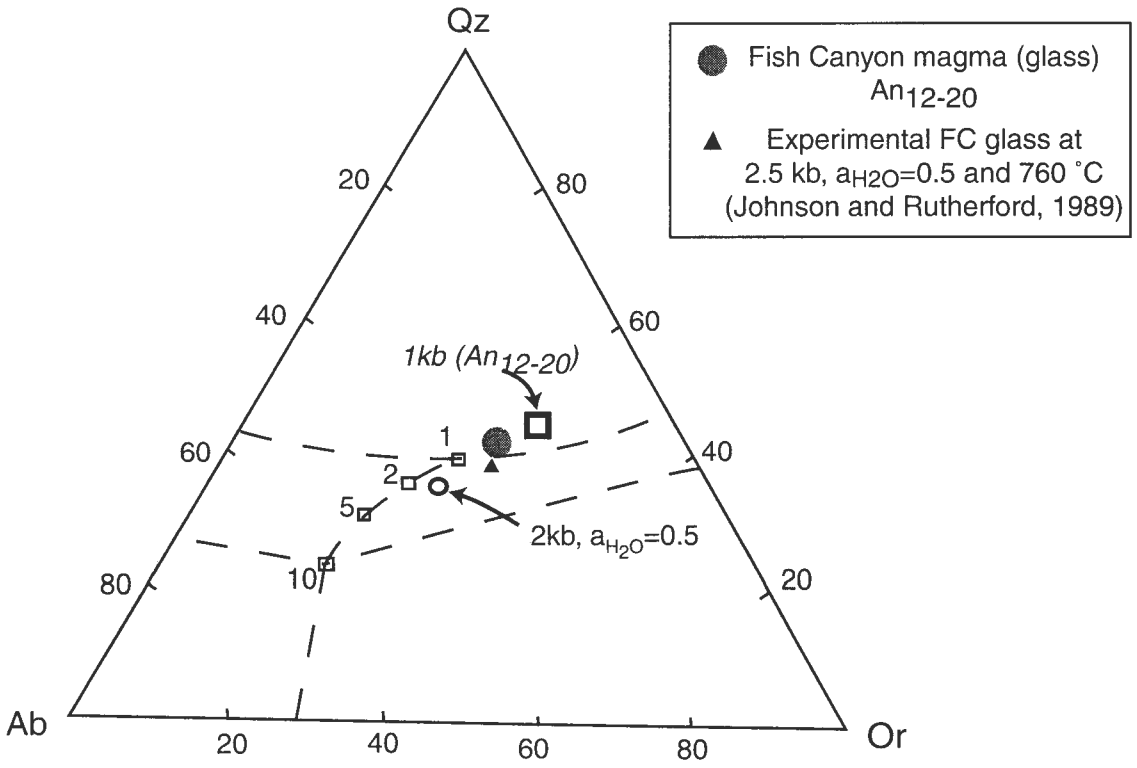

Figure 30: Ternary diagram showing the positions of eutectics, cotectics and minima in the haplogranitic Qz-Ab-Or system for select conditions (diagram modified from Johannes & Holtz, 1996). Dashed lines: cotectic lines for water-saturated conditions. Open squares: Minimum melt compositions at PH2O=1, 2, 5, 10 kb. Open circle: minimum melt composition at 2 kb and aH2O=0.5 (Johannes & Holtz, 1996; their Fig. 2.20). Large open square: minimum melt composition at PH2O=1 kb and minor anorthite component (An12-20). CIPW norms were calculated from average Pagosa Peak Dacite brown glass compositions (Table 9).

with concentrations of Sr and Ba up to 50 times higher than the Bishop, Bandelier, and Glass Mountain samples (Fig. 31). The Fish Canyon magma belongs to the high Sr-Ba group, suggesting formation of the interstitial liquid mainly by melting of a feldspar-rich assemblage, in agreement with textural observations.

For elements with high bulk partition coefficients (bulk D), which is the case for Sr and Ba in Fish Canyon magma (Table 11), equations for Rayleigh fractional crystallization ($^{Conc.\ liq.}/_{Conc.\ init.} = F^{D-1}$) and batch melting ($^{Conc.\ liq.}/_{Conc.\ init.} = {}^{1}/_{D+F*(1-D)}$), produce divergent results. This offers a test for the origin of interstitial liquid by remelting or crystallization of feldspars. Melting and crystallization curves of bulk D versus trace element concentrations have been calculated at constant melt fractions using initial Sr and Ba concentrations equivalent to those in bulk Fish Canyon magma (Fig. 32). Crystallization depletes these elements to levels far below the concentrations measured in the Fish Canyon glasses. Whereas fractional crystallization is a limiting case, it remains the best approximation for the partitioning of trace elements between melt and crystals in low temperature viscous magmas as diffusional exchanges are insufficiently rapid to achieve equilibrium crystallization (Zellmer et al., 1999). The higher bulk D for Sr in the Fish Canyon magma, in the range where melting and fractionation curves are widely separated, makes the case of Sr more reliable. The measured Ba concentrations in the crystallization-dominated systems are lower than the calculated crystallization curve, suggesting that the bulk partition coefficient for Ba may reach values >5 in highly evolved rhyolitic systems (Streck & Grunder, 1997).

7. Magmatic inclusions in the Fish Canyon magmatic system

Another previously unrecognized characteristic of the Fish Canyon magmatic system is the presence of a wide diversity of magmatic inclusions and solid xenoliths in the intracaldera facies of the Fish Canyon Tuff. We have documented five groups of included material, a few of which are present as well in the outflow facies and in the nutras Creek Dacite These include: (1) fragments of Precambrien basement, (2) holocrystalline granodioritic xenoliths with the same mineralogy and similar whole-rock and mineral chemistry as Fish Canyon magma, (3) Porphyritic granitic xenoliths, (4) Fine-grained crystal-rich inclusions, and (5) hybrid andesite inclusions (plag + san + hbl + cpx + ox + matrix). Apart from the xenoliths from the Precambrien basement, each of these groups appears to be co-genetic in some sense with the

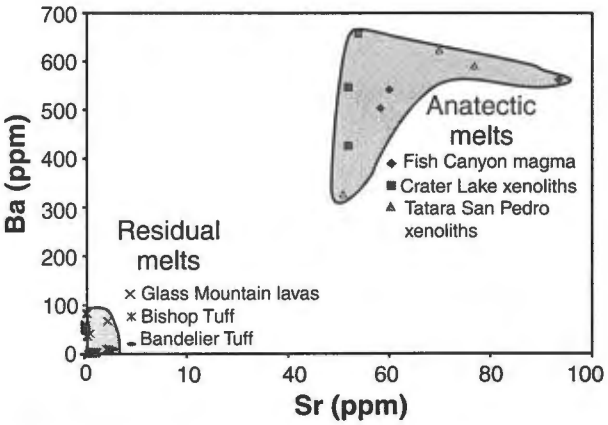

Figure 31: Comparison of Sr and Ba contents in the interstitial glasses of six high-silica rhyolite systems. Sr and Ba, due to their high partition coefficients in plagioclase and K-feldspar, have contrasting behaviors during anatexis and crystallization of feldspar rich assemblages and can be used as a criterion to constrain the petrologic origin of the glass. Glass mountain lavas: Halliday et al. (1989). Bishop Tuff (in melt inclusions): Anderson et al. (2000). Bandelier Tuff (in melt inclusions): Dunbar & Hervig (1992). Crater Lake xenoliths: Bacon (1992). Tatara-San Pedro xenoliths: Costa (2000).

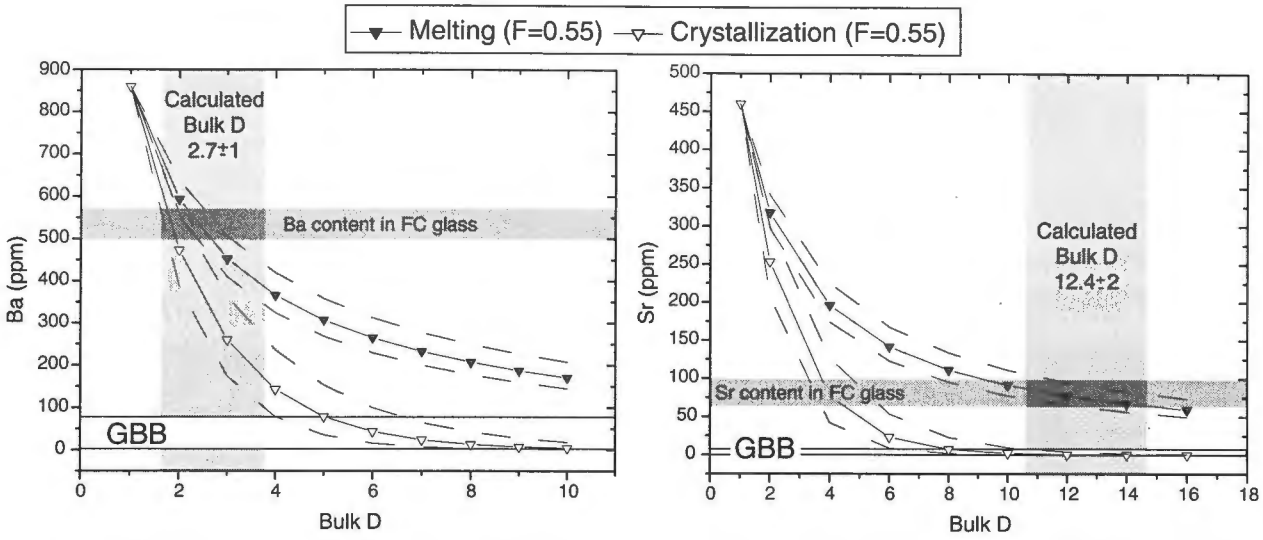

Figure 32: Variations in Sr and Ba concentrations in anatectic and fractionated liquids as functions variable bulk partition coefficient (bulk D) and fraction of liquid. The principal fractionation and melting curves (with symbols) are both calculated for F = 0.55, and associated curves represent envelopes between 0.45 (lower curves) and 0.65 (upper curves). Ba and Sr concentrations measured by ion microprobe in the Fish Canyon glass (horizontal gray rectangle) and in examples of residual glass (Glass Mountain, Bishop Tuff and Bandelier Tuff; GBB). The vertical boxes display the range of conservatively estimated bulk partition coefficients as calculated in Table 10. C0 = whole-rock analysis of the Pagosa Peak Dacite.

Fish Canyon magma. They are, therefore, likely to provide useful information about the origin and the evolution of the Fish Canyon magma.

7.1. Holocrystalline granodioritic xenoliths

Rare (<< 1%) fragments of holocrystalline granodiorite, 5 to 30 cm in diameter, are present in the late-erupted upper intracaldera Fish Canyon Tuff on the northern slopes of the resurgent dome. The granodiorites show no evidence of deformation, have the same mineral assemblage as Fish Canyon magma (plag+san+qtz+hbl+biot+sphn+ox+zirc; Fig. 33a), and have similar modal abundances for the hydrous phases (hbl and biot), sphene, and oxides. The modal differences reside in the higher proportions of quartz, K-feldspar, and plagioclase in the granodiorites, reflecting the absence of glass in these samples. They are coarse-grained (0.5-5 mm), with individual crystals similar in size to Fish Canyon phenocrysts. Hornblende, biotite, plagioclase, and sphene are generally euhedral, whereas K-feldspars and quartz are interstitial and anhedral (Fig. 33b). Some K-feldspar grains, like large sanidine crystals in Fish Canyon magma, contain numerous isolated, anhedral plagioclase inclusions in optical continuity, suggesting replacement of plagioclase by K-feldspar and development of Rapakivi textures. Ba-rich zones are also associated with these inclusions (Fig. 33c).

The whole-rock compositions of the granodiorites (~67.2 wt. % SiO_2) are close to the Fish Canyon magma composition. With the exception of Mn and Ca, relative differences in major and minor elements concentration are below 10 %. For the trace elements, Nd, Pb, Cr, and Zn are different by more than 50 %, but all the others are within 15 % of the Fish Canyon value (Table 2). Likewise, mineral compositions span similar ranges, although subtle variations are present, mainly in feldspars. Concentrations of all major elements in hornblendes and biotites from the granodiorite xenoliths largely overlap those of the Pagosa Peak Dacite (Fig. 34).

Table 11: Calculation of estimated bulk partition coefficients for Ba and Sr in the Fish Canyon magma.

	Partition coefficients for the Fish Canyon magma				
	Bulk	**Hornblende**	**Biotite**	**Plagioclase**	**Sanidine**
Ba	2.66	0.05	20	0.82	10
Sr	12.35	0.02	0.2	19.56	4.5
Phase fraction		0.09	0.08	0.60	0.14

All partition coefficients are for rhyolitic melts. Some are averages of several values given by different authors. Hornblende partition coefficient : (Arth, 1976). Biotite partition coefficient : (Nash and Crecraft, 1985) ; Arth (1976) ; (Mahood and Hildreth, 1983). Plagioclase partition coefficient : (Blundy and Wood, 1991). Temperature = 760°C An = 30. K-feldspar partition coefficient : Nash and Crecraft, (1983) ; Arth (1976) ; Mahood and Hildreth (1983). The phase fraction was calculated using the modal analyses normalized to 100% minerals.

The linear trends defined in variation diagrams by the Pagosa Peak Dacite hornblendes are slightly extended by the xenolith data toward lower Al_2O_3 (< 5 wt. % Al_2O_3), and correspondingly lower FeO_{tot} and higher MgO and SiO_2, consistent with crystallization at even lower temperatures than those recorded in the Fish Canyon hornblendes. Average K-feldspar compositions in the granodiorites are shifted toward lower K (~Or_{68} instead of Or_{72}) content (Fig. 35), whereas plagioclase is slightly more albitic (to ~$An_{20;}$ Fig. 23). The more albitic compositions are apparently restricted to the outermost rims of plagioclase. A microprobe traverse across a large plagioclase from a granodiorite yielded a core composition typical of Fish Canyon plagioclase (~An_{30}), overgrown by (Fig. 36) a ~200 mm thick normally zoned rim falling to An_{20}.

The similarities in mineralogy, texture, whole-rock composition and mineral chemistry displayed by the granodioritic fragments and the Fish Canyon magma do not support a purely accidental origin; the holocrystalline xenoliths are interpreted as relics of a marginal facies of the Fish Canyon protolith. Xenoliths with Fish Canyon mineralogy are also found in younger units, such as the Huerto Andesite (Parat, personal communication, 2001). Holocrystalline Fish Canyon material was thus still present in the crust after the caldera-forming eruption.

Some holocrystalline granodioritic xenoliths display the Fish Canyon mineral assemblage cemented by interstitial granophyre (Fig. 33d). These samples may relate to the granophyric overgrowths on Rapakivi K-feldpars in late-erupted material, and support the interpretation that parts of the Fish Canyon chamber solidified in response to eruption-induced decompression of the magma chamber. Such samples may be analogues to the granophyric blocks in the Alid volcanic field (Lowenstern *et al.*, 1997).

7.2. Porphyritic granitic xenoliths

Xenoliths of porphyric granite, some > 50 cm in diameter, are present in the northern intracaldera Fish Canyon Tuff, in the same exposures that contain the granodioritic xenoliths just described. These granitic fragments are holocrystalline, show no evidence of deformation, and have a mineral assemblage dominated by K-feldspar and quartz (>70 % of the rock). Plagio-

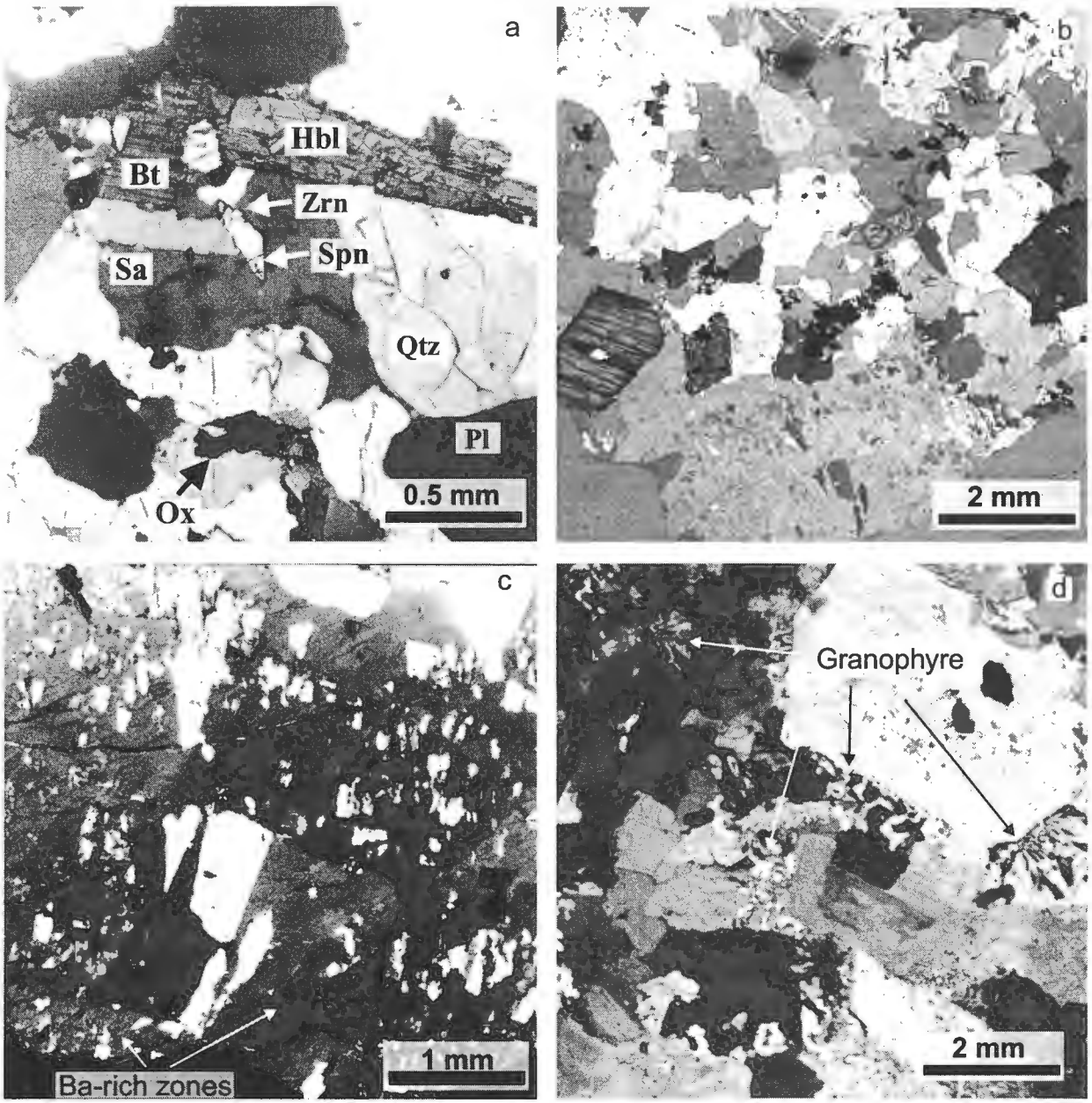

Figure 33: Photomicrographs of granodioritic fragments, entrained in the intracaldera Fish Canyon Tuff. (a) Fish Canyon mineral assemblage in a granodioritic xenolith (Bfc 187; partially crossed polars). (b) Photomicrograph showing euhedral hornblende and biotite, as well as a large poikilitic K-feldspar at the bottom of the picture (Bfc 187; partially crossed polars). (c) Enlargement of the large poikilitic K-feldspar, showing plagioclase inclusions in optical continuity and Ba-rich zones (Bfc 187; crossed polars). (d) Example of a granodioritic xenolith showing interstitial granophyre (CsGr10; crossed polars).

clase, biotite and Fe-Ti oxides filled the remaining 30 %, in roughly equal proportions (~10 % each). These granites have a bimodal texture, with milimetric grains of plagioclase and biotite in a finer matrix (~100 mm) of quartz, K-feldspar, plagioclase, biotite, and oxides (Fig. 37).

Although the mineralogy and whole rock composition (~76% SiO_2) are different from the Fish Canyon magma, this granitic facies appears to be related as well to the Fish Canyon magmatic system. The absence of deformation in xenoliths up to 50 cm in diameter seems to exclude the possibility that these are fragments of Precambrian wall-rocks. The porphyritic texture and the absence of microcline suggest that they rapidly cooled and crystallized from a porphyritic magma. This magma appear to

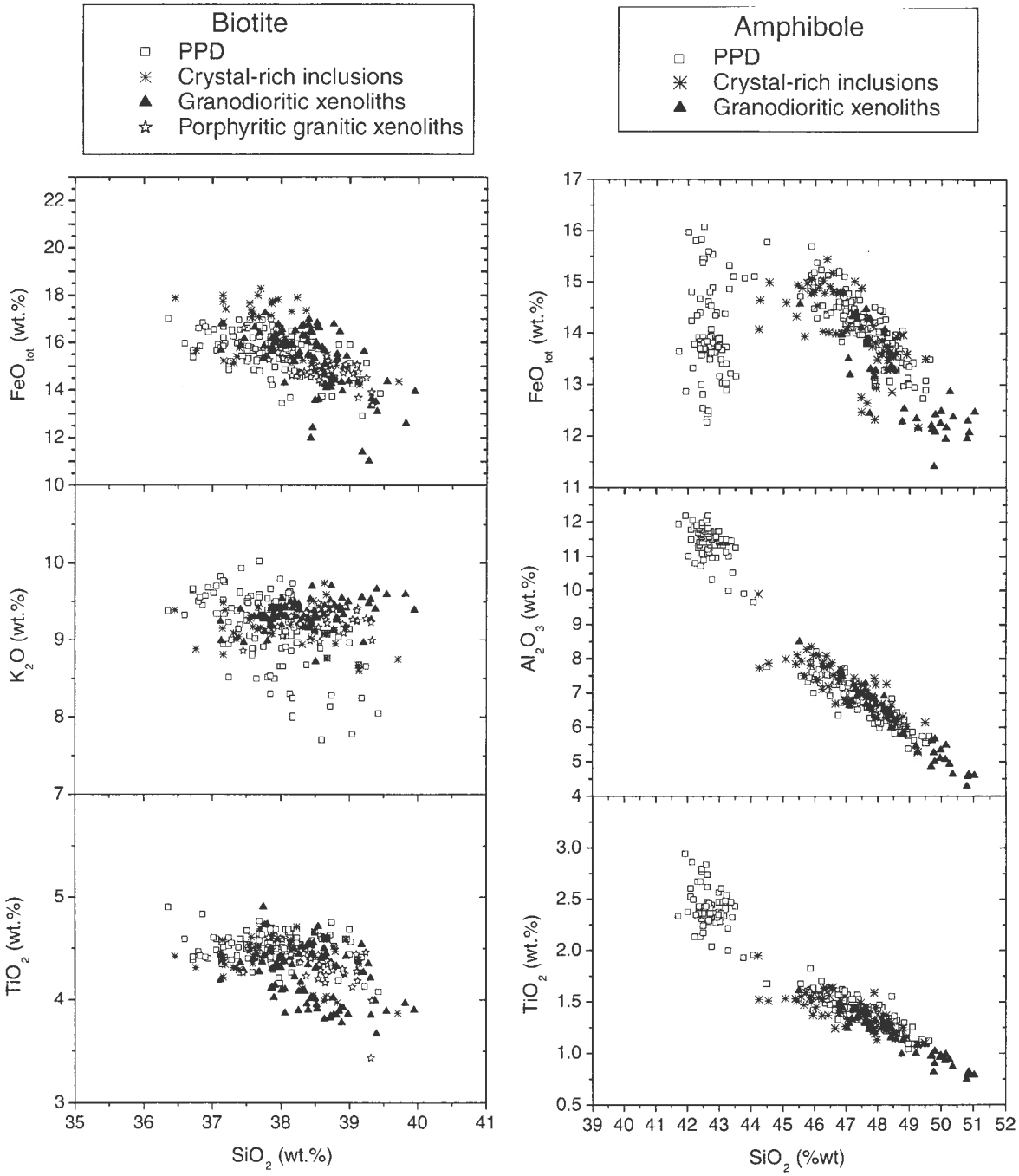

Figure 34: Major element variation diagrams plotted against silica comparing hornblendes and biotites of the Fish Canyon magma (PPD), the crystal-rich inclusions, and the granodioritic xenoliths. Biotites from the porphyritic granitic xenoliths are also reported.

be related to the Fish Canyon magma as the chemical characteristics of the large biotite and plagioclase are similar to those of the Fish Canyon minerals (Figs. 23 and 34). In particular, the large plagioclase in these granites have oscillatory zoned rims, and the chemical profiles across these rims not only span the same range of values as those measured in Fish Canyon plagioclases, but they also show the same narrow calcic excursions up to An_{40} and progressive inverse zoning typical of Fish Canyon plagioclase (Fig. 37), suggesting that these grains crystallized from Fish Canyon magma. The fine-grained interstitial feldspars are, in contrast, slightly different from Fish Canyon feldspars, with K-feldspar depleted in K ($Or_{61\ to\ 67}$; Fig. 35), and plagioclase depleted in Ca (down to Ab_{15}; Figs. 23

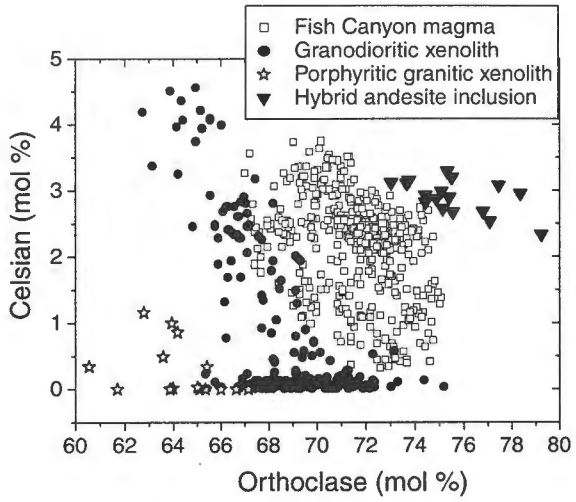

Figure 35: Ba-K variations in K-feldspars of the Fish Canyon magma body (including data from the PPD, NCD, outflow and intracaldera FCT), in the granodioritic xenolith and in the hybrid andesite inclusions.

and 36).

The whole-rock compositions of these xenoliths (Table 2) are similar to the Fish Canyon glass composition for the measured major and trace elements (Figs. 11 and 12), suggesting crystallization

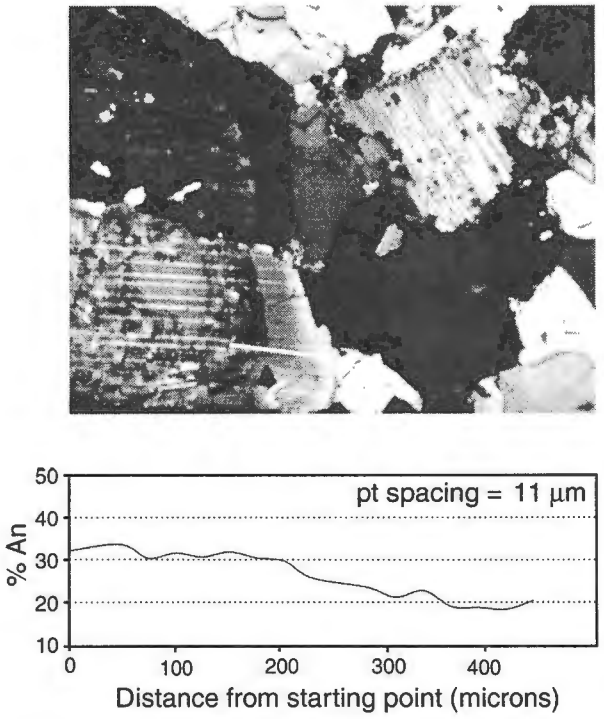

Figure 36: Electron microprobe traverse across a plagioclase from a granodioritic xenolith (Bfc 187), showing normal zoning in the outermost rim. This normally zoned rim reaches anorthite content lower than those measured in the Fish Canyon magmatic system (~An20).

from zones where melt percolating away from the main Fish Canyon chamber accumulated. The presence of a few trapped Fish Canyon plagioclase and biotite phenocrysts in these xenoliths could be explained by a transport along with this high viscosity melt. The fine-grained texture is reminiscent of an aplitic facies, described in the margins of granitic co-magmatic intrusions exposed in deeply eroded caldera systems (Lipman, 1988; Lipman et al., 1993), that are interpreted as the solidified remains of a magma chamber that was largely emptied by an ash-flow eruption.

7.3. Fine-grained crystal-rich inclusions

Fine-grained crystal-rich inclusions are present in the Pagosa Peak Dacite as well as in both outflow and intracaldera Fish Canyon Tuff (Fig. 38a). Occurrences in the Nutras Creek Dacite have not been documented. These inclusions contain > 70 % crystals in a glassy matrix. The mineral assemblage is dominated by plagioclase (~50 %), and comprises hornblende, biotite, and Fe-Ti oxides in roughly equal proportions. These inclusions have bimodal textures: a few large plagioclase, biotite and hornblende crystals (1-3 mm) similar in size to the Fish Canyon phenocrysts, are surrounded by crystals one order of magnitude smaller (~100 microns; Fig. 38b). Both size populations are largely euhedral. Contacts between inclusions and host are generally sharp, but some disaggregation in a few examples, produces more gradational boundaries.

Although these inclusions are less silicic (~58 wt. % SiO_2) than Fish Canyon magma, the major element compositions of the mineral phases and interstitial glass overlap with those of Fish Canyon phenocrysts and matrix glass (Figs. 23 and 34). These comparable phase chemistries indicate that these crystal-rich inclusions crystallized from the Fish Canyon magma under similar conditions of pres-

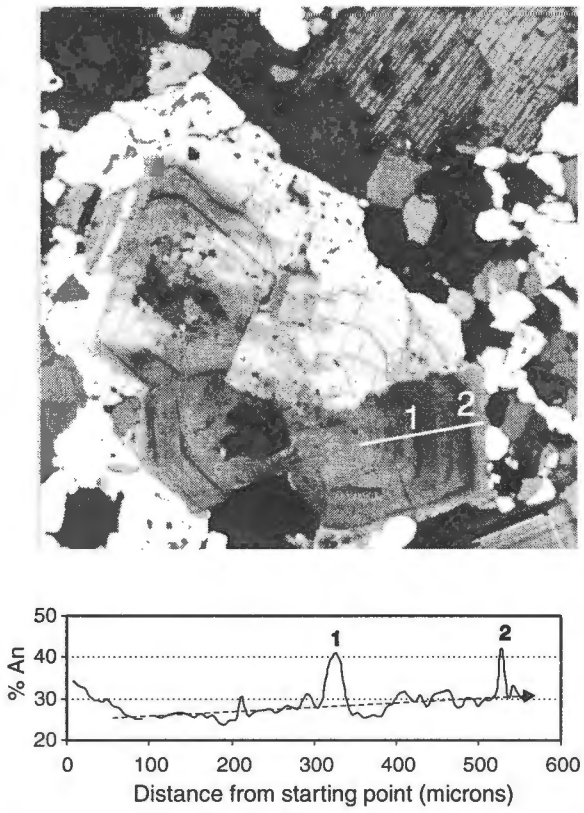

Figure 37: Electron microprobe traverse in anoscillatory zoned plagioclase from a porphyritic granitic xenolith (CsGr Big). The profile shows essentially the same characteristics as Fish Canyon plagioclase phenocrysts; i.e., more calcic core and spikes, as well as progressive inverse zoning. The two major calcic spikes are numbered. Note the bimodal size distribution of crystal in these granitic xenoliths.

sure and temperature. Their less silicic whole-rock compositions are a consequence of their low proportions of matrix glass and the absence of the near-solidus phases sanidine and quartz. They could not represent enclaves of true andesitic magma since their calcium-poor plagioclase compositions (~An_{30}) are incompatible with crystallization from a more mafic liquid. In Harker diagrams of selected major and trace elements, these inclusions plot along the extensions of linear trends defined by Fish Canyon glass composition, unfragmented magma samples (Pagosa Peak Dacite and Nutras Creek Dacite) and the Fish Canyon Tuff. In these diagrams, samples from the Fish Canyon Tuff define parallel sub-trends generated by crystal accumulation due to glass winnowing during ash-flow tuff emplacement (Figs. 11 and 12). By analogy, these crystal-rich inclusions could represent fragments of nearly solid areas in the magma chamber formed by crystal accumulation. A word of caution is, however, necessary in this interpretation of crystal accumulation, as an apparently compositionally unrelated mafic enclave containing clinopyroxene, described next, plots near the crystal-rich inclusions for almost all elements.

Comparable fine-grained, crystal-rich inclusions are found in other large ignimbrites such as the Cerro Galan ignimbrite in northwest Argentina and they have been described in detail in the Purico and Puripicar ignimbrites of northern Chile by de Silva (1989). In these last two occurrences, they display the same general features; i.e. a more mafic whole-rock composition than the host magma despite similar melt and mineral chemistries, an absence of low temperature phases (in the Chilean case quartz and allanite instead of quartz and sanidine for the Fish Canyon magma) with respect to the mineral assemblage in the host magma, and they plot as linear extensions of trends connecting their glass and host magma compositions. They have been interpreted as accumulated residues, which crystallized at the side-wall of the magma chamber. The fine-grained, crystal-rich texture is inferred to result from rapid crystallization on a relatively cold substrate to reach the necessary high degree of undercooling capable of producing such textures. The striking similarities between the two occurrences argue for an analogous petrologic origin and the mechanism proposed by de Silva (1989), invoking rapid crystallization on a relatively cold substrate with intermittent incorporation of larger phenocrysts from the host magma leading to the bimodal texture, seems reasonable.

7.4. Hybrid andesitic inclusions

Hybrid andesitic inclusions are rare, occurring only in the upper intracaldera Fish Ca-

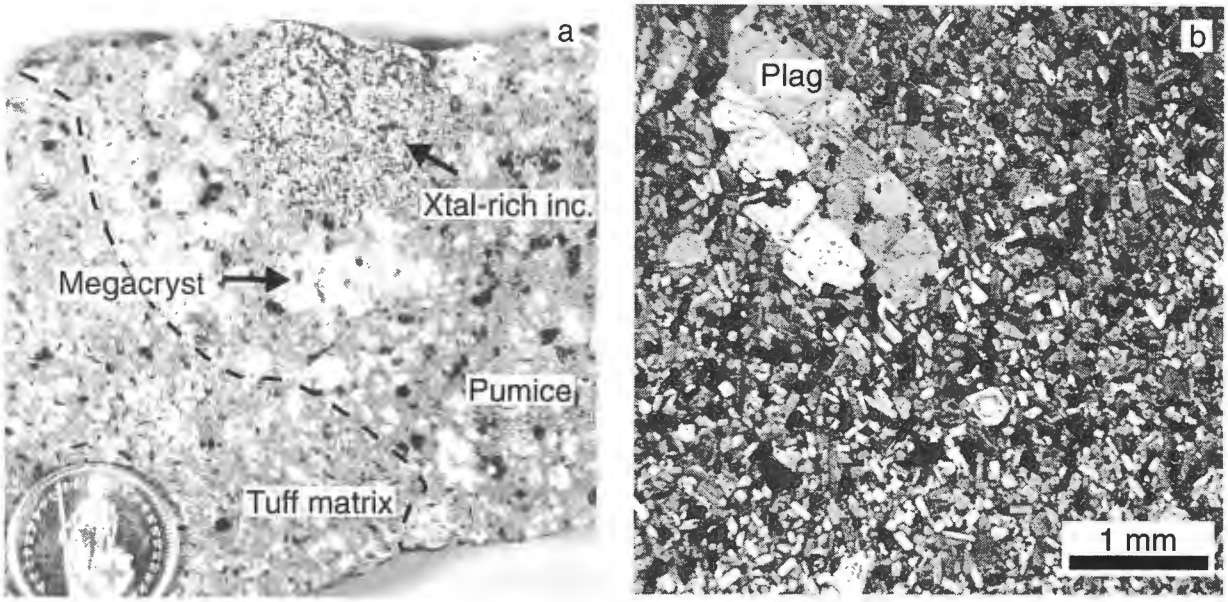

Figure 38: Crystal-rich inclusion in the Fish Canyon pumice (Intracaldera Fish Canyon Tuff; Bfc 129). (a) Pumice of the intracaldera Fish Canyon Tuff containing a crystal-rich inclusion and a feldspar megacryst. (b) Texture of crystal-rich inclusion in thin section, showing a bimodal size distribution with larger plagioclase, a fine-grained matrix containing small plagioclase, hornblende, biotite and oxide crystals. Hornblende and biotite also occur as large phenocrysts. All these mineral phases have the same compositions as those in typical Fish Canyon phenocrysts.

nyon Tuff. Macroscopically, they appear as fist-sized reddish enclaves with fine-grained textures and sharp boundaries with the host tuff (Fig. 39a). The mineral assemblage is hornblende, sanidine, plagioclase, clinopyroxene, and oxides in a microlite-rich devitrified matrix (Fig. 39b-c). Hornblende and sanidine reach 1 mm in diameter, whereas the other phases are smaller, ranging in size from 50 to 500 mm. The mafic minerals (hornblende and clinopyroxene) have reaction rims. Sanidine phenocrysts and plagioclase microlites are euhedral, and sanidine is commonly poikilitic.

The absence of biotite, presence of clinopyroxene, more calcic compositions of plagioclase microlites (An_{60-40}), and andesitic whole-rock composition indicate that these inclusions are related to a more mafic magma that was injected into the Fish Canyon system. A hybrid origin is inferred from the presence of zones rich in Fish Canyon minerals (Fig. 39a). In response to their incorporation in the hotter, more mafic liquid, the scavenged Fish Canyon phenocrysts have been corroded, and Fish Canyon plagioclase grains have euhedral overgrowths (50-100 mm thick) with more calcic compositions (An_{37-40}; Fig. 39d). Such textures are typical, following the entrainment of plagioclase phenocrysts in a more mafic magma (*i.e.,* Larsen et al, 1938; Feeley & Dungan, 1996). The mingled mafic inclusions show that the Fish Canyon magma interacted with a more mafic counterpart while both were still partly liquid.

8. Shallow batholith remobilization

The Fish Canyon magma displays a rich catalogue of textural and chemical information, from which its late magmatic evolution can be deduced. Evidence of thermal disequilibrium and remelting is provided by: (1) dissolution textures in quartz and feldspars, (2) the trace element signature of the glass that is compatible with remelting of a feldspar-rich

assemblage, (3) zoning profiles in hornblendes and plagioclases, and (4) coupled diffusion profiles across plagioclase-sanidine grain boundaries. All these record compositional changes consistent with a temperature increase near the time of eruption. Moreover, the near-solidus mineral assemblage and the different plutonic relics present in the magma, in particular the granodioritic xenoliths, indicate that the magma body crystallized to near-solidus conditions before being reheated and partially remelted by dissolution of quartz and feldspars. Finally, epitaxial plagioclase nucleation and growth on sanidine (Rapakivi textures), and multiple generations of sanidine as recorded by the Ba oscillatory zoning in the phenocrysts, support significant thermal disturbances prior to eruption. The magma body was thus apparently rejuvenated shortly before eruption, in response to a vigorous thermal event.

The heat engine responsible for these thermal fluctuations is inferred to be voluminous injections of mafic magma. Basaltic magmatism is well established as the main heat carrier in volcanically active areas (*e.g.*, Hildreth, 1981; Bergantz & Dawes, 1994), and interactions between the Fish Canyon magma and more mafic components have been recorded texturally, despite limited chemical mixing. Rare mafic enclaves exist in the upper part of the intracaldera Fish Canyon Tuff, which is inferred to represent the deepest part of the magma chamber. In addition to these enclaves, the Rapakivi textures also indicate mafic-felsic interaction. After much debate over the origin of these textures since the early work of Sederholm (1891), recent studies have isolated mafic-felsic magma interaction as the most important mechanism for Rapakivi development, especially for volcanic rocks (Hibbard, 1981; Bussy, 1990; Stimac & Wark, 1992; Wark & Stimac, 1992). Rapakivi growth does not necessitate important chemical mixing, but can occur during large-scale thermal underplating (Stimac & Wark, 1992). Calcic excursions in the rims of plagioclase phenocrysts suggest, nonetheless, that small amounts of less differentiated material may have been injected into the Fish Canyon magma, promoting short-term thermal and compositional perturbations leading to epitaxial plagioclase nucleation and growth.

Some of the mafic magma likely to have been responsible for the rejuvenation and remobilization of the Fish Canyon magma body apparently reached the surface. The Huerto Formation, which directly overlies the Fish Canyon Tuff, consists of ~200 km^3 of andesitic lavas and breccias exposed mainly in and around the southern La Garita caldera. $^{40}Ar/^{39}Ar$ ages on the three units of the Fish Canyon magmatic system, and on the Huerto andesite are indistinguishable (Parat, personal communication, 2001), indicating that the mafic lavas were erupted very shortly after the last Fish Canyon eruptions. The Huerto magma was the most primitive, and thus hottest, erupted from the central San Juan cluster (Riciputi et al., 1995).

Possibly analogous thermal oscillations have been documented in a Tertiary granite from Nevada (Robinson & Miller, 1999), through the observation of dissolution surfaces in accessory phases (zircon and sphene). In this plutonic example, mafic roots are preserved and suggest that mafic underplating caused the thermal oscillations. This grabbro-granite suite can be visualized as a congealed Fish Canyon-like magma chamber, providing complementary information to that conveyed by volcanism. The geometry and relative volume of the different magma batches suggest a schematic model for the Fish Canyon chamber shortly prior to onset of its eruptive cycle (Fig. 40). The near-absence of mixing between mafic and silicic magmas in the plutonic analogue also demonstrates that mafic-felsic interactions were largely limited to heat transfer. Small quantities of water can probably

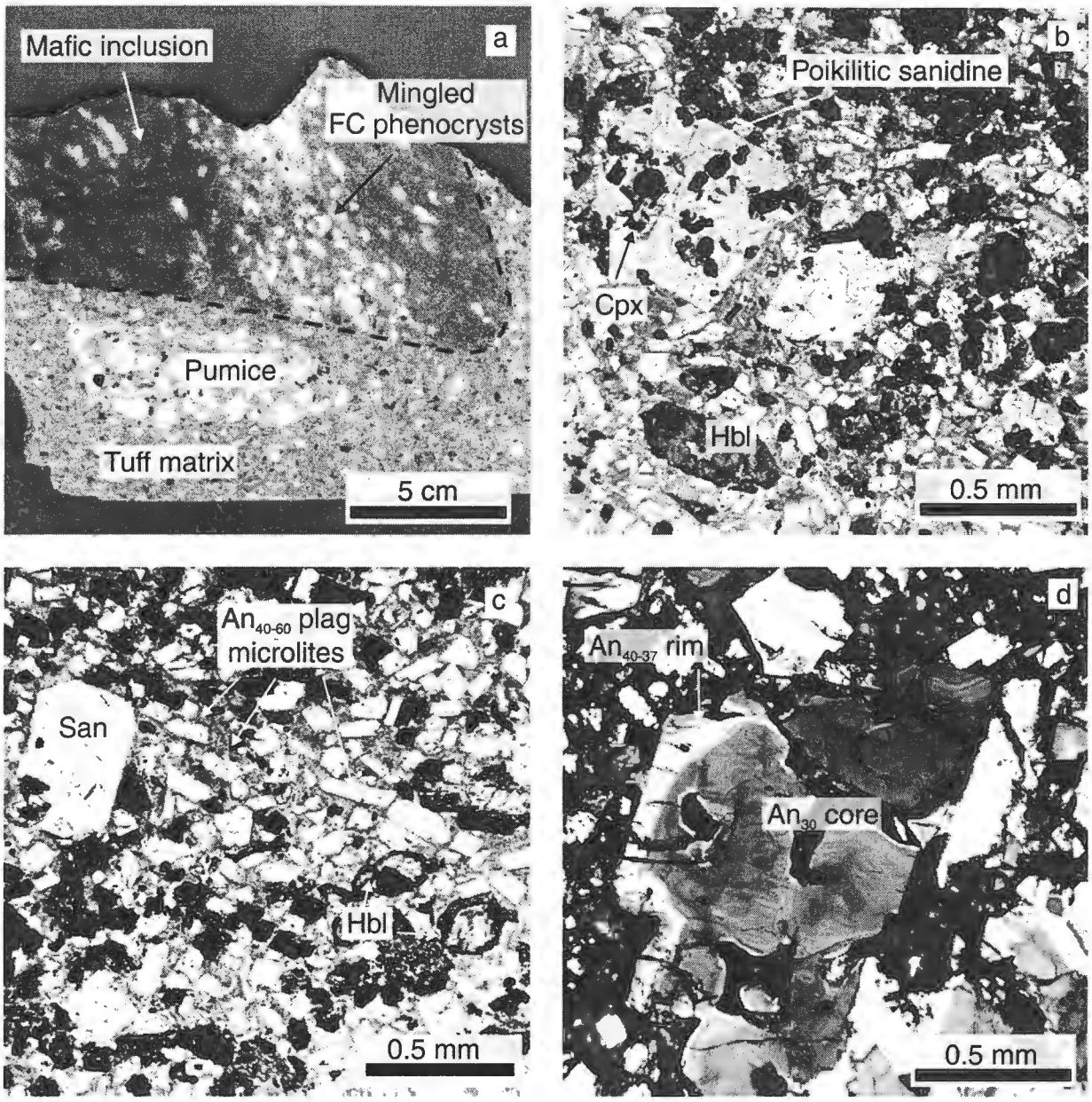

Figure 39: Hybrid andesite in the Fish Canyon magma (Intracaldera Fish Canyon Tuff; MLX QMI). (a) Macroscopic view of a mafic inclusion enclosed in the intracaldera Fish Canyon Tuff, showing a band of mingled Fish Canyon magma marked by a high concentration of phenocrysts. (b) The only occurrence of pyroxene in the Fish Canyon magmatic system, as inclusions in a poikilitic sanidine in the andesitic inclusion. These clinopyroxenes are also found free in the matrix and, like hornblendes, are always oxidized (QMI 2; plain polarized light). (c) Fine-grained texture showing sanidine (Or72-80), plagioclase microlites more calcic than the Fish Canyon phenocrysts, and hornblende with oxidation rims (QMI 2; plain polarized light). (d) Inversely zoned plagioclase in a mafic inclusion (QMI 2; crossed polars). The core has a composition around An30, similar to the Fish Canyon magma phenocrysts, but the rim is more calcic (~An40-37).

also diffuse across the mafic-silicic interface (Litvinovsky & Podladchikov, 1993), enhancing remelting in the overlying silicic body (Fig. 40).

8.1. Melting conditions

The close correspondence between the Fish Canyon glass composition and the quartz-plagioclase-alkali feldspar water-saturated eutectic at ~1.5-2 kb for a magma with normative An_{12-20} (Fig.

30) indicates that melting occurred at shallow depth. The temperature of 760 ± 30 °C determined for the Fish Canyon magma by Fe-Ti oxide thermometry (Johnson & Rutherford, 1989a) is consistent with the temperature of the eutectic at $X_{H2O} = 0.5$ (750 °C; Johannes & Holtz, 1996), the water partial pressure determined experimentally by Johnson & Rutherford (1989a). Under such conditions, shallow eutectic melting of a nearly crystalline magma chamber, due to heat flux from underplated mafic magma, provides a coherent scenario for the complex compositional and textural features of the Fish Canyon assemblage.

Determining whether the Fish Canyon magma body ever attained complete solidification prior to reheating and eruption is essential to understanding its melting regime. The holocrystalline co-magmatic xenoliths indicate that some parts of the magma chamber crystallized completely, but do not require that the whole chamber was ever entirely solidified. The preservation of multi-phase aggregates with solid-solid grain contacts, the remelting textures displayed by feldspars and quartz, and glass compositions with characteristics dominantly inherited from melting of feldspars, suggest that the whole magma batch reached a higher crystallinity than was recorded at eruption, but other evidence seems to require that interstitial liquid never completely disappeared. Water is essential for melting in the upper crust at temperatures below 800 °C. The dry solidus for the haplogranitic system is close to 1000 °C at 2 kb, whereas it decreases to 680 °C at water-saturated conditions (Johannes & Holtz, 1996). If the protolith had been completely solidified, the breakdown of hydrous phases to anhydrous minerals, particularly pyroxene, would be needed to provide water (dehydration melting), at least in the early stages (Clemens & Vielzeuf, 1987; Bergantz & Dawes, 1994). The textural evidence against hornblende and biotite breakdown and the absence of pyroxene in the system makes it highly unlikely that dehydration melting occurred during the remelting process and suggests instead that water-rich interstitial liquid was always present.

The water budget of the Fish Canyon magma also supports the inference that the magma never completely solidified. As crystallization proceeds, water has to leave the system, and completely solidifed magma, illustrated by the granodioritic xenoliths, would hold less than 1 wt. % H_2O, assuming 10-15 vol. % of hydrous phases, each containing less than 4 % water. If the erupted magma had completely crystallized at any stage, a large volume of water (2.5 to 3 wt. % H_2O) must have been transferred during reheating from the underlying crystallizing mafic magma to account for the inferred presence of 3-3.5 wt. % dissolved water immediately before eruption (Johnson & Rutherford, 1989a). Considering that the Huerto magmas contained ~2-4 wt. % H_2O (Askren *et al.*, 1991; Parat, 2001), a volume of mafic magma equivalent to the Fish Canyon magma would be required to supply enough water, even if H_2O were efficiently transferred from the underlying mafic reservoir. Thus, even though some external water was probably added, as suggested by the relatively high Cl in apatites (~1 wt %, twice as much as in the Bishop Tuff apatites; Parat, personal communication, 2001; Whitney & Stormer, 1985) and the growth of hornblende during reheating (Matthews et al., 1999), the quantities needed to promote partial remelting of a completely frozen Fish Canyon pluton seem unrealistically large.

9. Conclusion

The vast majority of silicic magmas are inferred to originate either by partial melting of a crustal source or progressive evolution of a more mafic magma (± variable amounts of crustal assimi-

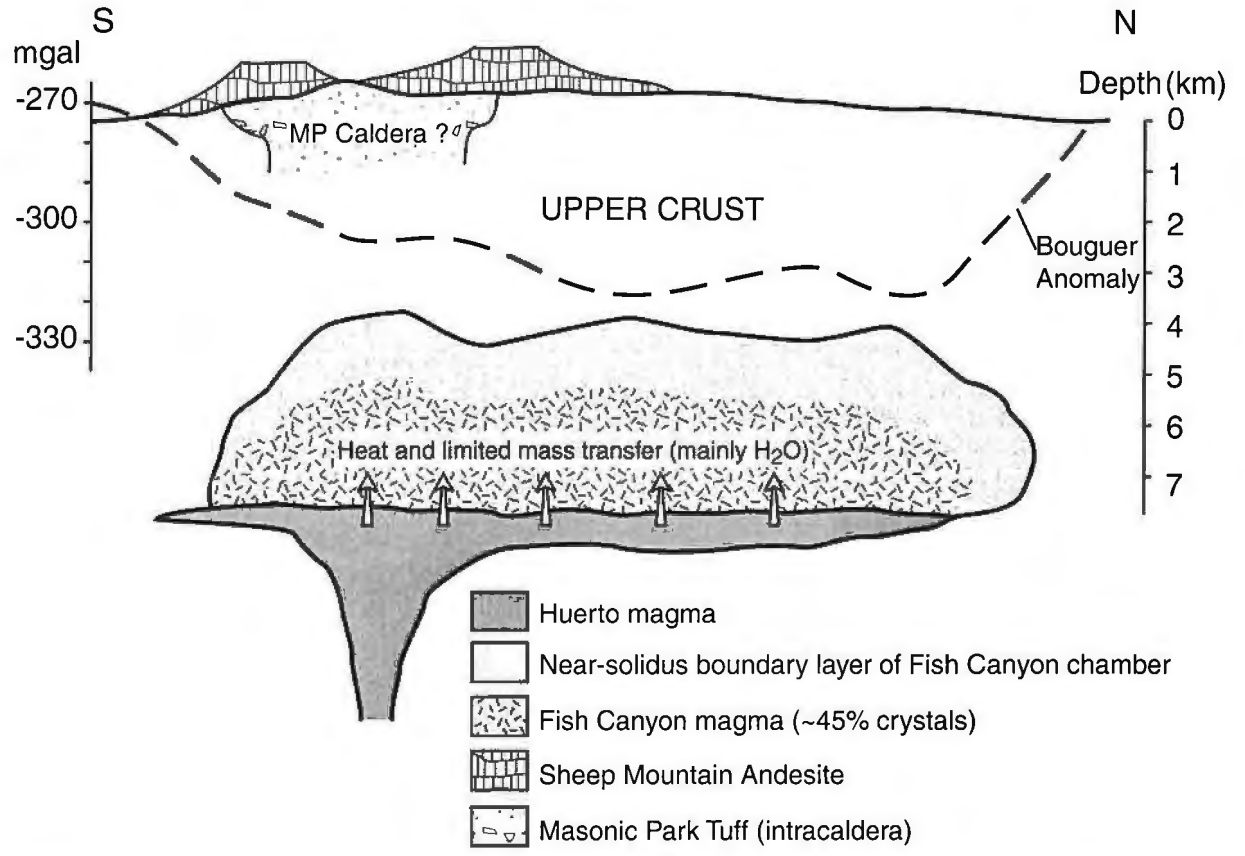

Figure 40: Schematic cross-section of the upper crust in the central San Juan region just prior to onset of the Fish Canyon cycle. Vertical exaggeration = 5 (horizontal extent of the chamber is close to 100 km). Thicknesses of the different magmatic components are highly speculative, and are constrained mainly by overall volume estimate of erupted magma, the area of the La Garita caldera, and barometric estimates from Fish Canyon hornblende. Asymmetry of Huerto intrusion with feeder in the south is based on field observations such as the focus of Huerto volcanism around the southern margin of the La Garita caldera (c.f. text and Lipman, 2000 for details) and on the shape of the Bouguer gravity anomaly (Plouff & Pakiser, 1972). It should be stressed that the negative Bouguer gravity anomaly is, however, a representation of the present day structure of the crust, and extrapolation to the time of the Fish Canyon cycle should be considered with caution. MP caldera = Masonic Park caldera, which formed approximately 600,000 years before the onset of Fish Canyon eruptions.

lation). In regions such as long-lived convergent continental margins, where the crust is characterized by elevated thermal gradients related to long term injection of mantle-derived magma, partial melting of the crust is a predictable consequence and is considered to be the primary mechanism responsible for generation of granitoid batholiths. Nonetheless, progressive evolution of mafic magma (± crustal contributions) is commonly cited as the process primarily responsible for generating ash-flow tuff magmas, particularly those which display compositional and thermal gradients (however, see Eichelberger *et al.*, 2000). Single stage differentiation of mafic magma is an unlikely mechanism for the 5,000 km^3 of Fish Canyon magma, which is one of the least compositionally heterogeneous large pyroclastic units. As the fraction of dacitic magma that can be derived by differentiation of primitive basalt is ~0.1-0.2, the volume of basalt parental to the Fish Canyon magma would be ~25,000-50,000 km^3, or ~60-125 % of the known erupted volume of the long-lived San Juan volcanic field.

As evolved magmas erupted from the Cen-

tral San Juan caldera cluster contain approximately equal proportions of crustal and mantle components (Riciputi *et al.*, 1995), they must be either the products of open system differentiation or they were generated by partial melting of crust which had been previously hybridized by injections of mantle derived magma. On the basis of textural and mineral chemical evidence presented in this paper, we favor a multi-stage model for the Fish Canyon magma wherein: (1) the protolith magma was first emplaced at shallow level following an origin by partial fusion at lower to mid-crustal depths, (2) the magma cooled to temperatures near the solidus, and (3) the magmatic system was rejuvenated by a shallow intrusion of mafic to andesitic magma that was in part later erupted as the post-caldera Huerto lavas. All available thermometric and barometric data derived from major element mineral and glass compositions in the Fish Canyon magma are consistent with pressures in the upper crust (2±0.5 kb) and temperatures less than ~100-120 °C above the water-saturated solidus at this pressure. Moreover, multiple independent lines of evidence, such as resorption textures, plagioclase mantling of sanidine (Rapakivi textures), trace element compositions of glasses, and mineral zoning profiles are all indicative of an up-temperature thermal evolution immediately prior to eruption. In addition, we have identified completely solid xenoliths which apparently represent fragments of the margin of the protolith.

Despite the occurrence of completely solid material, we stress that most of the erupted Fish Canyon magma represents remobilized portions of the protolith system that cooled to temperatures near the solidus but not below it. Remobilization occurred mainly through remelting of quartz and K-feldspar near the haplogranitic eutectic, as inverse zoning in plagioclase and hornblende implies that these minerals were growing as other phases melted. This counter-intuitive phenomenon of simultaneous crystallization and growth may in fact be a useful criteria to identify rejuvenating magmas, as it has been described in other systems that apparently followed similar up-temperature evolution paths (Matthews *et al.*, 1999; Murphy *et al.*, 2000). The absence of evidence for dehydration melting (hornblende and biotite grew while quartz and feldspars melted) is in concert with the prohibitive thermal and H_2O requirements for generating this volume of hydrous magma from a completely solid system. Although the enormous volume of the nearly homogeneous Fish Canyon magma requires that any thermal-mechanical model of its origin involves a substantial quantity of mafic magma at some stage, the model that we propose demands the lowest amount of mafic input of any plausible scenario. This general mechanism has been cited as the origin of volumetrically small quantities (<5 km^3) of intermediate to silicic magma associated with large calderas (Wolff & Gardner, 1995) and active arc volcanoes (Matthews *et al.*, 1999; Murphy *et al.*, 2000), as well as for ignimbrites of significant volume (Keller, 1970; Mahood, 1990). Although such a model has not been suggested previously for Monotonous Intermediates, this also may be the primary explanation for these voluminous and weakly zoned tuffs which, like the Fish Canyon magma, often have the characteristics of "erupted batholiths" (crystal-rich dacites, near-solidus mineral assemblages) and are located in convergent margin settings (Francis *et al.*, 1989; Lindsay *et al.*, 2001).

A recent analytical treatment of the thermal evolution of partly solidified magma chambers (Koyaguchi & Kaneko, 1999) demonstrates that near-solidus magma chambers are capable of remaining in the upper crust for long periods of time as crystal mushes. Cooling by convection is rapid, but as soon as the magma body becomes too crystalline to convect, conduction prevails and cooling rates decrease dramatically. Residence times

in the range of 10^5 years are inferred for such crystal mush zones, once cooling is controlled by conduction. The longevity of these highly crystalline magma bodies in the upper crust, and their potential for being reactivated and remobilized by mafic input to generate large volcanic eruptions, makes them potentially hazardous, as they may be capable of rapid evacuation of thousands of cubic kilometers of rejuvenated magma.

The eruption age of the Fish Canyon Tuff has been determined from $^{40}Ar/^{39}Ar$ dating at 28.0 Ma (Renne *et al.*, 1998; Villeneuve *et al.*, 2000), whereas the preponderance of U/Pb ages on Fish Canyon zircons are consistently older, at 28.4-28.5 Ma (Oberli *et al.*, 1990; Schmitz & Bowring, in press; our unpublished data). This discrepancy may reflect inherent intercalibration problems between U-Pb geochronology and the $^{40}Ar/^{39}Ar$ method, whose ages suffer from incertainties in ^{40}K decay constant and in $^{40}Ar^*/^{40}K$ of the mineral standard (Min *et al.*, 2000). However, a recent cross calibration of the two isotopic systems (Villeneuve *et al.*, 2000) suggests that the difference of 400,000 years between zircon U-Pb ages and sanidine $^{40}Ar/^{39}Ar$ ages may not be an analytical artifact and could thus constrain the timing of magmatic events that ultimately produced the Fish Canyon eruptions. Further investigations on Fish Canyon zircons are underway, in the hope of constraining more precisely the rate at which this magmatic system was reactivated.

Acknowledgments

The help of G.F. Marriner and M.F. Thirlwall (XRF; University of London at Royal Holloway and Bedford New College), N. Rodgers (INAA; Open University), R. Hinton (University of Edinburgh), F. Bussy, (electron microprobe; University of Lausanne), F. Capponi, (XRF; University of Geneva), J-M Boccard (Thin section preparation; University of Geneva) and J. Metzger (computer-aided drawing; University of Geneva) was greatly appreciated. This work benefited from numerous discussion with colleagues from the University of Geneva and other institutions. Thanks to the insight of B. Evans, who first mentioned that the complex Fish Canyon sanidines could be related to Rapakivi textures. Costs of fieldwork were supported by the USGS Volunteer Program and by Swiss FNRS grant # 20-49730.96, which also provided funding for laboratory analyses.

References

Anderson, A.T., Davis, A.M., and Fangqiong, L. (2000) Evolution of the Bishop Tuff rhyolitic magma based on melt and magnetite inclusions and zoned phenocrysts. Journal of Petrology, 41(3), 449-473.

Anderson, J.L., and Smith, D.R. (1995) The effects of temperature and f_{O2} on the Al-in-hornblende barometer. American Mineralogist, 80, 549-559.

Arth, J.G. (1976) Behavior of trace elements during magmatic processes: a summary of theoretical models and their applications. Journal of Research of the U.S. Geological Survey, 4, 41-47.

Askren, R.R., Whitney, J.A., and Roden, M.F. (1991) Petrology and geochemistry of the Huerto Andesite, San Juan volcanic field, Colorado. Contributions to Mineralogy and Petrology, 107, 373-386.

Bachmann, O., Dungan, M.A., and Lipman, P.W. (2000) Voluminous lava-like precursor to a major ash-flow tuff: low-column pyroclastic eruption of the Pagosa Peak Dacite, San Juan Volcanic field, Colorado. Journal of Volcanology and Geothermal Research, 98, 153-171.

Backlund, H.G. (1938) The problems of the rapakivi

granites. Journal of Geology, 46, 339-396.

Bacon, C.R. (1992) Partially melted granodiorite and related rocks ejected from Crater Lake caldera, Oregon. Transactions of the Royal Society of Edimburgh: Earth Sciences, 83, 27-47.

Bergantz, G.W., and Dawes, R. (1994) Aspects of magma generation and ascent in continental lithosphere. in Magmatic systems, edited by M. P. Ryan, Academic, San Diego, California, 291-317.

Bernal, J.D., and Mackay, A.L. (1965) Topotaxy. TMPM, 10, 331-340.

Best, M.G., and Christiansen, E.H. (1997) Origin of broken crystals in ash-flow tuffs. Geological Society of America Bulletin, 109, 63-73.

Blundy, J.D., and Holland, T.J.B. (1990) Calcic amphibole equilibria and a new amphibole-plagioclase geothermometer. Contributions to Mineralogy and Petrology, 104(2), 208-224.

Blundy, J.D., and Holland, T.J.B. (1992) «Calcic amphibole equilibria and a new amphibole-plagioclase geothermometer»: Reply to the comments of Hammarstrom and Zen, and Rutherford and Johnson. Contributions to Mineralogy and Petrology, 111, 269-272.

Blundy, J.D., and Wood, B.J. (1991) Crystal-chemical control on the partitioning of Sr and Ba between plagioclase feldspar, silicate melts, and hydrothermal solutions. Geochimica et Cosmochimica Acta, 55, 193-209.

Brown, S.J.A., and Fletcher, I.R. (1999) SHRIMP U-Pb dating of the preeruption growth history of zircons from the 340 ka Whakamaru Ignimbrite, New Zealand: Evidence for >250 k.y. magma residence times. Geology, 27(11), 1035-1038.

Bussy, F. (1990) The rapakivi texture of feldspars in a plutonic mixing environment; a dissolution-recrystallization process? Granite; proceedings of the symposium celebrating the 70th birthday of W. S. Pitcher. Geological Journal, 25(3-4), 319-324.

Clemens, J.D., and Vielzeuf, D. (1987) Constraints on melting and magma production in the crust. Earth and Planetary Science Letters, 86, 287-306.

Colucci, M.T., Dungan, M.A., and Fergusson, K.M. (1991) Precaldera lavas of the southeast San Juan volcanic field: Parent magmas and crustal interactions. Journal of Geophysical Research, 96(B8), 13,413-13,434.

Costa, F. (2001) The petrology and geochemistry of diverse crustal xenoliths, Tatara-San Pedro Volcanic Complex, Chilean Andes. Department of Mineralogy, p. 120. Geneva.

Davies, G.R., and Halliday, A.N. (1998) Development of the Long Valley rhyolitic magma system: Strontium and neodymium isotope evidence from glass and individual phenocrysts. Geochimica et Cosmochimica Acta, 62(21/22), 3561-3574.

de Silva S. L. (1989) The origin and significance of crystal-rich inclusions in pumices from two Chilean ignimbrites. *Geological Magazine* 126, 159-175.

Davis, J.M., Elston, W.E., and Hawkesworth, C.J. (1993) Basic and intermediate volcanism of the Mogollon-Datil volcanic field: implications for mid-Tertiary tectonic transitions in southwestern New Mexico, USA. Geological Society Special Publications, 76, 469-488.

de Silva, S.L. (1991) Styles of zoning in the central Andean ignimbrites: Insights into magma chamber processes. In Harmon, R.S., Rapela, C.W (eds): Andean magmatism and its tectonic setting, Geological Society of America Special Paper, 265, 233-243.

Dunbar, N.W., and Hervig, R.L. (1992) Volatile and trace element composition of melt inclusions from the lower Bandelier Tuff: Implications for magma chamber processes and eruptive style. Journal of Geophysical Research, 97(B11), 15151-15170.

Dymek, R.F. (1983) Titanium, aluminium and interlayer

cation substitutions in biotite from high-grade gneisses, West Greenland. American Mineralogist, 68, 880-899.

Eichelberger, J.C., Chertkoff, D.G., Dreher, S.T., and Nye, C.J. Magmas in collision; rethinking chemical zonation in silicic magmas. Geology, 28(7), 603-606.

Feeley, T.C., and Dungan, M.A. (1996) Compositional and dynamic controls on mafic-silicic magma interactions at continental arc volcanoes: Evidence from Cordôn El Guadal, Tatara-San Pedro Complex, Chile. Journal of Petrology, 37(6), 1547-1577.

Francis, P.W., Sparks, R.S.J., Hawkesworth, C.J., Thorpe, R.S., Pyle, D.M., Tait, S.R., Mantovani, M.S., and McDermott, F. (1989) Petrology and geochemistry of the Cerro Galan caldera, northwest Argentina. Geological Magazine, 126(5), 515-547.

Gardner, A., and McPhie, J. (1999) Partially melted lithic megablocks in the Yardea Dacite, Gawler Range Volcanics, Australia: implications for eruption and emplacement mechanisms. Bulletin of Volcanology, 61, 396-410.

Grove, T.L., Kinzler, R.J., Baker, M.B., Donnelly-Nolan, J.M., and Lesher, C.E. (1988) Assimilation of granite by basaltic magma at Burnt Lava flow, Medicine Lake volcano, northern California: Decoupling of heat and mass transfer. Contributions to Mineralogy and Petrology, 99, 320-343.

Grunder, A.L., and Boden, D.R. (1987) Comment on «... magmatic conditions of the Fish Canyon Tuff, central San Juan volcanic field, Colorado» by Whitney & Stormer (1985). Journal of Petrology, 28, 737-746.

Halliday, A.N. (1990) Reply to comment of R.S.J. Sparks, H.E. Huppert, and C.J.N. Wilson on «Evidence for long residence times of rhyolitic magma in the Long Valley magmatic system: the isotopic record in precaldera lavas of Glass Mountain». Earth and Planetary Science Letters, 99, 390-394.

Halliday, A.N., Davidson, J.P., Hildreth, W., and Holden, P. (1991) Modeling the petrogenesis of high Rb/Sr silicic magmas. Chemical Geology, 92, 107-114.

Halliday, A.N., Mahood, G.A., Holden, P., Metz, J.M., Dempster, T.J., and Davidson, J.P. (1989) Evidence for long residence times of rhyolitic magma in the Long Valley magmatic system: the isotopic record in precaldera lavas of Glass Mountain. Earth and Planetary Science Letters, 94, 274-290.

Hammarstrom, J.M., and Zen, E.-a. (1986) Aluminium in hornblende: An empirical igneous geobarometer. American Mineralogist, 71, 1297-1313.

Hammarstrom, J.M., and Zen, E.-a. (1992) Discussion of Blundy and Holland's (1990) «Calcic amphibole equilibria and a new amphibole-plagioclase geothermometer». Contributions to Mineralogy and Petrology, 111, 264-266.

Hibbard, M.J. (1981) The magma mixing origin of mantled feldspars. Contribution to Mineralogy and Petrology, 76, 158-170.

Hildreth, W. (1981) Gradients in silicic magma chambers: Implications for lithospheric magmatism. Journal of Geophysical Research, 86(B11), 10153-10192.

Holland, T., and Blundy, J. (1994) Non-ideal interactions in calcic amphiboles and their bearing on amphibole-plagioclase thermometry. Contributions to MIneralogy and Petrology, 116, 433-447.

Hollister, L.S., Grissom, G.C., Peters, E.K., Stowell, H.H., and Sisson, V.B. (1987) Confirmation of the empirical correlation of Al in hornblende with pressure of solidification of calc-alkaline plutons. American Mineralogist, 72, 231-239.

Housh, T.B., and Luhr, J.F. (1991) Plagioclase-melt

equilibria in hydrous systems. American Mineralogist, 76, 477-492.

Icenhower, J., and London, D. (1996) Experimental partitioning of Rb, Cs, Sr, and Ba between alkali feldspar and peraluminous melt. American Mineralogist, 81, 719-734.

Johannes, W., and Holtz, F. (1996) Petrogenesis and experimental petrology of granitic rocks. Springer-Verlag, 335 p.

Johnson, M., and Rutherford, M. (1989a) Experimentally determined conditions in the Fish Canyon Tuff, Colorado, magma chamber. Journal of Petrology, 30, 711-737.

Johnson, M.C., and Rutherford, M.J. (1989b) Experimental calibration of the aluminum-in-hornblende geobarometer with application to Long Valley Caldera (California) volcanic rocks. Geology, 17, 837-841.

Kaczor, S.M., Hanson, G.N., and Peterman, Z.E. (1988) Disequilibrium melting of granite at the contact with basic plug: A geochemical and petrographic study. Journal of Geology, 96, 61-78.

Keller, J. (1970) Origin of rhyolites by anatectic melting of granitic crustal rocks; the example of rhyolitic pumice from the island of Kos (Aegean sea). Bulletin of Volcanology, 33(3), 942-959.

Knesel, K.M., and Davidson, J.P. (1997) The origin and evolution of large-volume silicic magma systems: Long Valley caldera. International Geology Reviews, 39, 1033-1052.

Knesel, K.M., and Davidson, J.P. (1999) Sr systematics during melt generation by intrusion of basalt into continental crust. Contribution to Mineralogy and Petrology, 136, 285-295.

Leake, B.E., Wooley, A.R., Arps, C.E.S., Birch, W.D., Gilbert, M.C., Grice, J.D., Hawthrone, F.C., Kato, A., Kisch, H.J., Krivovichev, V.G., Linthout, K., Laird, J., Mandarino, J.A., Maresch, W.V., Nickel, E.H., Rock, N.M.S., Schumacher, J.C., Smith, D.C., Stephensen, N.C.N., Ungaretti, L., Whittaker, E.J.W., and Youzhi, G. (1997) Nomenclature of amphiboles: Report of the Subcommitee on Amphiboles of the International mineralogical Association, Commission on New Minerals and Mineral Names. American Mineralogist, 82, 1019-1037.

Lindsay, J.M., Schmitt, A.K., Trumbull, R.B., De Silva, S.L., Siebel, W., and Emmermann, R. (2001) Magmatic evolution of the La Pacana caldera system, Central Andes, Chile: Compositional variation of two cogenetic, large-volume felsic ignimbrites. Journal of Petrology, 42(3), 459-486.

Lipman, P.W. (1967) Mineral and chemical variations within an ash-flow sheet from Aso caldera, South Western Japan. Contributions to Mineralogy and Petrology, 16, 300-327.

Lipman, P.W. (1975) Evolution of the Platoro caldera complex and related volcanic rocks, southeastern San Juan mountains, Colorado. U.S. Geological Survey Professional Paper 852, 128 p.

Lipman, P.W., Doe, B., and Hedge, C. (1978) Petrologic evolution of the San Juan volcanic field, Southwestern Colorado: Pb and Sr isotope evidence. Geological Society of America Bulletin, 89, 59-82.

Lipman, P.W., Dungan, M.A., and Bachmann, O. (1997) Comagmatic granophyric granite in the Fish Canyon Tuff, Colorado: Implications for magma-chamber processes during a large ash-flow eruption. Geology, 25(10), 915-918.

Lipman, P.W., Dungan, M.A., Brown, L.L., and Deino, A.L. (1996) Recurrent eruption and subsidence at the Platoro Caldera complex, southeastern San Juan volcanic field, Colorado; new tales from old tuffs. Geological Society of America Bulletin, 108, 1039-1055.

Lipman, P.W., Protska, H.J., and Christiansen, R.L. (1972) Cenozoic volcanism and plate-tectonic

evolution of western United States, I, Early and middle Cenozoic. Philosophical Transactions of the Royal Society of London (serie A), 271, 217-248.

Lipman, P.W. (1988) Evolution of silicic magma in the upper crust. The mid-Tertiary Latir Volcanic field and its cogenetic granitic batholith, northern New Mexico, USA. Transactions of the Royal Society of Edimburgh, 79, 265-288.

Lipman, P.W., Bogatikov, O.A., Tsvetkov, A.A., Gazis, C., Gurbanov, A.G., Hon, K., Koronovsky, N.V., Kovalenko, V.I., and Marchev, P. (1993) 2.8-Ma ash-flow caldera at Chegem River in the northern Caucasus Mountains (Russia), contemporaneous granites, and associated ore deposits. Journal of Volcanology and Geothermal Research, 57, 85-124.

Litvinovsky, B.A., and Podladchikov, Y.Y. (1993) Crustal anatexis during the influx of mantle volatiles. Lithos, 30(2), 93-107.

Lowenstern, J.B., Clynne, M.A., and Bullen, T.D. (1997) Co-magmatic A-type granophyre and rhyolite from the Alid volcanic center, Eritrea, Northwest Africa. Journal of Petrology, 38(12), 1707-1721.

Mahood, G., and Hildreth, W. (1983) Large partition high-K calc-alkaline andesite in an intracontinental setting, San Juan volcanic field, Colorado, U.S.A. Department of Mineralogy, p. 164. Geneva.

Plouff, D., and Pakiser, L.C. (1972) Gravity study in the San Juan Mountains, Colorado. US Geological Survey Professional Paper, 800, B183-B190.

Poli, S., and Schmidt, M.W. (1992) A comment on Blundy and Holland's (1990) «Calcic amphibole equilibria and a new amphibole-plagioclase geothermometer» by J.D. Blundy and T.J.D. Holland. Contributions to Mineralogy and Petrology, 111, 273-278.

Reid, M.R., and Coath, C.D. (2000) In situ U-Pb ages of zircons from the Bishop Tuff: No evidence for long crystal residence times. Geology, 28(5), 443-446.

Reid, M.R., Coath, C.D., Harrison, T.M., and McKeegan, K.D. (1997) Prolonged residence times for the youngest rhyolites associated with Long Valley Caldera: ^{230}Th-^{238}U microprobe dating of young zircons. Earth and Planetary Science Letters, 150, 27-39.

Renne, P.R., Swisher, C.C., Deino, A.L., Karner, D.B., Owens, T.L., and DePaolo, D.J. (1998) Intercalibration of standards, absolute ages and uncertainties in (super 40) Ar/ (super 39) Ar dating. Chemical Geology, 145, 117-152.

Riciputi, L.R., Johnson, C.M., Sawyer, D.A., and Lipman, P.W. (1995) Crustal and magmatic evolution in a large multicyclic caldera complex: isotopic evidence from the central San Juan volcanic field. Journal of Volcanology and Geothermal Research, 67, 1-28.

Robinson, D.M., and Miller, C.F. (1999) Record of magma chamber processes preserved in accessory mineral assemblages, Aztec Wash pluton, Nevada. American Mineralogist, 84, 1346-1353.

Rutherford, M.J., and Devine, J.D. (1988) The May 18, 1980, eruption of Mount st. Helens:3. Stability and chemistry of amphibole in the magma chamber. Journal of Geophysical Research, 93, 11949-11959.

Rutherford, M.J., and Johnson, M.C. (1992) Comment on Blundy and Holland's (1990) «Calcic amphibole equilibria and a new amphibole-plagioclase geothermometer». Contributions to Mineralogy and Petrology, 111, 266-268.

Schmidt, M.W. (1992) Amphibole composition in tonalite as a function of pressure; an experimental calibration of the Al-in-hornblende barometer. Contributions to Mineralogy and Petrology, 110(2-3), 304-310.

Schmitz, M.D., and Bowring, S.A. (in press) U-Pb zircon and titanite systematics of the Fish Canyon Tuff. an assessment of high-precision U-Pb geochronology and its application to young

volcanic rocks. Geochimica et Cosmochimica Acta.

Sederholm, J.J. (1891) Uder die finnländischen Rapakivigesteine. Tschermak's Mineralogische und Petrographische Mitteilungen, 12, 1-31.

Smith, J.V. (1974) Feldspar Minerals: chemical and textural properties. 690 p. Springer-Verlag.

Sparks, R.S.J., Huppert, H.E., and Wilson, C.J.N. (1990) Comment on «Evidence for long residence times of rhyolitic magma in the Long Valley magmatic system: the isotopic record in precaldera lavas of Glass Mountain» by A.N. Halliday, G.A. Mahood, P. Holden, J.M. Metz, T.J. Dempster, J.P. Davidson,. Earth and Planetary Science Letters, 99, 387-389.

Spear, F.S. (1981) An experimental study of hornblende stability and compositional variability in amphibolite. American Journal of Science, 281, 697-734.

Steven, T.A. (1975) Mid-Tertiary volcanic field in the southern Rocky Mountains. Geol Soc Am Mem, 144, 75-94.

Steven, T.A., and Lipman, P.W. (1976) Calderas of the San Juan volcanic field, southwestern Colorado. U.S. Geological Survey Professional Paper, 958, 1-35.

Stimac, J.A., and Wark, D.A. (1992) Plagioclase mantles on sanidine in silicic lavas, Clear Lake, California; implications for the origin of rapakivi texture. Geological Society of America Bulletin, 104(6), 728-744.

Stormer, J.C., Jr., and Whitney, J.A. (1985) Two feldspar and iron-titanium oxide equilibria in silicic magmas and the depth of origin of large volume ash-flow tuffs. American Mineralogist, 70, 52-64.

Streck, M.J., and Grunder, A.L. (1997) Compositional gradients and gaps in high-silica rhyolites of the Rattlesnake Tuff, Oregon. Journal of Petrology, 38(1), 133-163.

Taylor, S.R., and McLennan, S.M. (1985) The continental crust: Its composition and evolution. 312 p. Balckwell, Cambridge, Mass.

Thomas, W.M., and Ernst, W.G. (1990) The aluminium content of hornblende in calc-alkaline granitic rocks: a mineralogic barometer calibrated experimentally to 12 kbars. In R.J. Spencer and I-M. Chou, eds., Fluid-mineral interactions: a tribute to H.P. Eugster. Geochemical Society Special Publications, 2, 59-63.

Tuttle, O.F., and Bowen, N.L. (1958) Origin of granite in light of experimental studies in the system NaAlSi3O8-KAlSi3O8_SiO2. Geological Society of America Memoir, 74, 153 pp.

van den Bogaard, P., and Schirnick, C. (1995) $^{40}Ar/^{39}Ar$ laser probe ages of Bishop Tuff quartz phenocrysts substantiate long-lived silicic magma chamber at Long Valley, United States. Geology, 23(8), 759-762.

Villeneuve, M., Sandeman, H.A., and Davis, W.J. (2000) A method for intercalibrations of U-Th-Pb and $^{40}Ar/^{39}Ar$ ages in the Phanerozoic. Geochimica et Cosmochimica Acta, 64(23), 4017-4030.

Vorma, A. (1971) Alkali feldspars of the Wiborg Massif in southeastern Finland. Bulletin de la Commission Géologique Finlande, 246, 1-72.

Vyhnal, C.R., McSween, H.Y., and Speer, J.A. (1991) Hornblende chemistry in southern Appalachian granitoids: Implications for aluminium hornblende thermobarometry and magmatic epidote stability. American Mineralogist, 76, 176-188.

Wahl, W. (1925) Die Gesteine des Wiborger Rapakiwigebietes. Fennia, 45(20), 1-127.

Walker, G.P.L. (1972) Crystal concentration in ignimbrites. Contributions to Mineralogy and Petrology, 36, 135-146.

Wark, D.A., and Stimac, J.A. (1992) Origin and mantled (rapakivi) feldspars; experimental evidence of a dissolution- and diffusion-controlled

mechanism. Contributions to Mineralogy and Petrology, 111(3), 345-361.

Watson, E.B. (1982) Basalt contamination by continental crust: Some experiments and models. Contribution to Mineralogy and Petrology, 56, 73-87.

Whitney, J.A., and Stormer, J.C., Jr. (1985) Mineralogy, petrology, and magmatic conditions from the Fish Canyon Tuff, central San Juan volcanic field, Colorado. Journal of Petrology, 26, 726-762.

Wolff, J.A., and Gardner, J.N. (1995) Is the Valles Caldera entering a new cycle of activity? Geology (Boulder), 23(5), 411-414.

Zellmer, G.F., Blake, S., Vance, D., Hawkesworth, C., and Turner, S. (1999) Plagioclase residence times at two island arc volcanoes (Kameni Islands, Santorini and Soufrière, St. Vincent) determined by Sr diffusion systematics. Contributions to Mineralogy and Petrology, 136, 345-357.

Appendix 1: $^{40}Ar/^{39}Ar$ and U-Pb geochronology on the Fish Canyon magmatic system, San Juan Volcanic field, Colorado: timing of eruptions and petrologic implications of age discrepancies between the different minerals of the Fish Canyon magma

Foreword

The reason for which this part of the study is included in the appendix is that U-Pb analyses are still in progress, and more work needs to be done to answer the questions raised by this geochronological study. The data is, nonetheless, reported, following a short review of the abundant literature in relation to Fish Canyon geochronology. At the end, a list of the main points and questions is included, to hopefully help to clarify the intricate results and provide a base for discussion.

1. Introduction

The evolution of caldera-forming volcanic systems is poorly understood due to the long recurrence intervals between large eruptions. The time scales involved pose great difficulty for addressing the critical question of whether modern day systems are waning or reawakening, thus hindering crucial predictions of destructive climactic eruptions. Probably one of the best tools available for examining the state of the underlying crustal column is the study of the smaller units erupted in between the major caldera-forming events (Wolff and Gardner, 1995). Documenting the petrology and chronology of these satellite eruptions in ancient settings is a key to understanding and predicting the behavior of modern day systems.

The Fish Canyon magmatic cycle, discussed in this paper, consists of both a voluminous ignimbrite and two well preserved co-magmatic satellite eruptions, emplaced shortly prior to and after the main unit from the same homogeneous magma chamber. Determining the time gaps between units of this eruptive sequence is crucial, in particular since the precursory eruption provoked intense syn-eruptive faulting and possibly triggered the caldera-forming event (Bachmann et al., 2000). The main goal of this study was to resolve whether it was possible to distinguish the eruption ages of the three units using $^{40}Ar/^{39}Ar$ and U-Pb geochronology, in order to constrain better the rate at which these systems develop.

Dating the Fish Canyon magma is not an ordinary geochronological study. Since it was proposed as a neutron fluence monitor (standard) for $^{40}Ar/^{39}Ar$ dating (Cebula et al., 1986), rarely has a unit received as much attention from the geochronological community as the Fish Canyon Tuff. $^{40}Ar/^{39}Ar$ geochronology is a relative dating method in which the accuracy is limited by the accuracy with which the age of the fluence monitor is known. For this reason, the best possible estimate for the eruption age of Fish Canyon Tuff has been investigated in a number of ways, including: (i) dating the different Fish Canyon Tuff minerals using several decay schemes, such as K-Ar on biotite and hornblende (Lanphere and Baadsgaard, 1997), Rb-Sr on plagioclase, sanidine and biotite (Lanphere and Baadsgaard, 1997), U-Pb on zircons (Oberli et al., 1990; Lanphere and Baadsgaard, 1997; Schmitz and Bowring, 1999) and $^{40}Ar/^{39}Ar$ ages of biotite and sanidine using primary standards dated by K-Ar (Lanphere and Baadsgaard, 1997; Renne et al., 1998b); (ii) reconciliation of age determination on plutonic units acquired by absolute U-Pb zircon ages, generally regarded as accurate, and $^{40}Ar/^{39}Ar$ ages, to reach the best value for the Fish Canyon sanidine, which was used as the $^{40}Ar/^{39}Ar$ fluence monitor (Villeneuve et al., 1998); (iii) $^{40}Ar/^{39}Ar$ dating of Fish Canyon Tuff sanidine relative to a fluence monitor whose age is known *a priori* (79AD eruption of Vesuvius; Renne and Min, 1998); and (iv) intercalibration of published $^{40}Ar/^{39}Ar$ ages polarity transitions based on the Fish canyon sanidine with the astronomical time scale (Renne et al., 1994). The results remain partly unsatisfying. Precision is not sufficient when using unequivocal reference points (79AD eruption of Vesuvius; ~5% error) or difficult to evaluate in the case of the orbital tuning for the astronomical time scale. Consensus on the ages of primary $^{40}Ar/^{39}Ar$ fluence monitors dated by K-Ar has not yet been reached (Lanphere and Dalrymple, 2000; Renne et al., 1998b), precluding unambiguous absolute age determination of unknown samples by $^{40}Ar/^{39}Ar$ geochronology. Finally, the ages obtained by the other geochronological methods do not seem to converge towards a precise value, with a total interlaboratory range in age over 3.5 % (Lanphere and Baadsgaard, 1997; Oberli et al., 1990; Schmitz and Bowring, 1999). Although this

absolute age determination is important for the future of $^{40}Ar/^{39}Ar$ geochronology, our first-order objective was not to participate in this debate. The ages obtained in this study were all calculated with respect to the age of the Taylor Creek Rhyolite sanidine (28.34 Ma) as published by Renne et al. (1998b), which suffers from the same uncertainty as all $^{40}Ar/^{39}Ar$ standards. We concentrated, rather, on the relative differences between our samples, avoiding dependence on the absolute age determination, to document the internal complexities of this important caldera-forming cycle.

In addition to documenting the chronology of eruptions, $^{40}Ar/^{39}Ar$ and U-Pb dating of several mineral phases from the same sample (Fish Canyon Tuff) were performed to assess whether the ages were consistent between them. This question of age coherence among the different phases of the same unit was raised by the petrologic reinvestigation of the Fish Canyon magma (Bachmann et al., submitted), which concludes that the batholithic-scale magma body developed through repeated thermal oscillations and was ultimately erupted upon a last reheating event after having cooled to near-solidus conditions. Minerals experiencing a relatively cold period followed by a reheating event may record a complex isotopic memory. Existing data on Fish Canyon zircons already points in this direction as U-Pb ages reported by Oberli et al. (1990) and Schmitz and Bowring (1999) seem slightly older (~0.4 Ma) than the sanidine ages.

2. Geological setting

The Fish Canyon magmatic system belongs to the voluminous mid-Tertiary ignimbrite sequence of the San Juan volcanic field in present day Colorado. This episode of voluminous explosive eruptions, consisting of at least 17 large ignimbrites, lasted from approximately 29 to 26 Ma, following a period of more than 5 Ma of intense andesitic activity (Lipman et al., 1978; Steven and Lipman, 1976). The Fish Canyon magmatic system comprises three volcanologically distinct units, emplaced in the central part of the field around 28 Ma ago. These three separate units show contrasting eruptive styles but tapped into the same magma chamber, as they are mineralogically and compositionally identical. They represent three pulses of activity from the same shallow batholithic-scale magma chamber (Bachmann et al., 2000). The dominant volume is formed by the Fish Canyon Tuff, the largest documented ignimbrite (>5000 km^3) in the volcanic record. It erupted as a highly fragmented ash-flow containing a relatively low pumice concentration and formed a large caldera, the La Garita caldera, with a present day surface exceeding 2500 km^2. The absence of welding breaks in the outflow or intracaldera exposures suggests a rapid emplacement, probably on the order of days. Based on decompression-induced granophyre crystallization around phenocrysts of the northern intracaldera tuff and the segmented aspect of the La Garita caldera, the eruption is thought to have started from the south and propagated northward (Lipman et al., 1997).

This vast ignimbrite was preceded by the Pagosa Peak Dacite, a poorly fragmented 200 km^3 deposit located around the southern margin of the La Garita caldera (Figure 1). This unusual pyroclastic unit is thought to have resulted from a low-energy fountaining of Fish Canyon magma, probably as a consequence of rapid syn-eruptive gas escape from the ascending magma (Bachmann et al., 2000). Although a few welding breaks can be observed locally, this unit was also rapidly emplaced as most of the exposures are glassy and sections of more than 1 km thick remained hot enough to flow rheomorphically (Bachmann et al., 2000). The contact between the Pagosa Peak Dacite and the Fish Canyon Tuff can be observed

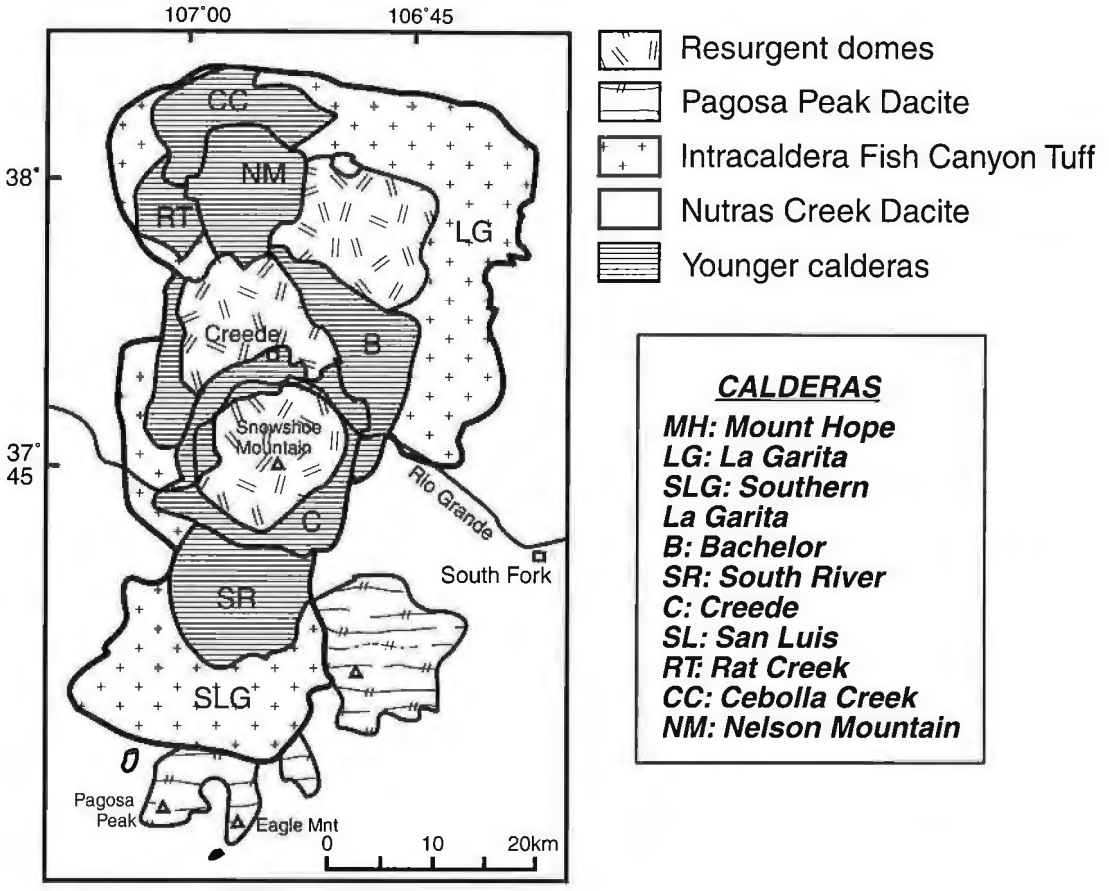

Figure 1: Map of the central San Juan caldera cluster, showing the location of the three units of the Fish Canyon magmatic system.

in a few localities, where the Fish Canyon Tuff rests directly on the top of the Pagosa Peak Dacite. Where the contact can be observed, neither erosion nor sediment deposition took place between the two eruptions, suggesting a relatively short time gap. The base of the Fish Canyon Tuff is non-welded and does not show fumarolic alteration that would be expected if the Pagosa Peak Dacite was still hot at the time of the Fish Canyon Tuff deposition. In the localities where the Fish Canyon Tuff overlies the Pagosa Peak Dacite, the latter is densely welded, even rheomorphic in places, and relatively thick (several hundreds of meters). Following the study of Riehle et al. (1995), degassing time for thick silicic deposits is estimated to last up to several months. The observed field relations thus imply a time gap at least on the order of months between the two eruptions, although it remained short enough to preclude significant erosion or deposition.

Postdating the Fish Canyon Tuff, a small lava flow (<1 km^3), referred to as the Nutras Creek Dacite, rests on the northern flank of the resurgent dome of the La Garita caldera (Figure 1). It is characterized by devitriphied exposures of flow-banded Fish Canyon magma. The base of the unit is not exposed, and field indications on the time gap between this flow and the Fish Canyon Tuff are lacking.

3. $^{40}Ar/^{39}Ar$ geochronology

3.1. Sample preparation

Mineral separates from four samples (two from the Pagosa Peak Dacite and one from the Fish Canyon Tuff and the Nutras Creek Dacite each) were processed for this experiment. Apart from the Nutras Creek Dacite, which did not retain glassy

exposures, the samples from the outflow Fish Canyon Tuff and the Pagosa Peak Dacite are basal vitrophyres. Due to the abundance of glassy material, two samples were analyzed from the Pagosa Peak Dacite, to control reproducibility within the same unit.

Mineral separates were prepared following the procedure described below. Rock samples were first crushed in a stainless steel mortar and sieved to the most appropriate fraction for the Fish Canyon phenocrysts (125-315 microns). Quartz and feldspars were then magnetically separated from the rest of the sieved fraction using a Frantz magnetic separator. Hornblende and biotite were easily handpicked from the magnetic residue. To obtain sanidine and plagioclase-rich fractions, two runs of heavy liquid separation, using Na-polytungstate salt dissolved in deionized water adjusted to the right density value (~2.60 g/cm^3), were necessary. Sanidine and plagioclase separates were then slightly etched in diluted HF (2% HF) for a few minutes and rinsed with distilled water. All separates were finally cleaned in an aceton ultra-sonic bath.

Carefully handpicked samples were wrapped in aluminum foils and loaded in 99.99 % pure copper planchettes. Neutron fluence monitors (Taylor Creek Rhyolite sanidine) were deposited in the small wells surrounding larger wells containing unknowns. This geometry was designed to keep the neutron fluence monitors as close as possible to the unknowns, ultimately to minimize the error on the J parameter. A J value was calculated for the whole planchette by averaging values found for each well. Sample irradiation took place in the Oregon State University Triga reactor and lasted for 50 hours.

3.2. $^{40}Ar/^{39}Ar$ analyses

$^{40}Ar/^{39}Ar$ analyses were done at the University of Geneva, and analytical procedures, equipment, mass discrimination, interfering neutron induced corrections factors and blank corrections are similar to those of Singer et al. (1999). 1 σ error estimates include the standard deviation of analytical precision on the peak signals, system blank, spectrometer mass discrimination, reactor correction for interfering reactions and determination of the J parameter. The uncertainty on J parameter was about 0.3 % of the age, largely dominating the total error estimate. Ages were originally calculated with respect to an age of 27.92 Ma for the Taylor Creek Rhyolite (Duffield and Dalrymple, 1990), and then multiplied by a factor of 1.015 following the age revision of Renne et al. (1998b), which set the Taylor Creek Rhyolite at 28.34 ± 0.28 Ma. Decay constants of Steiger and Jäger (1977) were used.

Both total fusion and incremental heating analyses were performed using a CO_2 laser. Total fusion experiments allowed the acquisition of high precision single grain data on biotite and sanidine at the chosen size fraction (125-315 mm). For K-poor minerals (plagioclase and hornblende), aliquots of 10 to 15 grains were necessary for each individual total fusion analysis. Incremental heating analyses, achieved through step-by-step increase of laser power, were done on all four mineral phases (sanidine, biotite, plagioclase, hornblende), as well as on a feldspar megacryst collected from an intracaldera Fish Canyon Tuff pumice. The megacryst was large enough to permit a 24 steps experiment on this single crystal, but regular Fish Canyon phenocrysts were too small for step heating single crystal analysis, and multi-grain wells were thus loaded for that purpose. For the K-rich minerals (sanidine and biotite), aliquots of 10 to 15 grains were used, whereas plagioclase and hornblende needed larger quantities (up to 50 grains). The numbers of steps varied from less than 10 to around 20 depending on the size of the aliquots and degassing behavior of the sample. Criteria used to

determine the quality of the incremental analyses and to calculate the plateau and isochron ages were based on standard definitions (McDougall and Harrison, 1999; Singer et al., 1999).

3.3. Results

3.3.1. Sanidine

Due to its high-K concentration and status of international neutron fluence monitor, sanidine was the obvious premier target mineral of this study and was dated from the three units by both total fusion and incremental heating methods. Our total fusion results were extremely reproducible. Out of more than 60 total fusion analyses performed (Table 1), only one gave an irrelevant age of 25.40 ± 0.09 Ma and was not included in the calculations. The Pagosa Peak Dacite yielded a weighted mean age of 27.93 ± 0.09 Ma for both samples, the Fish Canyon Tuff yielded 28.03 ± 0.08 Ma and the Nutras Creek Dacite gave an age of 28.06 ± 0.09 Ma.

All incremental heating experiments produced well-defined plateaus, including more than 98% of the gas (Table 2; Figure 2). A few steps at which the gas was released at very low laser power had to be omitted from the age calculations. These low temperature steps are referred to as pre-degassing steps and erroneous ages result from the fact that the superficial part of the grains is known to be unretentive of its radiogenic argon (i.e. Albarède, 1978). The weighted mean ages are 27.94

Table 1: Summary of $^{40}Ar/^{39}Ar$ Total fusion experiments on Fish Canyon magmatic system samples.

Sample #	K_2O (%)	K/Ca	Material	Total fusion age (ma)	N[a]	Weighted mean age ^{39}Ar (%)	Weighted mean age Age ± 1s (ma)	MSWD	Corrected age (Renne et al., 1998) Age ± 1s (ma)
Bfc 15 (PPD)	11	62.7	Sanidine	27.23 ± 0.08	15 of 16	86.6	27.52 ± 0.08	2.2	***27.93 ± 0.08***
Bfc 83 (PPD)	11	71.1	Sanidine	27.50 ± 0.09	7 of 7	100	27.52 ± 0.09	0.8	***27.93 ± 0.09***
Bfc 113 (FCT)	11	70.7	Sanidine	27.62 ± 0.09	12 of 12	100	27.62 ± 0.08	0.2	***28.03 ± 0.08***
Bfc 115 (NCD)	11	69.8	Sanidine	27.66 ± 0.08	27 of 27	100	27.65 ± 0.09	0.4	***28.06 ± 0.09***
Bfc 83 (PPD)	9	30.8	Biotite	27.83 ± 0.10	4 of 4	100	27.83 ± 0.10	0.4	***28.25 ± 0.10***
Bfc 113 (FCT)	9	33.3	Biotite	27.84 ± 0.09	4 of 4	100	27.83 ± 0.09	0.7	***28.25 ± 0.09***
Bfc 113 (FCT)	1	0.2	Plagioclase	27.89 ± 0.11	3 of 3	100	27.89 ± 0.11	0.6	***28.31 ± 0.11***
Bfc 113 (FCT)	1	0.2	Hornblende	27.81 ± 0.12	3 of 3	100	27.81 ± 0.12	0.2	***28.23 ± 0.12***

Table 2: Summary of $^{40}Ar/^{39}Ar$ incremental-heating experiments on Fish Canyon magmatic system samples.

Sample #	K_2O (%)	K/Ca	Material	Total fusion age (ma)	N[a]	Weighted mean age ^{39}Ar (%)	Weighted mean age Age ± 1s (ma)	MSWD	Corrected age (Renne et al., 1998) Age ± 1s (ma)
Bfc 15 (PPD)	11	64.6	Sanidine	27.51 ± 0.09	12 of 13	99	27.53 ± 0.09	2.2	***27.94 ± 0.09***
Bfc 113 (FCT)	11	70.4	Sanidine	27.63 ± 0.09	12 of 12	100	27.63 ± 0.09	1.9	***28.04 ± 0.09***
Bfc 115 (NCD) #1	11	70.1	Sanidine	27.68 ± 0.09	10 of 11	99.9	27.66 ± 0.09	2.6	***28.07 ± 0.09***
Bfc 115 (NCD) #2	11	72.2	Sanidine	27.61 ± 0.09	7 of 11	99.7	27.64 ± 0.09	0.4	***28.05 ± 0.09***
Bfc 83 (PPD)	9	21.5	Biotite	27.71 ± 0.18	6 of 14	96	27.74 ± 0.11	0.4	***28.16 ± 0.11***
Bfc 113 (FCT)	9	26.1	Biotite	27.77 ± 0.09	13 of 13	100	27.78 ± 0.09	1.3	***28.20 ± 0.09***
Bfc 113 (FCT)	1	0.2	Plagioclase	28.01 ± 0.10	11 of 12	94	27.83 ± 0.10	0.9	***28.25 ± 0.10***
Bfc 113 (FCT)	1	0.1	Hornblende	27.28 ± 0.13	9 of 11	97.8	27.30 ± 0.12	1.0	***27.71 ± 0.12***
Bfc 104 (Megacryst)	11	41.2	Sanidine	27.87 ± 0.09	8 of 24	70.3	27.81 ± 0.09	0.3	***28.23 ± 0.09***
Bfc 104 (Megacryst)	11	41.2	Sanidine	27.87 ± 0.09	19 of 24	88	27.84 ± 0.09	0.8	***28.26 ± 0.09***

Table 3: Summary of $^{40}Ar/^{39}Ar$ isochron analyses from incremental-heating experiments of Table 2

Sample #	K_2O (%)	K/Ca	Material	Isochron analysis $^{40}Ar/^{39}Ar$ ± 1s intercept	Isochron analysis SUMS (N-2)	Uncorrected age Age ± 1s (ma)	Corrected age (Renne et al., 1998) Age ± 1s (ma)
Bfc 15 (PPD)	11	64.6	Sanidine	272.1 ± 57.2	2.41	27.55 ± 0.09	***27.96 ± 0.09***
Bfc 113 (FCT)	11	70.4	Sanidine	344.7 ± 18.3	1.14	27.60 ± 0.09	***28.01 ± 0.09***
Bfc 115 (NCD) #1	11	70.1	Sanidine	529.5 ± 88.6	0.81	27.61 ± 0.09	***28.02 ± 0.09***
Bfc 115 (NCD) #2	11	72.2	Sanidine	249.6 ± 83.9	0.51	27.65 ± 0.09	***28.06 ± 0.09***
Bfc 83 (PPD)	9	21.5	Biotite	291.0 ± 15.4	0.42	27.77 ± 0.16	***28.19 ± 0.16***
Bfc 113 (FCT)	9	26.1	Biotite	296.3 ± 3.5	1.46	27.77 ± 0.09	***28.19 ± 0.09***
Bfc 113 (FCT)	1	0.2	Plagioclase	294.1 ± 15.3	0.97	27.84 ± 0.10	***28.26 ± 0.10***
Bfc 113 (FCT)	1	0.1	Hornblende	297.1 ± 2.0	1.07	27.24 ± 0.14	***27.65 ± 0.14***
Bfc 104 (Megacryst)	11	41.2	Sanidine	289.1 ± 18.0	0.31	27.88 ± 0.13	***28.30 ± 0.09***
Bfc 104 (Megacryst)	11	41.2	Sanidine	294.0 ± 2.1	0.78	27.85 ± 0.09	***28.27 ± 0.09***

N[a] = number of plateau/isochron used in regression. Preferred ages are in italics-bold.

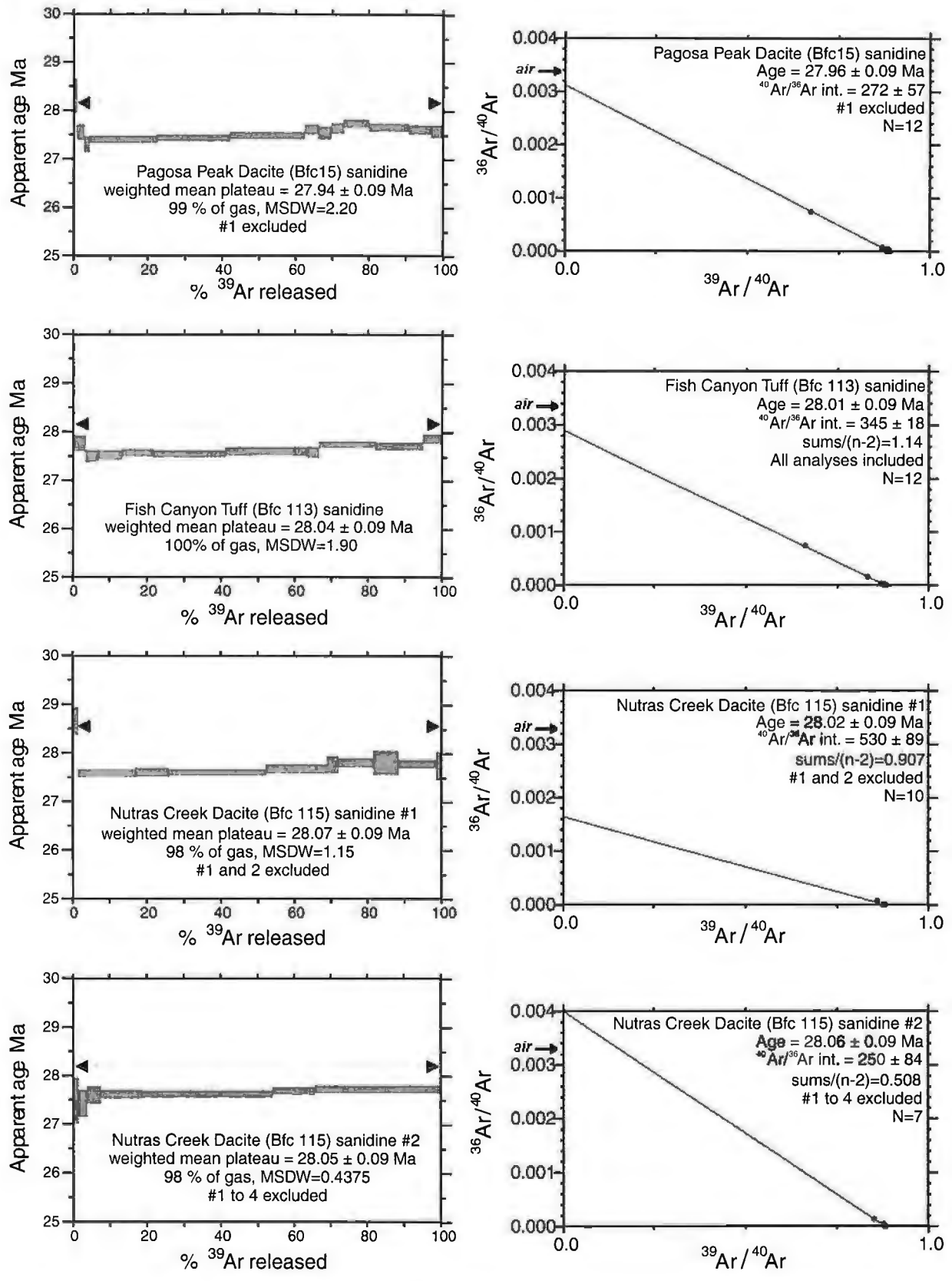

Figure 2: Incremental step-heating analyses of sanidine in the Fish Canyon magmatic system. Rectangle heights and all errors are 1 σ. Ages indicated by the text are all relative to the Taylor Creek sanidine (TCs).

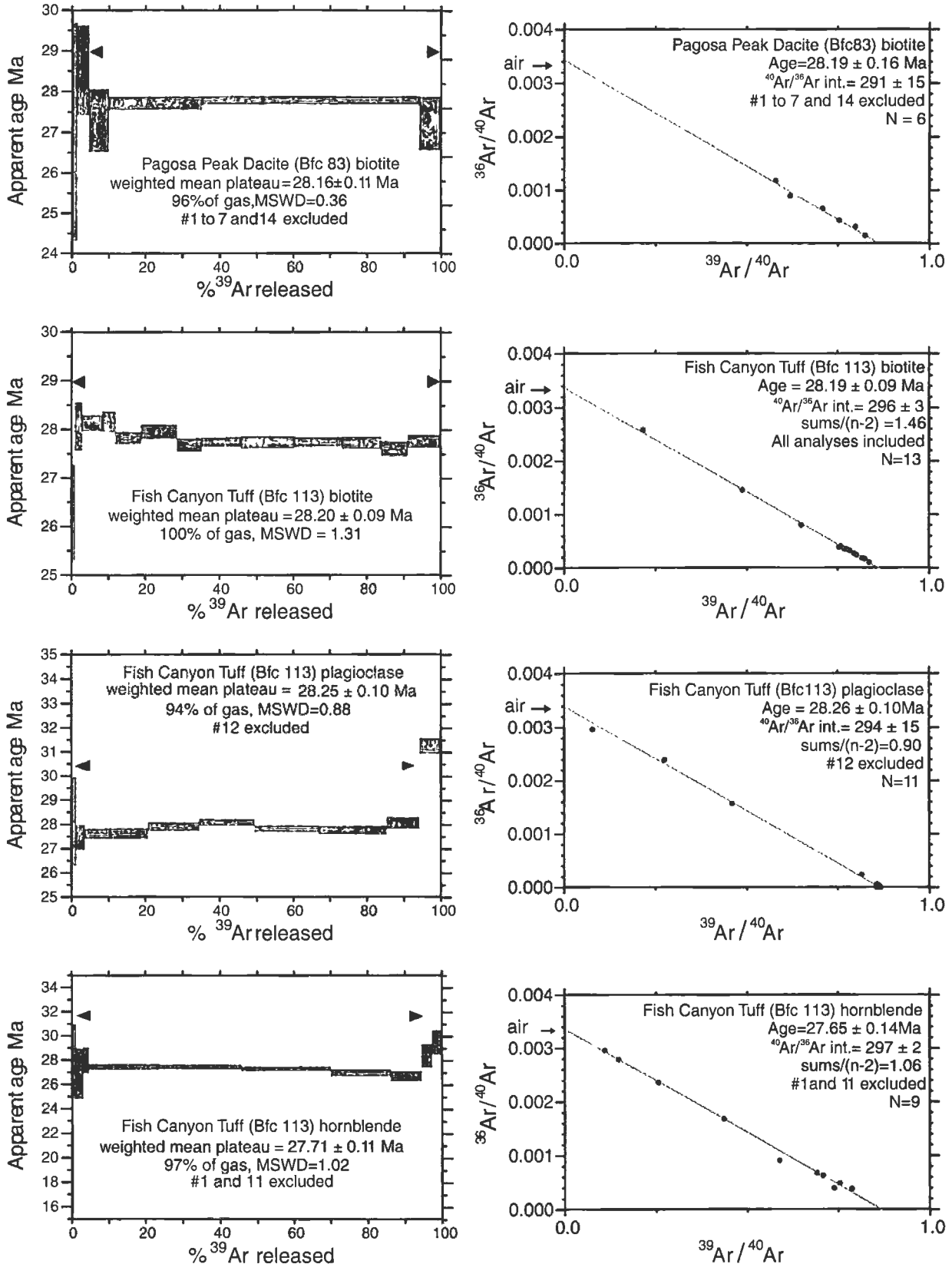

Figure 3: Incremental step-heating analyses of biotite, plagioclase and hornblende from the Fish Canyon Tuff and step-heating analysis from a Pagosa Peak Dacite biotite. Errors and age calculations identical to figure 2.

± 0.09 Ma and 28.04 ± 0.09 Ma for the Pagosa Peak Dacite (PPD) and Fish Canyon Tuff (FCT), respectively. Two replicates of the Nutras Creek Dacite (NCD) gave 28.07 ± 0.09 and 28.05 ± 0.09 Ma. Inverse isochrons ages calculated for the incremental heating analyses also gave ages consistent with plateau and total fusion results (PPD = 27.96 ± 0.09 Ma; FCT = 28.01 ± 0.09 Ma; and NCD = 28.02 ± 0.09 and 28.06 ± 0.09 Ma). The $^{36}Ar/^{40}Ar$ intercepts are generally imprecise due to the extremely high percentage of radiogenic argon yielded by all steps, which results in a poorly-constrained regression line.

All the ages obtained by total fusion and step heating analyses are thus indistinguishable at one sigma error for the three units and the three independent ages calculated. It is, however, striking that the ages of both Pagosa Peak Dacite samples are identical and slightly younger than the results obtained on the Fish Canyon Tuff and Nutras Creek Dacite. This cannot have any chronological significance, since stratigraphic relations unambiguously show that Pagosa Peak Dacite is the oldest.

3.3.2. Plagioclase, biotite, hornblende

Plagioclase, biotite and hornblende analyses were also analyzed by both total fusion and step heating methods, with the focus on the Fish Canyon Tuff sample. The underlying strategy was to constrain the age variability between the different mineral phases in the same unit. A biotite from the Pagosa Peak Dacite was, however, also acquired to compare internal age variability between samples. As it was the case for sanidine, total fusion analyses were highly reproducible and all analyses were included in the calculations. The three phases from the Fish Canyon Tuff and the biotite from the Pagosa Peak Dacite gave similar results ranging from 28.23 ± 0.12 for hornblende to 28.31 ± 0.11 for plagioclase (Table 1).

The results from the step heating experiments are slightly more complicated. Biotite is the most reliable phase of the three, with a weighted mean plateau age for the Pagosa Peak Dacite of 28.16 ± 0.11 Ma and of 28.20 ± 0.09 Ma for the Fish Canyon Tuff (Table 2). The biotite from the Fish Canyon Tuff shows a well-defined plateau comprising twelve steps forming 100% of the gas released. The Pagosa Peak Dacite biotite degassed much more abruptly, mainly in two steps. The first seven steps, forming only approximately 3 % of the total ^{39}Ar released, had to be excluded from the plateau. Both inverse isochrons gave results concordant with the plateau ages (28.19 ± 0.16 Ma for the Pagosa Peak Dacite and 28.19 ± 0.09 Ma for the Fish Canyon Tuff) and atmospheric $^{36}Ar/^{40}Ar$ intercepts (Figure 4).

Plagioclase also yielded consistent ages in the step heating experiment (28.25 ± 0.10 Ma for the plateau age and 28.26 ± 0.10 for the inverse isochron with an atmospheric $^{36}Ar/^{40}Ar$ intercept; Figure 3). The highest temperature step of this analysis, however, produced an age of more than 30 Ma and was excluded from the plateau age calculation. Thin section observation and microprobe analyses show that Fish Canyon plagioclases contain relic cores with anorthite content much higher than the average (up to An_{80}; Bachmann et al., submitted) indicating recycling from an earlier, more mafic stage of differentiation. These relic cores may be responsible for this older step.

Hornblende, a phase generally regarded in $^{40}Ar/^{39}Ar$ geochronology to have high argon retentivity (e.g. McDougall and Harrison, 1999), is apparently the least reliable mineral from the Fish Canyon magma. Although the three total fusion ages obtained are identical to the biotite and plagioclase ages at 1 s error, the incremental heating analysis

gave a much younger age of 27.71 ± 0.11 Ma for the plateau age and 27.65 ± 0.14 Ma for the inverse isochron (Figure 3). There is, however, no indication of argon loss from the release spectrum, which forms a well-defined plateau and the $^{36}Ar/^{40}Ar$ intercept on the inverse isochron is atmospheric within error. In thin sections, the Fish Canyon hornblendes appear as large poikilitic crystals, fresh and euhedral. As the ages obtained by both the plateau and inverse isochron are obviously too young, this example forces the admission that analyses giving erroneous ages do not always show signs of misbehavior.

Apart from the hornblende incremental heating experiment, all the ages obtained on Fish Canyon Tuff and Pagosa Peak Dacite minerals, excluding sanidine, overlap at 1 σ error and form a coherent set of data around 28.2 Ma. With respect to sanidine, however, the ages are shifted to slightly older values, concordant at 2 σ but differing at 1 σ error.

3.3.3. Age probability analysis

Age-probability plots (Deino and Potts, 1992) are now routinely used to display results from a serie of single step age data. The curves in these so-called "ideograms" represent the cumulative gaussian probability of individual analyses. They are mainly a function of the number of analyses and their estimated analytical uncertainties. Ideograms from this study compile all individual total fusion analyses and all steps included in plateau calculations from incremental heating experiments. They were used to compare the data obtained from sanidine of the three units (Figure 4a), and from the four phases analyzed from the Fish Canyon Tuff sample (Figure 4b).

In the graph compiling the sanidine data (Figure 4a), the curves overlap, but maximum probabilities for Pagosa Peak Dacite sanidine are shifted toward slightly younger ages. Biotite does not seem to reproduce this behaviour, as the ages of the Pagosa Peak Dacite biotites are very similar to the ages obtained on the Fish Canyon Tuff biotite for total fusion (PPD=28.25 ± 0.10; FCT=28.25 ± 0.09 Ma), weighted mean plateau (PPD=28.16 ± 0.11 Ma; FCT=28.20 ± 0.09 Ma) and inverse isochron (PPD=28.19 ± 0.16 Ma; FCT=28.19 ± 0.09 Ma). In Figure 4b, comparing the four analyzed phases of the Fish Canyon Tuff, the sanidine peak is shifted toward a younger age with respect to biotite and plagioclase peaks. Hornblende fits in the biotite-plagioclase group, but the very small number of analyses produces a poorly-defined peak.

3.3.4. Feldspar megacryst

Feldspar megacrysts, up to several centimeters in diameter, are present in pumices of the intracaldera Fish Canyon Tuff (Figure 5). These megacrysts, described in Lipman et al. (1997) and Bachmann et al. (submitted), record a complex petrologic history. The core is a relatively homogeneous K-feldspar, but the rims are composite, showing two types of overgrowths textures. First, development of plagioclase mantling, referred to as rapakivi textures, occurred following an interaction of the Fish Canyon magma with a more mafic body (Bachmann et al., submitted). Finally, the megacrysts were overgrown by granophyric rims (fine-scale intergrowths of quartz and K-feldspar), triggered by early eruptions of the Fish Canyon magmatic systems (Lipman et al., 1997).

A detailed step heating analysis (24 steps) on one of these megacrysts was performed in an attempt to question argon memory in these complex crystals (Figure 6). The degassing pattern of this megacryst is conveniently dividable in three stages of eight steps. The first group of eight, acquired at

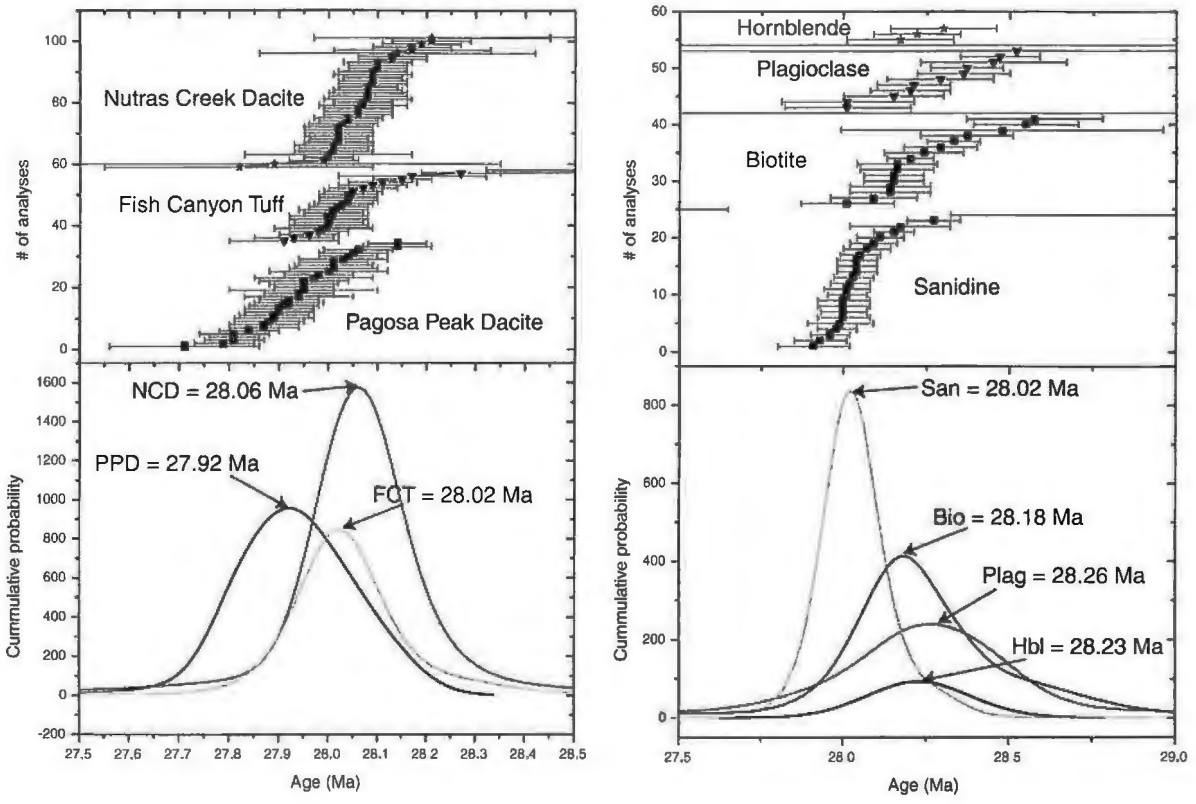

Figure 4: (a) Cumulative probability plots (Ideograms; (Deino and Potts, 1992) of all sanidine data from total fusion analyses and steps from incremental heating experiments included in plateau calculations. (b) Cumulative probability plots of all data from total fusion analyses and steps from incremental heating experiments included in plateau calculations from the four different mineral phases of the Fish Canyon Tuff. Ages reported are those giving the highest cumulative probability. Above are plotted the distributions of single analyses included in the calculations for each sample set, with their respective 1 σ error bars.

low laser power, shows a gradual rise from approximately 27 Ma to more than 28 Ma. Their low and variable K/Ca ratio indicates that these steps partially extracted argon from plagioclase. They contributed only to a small amount of the total ^{39}Ar release (< 9 %). The next eight steps produced the bulk of the argon release and define a plateau (28.23 ± 0.09 Ma), slightly older than the apparent eruption age of the Fish Canyon Tuff obtained on sanidine, but comparing well with the age found on biotite, hornblende and plagioclase. The last eight steps, forming a significant portion of the gas release (> 20 %), show a gradual rise from the plateau to almost 29 Ma. Their K/Ca ratio, very similar to the sanidine K/Ca ratio, argues for gas release from the homogeneous K-feldspar core of the megacrysts. The $^{36}Ar/^{40}Ar$ intercept defined by the inverse isochron of these last eight steps is atmospheric within error, and indicate that the ^{40}Ar was a mix of closed system ^{40}K decay and atmospheric sources. The age obtained by the $^{39}Ar/^{40}Ar$ intercept on this inverse isochron give an age of 28.75 ± 0.32 Ma (Figure 7).

4. U-Pb zircons geochronology

U-Pb dating on zircons is in process at the ETH Zürich. The results are unfortunately not available for the time being.

5. Some of the main points raised by this experiment

1. The results obtained on the sanidines

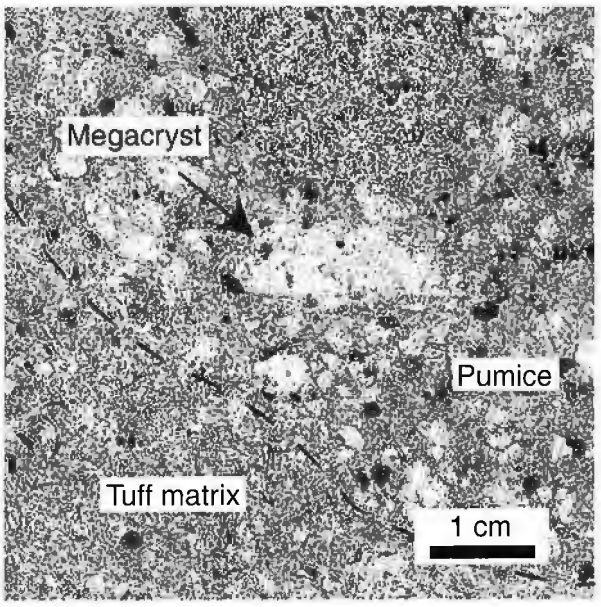

Figure 5: Photomicrograph of a megacryst in a Fish Canyon Tuff pumice collected in the intracaldera Tuff.

of the three stratigraphic units are indistinguishable within 1s error. The eruptions were too closely related in time for $^{39}Ar/^{40}Ar$ geochronology to resolve the age gap between them. Maximum time interval = 0.5 Ma, calculated by taking the youngest and the oldest value in the sanidine data set and subtract, respectively add the 2 s error of the analysis.

2. If the interpretation of the sanidine data is relatively straightforward, dating multiple mineral phases from the same unit (Fish Canyon Tuff) has proved more equivocal. In rapidly cooled volcanic rocks, such as the Fish Canyon Tuff, which contains high sanidine (Whitney and Stormer, 1985), the ages of the different minerals should give concordant ages. The ages range from 28.4 to 28.5, with error on the order of 0.05 for U-Pb ages on (Oberli et al., 1990; Schmitz and Bowring, 1999) to sanidine ages converging toward 28.0 Ma, with error larger than for zircons (0.1-0.4 Ma; Villeneuve et al., 1997;

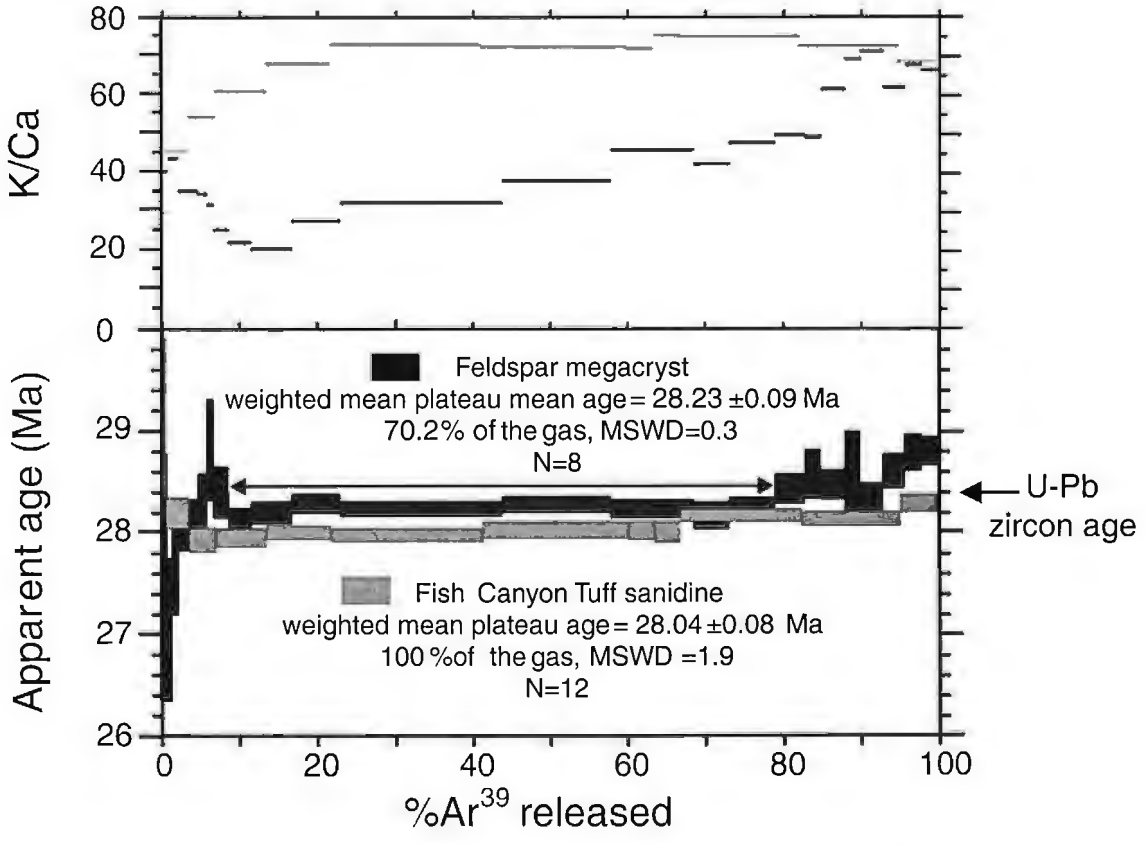

Figure 6: Release spectrum and K/Ca ratio of a step-heating analysis of a Fish Canyon feldspar megacryst, compared with results from a step-heating analysis of a Fish Canyon Tuff sanidine. U-Pb age on Fish Canyon zircon (Oberli et al., 1990; Schmitz and Bowring, 1999) are also reported for comparison. Errors and age calculations identical to figure 2.

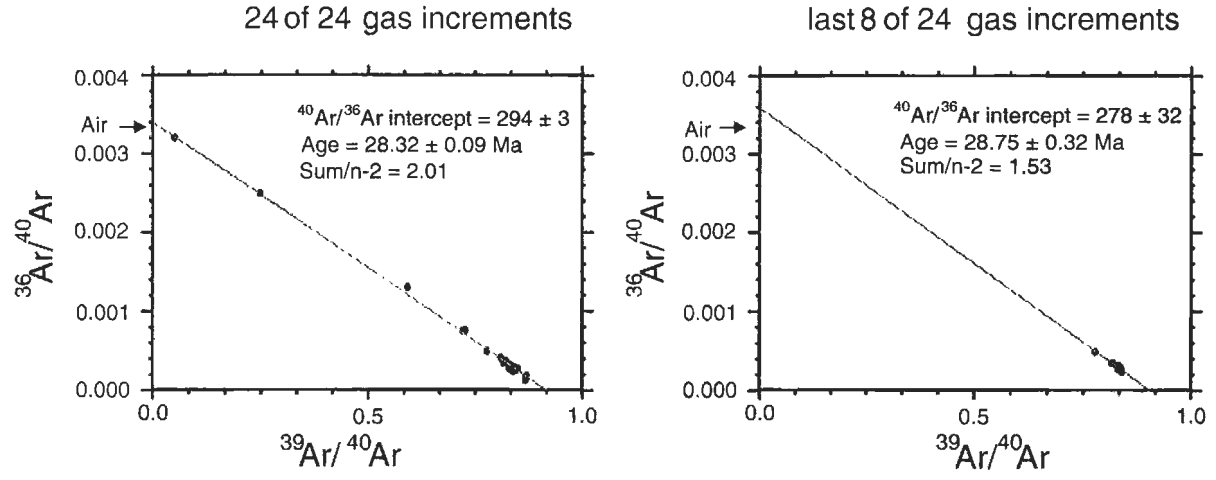

Figure 7: Inverse isochrons calculated on all 24 steps (left) and on the last eight steps (right) of the Fish Canyon Tuff megacryst analysis. Both have atmospheric $^{36}Ar/^{40}Ar$ intercepts. Errors and age calculations identical to figure 2.

Renne et al., 1994; Renne and Min, 1998; Renne et al., 1998). The absolute ages obtained on sanidine in this study (weighted mean age of total fusion and incremental heating analyses=28.03 ± 0.06 Ma) is indistinguishable from the estimates reported in these publications. With respect to the sanidine ages, hornblende, biotite and plagioclase ages obtained from this $^{40}Ar/^{39}Ar$ experiment cluster around 28.2 ± 0.1 Ma, overlapping at 2 s, but different at 1 s. Ages older by a few hundreds of thousands of years were also acquired from the high temperature steps of the megacryst incremental heating experiment, three of them being different at 2 s.

3. Do these differences reflect a geological process, or do they derive from analytical uncertainties? $^{40}Ar/^{39}Ar$ geochronology is substantially more precise than accurate (Lanphere and Baadsgaard, 1997; Renne et al., 1998a). Relative difference among $^{40}Ar/^{39}Ar$ ages acquired in this study should thus be meaningful, but they are of small magnitude, and do not meet the widely applied 2 σ criteria. The difference between the sanidine $^{40}Ar/^{39}Ar$ age and the U-Pb zircon age is larger, but the comparison between the results obtained by $^{40}Ar/^{39}Ar$ and U-Pb suffers from the relative inaccuracy of $^{40}Ar/^{39}Ar$ absolute age determination resulting from the incertitude on the ages of the standards and the value of the ^{40}K decay constant (Min et al., 2000). Yet, the conjuntion of these ages discrepancies with the shape of the argon release spectra produced by the incremental heating analysis of the megacryst, typically interpreted as an indication of argon inheritance (Singer et al., 1998), suggest that they may be real.

4. If they are real, what process could explain the ubiquitous presence of a dilute inherited component in the Fish Canyon minerals? Petrologic reinvestigation of the Fish Canyon magma has shown that a thermal oscillation occurred shortly prior to eruption. Cooling to near-solidus conditions followed by a reheating event is likely to have affected the isotopic memory of the Fish Canyon minerals. Argon inheritance in this thermally fluctuating conditions is not excluded. However, to retain a inherited component, minerals would need to cool below their closure temperature. Apart from zircon, which has a closure temperature of around 900 °C (Lee et al., 1997), the other phases are thought to start accumulating radiogenic isotopes only below 500 °C (Harrison and McDougall, 1999; Villa and Puddexu, 1994), but petrologic arguments suggests that the body remained at relatively high temperature

(>600 °C) at all time (Bachmann et al., submitted). Is it possible that some amounts of argon can start to accumulate in minerals, even at temperature above 600 °C?

References

Albarède F. (1978) The recovery of spatial isotope distributions from stepwise degassing data. Earth and Planetary Science Letters 39, 387-397.

Bachmann O., Dungan M. A., and Lipman P. W. (2000) Voluminous lava-like precursor to a major ash-flow tuff; low-column pyroclastic eruption of the Pagosa Peak Dacite, San Juan volcanic field, Colorado. Journal of Volcanology and Geothermal Research 98, 153-171.

Cebula G. T., Kunk M. J., Mehnert H. H., Naeser C. W., Obradovich J. D., Sutter J. F., and Anonymous. (1986) The Fish Canyon Tuff, a potential standard for the $^{40}Ar/^{39}Ar$ and fission-track dating methods (abs.). Terra Cognita 6, 139-140.

Deino A. and Potts R. (1992) Age-probability spectra for examination of single-crystal $^{40}Ar/^{39}Ar$ dating results; examples from Olorgesailie, southern Kenya Rift. Quaternary International 13-14, 47-53.

Duffield W. A. and Dalrymple G. B. (1990) The Taylor Creek Rhyolite of New Mexico; a rapidly emplaced field of lava domes and flows. Bulletin of Volcanology 52, 475-487.

Gillespie A. R., Huneke J. C., and Wasserburg G. J. (1982) An assessment of ^{40}Ar-^{39}Ar dating of incompletely degassed xenoliths. JGR. Journal of Geophysical Research. B 87, 9247-9257.

Gillespie A. R., Huneke J. C., and Wasserburg G. J. (1984) Eruption age of a approximately 100,000-year-old basalt from ^{40}Ar-^{39}Ar analysis of partially degassed xenoliths. JGR. Journal of Geophysical Research. B 89, 1033-1048.

Heizler M. T., Perry F. V., Crowe B. M., Peters L., and Appelt R. (1999) The age of the Lathrop Wells volcanic center: An $^{40}Ar/^{39}Ar$ dating investigation. Journal of Geophysical Research 104(B1), 767-804.

Lanphere M. A. and Baadsgaard H. (1997) The Fish Canyon Tuff; a standard for geochronology (abs.). Eos (American Geophysical Union Transactions) 78, S326.

Lanphere M. A. and Dalrymple G. B. (2000) First-principles calibration of ^{38}Ar tracers; implications for the ages of $^{40}Ar/^{39}Ar$ fluence monitors. U. S. Geological Survey Professional Paper, 10.

Lipman P. W. (1999) The central San Juan caldera cluster: Regional volcanic framework. in P.M. Bethke and R.L. Hay, eds., Ancient Lake Creede: Its Volcano-Tectonic Setting, History of Sedimentation, and Relation of Mineralization in the Creede Mining District: Geological Society of America Special Paper 356, 9-71.

Lipman P. W., Doe B., and Hedge C. (1978) Petrologic evolution of the San Juan volcanic field, Southwestern Colorado: Pb and Sr isotope evidence. Geological Society of America Bulletin 89, 59-82.

Lipman P. W., Dungan M. A., and Bachmann O. (1997) Comagmatic granophyric granite in the Fish Canyon Tuff, Colorado; implications for magma-chamber processes during a large ash-flow eruption. Geology (Boulder) 25, 915-918.

McDougall I. and Harrison T. M. (1999) Geochronology and Thermochronology by the $^{40}Ar/^{39}Ar$ method. Oxford University Press, 2nd ed., 269 p.

Min K., Mundil R., Renne P. R., and Ludwig K. R. (2000) A test for systematic errors in $^{40}Ar/^{39}Ar$ geochronology through comparison with U-Pbanalysis of a 1.1-Ga rhyolite. Geochimica et Cosmochimica Acta 64, 73-98.

Oberli F., Fischer H., and Meier M. (1990) High-resolution ^{238}U-^{206}Pb zircon dating of Tertiary bentonites and Fish Canyon Tuff; a test for age "concordance" by single-crystal analysis (abs.). Abstracts - Geological Society of Australia 27, 74.

Reid M. R., Coath C. D., Harrison T. M., and McKeegan K. D. (1997) Prolongued residence times for the youngest rhyolites associated with Long Valley Caldera: ^{230}Th-^{238}U microprobe dating of young zircons. Earth and Planetary Science Letters 150, 27-39.

Renne P. R., Deino A. L., Walter R. C., Turrin B. D., Swisher C. C., III, Becker T. A., Curtis G. H., Sharp W. D., and Jaouni A.-R. (1994) Intercalibration of astronomical and radioisotopic time. Geology (Boulder) 22, 783-786.

Renne P. R., Karner D. B., and Ludwig K. R. (1998a) Absolute ages aren't exactly. Science 282, 1840-1841.

Renne P. R. and Min K. (1998) $^{40}Ar/^{39}Ar$ dating of the 79AD eruption of Vesuvius: An ab initio basis for improved accuracy in $^{40}Ar/^{39}Ar$ geochronology (abs.). Goldschmidt conference Toulouse.

Renne P. R., Swisher C. C., Deino A. L., Karner D. B., Owens T. L., and DePaolo D. J. (1998b) Intercalibration of standards, absolute ages and uncertainties in $^{40}Ar/^{39}Ar$ dating. Chemical Geology 145, 117-152.

Riehle J. R., Miller T. F., and Bailey R. A. (1995) Cooling, degassing and compaction of rhyolitic ash flow tuffs; a computational model. Bulletin of Volcanology 57, 319-336.

Schmitz M. D. and Bowring S. A. (1999) An empirical assessmant of "ultra" high-precision U-Pb zircon geochronology: zircon and sphene systematics of the Fish Canyon Tuff. .

Singer B. S., Hoffman K. A., Chauvin A., Coe R. S., and Pringle M. S. (1999) Dating transitionally magnetized lavas of the late Matuyama Chron; toward a new (super 40) Ar/ (super 39) Ar timescale of reversals and events. Journal of Geophysical Research, B, Solid Earth and Planets 104, 679-693.

Singer B. S., Wijbrans J. R., Nelson S. T., Pringle M. S., Feeley T. C., and Dungan M. A. (1998) Inherited argon in a Pleistocene andesite lava; $^{40}Ar/^{39}Ar$ incremental-heating and laser-fusion analyses of plagioclase. Geology (Boulder) 26, 427-430.

Steiger R. H. and Jäger E. (1977) Subcommission on geochronology: Convention on the use of decay constants in geo- and cosmoschronology. Earth and Planetary Science Letters 36, 359-362.

Steven T. A. and Lipman P. W. (1976) Calderas of the San Juan volcanic field, southwestern Colorado. U.S. Geological Survey Professional Paper 958, 1-35.

Villeneuve M. E., Sandeman H. A., Davis W. J., Mortensen J. K., Dazé A., and Lee J. K. W. (1998) A multi-age, U-Pb and $^{40}Ar/^{39}Ar$ approach to the calibration of Fish Canyon Tuff sanidine as a flux monitor (abs.). Goldschmidt conference Toulouse.

Wolff J. A. and Gardner J. N. (1995) Is the Valles caldera entering a new cycle of activity? Geology 23(5), 411-414.

Table 3 : $^{40}Ar/^{39}Ar$ isotopic data for individual analyses

	$^{40}Ar/^{39}Ar$	$^{37}Ar/^{39}Ar$[a]	$^{36}Ar/^{39}Ar$	$^{40}Ar^*$ (10^{-14} mol)	$\%^{40}Ar^*$	K/Ca	Apparent age[b] (ma) ± 1σ	step used in isochron
Total fusion analyses								
FCT113 (san)	J=0.0135981							
GE111C1A	1.143632	0.007849	0.00000947	3.170645	99.40	62.4	28.09 ± 0.10	*
GE111C1B	1.137895	0.006783	0.00000250	3.921292	99.57	72.2	28.00 ± 0.11	*
GE111C1Q	1.141411	0.006640	0.00001290	1.370600	99.30	73.8	28.01 ± 0.10	*
GE111C1R	1.142623	0.006735	0.00001130	1.615103	99.35	72.8	28.05 ± 0.10	*
GE111C1S	1.142095	0.006690	0.00001300	2.103951	99.30	73.2	28.02 ± 0.11	*
GE111C1T	1.141244	0.007216	0.00001300	1.455636	99.31	67.9	28.00 ± 0.10	*
GE111C1U	1.141469	0.006979	0.00000881	1.501582	99.41	70.2	28.04 ± 0.10	*
GE111C1V	1.141990	0.006738	0.00001080	1.464530	99.36	72.7	28.04 ± 0.10	*
GE111C1W	1.140724	0.006783	0.00001087	1.411640	99.36	72.2	28.01 ± 0.11	*
GE111C1X	1.143119	0.006459	0.00001429	1.652432	99.27	75.9	28.04 ± 0.10	*
GE111C1Y	1.144296	0.007573	0.00001932	1.873154	99.15	64.7	28.03 ± 0.10	*
GE111C1Z	1.140346	0.006538	0.00000044	2.033967	99.63	74.9	28.07 ± 0.11	*
FCT113 (plag)	J=0.0134704							
GE112C2A	1.188852	2.965818	0.00091171	0.506163	96.70	0.2	28.20 ± 0.15	*
GE112C2B	1.170925	2.949725	0.00082255	0.636561	98.80	0.2	28.37 ± 0.14	*
GE112C2C	0.185213	2.981663	0.00088177	0.405925	97.55	0.2	28.36 ± 0.16	*
FCT113 (hbl)	J=0.0134704							
GE113C1A	1.643527	6.476819	0.00332080	0.750628	71.22	7.5	28.17 ± 0.18	*
GE113C1B	1.741333	6.439619	0.00360046	0.896456	66.91	7.6	28.30 ± 0.18	*
GE113C1C	1.575396	6.430503	0.00308951	0.819715	74.08	0.1	28.22 ± 0.16	*
FCT113 (bio)	J=0.013413							
GE112C4A	1.304446	0.010261	0.00048536	0.913047	88.71	47.8	28.20 ± 0.11	*
GE112C4B	1.288435	0.031729	0.00041952	1.103549	90.21	15.4	28.33 ± 0.11	*
GE112C4C	1.455079	0.012159	0.00100132	0.383163	79.41	40.3	28.16 ± 0.14	*
GE112C4D	1.475214	0.011877	0.00105205	0.477969	78.67	41.3	28.29 ± 0.14	*
PPD83 (Bio)	J=0.01341055							
GE112C3A	1.299564	0.021083	0.00046387	0.317999	89.22	23.2	28.25 ± 0.13	*
GE112C3B	1.330194	0.022642	0.00057502	0.755392	87.01	21.6	28.20 ± 0.13	*
GE112C3C	1.340554	0.012249	0.00060649	0.557696	86.36	40.0	28.21 ± 0.13	*
GE112C3D	1.277122	0.012947	0.00037412	0.589160	91.06	37.9	28.34 ± 0.13	*
BFC83 (san)	J=0.01365357							
GE111C3A	1.130576	0.006689	0.00001074	1.460864	99.35	73.3	27.87 ± 0.11	*
GE111C3B	1.137321	0.006794	0.00002190	1.878863	99.07	72.1	27.95 ± 0.12	*
GE111C3C	1.130359	0.006969	0.00000725	4.395066	99.45	70.3	27.89 ± 0.11	*
GE111C3D	1.133289	0.007397	0.00000252	0.877185	99.58	66.3	28.00 ± 0.14	*
GE111C3E	1.137308	0.007025	0.00000970	0.890388	99.39	69.8	28.04 ± 0.10	*
GE111C3F	1.130172	0.006975	0.00000527	1.647937	99.50	70.3	27.90 ± 0.11	*
GE111C3G	1.130322	0.006513	0.00000700	1.279671	99.45	75.2	27.89 ± 0.11	*
NCD115 (san)	J=0.01361595							
GE111C2A	1.142589	0.007385	0.00000885	3.706494	99.42	66.4	28.10 ± 0.13	*
GE111C2B	1.153482	0.007113	0.00004993	1.800781	98.37	68.9	28.07 ± 0.15	*
GE111C2C	1.140593	0.007079	0.00000575	1.042908	99.49	69.2	28.08 ± 0.11	*
GE111C2D	1.158803	0.007967	0.00006682	0.830779	97.95	61.5	28.08 ± 0.11	*
GE111C2E	1.146754	0.006716	0.00001389	1.461081	99.28	73.0	28.17 ± 0.11	*
GE111C2F	1.143278	0.006434	0.00001126	1.759253	99.35	76.2	28.10 ± 0.10	*
GE111C2G	1.140944	0.007606	0.00000910	1.254725	99.41	64.4	28.06 ± 0.11	*
GE111C2H	1.143054	0.188154	0.00005922	0.907363	99.37	2.6	28.10 ± 0.11	*
GE111C2I	1.142927	0.006775	0.00001238	1.293246	99.32	72.3	28.08 ± 0.11	*
GE111C2J	1.140710	0.006435	0.00001076	1.381541	99.36	76.1	28.04 ± 0.10	*
GE111C2K	1.144080	0.006811	0.00002482	2.166046	99.00	71.9	28.02 ± 0.11	*

GE111C2L	1.143661	0.006973	0.00001451	1.614954	99.27	70.3	28.09	± 0.11	*
GE111C2M	1.143490	0.006322	0.00001767	1.307181	99.18	77.5	28.06	± 0.11	*
GE111C2N	1.143596	0.006661	0.00001409	1.516003	99.28	73.6	28.09	± 0.10	*
GE111C2O	1.140572	0.006771	0.00001355	1.512893	99.29	72.4	28.02	± 0.11	*
GE111C2P	1.143522	0.006683	0.00002516	0.951612	98.99	73.3	28.01	± 0.11	*
GE111C2Q	1.141447	0.006884	0.00000810	1.845976	99.43	71.2	28.08	± 0.10	*
GE111C2R	1.145087	0.007630	0.00001342	1.478376	99.30	64.2	28.13	± 0.11	*
GE111C2S	1.142035	0.006998	0.00001889	1.401680	99.15	70.0	28.02	± 0.11	*
GE111C2T	1.141914	0.006765	0.00001745	0.776706	99.19	72.4	28.02	± 0.11	*
GE111C2U	1.141414	0.007192	0.00001427	1.373543	99.27	68.1	28.03	± 0.11	*
GE111C2V	1.142007	0.006583	0.00001891	1.364709	99.15	74.4	28.01	± 0.11	*
GE111C2W	1.141650	0.007043	0.00001030	1.598307	99.37	69.6	28.07	± 0.10	*
GE111C2X	1.141637	0.006521	0.00000720	0.942999	99.45	75.1	28.09	± 0.11	*
GE111C2Y	1.142860	0.006121	0.00001110	1.992892	99.35	80.1	28.09	± 0.11	*
GE111C2Z	1.143630	0.007092	0.00002161	1.841639	99.08	69.1	28.04	± 0.11	*
GE111C21	1.143112	0.006438	0.00001586	1.517976	99.23	76.1	28.06	± 0.11	*
PPD15 (san)	J=0.01329567								
GE111C4A	1.132945	0.007680	0.00003691	3.543552	98.69	63.8	27.94	± 0.07	*
GE111C4B	1.170666	0.010949	0.00044013	3.786444	88.57	44.8	25.78	± 0.09	
GE111C4C	1.134965	0.007635	0.00001977	1.340695	99.13	64.2	27.95	± 0.06	*
GE111C4D	1.131631	0.007382	0.00001305	1.192718	99.30	66.4	27.92	± 0.07	*
GE111C4E	1.143077	0.006662	0.00002104	2.070621	99.10	73.6	28.14	± 0.06	*
GE111C4F	1.130399	0.009385	0.00001680	1.515276	99.22	52.2	27.87	± 0.07	*
GE111C4G	1.131810	0.007315	0.00001301	1.955547	99.30	67.0	27.92	± 0.06	*
GE111C4H	1.138108	0.007896	0.00002220	1.360739	99.07	62.1	28.01	± 0.07	*
GE111C4I	1.137017	0.007374	0.00003279	0.945939	98.79	66.5	27.91	± 0.07	*
GE111C4J	1.126837	0.007554	0.00001502	1.815113	99.25	64.9	27.79	± 0.06	*
GE111C4K	1.130749	0.007334	0.00001219	1.552954	99.32	66.8	27.90	± 0.07	*
GE111C4L	1.133083	0.008341	0.00003304	1.973311	98.79	58.8	27.81	± 0.05	*
GE111C4M	1.155324	0.008003	0.00008511	1.794297	97.48	61.2	27.98	± 0.07	*
GE111C4N	1.137804	0.006869	0.00001636	1.611072	99.21	71.3	28.05	± 0.07	*
GE111C4O	1.128812	0.006954	0.00001845	2.185201	99.15	70.5	27.81	± 0.07	*
GE111C4P	1.133724	0.006821	0.00001524	1.672683	99.24	71.8	27.95	± 0.07	*
			Incremental heating analyses						
FCT113 (san)	J=0.0135981								
GE111C1C	1.515267	0.016252	0.00112693	0.055119	77.80	30.2	29.12	± 0.77	*
GE111C1E	1.155765	0.001075	0.00003956	0.330056	98.66	45.6	28.17	± 0.17	*
GE111C1F	1.143149	0.008958	0.00003277	0.381530	98.81	54.7	27.91	± 0.14	*
GE111C1G	1.140620	0.007994	0.00001956	0.726393	99.14	61.3	27.93	± 0.12	*
GE111C1H	1.139337	0.007179	0.00000964	0.919791	99.39	68.3	27.98	± 0.10	*
GE111C1I	1.137337	0.006685	0.00000591	2.175118	99.48	73.3	27.96	± 0.10	*
GE111C1K	1.139136	0.007674	0.00000556	2.107747	99.49	72.7	28.00	± 0.11	*
GE111C1L	1.144715	0.007680	0.00002466	0.372415	99.00	72.1	28.00	± 0.12	*
GE111C1M	1.143851	0.006491	0.00002406	0.360246	99.02	75.5	27.99	± 0.13	*
GE111C1N	1.143719	0.006513	0.00000128	1.738653	99.60	75.2	28.15	± 0.10	*
GE111C1O	1.147058	0.006731	0.00001734	1.432190	99.19	72.8	28.11	± 0.11	*
GE111C1P	1.205849	0.007133	0.00019532	0.577138	94.87	68.7	28.27	± 0.12	*
FCT113 (hbl)	J=0.01324858								
GE113C1D	25.214670	0.234863	0.08256177	0.009062	3.29	2.1	20.07	± 4.19	
GE113C1E	6.749717	0.204102	0.01889007	0.015517	17.42	2.4	28.31	± 3.00	*
GE113C1F	9.029773	0.404456	0.02681819	0.047635	12.54	1.2	27.27	± 2.02	*
GE113C1G	3.903025	1.728248	0.00967113	0.037028	30.17	0.3	28.38	± 1.04	*
GE113C1H	2.289285	5.558185	0.00532586	0.469746	50.28	0.1	27.82	± 0.21	*
GE113C1I	1.444540	5.912695	0.00256052	0.550023	79.72	0.1	27.84	± 0.16	*
GE113C1J	1.410654	5.968434	0.00251420	0.597246	80.51	0.1	27.46	± 0.17	*
GE113C1K	1.325337	6.041674	0.00232870	0.386733	83.83	0.1	26.87	± 0.24	*

GE113C1L	1.269737	5.173800	0.00205944	0.193305	83.98	0.1	25.78	± 0.33	*
GE113C1M	1.351698	6.681218	0.00232554	0.070397	87.96	0.1	28.75	± 0.92	*
GE113C1N	1.685116	15.662040	0.00572722	0.007190	72.90	0.0	29.89	± 0.96	
FCT113 (bio)	J=0.013413								
GE112C4E	4.632346	0.018140	0.01196300	0.040126	23.62	27.0	26.68	± 0.98	*
GE112C4F	2.059564	0.009771	0.00300200	0.090056	56.74	50.2	28.48	± 0.49	*
GE112C4G	1.543156	0.007962	0.00124416	0.246674	75.92	61.5	28.55	± 0.18	*
GE112C4H	1.331533	0.007297	0.00052428	0.163617	88.06	67.2	28.57	± 0.22	*
GE112C4I	1.323980	0.007157	0.00054607	0.314616	87.50	68.5	28.23	± 0.14	*
GE112C4J	1.307236	0.012144	0.00047232	0.430935	89.04	40.4	28.37	± 0.16	*
GE112C4K	1.282739	0.015173	0.00042883	0.300962	89.85	32.3	28.09	± 0.15	*
GE112C4L	1.295064	0.027547	0.00046516	0.471240	89.20	17.8	28.15	± 0.12	*
GE112C4M	1.262225	0.042203	0.00035941	0.652765	91.48	11.6	28.14	± 0.14	*
GE112C4N	1.250063	0.059624	0.00032212	0.586804	92.39	8.2	28.15	± 0.12	*
GE112C4O	1.228021	0.046771	0.00024585	0.467870	94.01	10.5	28.14	± 0.14	*
GE112C4P	1.216517	0.048496	0.00022561	0.315912	94.45	10.1	28.01	± 0.16	*
GE112C4Q	1.197908	0.024193	0.00013423	0.403137	96.46	20.3	28.16	± 0.15	*
FCT113 (plag)	J=0.0134704								
GE112C2D	12.779330	2.028861	0.03846334	0.001063	12.28	0.2	38.36	± 36.76	*
GE112C2E	3.655244	2.149893	0.00932203	0.008290	29.17	0.2	26.15	± 5.34	*
GE112C2F	2.176193	2.531674	0.00409048	0.022786	53.46	0.2	28.52	± 1.80	*
GE112C2G	1.227057	2.872734	0.00106415	0.059374	92.54	0.2	27.85	± 0.49	*
GE112C2H	1.167590	3.057303	0.00089056	0.178738	97.80	0.2	28.01	± 0.21	*
GE112C2I	1.159338	3.092190	0.00087153	0.262096	98.51	0.2	28.01	± 0.22	*
GE112C2J	1.162990	3.103459	0.00084833	0.355802	99.18	0.2	28.29	± 0.18	*
GE112C2K	1.168949	2.900963	0.00078877	0.385904	99.32	0.2	28.47	± 0.14	*
GE112C2L	1.154430	2.982237	0.00079828	0.453733	99.62	0.2	28.21	± 0.14	*
GE112C2M	1.153823	3.185253	0.00085910	0.474187	99.46	0.2	28.15	± 0.17	*
GE112C2N	1.156198	3.111044	0.00080497	0.229205	100.33	0.2	28.46	± 0.23	*
GE112C2O	1.355119	2.998234	0.00099663	0.169437	95.45	0.2	31.69	± 0.32	
PPD83 (bio)	J=0.01341055								
GE112C3E	12.274790	0.164141	0.02238711	0.001937	46.17	3.0	134.15	± 93.30	
GE112C3F	14.426170	0.075116	0.04640748	0.000980	4.95	6.5	17.45	± 26.08	
GE112C3G	3.779988	0.022265	0.00266025	0.002723	79.13	22.0	72.01	± 35.80	
GE112C3H	3.406739	0.048845	0.00738257	0.003478	35.94	10.0	29.82	± 12.00	
GE112C3I	2.180084	0.025176	0.00266371	0.012306	63.77	19.5	33.83	± 3.96	
GE112C3J	1.978369	0.009949	0.00321495	0.008168	51.78	49.3	24.99	± 4.51	
GE112C3K	1.954764	0.010120	0.00248500	0.013343	62.24	48.4	29.63	± 3.58	
GE112C3L	1.732329	0.010783	0.00204589	0.016317	64.88	45.4	27.39	± 2.68	*
GE112C3M	1.620220	0.009132	0.00145163	0.038303	73.28	53.7	28.93	± 1.09	*
GE112C3N	1.416182	0.011426	0.00093580	0.059778	80.21	42.9	27.68	± 0.77	*
GE112C3O	1.331065	0.039176	0.00059550	0.292263	86.66	12.5	28.38	± 0.17	*
GE112C3P	1.215875	0.029371	0.00019283	0.674640	95.12	16.7	28.18	± 0.12	*
GE112C3Q	1.256295	0.008345	0.00040381	0.067473	90.18	58.7	27.61	± 0.64	*
GE112C3R	16.054910	0.062058	0.05330003	0.001475	1.90	7.9	7.47	± 19.56	
NCD115 (san)	J=0.01361595								
GE111214	1.286336	0.124377	0.00460755	0.000071	5.44	3.9	-1.75	± 38.49	
GE111215	1.317837	0.012409	0.00625179	0.000765	40.46	39.5	-13.34	± 27.28	
GE111216	1.297691	0.016424	0.00143507	0.003968	67.06	29.8	21.57	± 7.44	
GE111217	1.226535	0.012201	0.00117044	0.010990	71.49	43.7	21.73	± 3.12	
GE111218	1.179669	0.009644	0.00016495	0.081848	95.54	50.8	27.89	± 0.46	*
GE111219	1.144946	0.008396	0.00005560	0.149604	98.22	58.4	27.82	± 0.28	*
GE111219	1.140643	0.007356	0.00001652	0.245638	99.22	66.6	28.00	± 0.19	*
GE111219	1.138790	0.007345	0.00000720	0.738067	99.46	66.7	28.02	± 0.11	*
GE111219	1.137817	0.006787	0.00000350	2.345597	99.55	72.2	28.02	± 0.10	*
GE111219	1.140259	0.006592	0.00000275	0.766621	99.57	74.3	28.09	± 0.11	*

GE111219	1.143943	0.006469	0.00000982	2.299892	99.38	75.8	28.13	± 0.11	•
NCD115#2 (san)	J=0.01361595								
GE111C22	3.394290	0.015334	0.00595435	0.005551	48.06	32.0	40.23	± 6.46	
GE111C23	1.238055	0.009164	0.00019836	0.135273	94.95	53.5	29.08	± 0.28	*
GE111C24	1.139121	0.007575	0.00001342	1.386110	99.30	64.7	27.99	± 0.11	*
GE111C25	1.136753	0.007186	0.00000180	0.805742	99.59	68.2	28.01	± 0.11	*
GE111C26	1.136391	0.006915	0.00000175	2.337171	99.59	70.9	28.00	± 0.10	*
GE111C27	1.139532	0.006843	0.00000148	1.503773	99.60	71.6	28.08	± 0.12	*
GE111C28	1.145006	0 006893	0.00000784	0.284465	99.44	71.1	28.17	± 0.18	*
GE111C29	1.145675	0.006713	0.00000450	0.868654	99.52	73.0	28.21	± 0.12	*
GE111C2Z	1.145567	0.006699	0.00000369	0.605347	99.55	73.2	28.21	± 0.25	*
GE111C12	1.147239	0.006690	0.00001299	0.926897	99.31	73.3	28.19	± 0.12	*
GE111C13	1.168215	0.006966	0.00008983	0.123843	97.38	70.3	28.14	± 0.29	*
FCT104 (megaX)	J=0.01432								
GE112A1A	19.895660	0.011835	0.06372681	0.015087	5.33	41.4	27.60	± 3.96	
GE112A1B	4.048245	0.014239	0.01010405	0.053807	26.16	34.4	27.56	± 1.22	
GE112A1C	1.696408	0.011992	0.00221141	0.062468	61.26	40.9	27.05	± 0.71	
GE112A1D	1.379510	0.011290	0.00104740	0.084631	77.29	43.4	27.75	± 0.55	
GE112A1E	1.393251	0.013775	0.00105089	0.253464	77.46	35.6	28.08	± 0 26	
GE112A1F	1.154371	0.014072	0.00022112	0.125421	94.03	34.8	28.24	± 0.34	
GE112A1G	1.157305	0.015665	0.00015665	0.088227	95.70	32.1	28.81	± 0.50	
GE112A1H	1 156125	0.019165	0.00020776	0 198480	94.42	25.6	28.40	± 0.26	
GE112A1I	1.181544	0.021967	0.00033467	0 297724	91.38	22.3	28.10	± 0.17	•
GE112A1J	1.219832	0.023804	0.00045188	0.546601	88.83	20.6	28.19	± 0.13	•
GE112A1K	1.204572	0.017584	0.00038639	0.637989	90.25	27.9	28.29	± 0.12	•
GE112A1L	1.192871	0.015081	0 00035355	2.154725	90.95	32.5	28.23	± 0.11	•
GE112A1M	1.184237	0.012812	0.00031748	1.458139	91.77	38.3	28.28	± 0.11	•
GE112A1N	1.233375	0.010626	0 00048898	1.105861	87 98	46.1	28.23	± 0.12	•
GE112A1O	1.240007	0.011541	0.00052046	0.472477	87.30	42.5	28.17	± 0.15	•
GE112A1P	1.225832	0.010244	0.00046292	0.600263	88.53	47.8	28.24	± 0.13	*
GE112A1Q	1.199371	0.009842	0.00034812	0.397658	91.10	49.8	28.43	± 0.16	
GE112A1R	1.291385	0.009926	0.00064059	0.210390	85.04	49.4	28.57	± 0.25	
GE112A1S	1.225796	0.007949	0.00043193	0.324657	89.26	61.6	28.47	± 0.16	
GE112A1T	1.209698	0.007060	0.00033429	0.213052	91.50	69.4	28.79	± 0.21	
GE112A1U	1.206592	0.006867	0.00038554	0.300223	90.22	71.4	28.32	± 0.17	
GE112A1V	1.231002	0.007882	0.00043246	0.296057	89.29	62.2	28.60	± 0.18	
GE112A1W	1.207817	0.007228	0.00032983	0.222594	91.59	67.8	28.78	± 0.20	
GE112A1X	1.196805	0.007377	0.00029032	0.254366	92.49	66.4	28.80	± 0.16	
PPD15 (san)	J=0.01329567								
GE111C4Q	1.488483	0.015367	0.00111217	0.101360	77.69	31.9	28.73	± 0.35	
GE111C4R	1.146072	0.012015	0.00005893	0.205951	98.17	36.5	27.95	± 0.15	*
GE111C4S	1.134260	0.012344	0.00005259	0.159221	98.31	39.7	27.71	± 0.15	*
GE111C4T	1.129736	0.008805	0.00002254	1.864145	99.06	55.7	27.81	± 0.06	*
GE111C4U	1.139961	0.007559	0.00005278	2.021732	98.28	64.8	27.84	± 0.05	*
GE111C4V	1.128413	0.007042	0.00000718	2.106350	99.45	69.6	27.88	± 0.07	*
GE111C4W	1.131792	0.006970	0.00000084	0.401575	99.62	70.3	28.01	± 0.09	*
GE111C4X	1.130612	0.006966	0.00000631	0.349381	99.47	70.3	27.94	± 0.11	*
GE111C4Y	1.146597	0.007030	0.00004812	0.358633	98.40	69.7	28.03	± 0.09	*
GE111C4Z	1.139796	0.007288	0.00001070	0.732127	99.37	67.2	28.14	± 0.07	*
GE111C41	1.140167	0.006895	0.00002293	1.113733	99.05	71.1	28.06	± 0.07	*
GE111C42	1.138577	0.007199	0.00002392	0.632368	99.02	68.1	28.01	± 0.08	*
GE111C43	1.156308	0.007031	0.00008891	0.322642	97.37	69.7	27.97	± 0.12	•

[a]Corrected for ^{37}Ar and ^{39}Ar decay: half-lives of 35 days and 259 years respectively. [b]All ages are calculated relative to 28.34 Ma Taylor Creek sanidine (Renne et al., 1998). Decay constants: $\lambda_E = 0.581 \times 10^{-10}$/yr;• $\lambda_B = 4.692 \times 10^{-10}$/yr. Power of CO_2 laser used: 25 W.

Annexe 2: Sample coordinates

			UTM Grid	
Sample #	Quadragle	Unit	X	Y
Bfc 1	Mt Hope	PPD	338-339	4154-4155
Bfc 2	Mt Hope	PPD	344-345	4159-4160
Bfc 3	Mt Hope	FCT (outflow)	344-345	4160-4161
Bfc 4	Mt Hope	FCT (outflow)	344-345	4161
Bfc 5	Mt Hope	PPD	341	4162
Bfc 6	Mt Hope	PPD	343-344	4157-4158
Bfc 7	Mt Hope	PPD	342-343	4156-4157
Bfc 8	Mt Hope	PPD	343-344	4154
Bfc 9	Mt Hope	PPD	344-345	4159-4160
Bfc 10	Mt Hope	PPD	344-345	4159-4160
Bfc 11	Mt Hope	PPD	344-345	4159-4160
Bfc 12	Mt Hope	PPD	344-345	4159-4160
Bfc 13	Mt Hope	PPD	344-345	4159-4160
Bfc 14	Mt Hope	PPD	344-345	4159-4160
Bfc 15	Mt Hope	PPD	344-345	4159-4160
Bfc 16	Mt Hope	PPD	344-345	4159-4160
Bfc 17	Mt Hope	PPD	344-345	4159-4160
Bfc 18	Mt Hope	FCT (outflow)	345-346	4160-4161
Bfc 19	Beaver Creek Res	FCT (outflow)	346-347	4161-4162
Bfc 20	Beaver Creek Res	FCT (outflow)	347-348	4161-4162
Bfc 21	Beaver Creek Res	FCT (outflow)	347-348	4161-4162
Bfc 22	Beaver Creek Res	FCT (outflow)	348	4162

Bfc 23	Beaver Creek Res	FCT (outflow)	347	4164-4165
Bfc 24	Beaver Creek Res	FCT (outflow)	348	4164-4165
Bfc 25	Beaver Creek Res	FCT (outflow)	349	4164-4165
Bfc 26	Beaver Creek Res	FCT (outflow)	349	4164-4165
Bfc 27	Beaver Creek Res	FCT (outflow)	349-350	4164-4165
Bfc 28	Beaver Creek Res	FCT (outflow)	349-350	4164-4165
Bfc 29	Beaver Creek Res	FCT (outflow)	349-350	4164-4165
Bfc 30	No sample			
Bfc 31	Mt Hope	PPD	343-344	4156-4157
Bfc 32	Mt Hope	PPD	343-344	4156-4157
Bfc33	Mt Hope	PPD	343-344	4156-4157
Bfc 34	Mt Hope	PPD	341-342	4159-4160
Bfc 35	Mt Hope	PPD	341-342	4158
Bfc 36	Mt Hope	PPD	341-342	4158
Bfc 37	Mt Hope	PPD	341-342	4159-4160
Bfc 38	South Fork	FCT (outflow)	?	?
Bfc 39	Mt Hope	PPD	342-343	4158-4159
Bfc 40	Wolf Creek Pass	PPD	335-336	4150-4151
Bfc 41	Wolf Creek Pass	PPD	335-336	4150-4151
Bfc 42	Wolf Creek Pass	PPD	335-336	4150-4151
Bfc 43	Mt Hope	Lithic breccia	342-343	4156-4157
Bfc 44	Mt Hope	Black andesite	342-343	4156-4157
Bfc 45	South River Peak	PPD	334-335	4152-4153
Bfc 46	Mt Hope	PPD	335	4156-4157
Bfc 47	Lake Humphrey	FCT (outflow)	334-335	4166-4167
Bfc 48	Mt Hope	PPD	340-341	4156-4157

Bfc 49	Wolf Creek Pass	FCT (outflow)	341-342	4146-4147
Bfc 50	Mt Hope	PPD	342-343	4156-4157
Bfc 51	Mt Hope	PPD	341-342	4156-4157
Bfc 52	Palomino Mountain	FCT (Intracaldera S)	317-318	4154-4155
Bfc 53	Palomino Mountain	FCT (Intracaldera S)	318-319	4156-4157
Bfc 54	Palomino Mountain	FCT (outflow S)	~315	~4155
Bfc 55	Pagosa Peak	PPD	320-321	4148-4149
Bfc 56	Pagosa Peak	FCT (outflow S)	320-321	4148-4149
Bfc 57	Pagosa Peak	PPD (loose block)	319-321	4144-4147
Bfc 58	Wolf Creek Pass	FCT (outflow)	335-336	4150-4151
Bfc 59	Saddle Mountain	PPD	332-333	4150-4151
Bfc 60	Mt Hope	PPD	341-342	4158
Bfc 61	Pagosa Peak	PPD	315-316	4147-4148
Bfc 62	Pagosa Peak	PPD	315-316	4147-4148
Bfc 63	Pagosa Peak	PPD	317-318	4146-4147
Bfc 64	Pagosa Peak	PPD	314-315	4145-4146
Bfc 65	Pagosa Peak	PPD	318-319	4144
Bfc 66	Pagosa Peak	PPD	318	4144-4145
Bfc 67	Pagosa Peak	PPD	319-320	4144-4145
Bfc 68	Pagosa Peak	PPD	319-320	4144-4145
Bfc 69	Pagosa Peak	PPD	319-320	4144-4145
Bfc 70	Pagosa Peak	PPD	318-319	4145-4146
Bfc 71	Mt Hope	PPD	339-340	4158-4159
Bfc 72	Mt Hope	PPD	339-340	4158-4159
Bfc 73	Mt Hope	PPD	339-340	4158-4159
Bfc 74	Mt Hope	PPD	341-342	4157-4158

Bfc 75	Mt Hope	PPD	341-342	4157-4158
Bfc 76	Mt Hope	PPD	338-339	4157-4158
Bfc 77	South River Peak	PPD	332-333	4163
Bfc 78	South River Peak	PPD	332-333	4163
Bfc 79	Pagosa Peak	PPD	319-320	4144-4145
Bfc 80	Pagosa Peak	PPD	314-315	4145-4146
Bfc 81	Mt Hope	PPD	344-345	4159-4160
Bfc 82	Mt Hope	PPD	342-343	4156-4157
Bfc 83	Wolf Creek Pass	PPD	334-335	4150-4151
Bfc 84	Pagosa Peak	FCT (outflow)	322-323	4149-4150
Bfc 85	Pagosa Peak	FCT (outflow)	320-321	4147-4148
Bfc 86	Pagosa Peak	PPD	~322	~4148
Bfc 87	Pagosa Peak	PPD	322-323	4147-4148
Bfc 88	Pagosa Peak	PPD	322-323	4147-4148
Bfc 89	Pagosa Peak	PPD	322-323	4147
Bfc 90	Pagosa Peak	Huerto Andesite (dyke)	322-323	4146-4147
Bfc 91	Pagosa Peak	PPD	323	4148
Bfc 92	Pagosa Peak	PPD	321-322	4147-4148
Bfc 93	Pagosa Peak	FCT (outflow)	321-322	4147-4148
Bfc 94	Pagosa Peak	FCT (outflow)	321-322	4147-4148
Bfc 95	Pagosa Peak	FCT (outflow)	321-322	4147-4148
Bfc 96	Pagosa Peak	FCT (outflow)	321-322	4147-4148
Bfc 97	Saddle Mountain	PPD	332-333	4150-4151
Bfc 98	Saddle Mountain	PPD	332-333	4150-4151
Bfc 99	Saddle Mountain	PPD	332-333	4150-4151
Bfc100	Saddle Mountain	PPD	332-333	4150-4151

Bfc 101	Saddle Mountain	PPD	332-333	4150-4151
Bfc 102	Saddle Mountain	PPD	332-333	4151
Bfc 103	Saddle Mountain	PPD	331-332	4149-4150
Bfc 104	North Mineral County	FCT (intracaldera N)	~330-335	~4195-4200
Bfc 105	North Mineral County	FCT (intracaldera N)	~330-335	~4195-4200
Bfc 106	North Mineral County	FCT (intracaldera N)	~330-335	~4195-4200
Bfc 107	Rio Grande	FCT (outflow)	~350	~4190
Bfc 108	Rio Grande	FCT (outflow)	~350	~4190
Bfc 109	Rio Grande	FCT (outflow)	~350	~4180
Bfc 110	Rio Grande	FCT (outflow)	~355	~4180
Bfc 111	Rio Grande	FCT (outflow)	~360	~4180
Bfc 112	Rio Grande	FCT (outflow)	~360	~4180
Bfc 113	Rio Grande	FCT (outflow)	~360	~4180
Bfc 114	Wolf Creek Pass	PPD	336-337	4150-4151
Bfc 115	Elk Park	Nutras Creek Dacite	337-338	~4211
Bfc 116	Saguache Park	FCT (Intracaldera N)	~330	~4210
Bfc 117	Saguache Park	FCT (Intracaldera N)	~330	~4210
Bfc 118	Saguache Park	FCT (Intracaldera N)	~330	~4210
Bfc 119	Saguache Park	FCT (Intracaldera N)	~330	~4210
Bfc 120	Saguache Park	FCT (Intracaldera N)	~330	~4210
Bfc121	Saguache Park	FCT (Intracaldera N)	~330	~4210
Bfc122	Saguache Park	FCT (Intracaldera N)	~330	~4210
Bfc123	Saguache Park	FCT (Intracaldera N)	~330	~4210
Bfc124	Saguache Park	FCT (outflow)	~350	~4205
Bfc125	Saguache Park	FCT (outflow)	~360	~4220
Bfc126	Saddle Mountain	PPD	332-333	4150-4151

Bfc127	Halfmoon Pass	FCT (Intracaldera)	338-339	~4197
Bfc128	Halfmoon Pass	FCT (Intracaldera)	338-339	~4197
Bfc129	Halfmoon Pass	FCT (Intracaldera)	~339	4197-4198
Bfc130	Halfmoon Pass	FCT (Intracaldera)	~339	4197-4198
Bfc131	Halfmoon Pass	FCT (Intracaldera)	~339	4197-4198
Bfc132	Halfmoon Pass	FCT (Intracaldera)	~339	~4198
Bfc133	Halfmoon Pass	FCT (Intracaldera)	339-340	4198
Bfc134	Halfmoon Pass	FCT (Intracaldera)	338-339	4198
Bfc135	Halfmoon Pass	FCT (Intracaldera)	336-337	4199-4200
Bfc136	Halfmoon Pass	FCT (Intracaldera)	336	4200-4201
Bfc137	San Luis Peak	FCT (Intracaldera)	334-335	4199-4200
Bfc138	San Luis Peak	FCT (Intracaldera)	333-334	4199-4200
Bfc139	Wolf Creek Pass	PPD	340-341	4150-4151
Bfc140	Pagosa Peak	FCT (outflow)	314-315	4152-4153
Bfc141	Pagosa Peak	FCT (outflow)	314-315	4152-4153
Bfc142	Pagosa Peak	PPD	322-323	4144-4145
Bfc143	Saddle Mountain	FCT (outflow)	327-328	4145-4146
Bfc144	Saddle Mountain	FCT (outflow)	326-327	4145-4146
Bfc145	Saddle Mountain	FCT (outflow)	326-327	4145-4146
Bfc146	Saddle Mountain	PPD	326-327	4147-4148
Bfc147	Saddle Mountain	PPD	327-328	4147-4148
Bfc148	Saddle Mountain	PPD	325-326	4146-4147
Bfc149	Saddle Mountain	PPD	324-325	4147-4148
Bfc150	Saddle Mountain	PPD	323-324	4147-4148
Bfc151	Saddle Mountain	PPD	323-324	4147-4148
Bfc152	Saddle Mountain	PPD	323-324	4147-4148

Bfc153	South River Peak	South River volcanics	332-333	4165-4166
Bfc154	Workman Creek	FCT (intracaldera C)	~317	~4180
Bfc155	Workman Creek	FCT (intracaldera C)	~317	~4180
Bfc156	Workman Creek	FCT (intracaldera C)	~317	~4180
Bfc157	South River Peak	FCT (intracaldera S)	332-333	4161-4162
Bfc158	South River Peak	FCT (outflow)	333-334	4161-4162
Bfc159	Workman Creek	FCT (intracaldera C)	~320	4170-4175
Bfc160	Workman Creek	FCT (intracaldera C)	~320	4170-4175
Bfc161	Workman Creek	FCT (intracaldera C)	~320	4170-4175
Bfc162	Workman Creek	FCT (intracaldera C)	~320	4170-4175
Bfc163	Workman Creek	FCT (intracaldera C)	~320	4170-4175
Bfc164	Workman Creek	FCT (intracaldera C)	~320	4170-4175
Bfc165	South River Peak	PPD	332-333	4165-4166
Bfc166	South River Peak	FCT (outflow)	332-333	4155
Bfc167	Pagosa Peak	PPD	~316	41504151
Bfc168	Pagosa Peak	PPD	~316	41504151
Bfc169	Pagosa Peak	PPD	316-317	4148-4149
Bfc170	Pagosa Peak	PPD	316-317	4148-4149
Bfc171	Pagosa Peak	PPD	316-317	4148-4149
Bfc172	Pagosa Peak	PPD	319-320	4144-4145
Bfc173	Pagosa Peak	PPD	322-323	4145-4146
Bfc174	Saddle Mountain	PPD	332-333	4149-4150
Bfc175	Saddle Mountain	PPD	329-330	4150-4151
Bfc176	South River Peak	FCT (Intracaldera S)	325-326	4153-4154
Bfc177	South River Peak	FCT (Intracaldera S)	325-326	4153-4154
Bfc178	South River Peak	FCT (Intracaldera S)	325-326	4153-4154

Bfc179	Saddle Mountain	FCT (intracaldera S)	325-326	4149-4150
Bfc180	Saddle Mountain	PPD	326-327	4145-4146
Bfc181	Saddle Mountain	PPD	326-327	4145-4146
Bfc182	Palomino Mountain	FCT (outflow)	314-315	4155-4156
Bfc183	Palomino Mountain	FCT (outflow)	312-313	4155-4156
Bfc184	Halfmoon Pass	FCT (Intracaldera N)	342-343	4196-4198
Bfc185	Halfmoon Pass	FCT (Intracaldera N)	340-342	4195-4200
Bfc186	Halfmoon Pass	FCT (Intracaldera N)	~340	4195-4200
Bfc187	Halfmoon Pass	FCT (Intracaldera N)	340-341	4195-4200
Bfc188	Halfmoon Pass	FCT (Intracaldera N)	338-340	~4200
Bfc189	Halfmoon Pass	FCT (Intracaldera N)	340-342	4200-4205
Bfc190	Halfmoon Pass	FCT (Intracaldera N)	340-345	4200-4205
Bfc191	Halfmoon Pass	FCT (Intracaldera N)	343-345	4200-4205
Bfc192	Saguache CO	FCT (Intracaldera N)	354-355	~4210
Bfc193	Saguache CO	FCT (Intracaldera N)	354-355	~4210
Bfc194	Saguache CO	FCT (Intracaldera N)	354-355	~4210
Bfc195	Fish Canyon	FCT (outflow)		
98fc1	Wolf Creek Pass	FCT(outflow)	337-338	4151-4152
98fc2	Mount Hope	FCT (outflow)	338-339	4151-4152
98fc3	Wolf Creek Pass	FCT(outflow)	339-340	4151-4152
98fc4	Wolf Creek Pass	FCT(outflow)	340-341	4150-4151
98fc5	Cimarrona Peak	FCT(outflow)	310-311	4157-4158
98fc6	Cimarrona Peak	FCT(outflow)	312	4159-4160
98fc7	Cimarrona Peak	FCT(outflow)	311-312	4159-4160
98fc8	Cimarrona Peak	FCT(outflow)	312	4160-4161
98fc9	Saddle Mountain	FCT(outflow)	326-327	4145-4146

98ppd1	Wolf Creek Pass	PPD	336-337	4150-4151
98ppd2	Wolf Creek Pass	PPD	337-338	4150-4151
98ppd3	Wolf Creek Pass	PPD	340-341	4150-4151
98ppd4	Saddle Mountain	PPD	326-327	4145-4146
98ppd5	Saddle Mountain	PPD	326-327	4145-4146
98ppd6	Saddle Mountain	PPD	326-327	4145-4146
98ppd7	Saddle Mountain	PPD	326-327	4145-4146

All MLX samples on Halfmoon Pass quad (Upper Intracaldera FCT)

MLXQMI 1 to 3	Mafic inclusions	335-345	4195-4205
MLXCsGr1 to 16	Coarse-grained xenoliths	335-345	4195-4205
MLXFnGr 1 to 3	Fine-grained xenoliths	335-345	4195-4205
MLX Big and Big'	Bimodal xenoliths	335-345	4195-4205
MLXAmph 1 to 4	Amphibolite xenolith	335-345	4195-4205
MLXSHSG1-2	Coarse-grained glass bearing rocks	335-345	4195-4205

Annexe 3: Major element analyses and structural formulae of single electron microprobe analyses in Fish Canyon hornblendes

Label	68hb.I1	68hb.I2	68hb.I3	68hb.I4	68hb.I5	68hb.I6	68hb.I7	68hb.I8	68hb.I9	68hb.I10	68hb.I11	68hb.I12
SiO_2	47.56	48.31	48.73	48.72	48.75	49.09	48.66	49.19	49.12	48.83	48.80	48.47
TiO_2	1.34	1.30	1.22	1.24	1.24	1.23	1.25	1.19	1.16	1.18	1.14	1.20
Al_2O_3	6.97	7.03	6.77	6.39	6.52	6.42	6.38	6.26	6.17	6.19	6.41	6.34
FeO_{tot}	14.17	14.06	13.52	13.62	13.41	13.62	13.42	13.30	13.20	13.48	13.63	13.60
MnO	0.68	0.71	0.76	0.73	0.81	0.82	0.67	0.67	0.74	0.76	0.79	0.74
MgO	13.98	13.99	14.37	14.40	14.54	14.38	14.48	14.57	14.54	14.74	14.39	14.65
CaO	11.96	11.96	11.87	12.01	11.97	11.95	11.78	12.06	12.10	11.84	11.81	12.02
Na_2O	1.49	1.51	1.45	1.33	1.38	1.49	1.38	1.41	1.39	1.41	1.39	1.39
K_2O	0.84	0.79	0.72	0.77	0.70	0.71	0.68	0.69	0.68	0.69	0.71	0.71
F	0.28	0.35	0.23	0.31	0.37	0.31	0.33	0.28	0.34	0.29	0.32	0.27
Cl	0.11	0.09	0.09	0.08	0.06	0.09	0.08	0.09	0.08	0.06	0.10	0.09
Sum Oxides	99.38	100.11	99.73	99.60	99.73	100.12	99.10	99.72	99.52	99.47	99.50	99.48
Si	6.87	6.92	6.96	6.99	6.97	7.00	6.99	7.04	7.05	6.98	6.99	6.95
Al^{IV}	1.13	1.08	1.04	1.01	1.03	1.00	1.01	0.96	0.95	1.02	1.01	1.05
Σ(T)	8.00	8.00	8.00	8.00	8.00	8.00	8.00	8.00	8.00	8.00	8.00	8.00
Al^{VI}(M1-2-3)	0.05	0.10	0.10	0.07	0.07	0.08	0.07	0.09	0.09	0.03	0.07	0.02
Ti(M1-2-3)	0.15	0.14	0.13	0.13	0.13	0.13	0.13	0.13	0.13	0.13	0.12	0.13
Fe^{3+}(M1-2-3)	0.52	0.46	0.51	0.48	0.52	0.45	0.53	0.40	0.38	0.59	0.54	0.57
Fe^{2+}(M1-2-3)	1.19	1.22	1.11	1.15	1.08	1.17	1.08	1.19	1.21	1.02	1.09	1.06
Mg(M1-2-3)	3.01	2.99	3.06	3.08	3.10	3.06	3.10	3.11	3.11	3.14	3.07	3.13
Mn(M1-2-3)	0.08	0.09	0.09	0.09	0.10	0.10	0.08	0.08	0.09	0.09	0.10	0.09
Σ	13.00	13.00	13.00	13.00	13.00	13.00	13.00	13.00	13.00	13.00	13.00	13.00
Ca(M4)	1.85	1.84	1.82	1.84	1.83	1.83	1.81	1.85	1.86	1.81	1.81	1.85
Na(M4)	0.15	0.16	0.18	0.16	0.17	0.17	0.19	0.15	0.14	0.19	0.19	0.15
Σ	15.00	15.00	15.00	15.00	15.00	15.00	15.00	15.00	15.00	15.00	15.00	15.00
Na(A)	0.27	0.25	0.22	0.22	0.22	0.24	0.20	0.24	0.25	0.21	0.20	0.23
K(A)	0.15	0.14	0.13	0.14	0.13	0.13	0.12	0.13	0.13	0.13	0.13	0.13
Σ	15.42	15.40	15.35	15.36	15.34	15.37	15.32	15.37	15.37	15.33	15.33	15.36

Label	196hb4.1	196hb4.2	196hb4.3	196hb4.4	196hb4.5	196hb4.6	196hb4.7	196hb4.8	196hb4.9	196hb4.10	196hb4.11	196hb4.12
SiO_2	48.66	48.63	48.54	48.40	48.46	49.63	49.37	49.86	49.01	48.97	48.95	48.96
TiO_2	1.19	1.15	1.15	1.23	1.22	1.12	1.08	1.03	1.08	1.13	1.12	1.10
Al_2O_3	6.16	6.01	6.14	6.24	6.21	5.75	5.60	5.53	5.60	5.65	5.80	5.74
FeO_{tot}	13.71	13.94	13.57	13.47	13.81	13.48	12.95	13.20	13.02	12.63	13.00	12.99
MnO	0.76	0.72	0.79	0.79	0.81	0.88	0.83	0.88	0.85	1.02	1.02	0.96
MgO	14.06	14.09	14.02	13.83	13.83	14.14	14.56	14.41	14.35	14.37	14.37	14.43
CaO	11.57	11.76	11.55	11.52	11.27	11.48	11.44	11.48	11.38	11.37	11.51	11.60
Na_2O	1.24	1.29	1.27	1.39	1.33	1.27	1.22	1.24	1.26	1.37	1.22	1.22
K_2O	0.67	0.65	0.68	0.68	0.72	0.63	0.57	0.60	0.60	0.64	0.66	0.66
F	0.13	0.10	0.13	0.14	0.13	0.13	0.12	0.09	0.13	0.13	0.12	0.13
Cl	0.02	0.02	0.02	0.02	0.02	0.02	0.02	0.02	0.03	0.03	0.02	0.02
Sum Oxides	100.68	100.87	100.33	100.10	100.34	100.98	100.29	100.86	99.81	99.73	100.29	100.29
Si	7.04	7.04	7.05	7.05	7.03	7.14	7.13	7.17	7.12	7.13	7.09	7.09
Al^{IV}	0.96	0.96	0.95	0.95	0.97	0.86	0.87	0.83	0.88	0.87	0.91	0.91
Σ(T)	8.00	8.00	8.00	8.00	8.00	8.00	8.00	8.00	8.00	8.00	8.00	8.00
Al^{VI}(M1-2-3)	0.09	0.06	0.10	0.12	0.10	0.12	0.08	0.11	0.08	0.10	0.08	0.07
Ti(M1-2-3)	0.13	0.13	0.13	0.13	0.13	0.12	0.12	0.11	0.12	0.12	0.12	0.12
Fe^{3+}(M1-2-3)	3.03	3.04	3.03	3.00	2.99	3.03	3.13	3.09	3.11	3.12	3.10	3.12
Fe^{2+}(M1-2-3)	1.10	1.16	1.12	1.20	1.09	1.13	1.00	1.08	1.04	1.06	1.02	1.04
Mg(M1-2-3)	0.56	0.53	0.53	0.44	0.59	0.49	0.57	0.51	0.54	0.48	0.56	0.53
Mn(M1-2-3)	0.09	0.09	0.10	0.10	0.10	0.11	0.10	0.11	0.10	0.13	0.13	0.12
Σ	13.00	13.00	13.00	13.00	13.00	13.00	13.00	13.00	13.00	13.00	13.00	13.00
Ca(M4)	1.79	1.82	1.80	1.80	1.75	1.77	1.77	1.77	1.77	1.77	1.79	1.80
Na(M4)	0.21	0.18	0.20	0.20	0.25	0.23	0.23	0.23	0.23	0.23	0.21	0.20
Σ	15.00	15.00	15.00	15.00	15.00	15.00	15.00	15.00	15.00	15.00	15.00	15.00
Na(A)	0.14	0.18	0.15	0.19	0.13	0.12	0.11	0.11	0.13	0.16	0.13	0.14
K(A)	0.12	0.12	0.13	0.13	0.13	0.12	0.10	0.11	0.11	0.12	0.12	0.12
Σ	15.26	15.30	15.28	15.32	15.26	15.24	15.22	15.22	15.24	15.28	15.25	15.26

Note: Data points with totals lower than 98 and higher than 101 were excluded from this data table and from profiles

Structural formulas were calculated using the Leake et al. (1997) method (13eCNK)

Label	68hb.l13	68hb.l14	68hb.l15	68hb.l16	68hb.l17	68hb.l18	68hb.l19	68hb.l20	68hb.l21	68hb.l22	68hb.l23	68hb.l24
SiO_2	48.66	48.87	48.68	48.68	49.04	49.20	48.37	48.99	48.62	48.97	48.92	48.30
TiO_2	1.19	1.19	1.28	1.21	1.17	1.18	1.20	1.19	1.14	1.14	1.25	1.27
Al_2O_3	6.44	6.47	6.49	6.49	6.20	6.10	6.03	6.14	6.11	6.01	6.10	6.39
FeO_{tot}	13.45	13.18	13.65	13.43	13.54	13.40	13.30	13.30	13.48	13.49	13.57	13.48
MnO	0.75	0.76	0.79	0.73	0.79	0.80	0.72	0.76	0.80	0.76	0.77	0.81
MgO	14.51	14.37	14.44	14.27	14.67	14.61	14.52	14.68	14.63	14.63	14.53	14.30
CaO	12.03	11.74	11.93	11.68	11.98	11.84	11.92	11.86	11.94	11.82	12.00	11.84
Na_2O	1.37	1.51	1.45	1.38	1.37	1.34	1.39	1.38	1.35	1.28	1.36	1.40
K_2O	0.71	0.71	0.75	0.72	0.70	0.69	0.72	0.70	0.68	0.72	0.67	0.68
F	0.31	0.32	0.32	0.26	0.28	0.26	0.29	0.28	0.31	0.23	0.30	0.28
Cl	0.08	0.08	0.08	0.09	0.09	0.11	0.09	0.09	0.07	0.06	0.10	0.13
Sum Oxides	99.51	99.19	99.85	98.94	99.83	99.52	98.55	99.37	99.14	99.11	99.56	98.87
Si	6.98	7.02	6.96	7.00	7.00	7.03	7.01	7.02	6.99	7.02	7.01	6.97
Al^{IV}	1.02	0.98	1.04	1.00	1.00	0.97	0.99	0.98	1.01	0.98	0.99	1.03
Σ(T)	8.00	8.00	8.00	8.00	8.00	8.00	8.00	8.00	8.00	8.00	8.00	8.00
Al^{VI}(M1-2-3)	0.07	0.12	0.06	0.10	0.04	0.06	0.04	0.05	0.02	0.04	0.04	0.06
Ti(M1-2-3)	0.13	0.13	0.14	0.13	0.13	0.13	0.13	0.13	0.12	0.12	0.13	0.14
Fe^{3+}(M1-2-3)	0.49	0.44	0.51	0.51	0.54	0.53	0.47	0.52	0.56	0.57	0.49	0.51
Fe^{2+}(M1-2-3)	1.12	1.15	1.12	1.10	1.08	1.07	1.14	1.07	1.06	1.04	1.14	1.11
Mg(M1-2-3)	3.10	3.08	3.08	3.06	3.12	3.11	3.13	3.13	3.14	3.13	3.10	3.08
Mn(M1-2-3)	0.09	0.09	0.10	0.09	0.10	0.10	0.09	0.09	0.10	0.09	0.09	0.10
Σ	13.00	13.00	13.00	13.00	13.00	13.00	13.00	13.00	13.00	13.00	13.00	13.00
Ca(M4)	1.85	1.81	1.83	1.80	1.83	1.81	1.85	1.82	1.84	1.82	1.84	1.83
Na(M4)	0.15	0.19	0.17	0.20	0.17	0.19	0.15	0.18	0.16	0.18	0.16	0.17
Σ	15.00	15.00	15.00	15.00	15.00	15.00	15.00	15.00	15.00	15.00	15.00	15.00
Na(A)	0.23	0.23	0.23	0.18	0.21	0.18	0.24	0.20	0.21	0.17	0.22	0.22
K(A)	0.13	0.13	0.14	0.13	0.13	0.13	0.13	0.13	0.13	0.13	0.12	0.12
Σ	15.36	15.36	15.37	15.32	15.34	15.31	15.37	15.33	15.34	15.30	15.34	15.35

Label	196hb4.13	196hb4.15	196hb4.16	196hb4.17	196hb4.18	196hb4.19	196hb4.20	196hb4.21	196hb4.22	196hb4.23	196hb4.24	196hb4.25
SiO_2	49.03	49.52	49.17	49.52	49.04	49.07	49.30	48.80	49.12	48.77	48.75	48.50
TiO_2	1.09	1.09	1.10	1.11	1.06	1.16	1.10	1.15	1.08	1.14	1.14	1.14
Al_2O_3	5.79	5.56	5.61	5.54	5.54	5.75	5.68	5.75	5.64	5.92	5.78	5.91
FeO_{tot}	13.16	12.89	12.95	13.09	12.66	12.72	12.62	12.96	12.98	13.43	13.05	12.90
MnO	0.90	0.98	1.01	0.95	0.97	0.96	0.99	0.95	0.88	0.91	0.95	0.88
MgO	14.51	14.58	14.63	14.51	14.33	14.50	14.36	14.46	14.53	14.46	14.29	14.15
CaO	11.34	11.42	11.42	11.34	11.33	11.48	11.46	11.47	11.51	11.31	11.50	11.50
Na_2O	1.35	1.26	1.32	1.19	1.26	1.19	1.30	1.35	1.22	1.29	1.41	1.33
K_2O	0.66	0.60	0.59	0.63	0.64	0.65	0.63	0.65	0.69	0.68	0.68	0.68
F	0.15	0.13	0.14	0.13	0.13	0.12	0.12	0.13	0.12	0.12	0.12	0.11
Cl	0.02	0.02	0.02	0.02	0.02	0.02	0.02	0.02	0.02	0.02	0.02	0.02
Sum Oxides	100.54	100.60	100.53	100.60	99.43	100.11	99.99	100.18	100.30	100.69	100.13	99.53
Si	7.08	7.13	7.09	7.13	7.15	7.11	7.15	7.08	7.11	7.03	7.09	7.09
Al^{IV}	0.92	0.87	0.91	0.87	0.85	0.89	0.85	0.92	0.89	0.97	0.91	0.91
Σ(T)	8.00	8.00	8.00	8.00	8.00	8.00	8.00	8.00	8.00	8.00	8.00	8.00
Al^{VI}(M1-2-3)	0.06	0.08	0.05	0.07	0.10	0.09	0.12	0.06	0.07	0.04	0.08	0.11
Ti(M1-2-3)	0.12	0.12	0.12	0.12	0.12	0.13	0.12	0.13	0.12	0.12	0.12	0.13
Fe^{3+}(M1-2-3)	3.12	3.13	3.15	3.12	3.12	3.13	3.11	3.13	3.13	3.11	3.10	3.08
Fe^{2+}(M1-2-3)	0.97	0.99	0.95	0.97	1.05	1.00	1.09	1.02	1.02	0.92	1.10	1.13
Mg(M1-2-3)	0.62	0.56	0.61	0.61	0.50	0.54	0.44	0.55	0.55	0.70	0.48	0.45
Mn(M1-2-3)	0.11	0.12	0.12	0.12	0.12	0.12	0.12	0.12	0.11	0.11	0.12	0.11
Σ	13.00	13.00	13.00	13.00	13.00	13.00	13.00	13.00	13.00	13.00	13.00	13.00
Ca(M4)	1.75	1.76	1.77	1.75	1.77	1.78	1.78	1.78	1.78	1.75	1.79	1.80
Na(M4)	0.25	0.24	0.23	0.25	0.23	0.22	0.22	0.22	0.22	0.25	0.21	0.20
Σ	15.00	15.00	15.00	15.00	15.00	15.00	15.00	15.00	15.00	15.00	15.00	15.00
Na(A)	0.13	0.11	0.13	0.08	0.13	0.11	0.15	0.16	0.13	0.11	0.19	0.18
K(A)	0.12	0.11	0.11	0.12	0.12	0.12	0.12	0.12	0.13	0.13	0.13	0.13
Σ	15.25	15.22	15.24	15.20	15.25	15.23	15.26	15.28	15.25	15.23	15.31	15.30

Label	68hb.I25	68hb.I26	68hb.I27	68hb.I28	68hb.I29	68hb.I30	68hb.I31	68hb.I32	68hb.I33	68hb.I34	68hb.I35	68hb.I36
SiO_2	48.05	48.33	48.21	48.84	49.24	49.44	49.55	49.94	49.49	49.98	49.76	49.36
TiO_2	1.33	1.37	1.30	1.24	1.17	1.14	1.10	1.17	1.09	1.10	1.10	1.11
Al_2O_3	6.64	6.58	6.51	6.29	5.88	5.72	5.78	5.57	5.63	5.62	5.61	5.63
FeO_{tot}	13.95	14.02	13.85	13.53	13.24	13.08	13.04	13.12	13.08	12.90	12.87	12.97
MnO	0.81	0.81	0.78	0.79	0.83	0.79	0.77	0.76	0.86	0.81	0.76	0.79
MgO	14.18	14.08	14.31	14.56	14.59	14.86	14.77	14.42	15.07	14.98	15.00	14.86
CaO	11.94	11.86	11.87	12.05	11.84	11.81	11.94	11.69	12.01	12.02	11.90	11.72
Na_2O	1.47	1.45	1.58	1.50	1.26	1.28	1.39	1.30	1.22	1.30	1.22	1.29
K_2O	0.79	0.75	0.73	0.70	0.64	0.62	0.66	0.61	0.62	0.63	0.62	0.62
F	0.24	0.28	0.30	0.32	0.22	0.29	0.28	0.33	0.25	0.22	0.36	0.30
Cl	0.10	0.11	0.14	0.11	0.06	0.11	0.09	0.07	0.09	0.09	0.07	0.09
Sum Oxides	99.50	99.64	99.57	99.93	98.97	99.16	99.39	98.96	99.39	99.65	99.28	98.74
Si	6.91	6.94	6.93	6.99	7.07	7.08	7.10	7.17	7.07	7.12	7.11	7.09
Al^{IV}	1.09	1.06	1.07	1.01	0.93	0.92	0.90	0.83	0.93	0.88	0.89	0.91
Σ(T)	8.00	8.00	8.00	8.00	8.00	8.00	8.00	8.00	8.00	8.00	8.00	8.00
Al^{VI}(M1-2-3)	0.04	0.05	0.03	0.05	0.06	0.04	0.07	0.12	0.01	0.07	0.06	0.04
Ti(M1-2-3)	0.14	0.15	0.14	0.13	0.13	0.12	0.12	0.13	0.12	0.12	0.12	0.12
Fe^{3+}(M1-2-3)	0.53	0.52	0.53	0.46	0.51	0.54	0.42	0.39	0.57	0.43	0.50	0.54
Fe^{2+}(M1-2-3)	1.15	1.17	1.14	1.16	1.08	1.03	1.14	1.19	1.00	1.11	1.04	1.01
Mg(M1-2-3)	3.04	3.02	3.07	3.11	3.12	3.17	3.15	3.09	3.21	3.18	3.20	3.18
Mn(M1-2-3)	0.10	0.10	0.10	0.10	0.10	0.10	0.09	0.09	0.10	0.10	0.09	0.10
Σ	13.00	13.00	13.00	13.00	13.00	13.00	13.00	13.00	13.00	13.00	13.00	13.00
Ca(M4)	1.84	1.83	1.83	1.85	1.82	1.81	1.83	1.80	1.84	1.83	1.82	1.80
Na(M4)	0.16	0.17	0.17	0.15	0.18	0.19	0.17	0.20	0.16	0.17	0.18	0.20
Σ	15.00	15.00	15.00	15.00	15.00	15.00	15.00	15.00	15.00	15.00	15.00	15.00
Na(A)	0.25	0.23	0.27	0.26	0.17	0.17	0.22	0.16	0.17	0.20	0.16	0.17
K(A)	0.14	0.14	0.13	0.13	0.12	0.11	0.12	0.11	0.11	0.11	0.11	0.11
Σ	15.39	15.37	15.40	15.39	15.29	15.28	15.34	15.27	15.29	15.31	15.27	15.28

Label	196hb4.26	196hb4.27	196hb4.28	196hb4.29	196hb4.30	196hb4.31	196hb4.32	196hb4.33	196hb4.34	196hb4.35	196hb4.36	196hb4.37
SiO_2	48.55	48.13	48.51	47.90	48.58	47.96	47.88	47.87	48.20	47.74	48.10	48.01
TiO_2	1.14	1.18	1.21	1.25	1.26	1.24	1.26	1.23	1.37	1.23	1.27	1.31
Al_2O_3	5.94	6.07	6.06	6.26	6.16	6.41	6.35	6.44	6.43	6.43	6.43	6.35
FeO_{tot}	13.27	12.99	13.21	12.99	13.27	13.73	13.63	13.44	13.93	13.65	13.38	13.91
MnO	0.92	0.89	0.93	0.86	0.88	0.92	1.01	0.94	0.89	0.90	0.92	0.88
MgO	14.22	13.80	14.04	14.06	13.91	14.01	13.78	13.88	13.87	13.94	13.78	14.00
CaO	11.44	11.26	11.44	11.44	11.55	11.26	11.54	11.39	11.54	11.46	11.50	11.36
Na_2O	1.34	1.33	1.37	1.35	1.36	1.37	1.41	1.44	1.38	1.32	1.45	1.41
K_2O	0.73	0.70	0.67	0.73	0.69	0.77	0.75	0.77	0.73	0.73	0.69	0.77
F	0.10	0.15	0.13	0.10	0.14	0.12	0.11	0.12	0.12	0.15	0.11	0.14
Cl	0.02	0.02	0.02	0.02	0.02	0.03	0.03	0.02	0.02	0.02	0.02	0.02
Sum Oxides	100.18	98.87	100.03	99.42	100.21	100.45	100.24	100.03	100.99	100.10	100.05	100.76
Si	7.05	7.08	7.06	7.01	7.07	6.96	6.99	6.98	6.97	6.96	7.01	6.96
Al^{IV}	0.95	0.92	0.94	0.99	0.93	1.04	1.01	1.02	1.03	1.04	0.99	1.04
Σ(T)	8.00	8.00	8.00	8.00	8.00	8.00	8.00	8.00	8.00	8.00	8.00	8.00
Al^{VI}(M1-2-3)	0.07	0.13	0.10	0.10	0.12	0.06	0.08	0.09	0.07	0.06	0.12	0.04
Ti(M1-2-3)	0.12	0.13	0.13	0.14	0.14	0.14	0.14	0.13	0.15	0.13	0.14	0.14
Fe^{3+}(M1-2-3)	3.08	3.03	3.05	3.07	3.02	3.03	3.00	3.02	2.99	3.03	3.00	3.02
Fe^{2+}(M1-2-3)	1.06	1.13	1.11	1.09	1.19	0.98	1.15	1.09	1.12	1.04	1.18	1.03
Mg(M1-2-3)	0.55	0.46	0.50	0.51	0.42	0.69	0.52	0.54	0.57	0.62	0.45	0.65
Mn(M1-2-3)	0.11	0.11	0.11	0.11	0.11	0.11	0.12	0.12	0.11	0.11	0.11	0.11
Σ	13.00	13.00	13.00	13.00	13.00	13.00	13.00	13.00	13.00	13.00	13.00	13.00
Ca(M4)	1.78	1.77	1.78	1.79	1.80	1.75	1.80	1.78	1.79	1.79	1.80	1.76
Na(M4)	0.22	0.23	0.22	0.21	0.20	0.25	0.20	0.22	0.21	0.21	0.20	0.24
Σ	15.00	15.00	15.00	15.00	15.00	15.00	15.00	15.00	15.00	15.00	15.00	15.00
Na(A)	0.16	0.15	0.17	0.18	0.18	0.14	0.20	0.19	0.17	0.16	0.21	0.16
K(A)	0.14	0.13	0.12	0.14	0.13	0.14	0.14	0.14	0.13	0.14	0.13	0.14
Σ	15.29	15.29	15.29	15.31	15.31	15.28	15.34	15.33	15.31	15.30	15.34	15.30

Label	68hb.l37	68hb.l38	68hb.l39	68hb.l40	68hb.l41	68hb.l42	68hb.l43	68hb.l44	68hb.l45	68hb.l46	68hb.l47	68hb.l48
SiO_2	49.71	49.45	49.33	49.59	49.97	49.83	49.85	49.25	49.29	49.51	49.74	49.57
TiO_2	1.09	1.09	1.08	1.04	1.03	1.04	1.06	1.08	1.12	1.13	1.16	1.11
Al_2O_3	5.63	5.71	5.60	5.52	5.48	5.45	5.49	5.65	5.57	5.64	5.64	5.62
FeO_{tot}	12.89	13.06	13.37	13.02	13.04	12.87	12.89	12.73	13.35	13.26	12.93	13.38
MnO	0.79	0.78	0.84	0.80	0.78	0.76	0.85	0.95	0.87	0.86	0.91	0.83
MgO	14.95	14.85	15.03	15.13	15.10	15.06	15.07	15.05	14.99	15.03	15.03	14.95
CaO	12.02	11.93	11.81	11.77	11.88	11.86	11.73	11.93	11.73	11.92	11.79	11.89
Na_2O	1.28	1.38	1.40	1.31	1.26	1.22	1.27	1.28	1.28	1.37	1.26	1.30
K_2O	0.66	0.64	0.59	0.63	0.58	0.60	0.61	0.60	0.62	0.62	0.65	0.62
F	0.28	0.26	0.31	0.32	0.26	0.30	0.33	0.29	0.33	0.31	0.29	0.33
Cl	0.09	0.08	0.08	0.09	0.06	0.07	0.06	0.14	0.09	0.09	0.11	0.07
Sum Oxides	99.38	99.21	99.43	99.21	99.43	99.06	99.21	98.94	99.24	99.73	99.51	99.67
Si	7.11	7.09	7.05	7.08	7.12	7.13	7.12	7.07	7.05	7.06	7.09	7.07
Al^{IV}	0.89	0.91	0.95	0.92	0.88	0.87	0.88	0.93	0.95	0.94	0.91	0.93
Σ(T)	8.00	8.00	8.00	8.00	8.00	8.00	8.00	8.00	8.00	8.00	8.00	8.00
Al^{VI}(M1-2-3)	0.06	0.05	-0.01	0.01	0.04	0.04	0.04	0.02	-0.02	0.00	0.03	0.01
Ti(M1-2-3)	0.12	0.12	0.12	0.11	0.11	0.11	0.11	0.12	0.12	0.12	0.12	0.12
Fe^{3+}(M1-2-3)	0.44	0.46	0.63	0.60	0.54	0.52	0.57	0.54	0.67	0.57	0.57	0.58
Fe^{2+}(M1-2-3)	1.10	1.10	0.97	0.96	1.01	1.02	0.97	0.98	0.93	1.01	0.97	1.01
Mg(M1-2-3)	3.19	3.17	3.20	3.22	3.21	3.21	3.21	3.22	3.20	3.19	3.19	3.18
Mn(M1-2-3)	0.10	0.09	0.10	0.10	0.09	0.09	0.10	0.12	0.11	0.10	0.11	0.10
Σ	13.00	13.00	13.00	13.00	13.00	13.00	13.00	13.00	13.00	13.00	13.00	13.00
Ca(M4)	1.84	1.83	1.81	1.80	1.81	1.82	1.79	1.83	1.80	1.82	1.80	1.82
Na(M4)	0.16	0.17	0.19	0.20	0.19	0.18	0.21	0.17	0.20	0.18	0.20	0.18
Σ	15.00	15.00	15.00	15.00	15.00	15.00	15.00	15.00	15.00	15.00	15.00	15.00
Na(A)	0.20	0.21	0.19	0.16	0.16	0.16	0.15	0.19	0.15	0.20	0.15	0.18
K(A)	0.12	0.12	0.11	0.11	0.10	0.11	0.11	0.11	0.11	0.11	0.12	0.11
Σ	15.32	15.33	15.30	15.28	15.27	15.27	15.26	15.30	15.27	15.31	15.27	15.29

Label	196hb4.38	196hb4.39	196hb4.40	196hb4.41	196hb4.42	196hb4.43	196hb4.44	196hb4.45	196hb4.46	196hb4.47	196hb4.48	196hb4.49
SiO_2	48.42	48.32	48.24	48.25	48.00	48.02	47.99	47.99	48.05	48.13	48.19	48.61
TiO_2	1.29	1.30	1.27	1.28	1.30	1.32	1.38	1.32	1.35	1.33	1.33	1.32
Al_2O_3	6.32	6.32	6.43	6.37	6.28	6.41	6.27	6.37	6.28	6.37	6.32	6.42
FeO_{tot}	13.56	13.30	13.42	13.42	13.65	13.65	13.18	13.41	13.56	13.55	13.48	13.55
MnO	0.95	0.93	0.79	0.85	0.94	0.86	0.89	0.85	0.86	0.83	0.90	0.87
MgO	14.00	14.08	13.91	13.87	13.91	13.81	13.79	13.87	13.86	13.79	14.01	13.96
CaO	11.53	11.52	11.46	11.35	11.63	11.45	11.46	11.38	11.35	11.36	11.40	11.53
Na_2O	1.28	1.38	1.46	1.47	1.37	1.47	1.38	1.48	1.35	1.42	1.31	1.43
K_2O	0.74	0.71	0.75	0.69	0.69	0.70	0.71	0.71	0.71	0.70	0.70	0.69
F	0.15	0.14	0.13	0.12	0.15	0.11	0.11	0.15	0.10	0.15	0.13	0.13
Cl	0.02	0.03	0.02	0.02	0.02	0.02	0.02	0.02	0.02	0.02	0.02	0.02
Sum Oxides	100.76	100.51	100.30	100.16	100.39	100.31	99.58	99.97	100.01	100.09	100.30	100.98
Si	7.01	7.01	7.02	7.02	6.99	6.99	7.03	7.00	7.00	7.01	7.00	7.02
Al^{IV}	0.99	0.99	0.98	0.98	1.01	1.01	0.97	1.00	1.00	0.99	1.00	0.98
Σ(T)	8.00	8.00	8.00	8.00	8.00	8.00	8.00	8.00	8.00	8.00	8.00	8.00
Al^{VI}(M1-2-3)	0.08	0.09	0.12	0.11	0.06	0.09	0.11	0.10	0.08	0.11	0.08	0.11
Ti(M1-2-3)	0.14	0.14	0.14	0.14	0.14	0.14	0.15	0.14	0.15	0.15	0.15	0.14
Fe^{3+}(M1-2-3)	3.02	3.04	3.02	3.01	3.02	3.00	3.01	3.02	3.01	3.00	3.03	3.00
Fe^{2+}(M1-2-3)	1.08	1.09	1.16	1.13	1.14	1.15	1.18	1.13	1.09	1.14	1.04	1.14
Mg(M1-2-3)	0.56	0.52	0.47	0.50	0.53	0.51	0.43	0.50	0.56	0.51	0.59	0.49
Mn(M1-2-3)	0.12	0.11	0.10	0.10	0.12	0.11	0.11	0.11	0.11	0.10	0.11	0.11
Σ	13.00	13.00	13.00	13.00	13.00	13.00	13.00	13.00	13.00	13.00	13.00	13.00
Ca(M4)	1.79	1.79	1.79	1.77	1.81	1.79	1.80	1.78	1.77	1.77	1.77	1.78
Na(M4)	0.21	0.21	0.21	0.23	0.19	0.21	0.20	0.22	0.23	0.23	0.23	0.22
Σ	15.00	15.00	15.00	15.00	15.00	15.00	15.00	15.00	15.00	15.00	15.00	15.00
Na(A)	0.15	0.18	0.20	0.18	0.20	0.20	0.19	0.20	0.15	0.17	0.14	0.18
K(A)	0.14	0.13	0.14	0.13	0.13	0.13	0.13	0.13	0.13	0.13	0.13	0.13
Σ	15.28	15.31	15.34	15.31	15.33	15.33	15.32	15.33	15.29	15.30	15.27	15.31

Label	68hb.I49	68hb.I50	68hb.I51	68hb.I52	68hb.I53	68hb.I54	68hb.I55	68hb.I56	68hb.I57	68hb.I58	68hb.I59	68hb.I60
SiO_2	49.35	49.51	49.61	49.09	49.24	50.11	49.55	49.71	49.85	49.73	49.83	49.80
TiO_2	1.09	1.07	1.12	1.06	1.11	1.07	1.02	1.09	1.11	1.09	1.06	1.07
Al_2O_3	5.70	5.66	5.71	5.61	5.57	5.57	5.57	5.55	5.64	5.55	5.55	5.49
FeO_{tot}	13.16	13.05	12.95	13.03	13.04	13.04	13.06	13.05	12.92	12.68	12.97	12.89
MnO	0.81	0.82	0.91	0.92	0.98	0.90	0.96	1.00	1.01	0.99	0.99	0.99
MgO	14.87	14.94	15.12	15.05	15.07	14.98	15.12	15.24	15.06	15.20	15.22	15.30
CaO	11.65	11.80	11.96	11.81	11.70	11.63	11.83	11.65	11.69	11.76	11.70	11.80
Na_2O	1.28	1.30	1.39	1.31	1.26	1.26	1.33	1.39	1.30	1.26	1.31	1.24
K_2O	0.60	0.61	0.66	0.64	0.65	0.64	0.67	0.64	0.62	0.65	0.62	0.63
F	0.30	0.37	0.29	0.23	0.38	0.27	0.26	0.29	0.34	0.35	0.27	0.29
Cl	0.07	0.09	0.09	0.08	0.10	0.06	0.08	0.07	0.08	0.10	0.06	0.09
Sum Oxides	98.87	99.21	99.80	98.84	99.09	99.52	99.44	99.68	99.63	99.35	99.57	99.60
Si	7.07	7.08	7.06	7.04	7.05	7.12	7.07	7.06	7.09	7.09	7.08	7.08
Al^{IV}	0.93	0.92	0.94	0.96	0.95	0.88	0.93	0.94	0.91	0.91	0.92	0.92
Σ(T)	8.00	8.00	8.00	8.00	8.00	8.00	8.00	8.00	8.00	8.00	8.00	8.00
Al^{VI}(M1-2-3)	0.03	0.04	0.02	-0.01	-0.01	0.05	0.00	-0.01	0.03	0.02	0.01	-0.01
Ti(M1-2-3)	0.12	0.12	0.12	0.11	0.12	0.11	0.11	0.12	0.12	0.12	0.11	0.11
Fe^{3+}(M1-2-3)	0.62	0.56	0.53	0.62	0.67	0.59	0.61	0.68	0.61	0.60	0.66	0.65
Fe^{2+}(M1-2-3)	0.95	1.00	1.02	0.94	0.89	0.96	0.95	0.87	0.93	0.91	0.88	0.88
Mg(M1-2-3)	3.18	3.19	3.21	3.22	3.21	3.17	3.21	3.23	3.19	3.23	3.22	3.24
Mn(M1-2-3)	0.10	0.10	0.11	0.11	0.12	0.11	0.12	0.12	0.12	0.12	0.12	0.12
Σ	13.00	13.00	13.00	13.00	13.00	13.00	13.00	13.00	13.00	13.00	13.00	13.00
Ca(M4)	1.79	1.81	1.82	1.82	1.79	1.77	1.81	1.77	1.78	1.80	1.78	1.80
Na(M4)	0.21	0.19	0.18	0.18	0.21	0.23	0.19	0.23	0.22	0.20	0.22	0.20
Σ	15.00	15.00	15.00	15.00	15.00	15.00	15.00	15.00	15.00	15.00	15.00	15.00
Na(A)	0.14	0.17	0.21	0.18	0.14	0.12	0.17	0.15	0.14	0.14	0.14	0.14
K(A)	0.11	0.11	0.12	0.12	0.12	0.12	0.12	0.12	0.11	0.12	0.11	0.11
Σ	15.25	15.28	15.33	15.30	15.26	15.23	15.30	15.27	15.25	15.26	15.25	15.25

Label	196hb4.50	196hb4.51	196hb4.52	196hb4.53	196hb4.54	196hb4.55	196hb4.56	196hb4.57	196hb4.58	196hb4.59	196hb4.60	196hb4.61
SiO_2	48.36	48.41	48.36	47.94	47.55	48.65	48.20	48.18	48.25	48.24	48.38	48.41
TiO_2	1.32	1.29	1.32	1.32	1.29	1.26	1.32	1.30	1.26	1.24	1.32	1.29
Al_2O_3	6.34	6.19	6.29	6.33	5.76	6.22	6.28	6.27	6.34	6.28	6.25	6.19
FeO_{tot}	13.47	13.21	13.48	13.46	12.77	13.36	13.29	13.30	12.86	13.01	13.39	12.88
MnO	0.94	1.00	0.91	1.02	0.86	0.92	0.93	1.06	0.92	0.98	1.03	1.03
MgO	14.01	14.03	13.92	14.05	13.91	14.01	14.07	13.96	14.05	13.99	14.09	14.01
CaO	11.46	11.54	11.41	11.46	13.04	11.56	11.46	11.53	11.55	11.55	11.51	11.40
Na_2O	1.39	1.38	1.42	1.39	1.49	1.39	1.47	1.27	1.49	1.27	1.36	1.34
K_2O	0.74	0.71	0.74	0.69	0.60	0.71	0.73	0.74	0.74	0.69	0.69	0.71
F	0.10	0.13	0.13	0.13	0.16	0.12	0.13	0.09	0.15	0.16	0.13	0.13
Cl	0.02	0.02	0.02	0.03	0.03	0.02	0.02	0.02	0.02	0.02	0.02	0.02
Sum Oxides	100.67	100.34	100.47	100.37	99.41	100.64	100.35	100.23	99.94	99.82	100.68	99.81
Si	7.00	7.03	7.02	6.97	7.07	7.05	7.00	7.01	7.04	7.04	7.00	7.06
Al^{IV}	1.00	0.97	0.98	1.03	0.93	0.95	1.00	0.99	0.96	0.96	1.00	0.94
Σ(T)	8.00	8.00	8.00	8.00	8.00	8.00	8.00	8.00	8.00	8.00	8.00	8.00
Al^{VI}(M1-2-3)	0.08	0.09	0.10	0.05	0.08	0.11	0.08	0.08	0.13	0.12	0.07	0.12
Ti(M1-2-3)	0.14	0.14	0.14	0.14	0.14	0.14	0.14	0.14	0.14	0.14	0.14	0.14
Fe^{3+}(M1-2-3)	3.02	3.04	3.01	3.04	3.08	3.02	3.05	3.03	3.05	3.04	3.04	3.04
Fe^{2+}(M1-2-3)	1.09	1.12	1.12	1.03	1.72	1.15	1.10	1.08	1.17	1.11	1.06	1.10
Mg(M1-2-3)	0.54	0.48	0.51	0.61	-0.13	0.46	0.51	0.54	0.39	0.48	0.56	0.47
Mn(M1-2-3)	0.12	0.12	0.11	0.13	0.11	0.11	0.11	0.13	0.11	0.12	0.13	0.13
Σ	13.00	13.00	13.00	13.00	13.00	13.00	13.00	13.00	13.00	13.00	13.00	13.00
Ca(M4)	1.78	1.80	1.77	1.78	2.08	1.79	1.78	1.80	1.80	1.80	1.78	1.78
Na(M4)	0.22	0.20	0.23	0.22	-0.08	0.21	0.22	0.20	0.20	0.20	0.22	0.22
Σ	15.00	15.00	15.00	15.00	15.00	15.00	15.00	15.00	15.00	15.00	15.00	15.00
Na(A)	0.17	0.18	0.17	0.18	0.51	0.18	0.20	0.15	0.23	0.16	0.17	0.16
K(A)	0.14	0.13	0.14	0.13	0.11	0.13	0.14	0.14	0.14	0.13	0.13	0.13
Σ	15.30	15.32	15.31	15.30	15.62	15.32	15.33	15.29	15.36	15.29	15.29	15.29

Label	68hb.I61	68hb.I62	68hb.I63	68hb.I64	68hb.I65	68hb.I66	68hb.I67	68hb.I68	68hb.I69	68hb.I70	68hb.I71	68hb.I72
SiO_2	49.21	50.04	49.61	49.20	49.38	49.87	49.46	49.67	49.81	49.61	49.30	49.75
TiO_2	1.11	1.04	1.02	1.00	1.05	1.08	1.05	1.03	1.04	1.06	1.07	1.11
Al_2O_3	5.46	5.59	5.46	5.44	5.51	5.46	5.49	5.51	5.48	5.46	5.42	5.48
FeO_{tot}	12.97	12.88	12.72	12.70	12.71	12.73	12.84	12.77	12.40	12.86	12.83	12.75
MnO	1.00	1.09	0.96	1.00	0.99	1.03	1.08	1.07	1.08	1.06	1.10	1.10
MgO	15.11	15.30	15.09	15.38	15.39	15.34	15.23	15.44	15.19	15.25	15.33	15.29
CaO	11.73	11.71	11.70	11.67	11.75	11.75	11.74	11.64	11.53	11.54	11.71	11.82
Na_2O	1.27	1.35	1.37	1.27	1.33	1.38	1.22	1.28	1.28	1.30	1.25	1.22
K_2O	0.60	0.63	0.64	0.64	0.60	0.66	0.61	0.59	0.63	0.65	0.60	0.62
F	0.24	0.25	0.29	0.26	0.32	0.29	0.30	0.36	0.28	0.32	0.31	0.34
Cl	0.09	0.10	0.06	0.09	0.10	0.09	0.11	0.05	0.07	0.07	0.09	0.08
Sum Oxides	98.79	99.97	98.91	98.64	99.13	99.67	99.12	99.40	98.80	99.18	99.00	99.57
Si	7.05	7.08	7.11	7.05	7.05	7.09	7.06	7.05	7.12	7.07	7.04	7.07
Al^{IV}	0.95	0.92	0.89	0.95	0.95	0.91	0.94	0.95	0.88	0.93	0.96	0.93
Σ(T)	8.00	8.00	8.00	8.00	8.00	8.00	8.00	8.00	8.00	8.00	8.00	8.00
Al^{VI}(M1-2-3)	-0.02	0.01	0.03	-0.03	-0.02	0.00	-0.02	-0.02	0.04	-0.01	-0.04	-0.01
Ti(M1-2-3)	0.12	0.11	0.11	0.11	0.11	0.12	0.11	0.11	0.11	0.11	0.11	0.12
Fe^{3+}(M1-2-3)	0.67	0.66	0.56	0.72	0.68	0.61	0.69	0.75	0.62	0.71	0.73	0.65
Fe^{2+}(M1-2-3)	0.89	0.86	0.97	0.80	0.84	0.91	0.84	0.77	0.86	0.82	0.80	0.87
Mg(M1-2-3)	3.23	3.23	3.22	3.28	3.28	3.25	3.24	3.27	3.24	3.24	3.26	3.24
Mn(M1-2-3)	0.12	0.13	0.12	0.12	0.12	0.12	0.13	0.13	0.13	0.13	0.13	0.13
Σ	13.00	13.00	13.00	13.00	13.00	13.00	13.00	13.00	13.00	13.00	13.00	13.00
Ca(M4)	1.80	1.77	1.80	1.79	1.80	1.79	1.80	1.77	1.77	1.76	1.79	1.80
Na(M4)	0.20	0.23	0.20	0.21	0.20	0.21	0.20	0.23	0.23	0.24	0.21	0.20
Σ	15.00	15.00	15.00	15.00	15.00	15.00	15.00	15.00	15.00	15.00	15.00	15.00
Na(A)	0.15	0.14	0.18	0.14	0.16	0.17	0.13	0.12	0.12	0.12	0.14	0.14
K(A)	0.11	0.11	0.12	0.12	0.11	0.12	0.11	0.11	0.11	0.12	0.11	0.11
Σ	15.26	15.26	15.29	15.26	15.27	15.29	15.24	15.23	15.23	15.24	15.25	15.25

Label	196hb4.62	196hb4.64	196hb4.65	196hb4.66	196hb4.67	196hb4.68	196hb4.69	196hb4.70	196hb4.71	196hb4.72	196hb4.73	196hb4.74
SiO_2	48.26	48.45	48.80	48.52	48.44	48.22	48.13	48.10	48.43	48.35	48.37	48.12
TiO_2	1.32	1.25	1.29	1.25	1.23	1.27	1.29	1.30	1.29	1.29	1.27	1.18
Al_2O_3	6.23	6.12	6.17	6.19	6.21	6.31	6.26	6.27	6.45	6.14	6.25	6.16
FeO_{tot}	13.11	13.10	13.00	13.01	13.02	13.39	13.51	13.41	13.12	13.33	13.24	13.39
MnO	0.93	0.97	1.03	0.98	0.90	0.90	0.99	0.94	0.88	0.97	0.86	0.98
MgO	14.00	14.21	14.14	14.06	14.01	14.04	14.06	13.89	14.03	14.08	14.10	14.17
CaO	11.43	11.35	11.50	11.41	11.51	11.42	11.28	11.49	11.50	11.47	11.40	11.62
Na_2O	1.40	1.30	1.39	1.38	1.41	1.40	1.41	1.37	1.48	1.43	1.33	1.35
K_2O	0.70	0.65	0.70	0.66	0.70	0.76	0.74	0.71	0.68	0.70	0.70	0.74
F	0.13	0.13	0.11	0.13	0.14	0.13	0.13	0.11	0.12	0.11	0.11	0.16
Cl	0.02	0.02	0.03	0.02	0.02	0.01	0.02	0.02	0.03	0.03	0.02	0.02
Sum Oxides	99.96	100.11	100.61	100.05	99.96	100.34	100.40	100.08	100.43	100.40	100.16	100.36
Si	7.03	7.03	7.06	7.05	7.06	7.00	6.99	7.01	7.02	7.02	7.03	7.00
Al^{IV}	0.97	0.97	0.94	0.95	0.94	1.00	1.01	0.99	0.98	0.98	0.97	1.00
Σ(T)	8.00	8.00	8.00	8.00	8.00	8.00	8.00	8.00	8.00	8.00	8.00	8.00
Al^{VI}(M1-2-3)	0.10	0.08	0.11	0.11	0.12	0.08	0.06	0.09	0.13	0.07	0.10	0.05
Ti(M1-2-3)	0.14	0.14	0.14	0.14	0.13	0.14	0.14	0.14	0.14	0.14	0.14	0.13
Fe^{3+}(M1-2-3)	3.04	3.07	3.05	3.05	3.04	3.04	3.04	3.02	3.03	3.05	3.05	3.07
Fe^{2+}(M1-2-3)	1.12	0.99	1.11	1.09	1.16	1.08	1.00	1.13	1.14	1.10	1.06	1.07
Mg(M1-2-3)	0.48	0.60	0.47	0.49	0.43	0.55	0.64	0.51	0.45	0.52	0.55	0.56
Mn(M1-2-3)	0.11	0.12	0.13	0.12	0.11	0.11	0.12	0.12	0.11	0.12	0.11	0.12
Σ	13.00	13.00	13.00	13.00	13.00	13.00	13.00	13.00	13.00	13.00	13.00	13.00
Ca(M4)	1.78	1.76	1.78	1.78	1.80	1.78	1.75	1.79	1.79	1.78	1.77	1.81
Na(M4)	0.22	0.24	0.22	0.22	0.20	0.22	0.25	0.21	0.21	0.22	0.23	0.19
Σ	15.00	15.00	15.00	15.00	15.00	15.00	15.00	15.00	15.00	15.00	15.00	15.00
Na(A)	0.18	0.13	0.17	0.17	0.20	0.17	0.15	0.18	0.20	0.19	0.15	0.19
K(A)	0.13	0.12	0.13	0.12	0.13	0.14	0.14	0.13	0.13	0.13	0.13	0.14
Σ	15.31	15.25	15.30	15.29	15.33	15.31	15.29	15.31	15.33	15.32	15.28	15.33

Label	68hb.I73	68hb.I74	68hb.I75	68hb.I76	68hb.I77	68hb.I78	68hb.I79	68hb.I80	68hb.I81	68hb.I82	68hb.I83	68hb.I84
SiO_2	49.33	48.87	48.71	48.38	48.99	49.52	49.43	49.54	49.26	49.83	49.70	49.76
TiO_2	1.09	1.14	1.22	1.20	1.18	1.12	1.05	1.09	1.06	1.01	1.03	1.11
Al_2O_3	5.54	5.88	6.15	6.12	5.90	5.65	5.66	5.52	5.42	5.41	5.54	5.80
FeO_{tot}	12.92	13.04	13.31	13.24	12.87	12.86	12.91	12.61	12.70	12.65	12.64	12.79
MnO	1.01	1.05	1.03	1.06	0.98	1.04	1.00	0.96	1.00	1.10	0.99	1.02
MgO	15.39	15.15	14.88	14.84	14.96	15.06	15.14	15.30	15.34	15.43	15.36	15.47
CaO	11.72	11.78	11.73	11.67	11.70	11.75	11.71	11.82	11.68	11.78	11.80	11.83
Na_2O	1.29	1.45	1.45	1.31	1.50	1.35	1.29	1.35	1.31	1.22	1.40	1.39
K_2O	0.59	0.70	0.71	0.71	0.67	0.67	0.62	0.62	0.61	0.61	0.59	0.67
F	0.33	0.29	0.31	0.30	0.38	0.24	0.34	0.38	0.37	0.31	0.28	0.30
Cl	0.09	0.07	0.10	0.09	0.10	0.10	0.08	0.12	0.09	0.09	0.04	0.10
Sum Oxides	99.29	99.41	99.60	98.93	99.23	99.36	99.24	99.32	98.83	99.44	99.37	100.25
Si	7.03	6.98	6.95	6.94	7.02	7.07	7.05	7.07	7.06	7.08	7.08	7.03
Al^{IV}	0.97	1.02	1.05	1.06	0.98	0.93	0.95	0.93	0.94	0.92	0.92	0.97
Σ(T)	8.00	8.00	8.00	8.00	8.00	8.00	8.00	8.00	8.00	8.00	8.00	8.00
Al^{VI}(M1-2-3)	-0.04	-0.03	-0.01	-0.02	0.02	0.02	0.00	0.00	-0.03	-0.01	0.01	-0.01
Ti(M1-2-3)	0.12	0.12	0.13	0.13	0.13	0.12	0.11	0.12	0.11	0.11	0.11	0.12
Fe^{3+}(M1-2-3)	0.75	0.67	0.68	0.74	0.58	0.59	0.67	0.58	0.69	0.68	0.60	0.67
Fe^{2+}(M1-2-3)	0.79	0.88	0.91	0.85	0.96	0.95	0.87	0.92	0.83	0.82	0.90	0.85
Mg(M1-2-3)	3.27	3.23	3.17	3.18	3.20	3.20	3.22	3.26	3.27	3.27	3.26	3.26
Mn(M1-2-3)	0.12	0.13	0.12	0.13	0.12	0.13	0.12	0.12	0.12	0.13	0.12	0.12
Σ	13.00	13.00	13.00	13.00	13.00	13.00	13.00	13.00	13.00	13.00	13.00	13.00
Ca(M4)	1.79	1.80	1.79	1.79	1.80	1.80	1.79	1.81	1.79	1.79	1.80	1.79
Na(M4)	0.21	0.20	0.21	0.21	0.20	0.20	0.21	0.19	0.21	0.21	0.20	0.21
Σ	15.00	15.00	15.00	15.00	15.00	15.00	15.00	15.00	15.00	15.00	15.00	15.00
Na(A)	0.14	0.20	0.19	0.16	0.21	0.17	0.15	0.18	0.15	0.13	0.19	0.17
K(A)	0.11	0.13	0.13	0.13	0.12	0.12	0.11	0.11	0.11	0.11	0.11	0.12
Σ	15.25	15.33	15.32	15.29	15.33	15.29	15.26	15.30	15.27	15.24	15.29	15.29

Label	196hb4.75	196hb4.77	196hb4.78	196hb4.79	196hb4.80	196hb4.81	196hb4.82	196hb4.83	196hb4.84	196hb4.85	196hb4.86	196hb4.87
SiO_2	48.41	48.72	48.84	49.26	48.78	48.96	49.04	49.24	49.15	49.27	49.42	49.75
TiO_2	1.22	1.14	1.14	1.07	1.12	1.09	1.09	1.08	1.10	1.08	1.09	1.07
Al_2O_3	6.24	5.95	5.82	5.74	5.69	5.58	5.72	5.63	5.57	5.52	5.39	5.43
FeO_{tot}	13.21	13.04	13.07	13.06	12.94	12.88	12.81	12.79	12.85	12.39	12.84	12.59
MnO	0.93	0.98	0.98	0.97	1.02	0.87	0.95	1.02	1.00	1.04	1.03	1.01
MgO	14.01	14.31	14.39	14.54	14.53	14.47	14.53	14.54	14.56	14.79	14.83	14.60
CaO	11.33	11.53	11.45	11.63	11.61	11.53	11.66	11.57	11.57	11.41	11.51	11.50
Na_2O	1.37	1.27	1.31	1.29	1.23	1.20	1.33	1.30	1.18	1.28	1.24	1.35
K_2O	0.73	0.69	0.69	0.63	0.61	0.65	0.65	0.63	0.64	0.55	0.61	0.62
F	0.11	0.13	0.16	0.11	0.13	0.15	0.15	0.16	0.17	0.16	0.13	0.12
Cl	0.02	0.02	0.02	0.02	0.03	0.02	0.02	0.02	0.02	0.03	0.02	0.02
Sum Oxides	100.09	100.24	100.36	100.85	100.23	99.87	100.37	100.44	100.29	100.04	100.68	100.47
Si	7.04	7.06	7.07	7.10	7.07	7.12	7.10	7.12	7.11	7.13	7.11	7.18
Al^{IV}	0.96	0.94	0.93	0.90	0.93	0.88	0.90	0.88	0.89	0.87	0.89	0.82
Σ(T)	8.00	8.00	8.00	8.00	8.00	8.00	8.00	8.00	8.00	8.00	8.00	8.00
Al^{VI}(M1-2-3)	0.11	0.08	0.07	0.07	0.04	0.07	0.08	0.08	0.06	0.07	0.03	0.10
Ti(M1-2-3)	0.13	0.12	0.12	0.12	0.12	0.12	0.12	0.12	0.12	0.12	0.12	0.12
Fe^{3+}(M1-2-3)	3.04	3.09	3.11	3.12	3.14	3.14	3.14	3.13	3.14	3.19	3.18	3.14
Fe^{2+}(M1-2-3)	1.07	1.04	1.02	1.04	0.99	1.04	1.08	1.04	1.00	0.92	0.93	1.08
Mg(M1-2-3)	0.53	0.54	0.56	0.54	0.58	0.52	0.47	0.50	0.55	0.57	0.61	0.44
Mn(M1-2-3)	0.11	0.12	0.12	0.12	0.13	0.11	0.12	0.12	0.12	0.13	0.13	0.12
Σ	13.00	13.00	13.00	13.00	13.00	13.00	13.00	13.00	13.00	13.00	13.00	13.00
Ca(M4)	1.76	1.79	1.78	1.79	1.80	1.80	1.81	1.79	1.79	1.77	1.78	1.78
Na(M4)	0.24	0.21	0.22	0.21	0.20	0.20	0.19	0.21	0.21	0.23	0.22	0.22
Σ	15.00	15.00	15.00	15.00	15.00	15.00	15.00	15.00	15.00	15.00	15.00	15.00
Na(A)	0.15	0.15	0.14	0.16	0.15	0.13	0.18	0.16	0.12	0.13	0.12	0.16
K(A)	0.14	0.13	0.13	0.12	0.11	0.12	0.12	0.12	0.12	0.10	0.11	0.11
Σ	15.29	15.28	15.27	15.27	15.26	15.25	15.30	15.27	15.24	15.23	15.23	15.27

Label	68hb.I85	68hb.I86	68hb.I87	68hb.I88	68hb.I89	68hb.I90	68hb.I91	68hb.I92	68hb.I93	68hb.I94	68hb.I95	68hb.I96
SiO_2	49.03	49.32	48.66	48.37	48.63	48.64	48.36	48.37	48.66	48.73	46.99	46.18
TiO_2	1.07	1.08	1.18	1.24	1.31	1.20	1.17	1.15	1.21	1.18	1.35	1.47
Al_2O_3	5.66	5.71	6.03	6.55	6.57	6.38	6.32	6.28	6.28	6.17	7.27	7.79
FeO_{tot}	12.87	12.53	13.03	13.21	13.59	13.04	13.07	13.14	13.17	12.93	13.73	13.85
MnO	1.00	1.05	1.07	1.00	1.05	1.01	1.03	0.97	1.01	1.02	1.01	1.11
MgO	15.18	15.23	14.85	14.49	14.74	14.73	14.59	14.61	14.86	14.75	14.01	13.63
CaO	11.58	11.81	11.76	11.65	11.83	11.72	11.57	11.68	11.77	11.91	11.57	11.82
Na_2O	1.35	1.43	1.45	1.45	1.48	1.54	1.51	1.42	1.39	1.36	1.49	1.66
K_2O	0.63	0.64	0.74	0.74	0.76	0.71	0.74	0.71	0.68	0.71	0.86	0.93
F	0.32	0.44	0.35	0.30	0.29	0.27	0.33	0.24	0.29	0.28	0.29	0.26
Cl	0.09	0.10	0.12	0.12	0.08	0.10	0.06	0.06	0.08	0.12	0.13	0.16
Sum Oxides	98.78	99.35	99.24	99.11	100.33	99.35	98.73	98.64	99.39	99.16	98.71	98.88
Si	7.02	7.05	6.98	6.95	6.90	6.96	6.97	6.97	6.95	7.00	6.80	6.72
Al^{IV}	0.98	0.95	1.02	1.05	1.10	1.04	1.03	1.03	1.05	1.00	1.20	1.28
Σ(T)	8.00	8.00	8.00	8.00	8.00	8.00	8.00	8.00	8.00	8.00	8.00	8.00
Al^{VI}(M1-2-3)	-0.02	0.01	0.00	0.06	0.00	0.04	0.04	0.03	0.01	0.04	0.04	0.06
Ti(M1-2-3)	0.12	0.12	0.13	0.13	0.14	0.13	0.13	0.13	0.13	0.13	0.15	0.16
Fe^{3+}(M1-2-3)	0.72	0.58	0.61	0.60	0.67	0.58	0.61	0.61	0.67	0.54	0.69	0.57
Fe^{2+}(M1-2-3)	0.82	0.92	0.96	0.98	0.94	0.98	0.96	0.97	0.91	1.01	0.97	1.12
Mg(M1-2-3)	3.24	3.25	3.18	3.10	3.12	3.14	3.13	3.14	3.17	3.16	3.02	2.96
Mn(M1-2-3)	0.12	0.13	0.13	0.12	0.13	0.12	0.13	0.12	0.12	0.12	0.12	0.14
Σ	13.00	13.00	13.00	13.00	13.00	13.00	13.00	13.00	13.00	13.00	13.00	13.00
Ca(M4)	1.78	1.81	1.81	1.79	1.80	1.80	1.79	1.80	1.80	1.83	1.80	1.84
Na(M4)	0.22	0.19	0.19	0.21	0.20	0.20	0.21	0.20	0.20	0.17	0.20	0.16
Σ	15.00	15.00	15.00	15.00	15.00	15.00	15.00	15.00	15.00	15.00	15.00	15.00
Na(A)	0.15	0.20	0.21	0.20	0.21	0.22	0.21	0.20	0.19	0.21	0.21	0.31
K(A)	0.12	0.12	0.14	0.13	0.14	0.13	0.14	0.13	0.12	0.13	0.16	0.17
Σ	15.27	15.32	15.35	15.33	15.34	15.35	15.34	15.33	15.31	15.34	15.37	15.48

Label	196hb4.88	196hb4.89	196hb4.90	196hb4.91	196hb4.92	196hb4.93	196hb4.94	196hb4.95	196hb4.97	196hb4.99	196hb4.101	196hb4.102
SiO_2	49.43	49.33	49.31	49.99	49.38	49.77	49.65	49.27	48.95	49.17	49.30	49.54
TiO_2	1.06	1.03	1.03	1.09	1.05	0.95	1.04	1.02	1.09	1.13	1.07	1.10
Al_2O_3	5.43	5.52	5.47	5.59	5.48	5.40	5.44	5.58	5.70	5.57	5.60	5.58
FeO_{tot}	12.59	12.76	12.75	12.71	12.67	12.91	12.83	12.51	12.98	12.34	12.27	12.49
MnO	0.97	1.03	0.97	1.04	1.05	0.90	1.05	1.00	1.02	1.00	0.97	1.00
MgO	14.85	14.67	14.83	14.67	14.78	14.81	14.76	14.77	14.35	14.40	14.49	14.71
CaO	11.63	11.39	11.48	11.18	11.52	11.47	11.42	11.67	11.31	11.32	11.38	11.33
Na_2O	1.32	1.23	1.26	1.24	1.24	1.25	1.29	1.20	1.28	1.27	1.26	1.25
K_2O	0.61	0.59	0.61	0.63	0.60	0.60	0.57	0.66	0.58	0.61	0.62	0.59
F	0.12	0.17	0.14	0.14	0.16	0.17	0.14	0.14	0.12	0.08	0.12	0.14
Cl	0.02	0.02	0.01	0.02	0.02	0.02	0.02	0.02	0.02	0.02	0.02	0.02
Sum Oxides	100.49	100.27	100.39	100.87	100.46	100.77	100.79	100.31	99.95	99.36	99.51	100.27
Si	7.13	7.12	7.11	7.16	7.12	7.15	7.13	7.12	7.10	7.16	7.17	7.14
Al^{IV}	0.87	0.88	0.89	0.84	0.88	0.85	0.87	0.88	0.90	0.84	0.83	0.86
Σ(T)	8.00	8.00	8.00	8.00	8.00	8.00	8.00	8.00	8.00	8.00	8.00	8.00
Al^{VI}(M1-2-3)	0.05	0.06	0.04	0.10	0.05	0.06	0.06	0.07	0.08	0.12	0.13	0.09
Ti(M1-2-3)	0.12	0.11	0.11	0.12	0.11	0.10	0.11	0.11	0.12	0.12	0.12	0.12
Fe^{3+}(M1-2-3)	3.19	3.16	3.19	3.13	3.18	3.17	3.16	3.18	3.10	3.13	3.14	3.16
Fe^{2+}(M1-2-3)	1.01	0.93	0.93	0.91	0.95	0.96	0.94	1.00	0.98	1.04	1.04	0.94
Mg(M1-2-3)	0.51	0.61	0.61	0.61	0.58	0.59	0.60	0.51	0.60	0.46	0.45	0.57
Mn(M1-2-3)	0.12	0.13	0.12	0.13	0.13	0.11	0.13	0.12	0.13	0.12	0.12	0.12
Σ	13.00	13.00	13.00	13.00	13.00	13.00	13.00	13.00	13.00	13.00	13.00	13.00
Ca(M4)	1.80	1.76	1.77	1.72	1.78	1.77	1.76	1.81	1.76	1.77	1.77	1.75
Na(M4)	0.20	0.24	0.23	0.28	0.22	0.23	0.24	0.19	0.24	0.23	0.23	0.25
Σ	15.00	15.00	15.00	15.00	15.00	15.00	15.00	15.00	15.00	15.00	15.00	15.00
Na(A)	0.17	0.11	0.13	0.06	0.13	0.11	0.12	0.14	0.12	0.13	0.13	0.10
K(A)	0.11	0.11	0.11	0.12	0.11	0.11	0.10	0.12	0.11	0.11	0.12	0.11
Σ	15.28	15.22	15.24	15.17	15.24	15.22	15.22	15.27	15.23	15.24	15.24	15.21

Label	68hb.l98	68hb.l99	68hb.l100	68hb.l101	68hb.l102	68hb.l103	68hb.l104	68hb.l105	68hb.l106	68hb.l107	68hb.l108
SiO_2	47.94	48.36	48.33	47.90	48.16	48.67	48.57	48.22	48.05	47.69	47.50
TiO_2	1.21	1.22	1.24	1.31	1.23	1.25	1.16	1.33	1.32	1.35	1.36
Al_2O_3	6.65	6.62	6.59	6.63	6.46	6.36	6.25	6.41	6.70	6.95	6.97
FeO_{tot}	13.59	13.18	13.51	13.57	13.49	13.08	12.97	13.13	13.58	13.93	13.90
MnO	1.01	0.99	1.02	1.09	0.99	1.02	0.94	0.93	0.95	0.98	0.98
MgO	14.56	14.41	14.45	14.68	14.60	14.76	14.75	14.54	14.22	14.09	14.14
CaO	11.85	11.89	11.79	11.57	11.69	11.77	11.82	11.69	11.83	11.72	11.77
Na_2O	1.43	1.42	1.54	1.55	1.52	1.40	1.38	1.41	1.49	1.50	1.60
K_2O	0.74	0.74	0.73	0.79	0.77	0.70	0.65	0.71	0.82	0.83	0.77
F	0.34	0.22	0.30	0.30	0.29	0.30	0.31	0.27	0.33	0.32	0.33
Cl	0.10	0.09	0.11	0.11	0.13	0.10	0.08	0.10	0.09	0.12	0.10
Sum Oxides	99.42	99.15	99.62	99.49	99.34	99.40	98.88	98.75	99.38	99.48	99.42
Si	6.88	6.95	6.92	6.85	6.91	6.96	6.98	6.95	6.92	6.86	6.84
Al^{IV}	1.12	1.05	1.08	1.15	1.09	1.04	1.02	1.05	1.08	1.14	1.16
Σ(T)	8.00	8.00	8.00	8.00	8.00	8.00	8.00	8.00	8.00	8.00	8.00
Al^{VI}(M1-2-3)	0.00	0.07	0.04	-0.03	0.00	0.03	0.04	0.04	0.05	0.04	0.02
Ti(M1-2-3)	0.13	0.13	0.13	0.14	0.13	0.13	0.13	0.14	0.14	0.15	0.15
Fe^{3+}(M1-2-3)	0.68	0.52	0.59	0.77	0.66	0.62	0.58	0.60	0.53	0.63	0.62
Fe^{2+}(M1-2-3)	0.95	1.07	1.03	0.85	0.96	0.94	0.98	0.99	1.10	1.05	1.06
Mg(M1-2-3)	3.11	3.09	3.09	3.13	3.12	3.15	3.16	3.12	3.05	3.02	3.04
Mn(M1-2-3)	0.12	0.12	0.12	0.13	0.12	0.12	0.11	0.11	0.12	0.12	0.12
Σ	13.00	13.00	13.00	13.00	13.00	13.00	13.00	13.00	13.00	13.00	13.00
Ca(M4)	1.82	1.83	1.81	1.77	1.80	1.80	1.82	1.80	1.82	1.81	1.82
Na(M4)	0.18	0.17	0.19	0.23	0.20	0.20	0.18	0.20	0.18	0.19	0.18
Σ	15.00	15.00	15.00	15.00	15.00	15.00	15.00	15.00	15.00	15.00	15.00
Na(A)	0.22	0.23	0.24	0.20	0.22	0.19	0.21	0.20	0.24	0.22	0.26
K(A)	0.13	0.14	0.13	0.14	0.14	0.13	0.12	0.13	0.15	0.15	0.14
Σ	15.35	15.36	15.37	15.35	15.36	15.32	15.32	15.33	15.39	15.38	15.41

Label	196hb4.103	196hb4.104	196hb4.105	196hb4.106	196hb4.107	196hb4.108	196hb4.109	196hb4.110	196hb4.111	196hb4.112	196hb4.113
SiO_2	49.44	48.92	48.93	48.58	48.81	48.69	48.82	48.85	48.98	49.09	48.97
TiO_2	1.07	1.05	1.14	1.18	1.16	1.15	1.19	1.15	1.11	1.13	1.12
Al_2O_3	5.53	5.59	5.88	6.13	6.00	5.88	5.96	5.85	5.83	5.69	5.72
FeO_{tot}	12.52	12.77	12.81	13.32	12.89	12.84	12.97	13.12	12.91	13.04	12.73
MnO	1.02	1.07	1.00	1.00	0.98	0.89	1.00	1.04	1.01	1.00	1.00
MgO	14.73	14.68	14.37	14.21	14.55	14.42	14.39	14.33	14.39	14.51	14.46
CaO	11.47	11.60	11.45	11.45	11.52	11.37	11.40	11.28	11.33	11.55	11.42
Na_2O	1.37	1.30	1.42	1.43	1.29	1.29	1.31	1.39	1.29	1.28	1.28
K_2O	0.64	0.64	0.70	0.71	0.68	0.62	0.66	0.66	0.66	0.66	0.70
F	0.12	0.12	0.12	0.15	0.13	0.13	0.11	0.09	0.11	0.10	0.15
Cl	0.02	0.02	0.02	0.03	0.03	0.02	0.03	0.02	0.02	0.01	0.02
Sum Oxides	100.41	100.29	100.28	100.68	100.58	99.81	100.39	100.36	100.18	100.58	100.04
Si	7.14	7.08	7.09	7.03	7.05	7.07	7.06	7.07	7.09	7.09	7.11
Al^{IV}	0.86	0.92	0.91	0.97	0.95	0.93	0.94	0.93	0.91	0.91	0.89
Σ(T)	8.00	8.00	8.00	8.00	8.00	8.00	8.00	8.00	8.00	8.00	8.00
Al^{VI}(M1-2-3)	0.08	0.04	0.10	0.07	0.07	0.08	0.08	0.07	0.09	0.06	0.08
Ti(M1-2-3)	0.12	0.11	0.12	0.13	0.13	0.13	0.13	0.13	0.12	0.12	0.12
Fe^{3+}(M1-2-3)	3.17	3.17	3.10	3.06	3.13	3.12	3.10	3.09	3.11	3.12	3.13
Fe^{2+}(M1-2-3)	1.01	0.98	1.07	1.05	0.97	0.98	0.99	0.99	0.98	1.02	1.02
Mg(M1-2-3)	0.50	0.57	0.48	0.56	0.59	0.58	0.58	0.60	0.58	0.56	0.53
Mn(M1-2-3)	0.12	0.13	0.12	0.12	0.12	0.11	0.12	0.13	0.12	0.12	0.12
Σ	13.00	13.00	13.00	13.00	13.00	13.00	13.00	13.00	13.00	13.00	13.00
Ca(M4)	1.77	1.80	1.78	1.77	1.78	1.77	1.77	1.75	1.76	1.79	1.78
Na(M4)	0.23	0.20	0.22	0.23	0.22	0.23	0.23	0.25	0.24	0.21	0.22
Σ	15.00	15.00	15.00	15.00	15.00	15.00	15.00	15.00	15.00	15.00	15.00
Na(A)	0.16	0.16	0.18	0.18	0.14	0.13	0.13	0.14	0.12	0.15	0.14
K(A)	0.12	0.12	0.13	0.13	0.13	0.11	0.12	0.12	0.12	0.12	0.13
Σ	15.28	15.28	15.31	15.31	15.27	15.25	15.26	15.26	15.24	15.27	15.26

Label	68hb.I109	68hb.I110	68hb.I111	68hb.I112	68hb.I113	68hb.I114	68hb.I115	68hb.I116	68hb.I117	68hb.I118	68hb.I119
SiO_2	47.39	47.86	47.76	48.25	48.59	48.82	48.23	47.83	48.75	47.98	47.59
TiO_2	1.42	1.33	1.35	1.26	1.21	1.14	1.26	1.27	1.24	1.32	1.34
Al_2O_3	7.00	6.91	6.68	6.47	6.39	6.09	6.55	6.69	6.28	6.65	6.79
FeO_{tot}	13.87	13.88	13.63	13.60	13.13	13.09	13.39	13.55	13.64	13.83	13.37
MnO	1.01	1.03	0.89	0.87	0.91	0.95	0.98	0.86	0.87	0.92	0.87
MgO	14.18	14.07	14.31	14.56	14.75	14.81	14.45	14.38	14.50	14.47	14.14
CaO	11.83	11.73	11.75	12.04	11.79	11.69	11.65	11.74	11.73	11.91	11.76
Na_2O	1.64	1.51	1.48	1.47	1.38	1.47	1.54	1.54	1.47	1.56	1.51
K_2O	0.83	0.81	0.79	0.75	0.72	0.65	0.81	0.75	0.70	0.82	0.77
F	0.26	0.28	0.30	0.25	0.29	0.27	0.38	0.28	0.28	0.27	0.32
Cl	0.11	0.08	0.11	0.08	0.12	0.08	0.10	0.09	0.08	0.13	0.09
Sum Oxides	99.54	99.48	99.05	99.59	99.29	99.04	99.35	98.98	99.55	99.85	98.55
Si	6.82	6.88	6.89	6.92	6.96	7.00	6.93	6.90	6.98	6.88	6.91
Al^{IV}	1.18	1.12	1.11	1.08	1.04	1.00	1.07	1.10	1.02	1.12	1.09
Σ(T)	8.00	8.00	8.00	8.00	8.00	8.00	8.00	8.00	8.00	8.00	8.00
Al^{VI}(M1-2-3)	0.01	0.05	0.02	0.01	0.04	0.03	0.04	0.03	0.04	0.00	0.07
Ti(M1-2-3)	0.15	0.14	0.15	0.14	0.13	0.12	0.14	0.14	0.13	0.14	0.15
Fe^{3+}(M1-2-3)	0.60	0.61	0.60	0.55	0.61	0.61	0.59	0.60	0.59	0.60	0.51
Fe^{2+}(M1-2-3)	1.07	1.06	1.04	1.08	0.96	0.96	1.01	1.03	1.05	1.06	1.11
Mg(M1-2-3)	3.04	3.02	3.08	3.11	3.15	3.17	3.10	3.09	3.09	3.09	3.06
Mn(M1-2-3)	0.12	0.13	0.11	0.11	0.11	0.11	0.12	0.11	0.11	0.11	0.11
Σ	13.00	13.00	13.00	13.00	13.00	13.00	13.00	13.00	13.00	13.00	13.00
Ca(M4)	1.82	1.81	1.82	1.85	1.81	1.80	1.79	1.81	1.80	1.83	1.83
Na(M4)	0.18	0.19	0.18	0.15	0.19	0.20	0.21	0.19	0.20	0.17	0.17
Σ	15.00	15.00	15.00	15.00	15.00	15.00	15.00	15.00	15.00	15.00	15.00
Na(A)	0.28	0.23	0.23	0.26	0.19	0.20	0.22	0.24	0.21	0.26	0.25
K(A)	0.15	0.15	0.15	0.14	0.13	0.12	0.15	0.14	0.13	0.15	0.14
Σ	15.43	15.37	15.38	15.40	15.32	15.32	15.37	15.38	15.34	15.41	15.40

Label	196hb4.114	196hb4.115	196hb4.116	196hb4.117	196hb4.118	196hb4.119	196hb4.120	196hb4.121	196hb4.122	196hb4.123	196hb4.124
SiO_2	48.87	48.19	48.47	48.46	48.22	48.57	48.29	47.46	47.72	49.00	48.56
TiO_2	1.23	1.20	1.24	1.22	1.20	1.17	1.26	1.31	1.33	1.14	1.26
Al_2O_3	6.18	6.20	6.18	6.20	6.32	6.05	6.51	6.66	6.56	6.00	6.20
FeO_{tot}	13.04	13.03	13.56	13.39	13.42	12.84	13.28	13.50	13.55	12.98	12.93
MnO	1.15	1.00	0.99	0.99	0.99	1.08	0.99	0.96	0.97	0.98	1.05
MgO	14.14	14.26	14.28	14.02	14.05	14.23	13.90	13.83	13.74	14.23	13.93
CaO	11.31	11.31	11.51	11.35	11.51	11.42	11.43	11.38	11.58	11.47	11.45
Na_2O	1.32	1.30	1.30	1.33	1.42	1.36	1.52	1.44	1.39	1.27	1.40
K_2O	0.76	0.71	0.68	0.69	0.71	0.70	0.75	0.79	0.76	0.71	0.73
F	0.14	0.15	0.14	0.14	0.15	0.11	0.15	0.13	0.12	0.11	0.17
Cl	0.02	0.02	0.02	0.03	0.02	0.02	0.03	0.03	0.02	0.02	0.03
Sum Oxides	100.67	99.93	100.96	100.34	100.50	100.04	100.55	100.01	100.20	100.39	100.06
Si	7.06	7.01	6.99	7.03	7.00	7.06	7.01	6.93	6.96	7.09	7.07
Al^{IV}	0.94	0.99	1.01	0.97	1.00	0.94	0.99	1.07	1.04	0.91	0.93
Σ(T)	8.00	8.00	8.00	8.00	8.00	8.00	8.00	8.00	8.00	8.00	8.00
Al^{VI}(M1-2-3)	0.11	0.07	0.04	0.09	0.08	0.10	0.12	0.08	0.09	0.11	0.13
Ti(M1-2-3)	0.13	0.13	0.13	0.13	0.13	0.13	0.14	0.14	0.15	0.12	0.14
Fe^{3+}(M1-2-3)	3.04	3.09	3.07	3.03	3.04	3.08	3.01	3.01	2.99	3.07	3.02
Fe^{2+}(M1-2-3)	1.01	0.95	0.98	1.04	1.08	1.04	1.14	1.06	1.16	1.07	1.16
Mg(M1-2-3)	0.56	0.64	0.66	0.59	0.55	0.52	0.47	0.59	0.50	0.50	0.42
Mn(M1-2-3)	0.14	0.12	0.12	0.12	0.12	0.13	0.12	0.12	0.12	0.12	0.13
Σ	13.00	13.00	13.00	13.00	13.00	13.00	13.00	13.00	13.00	13.00	13.00
Ca(M4)	1.75	1.76	1.78	1.76	1.79	1.78	1.78	1.78	1.81	1.78	1.79
Na(M4)	0.25	0.24	0.22	0.24	0.21	0.22	0.22	0.22	0.19	0.22	0.21
Σ	15.00	15.00	15.00	15.00	15.00	15.00	15.00	15.00	15.00	15.00	15.00
Na(A)	0.12	0.13	0.14	0.14	0.19	0.16	0.20	0.19	0.20	0.13	0.18
K(A)	0.14	0.13	0.13	0.13	0.13	0.13	0.14	0.15	0.14	0.13	0.14
Σ	15.26	15.26	15.27	15.27	15.32	15.29	15.34	15.34	15.35	15.27	15.32

Label	68hb.l120	68hb.l121	68hb.l122	68hb.l123	68hb.l124	68hb.l125	68hb.l126	68hb.l127	68hb.l128	68hb.l129	68hb.l130
SiO_2	48.22	48.47	48.46	47.38	47.89	47.48	48.04	48.07	48.27	48.08	47.59
TiO_2	1.28	1.20	1.27	1.41	1.36	1.37	1.40	1.36	1.35	1.37	1.42
Al_2O_3	6.64	6.19	6.45	7.11	6.97	7.07	6.91	6.88	6.89	7.03	7.22
FeO_{tot}	13.55	13.37	13.54	13.87	13.91	13.81	13.75	13.76	13.59	13.87	14.17
MnO	0.85	0.90	0.79	0.86	0.81	0.90	0.89	0.86	0.81	0.78	0.81
MgO	14.27	14.69	14.32	14.11	14.08	13.96	14.26	14.22	14.10	14.06	13.97
CaO	11.84	11.74	11.88	11.92	11.91	11.84	11.97	11.86	11.76	11.62	11.84
Na_2O	1.42	1.34	1.48	1.58	1.60	1.59	1.49	1.40	1.51	1.55	1.58
K_2O	0.73	0.69	0.71	0.82	0.80	0.81	0.76	0.75	0.78	0.78	0.89
F	0.31	0.30	0.27	0.31	0.26	0.28	0.26	0.33	0.30	0.29	0.28
Cl	0.10	0.10	0.09	0.10	0.12	0.11	0.10	0.11	0.13	0.11	0.10
Sum Oxides	99.21	98.97	99.26	99.47	99.69	99.23	99.82	99.58	99.49	99.53	99.87
Si	6.94	6.96	6.97	6.83	6.88	6.86	6.88	6.89	6.94	6.90	6.83
Al^{IV}	1.06	1.04	1.03	1.17	1.12	1.14	1.12	1.11	1.06	1.10	1.17
Σ(T)	8.00	8.00	8.00	8.00	8.00	8.00	8.00	8.00	8.00	8.00	8.00
Al^{VI}(M1-2-3)	0.07	0.01	0.07	0.04	0.07	0.06	0.05	0.06	0.10	0.09	0.06
Ti(M1-2-3)	0.14	0.13	0.14	0.15	0.15	0.15	0.15	0.15	0.15	0.15	0.15
Fe^{3+}(M1-2-3)	0.54	0.66	0.48	0.55	0.50	0.51	0.54	0.58	0.49	0.58	0.56
Fe^{2+}(M1-2-3)	1.09	0.95	1.15	1.12	1.17	1.16	1.10	1.07	1.15	1.09	1.15
Mg(M1-2-3)	3.06	3.15	3.07	3.03	3.02	3.01	3.05	3.04	3.02	3.01	2.99
Mn(M1-2-3)	0.10	0.11	0.10	0.11	0.10	0.11	0.11	0.10	0.10	0.10	0.10
Σ	13.00	13.00	13.00	13.00	13.00	13.00	13.00	13.00	13.00	13.00	13.00
Ca(M4)	1.82	1.81	1.83	1.84	1.83	1.83	1.84	1.82	1.81	1.79	1.82
Na(M4)	0.18	0.19	0.17	0.16	0.17	0.17	0.16	0.18	0.19	0.21	0.18
Σ	15.00	15.00	15.00	15.00	15.00	15.00	15.00	15.00	15.00	15.00	15.00
Na(A)	0.22	0.18	0.24	0.28	0.28	0.28	0.25	0.21	0.23	0.22	0.26
K(A)	0.13	0.13	0.13	0.15	0.15	0.15	0.14	0.14	0.14	0.14	0.16
Σ	15.35	15.31	15.37	15.43	15.43	15.43	15.39	15.35	15.37	15.36	15.42

Label	196hb4.125	196hb4.126	196hb4.127	196hb4.129	196hb4.130	196hb4.131	196hb4.132	196hb4.134	196hb4.135	196hb4.136	196hb4.137
SiO_2	48.14	48.32	48.23	47.76	48.30	47.91	48.40	48.40	47.12	47.51	47.79
TiO_2	1.20	1.20	1.21	1.22	1.24	1.24	1.24	1.18	1.32	1.29	1.30
Al_2O_3	6.50	6.30	6.24	6.52	6.28	6.51	6.30	6.29	6.77	6.76	6.80
FeO_{tot}	13.20	13.17	13.36	13.39	13.17	13.35	13.22	13.04	13.74	13.38	13.95
MnO	0.95	1.04	0.98	1.04	1.00	0.93	0.89	0.88	0.86	0.90	0.93
MgO	13.84	14.14	14.05	13.94	14.02	13.93	14.01	14.27	13.74	13.82	13.77
CaO	11.46	11.44	11.48	11.38	11.42	11.61	11.61	11.52	11.37	11.56	11.46
Na_2O	1.35	1.31	1.35	1.39	1.26	1.48	1.33	1.33	1.46	1.39	1.39
K_2O	0.75	0.75	0.70	0.72	0.72	0.74	0.74	0.74	0.74	0.79	0.80
F	0.13	0.11	0.12	0.11	0.13	0.12	0.13	0.14	0.12	0.13	0.11
Cl	0.03	0.02	0.02	0.02	0.02	0.02	0.01	0.02	0.03	0.03	0.02
Sum Oxides	99.98	100.34	100.26	100.05	100.06	100.25	100.27	100.29	99.83	100.02	100.91
Si	7.02	7.01	7.01	6.96	7.02	6.98	7.03	7.02	6.90	6.94	6.92
Al^{IV}	0.98	0.99	0.99	1.04	0.98	1.02	0.97	0.98	1.10	1.06	1.08
Σ(T)	8.00	8.00	8.00	8.00	8.00	8.00	8.00	8.00	8.00	8.00	8.00
Al^{VI}(M1-2-3)	0.13	0.09	0.08	0.08	0.10	0.10	0.11	0.10	0.07	0.10	0.08
Ti(M1-2-3)	0.13	0.13	0.13	0.13	0.14	0.14	0.14	0.13	0.15	0.14	0.14
Fe^{3+}(M1-2-3)	3.01	3.06	3.04	3.03	3.04	3.03	3.04	3.09	3.00	3.01	2.97
Fe^{2+}(M1-2-3)	1.12	1.02	1.06	1.02	1.04	1.16	1.15	1.05	1.06	1.12	1.07
Mg(M1-2-3)	0.48	0.58	0.56	0.62	0.56	0.47	0.45	0.54	0.62	0.52	0.62
Mn(M1-2-3)	0.12	0.13	0.12	0.13	0.12	0.11	0.11	0.11	0.11	0.11	0.11
Σ	13.00	13.00	13.00	13.00	13.00	13.00	13.00	13.00	13.00	13.00	13.00
Ca(M4)	1.79	1.78	1.79	1.78	1.78	1.81	1.81	1.79	1.78	1.81	1.78
Na(M4)	0.21	0.22	0.21	0.22	0.22	0.19	0.19	0.21	0.22	0.19	0.22
Σ	15.00	15.00	15.00	15.00	15.00	15.00	15.00	15.00	15.00	15.00	15.00
Na(A)	0.17	0.15	0.17	0.17	0.13	0.23	0.18	0.16	0.20	0.20	0.17
K(A)	0.14	0.14	0.13	0.13	0.13	0.14	0.14	0.14	0.14	0.15	0.15
Σ	15.31	15.28	15.30	15.30	15.27	15.37	15.32	15.30	15.34	15.35	15.32

Label	68hb.l131	68hb.l132	68hb.l133	68hb.l134	68hb.l135	68hb.l136	68hb.l137	68hb.l138	68hb.l139	68hb.l140	68hb.l141
SiO_2	47.46	47.78	47.19	47.82	47.50	46.42	47.03	47.01	46.39	46.61	46.22
TiO_2	1.39	1.39	1.42	1.33	1.35	1.46	1.45	1.42	1.49	1.52	1.56
Al_2O_3	7.02	7.01	7.31	6.85	7.13	7.24	7.42	7.52	7.89	8.03	8.26
FeO_{tot}	13.92	14.04	14.10	14.05	14.18	14.47	14.29	14.61	14.59	14.71	15.02
MnO	0.80	0.84	0.75	0.81	0.82	0.76	0.71	0.70	0.73	0.68	0.71
MgO	13.92	13.99	13.78	13.97	13.92	13.65	13.48	13.46	13.31	13.20	13.04
CaO	12.00	11.85	11.86	11.91	11.99	12.00	12.20	11.89	11.99	11.97	11.91
Na_2O	1.59	1.51	1.54	1.54	1.49	1.58	1.45	1.64	1.75	1.56	1.66
K_2O	0.81	0.84	0.85	0.78	0.84	0.91	0.90	0.88	0.96	0.96	1.03
F	0.26	0.28	0.31	0.33	0.28	0.26	0.32	0.33	0.28	0.24	0.24
Cl	0.11	0.13	0.13	0.13	0.13	0.10	0.08	0.13	0.13	0.15	0.17
Sum Oxides	99.29	99.66	99.24	99.51	99.63	98.86	99.33	99.58	99.50	99.64	99.81
Si	6.87	6.87	6.83	6.90	6.84	6.77	6.83	6.80	6.74	6.75	6.70
Al^{IV}	1.13	1.13	1.17	1.10	1.16	1.23	1.17	1.20	1.26	1.25	1.30
Σ(T)	8.00	8.00	8.00	8.00	8.00	8.00	8.00	8.00	8.00	8.00	8.00
Al^{VI}(M1-2-3)	0.06	0.06	0.07	0.06	0.06	0.01	0.10	0.09	0.09	0.12	0.11
Ti(M1-2-3)	0.15	0.15	0.15	0.14	0.15	0.16	0.16	0.15	0.16	0.17	0.17
Fe^{3+}(M1-2-3)	0.45	0.54	0.52	0.50	0.53	0.53	0.38	0.49	0.44	0.47	0.50
Fe^{2+}(M1-2-3)	1.23	1.15	1.18	1.19	1.17	1.24	1.35	1.28	1.33	1.31	1.32
Mg(M1-2-3)	3.00	3.00	2.97	3.00	2.99	2.97	2.92	2.90	2.88	2.85	2.82
Mn(M1-2-3)	0.10	0.10	0.09	0.10	0.10	0.09	0.09	0.09	0.09	0.08	0.09
Σ	13.00	13.00	13.00	13.00	13.00	13.00	13.00	13.00	13.00	13.00	13.00
Ca(M4)	1.86	1.83	1.84	1.84	1.85	1.88	1.90	1.84	1.87	1.86	1.85
Na(M4)	0.14	0.17	0.16	0.16	0.15	0.12	0.10	0.16	0.13	0.14	0.15
Σ	15.00	15.00	15.00	15.00	15.00	15.00	15.00	15.00	15.00	15.00	15.00
Na(A)	0.31	0.25	0.27	0.27	0.27	0.32	0.31	0.30	0.36	0.30	0.32
K(A)	0.15	0.15	0.16	0.14	0.15	0.17	0.17	0.16	0.18	0.18	0.19
Σ	15.46	15.40	15.43	15.41	15.42	15.49	15.47	15.47	15.53	15.47	15.51

Label	196hb4.138	196hb4.139	196hb4.140	196hb4.141	196hb4.142	196hb4.143	196hb4.144	196hb4.146	196hb4.147	196hb4.148	196hb4.149
SiO_2	48.16	47.40	47.48	47.55	47.55	47.38	46.76	46.52	46.94	47.19	46.52
TiO_2	1.28	1.35	1.35	1.35	1.31	1.48	1.44	1.49	1.39	1.36	1.45
Al_2O_3	6.68	7.03	6.87	7.10	6.76	7.22	7.39	7.49	7.26	7.21	7.28
FeO_{tot}	13.51	13.64	13.81	13.15	13.94	13.78	14.10	14.06	14.21	13.95	14.39
MnO	0.78	0.90	0.86	0.75	0.88	0.70	0.75	0.71	0.81	0.73	0.71
MgO	13.64	13.52	13.59	13.42	13.55	13.30	13.29	12.97	13.24	13.30	13.02
CaO	11.51	11.41	11.56	11.45	11.59	11.84	11.52	11.66	11.63	11.59	11.70
Na_2O	1.32	1.47	1.42	1.42	1.36	1.43	1.46	1.54	1.42	1.50	1.45
K_2O	0.77	0.83	0.82	0.77	0.78	0.76	0.81	0.93	0.84	0.83	0.87
F	0.11	0.12	0.09	0.10	0.11	0.12	0.12	0.09	0.09	0.09	0.13
Cl	0.03	0.03	0.02	0.02	0.02	0.02	0.03	0.03	0.03	0.03	0.02
Sum Oxides	100.20	100.17	100.35	99.39	100.33	100.31	100.15	99.81	100.34	100.16	99.89
Si	7.01	6.92	6.93	6.98	6.94	6.92	6.85	6.86	6.87	6.91	6.85
Al^{IV}	0.99	1.08	1.07	1.02	1.06	1.08	1.15	1.14	1.13	1.09	1.15
Σ(T)	8.00	8.00	8.00	8.00	8.00	8.00	8.00	8.00	8.00	8.00	8.00
Al^{VI}(M1-2-3)	0.16	0.13	0.11	0.21	0.10	0.17	0.12	0.16	0.12	0.15	0.12
Ti(M1-2-3)	0.14	0.15	0.15	0.15	0.14	0.16	0.16	0.17	0.15	0.15	0.16
Fe^{3+}(M1-2-3)	2.96	2.94	2.96	2.94	2.95	2.90	2.90	2.85	2.89	2.90	2.86
Fe^{2+}(M1-2-3)	1.20	1.16	1.18	1.25	1.18	1.36	1.19	1.38	1.24	1.28	1.34
Mg(M1-2-3)	0.44	0.51	0.51	0.37	0.52	0.33	0.54	0.35	0.50	0.43	0.44
Mn(M1-2-3)	0.10	0.11	0.11	0.09	0.11	0.09	0.09	0.09	0.10	0.09	0.09
Σ	13.00	13.00	13.00	13.00	13.00	13.00	13.00	13.00	13.00	13.00	13.00
Ca(M4)	1.80	1.79	1.81	1.80	1.81	1.85	1.81	1.84	1.82	1.82	1.85
Na(M4)	0.20	0.21	0.19	0.20	0.19	0.15	0.19	0.16	0.18	0.18	0.15
Σ	15.00	15.00	15.00	15.00	15.00	15.00	15.00	15.00	15.00	15.00	15.00
Na(A)	0.17	0.20	0.21	0.20	0.20	0.26	0.22	0.28	0.23	0.24	0.26
K(A)	0.14	0.15	0.15	0.14	0.15	0.14	0.15	0.17	0.16	0.16	0.16
Σ	15.31	15.36	15.36	15.35	15.34	15.40	15.37	15.46	15.38	15.40	15.42

Label	68hb.I142	68hb.I1_144	68hb.I1_145	68hb.I1_146	68hb.I1_147	68hb.I1_148	68hb.I1_149
SiO_2	45.78	47.26	48.11	46.67	47.61	47.32	46.67
TiO_2	1.58	1.41	1.30	1.46	1.35	1.36	1.42
Al_2O_3	8.31	7.48	6.94	7.74	7.32	7.39	7.47
FeO_{tot}	15.11	14.49	14.12	14.74	14.06	14.31	13.96
MnO	0.71	0.69	0.71	0.70	0.66	0.76	0.74
MgO	12.96	13.69	14.11	13.22	13.86	13.71	13.62
CaO	12.01	12.05	12.05	11.90	12.06	11.97	11.93
Na_2O	1.76	1.56	1.46	1.57	1.48	1.58	1.52
K_2O	1.03	0.92	0.79	0.88	0.87	0.84	0.88
F	0.22	0.29	0.32	0.32	0.32	0.25	0.25
Cl	0.16	0.15	0.09	0.10	0.14	0.12	0.10
Sum Oxides	99.62	99.99	100.00	99.29	99.74	99.59	98.57
Si	6.66	6.81	6.90	6.78	6.86	6.83	6.81
Al^{IV}	1.34	1.19	1.10	1.22	1.14	1.17	1.19
Σ(T)	8.00	8.00	8.00	8.00	8.00	8.00	8.00
Al^{VI}(M1-2-3)	0.09	0.08	0.07	0.10	0.10	0.08	0.09
Ti(M1-2-3)	0.17	0.15	0.14	0.16	0.15	0.15	0.16
Fe^{3+}(M1-2-3)	0.47	0.49	0.51	0.49	0.45	0.50	0.47
Fe^{2+}(M1-2-3)	1.37	1.26	1.18	1.30	1.24	1.23	1.23
Mg(M1-2-3)	2.81	2.94	3.01	2.86	2.98	2.95	2.96
Mn(M1-2-3)	0.09	0.08	0.09	0.09	0.08	0.09	0.09
Σ	13.00	13.00	13.00	13.00	13.00	13.00	13.00
Ca(M4)	1.87	1.86	1.85	1.85	1.86	1.85	1.86
Na(M4)	0.13	0.14	0.15	0.15	0.14	0.15	0.14
Σ	15.00	15.00	15.00	15.00	15.00	15.00	15.00
Na(A)	0.37	0.29	0.26	0.29	0.27	0.29	0.29
K(A)	0.19	0.17	0.14	0.16	0.16	0.15	0.16
Σ	15.56	15.46	15.40	15.46	15.43	15.45	15.46

Label	196hb4.150
SiO_2	47.00
TiO_2	1.36
Al_2O_3	7.23
FeO_{tot}	14.49
MnO	0.70
MgO	13.07
CaO	11.62
Na_2O	1.47
K_2O	0.82
F	0.08
Cl	0.02
Sum Oxides	100.29
Si	6.89
Al^{IV}	1.11
Σ(T)	8.00
Al^{VI}(M1-2-3)	0.13
Ti(M1-2-3)	0.15
Fe^{3+}(M1-2-3)	2.85
Fe^{2+}(M1-2-3)	1.31
Mg(M1-2-3)	0.46
Mn(M1-2-3)	0.09
Σ	13.00
Ca(M4)	1.82
Na(M4)	0.18
Σ	15.00
Na(A)	0.24
K(A)	0.15
Σ	15.39

Remerciements

Je remercie mon directeur de thèse Michael Dungan de m'avoir proposé ce sujet, subventionné par la bourse FNRS # 20-49730.96, et fait confiance depuis le diplôme. Son enthousiasme et son dynamisme scientifique m'ont permis de travailler dans des conditions excellentes, avec une motivation sans cesse renouvelée. Je le remercie également de m'avoir permis de participer à plusieurs congrès et de rencontrer un grand nombre de personnes d'horizons différents.

Je remercie Peter Lipman de m'avoir initié, conseillé, et dirigé pendant près de 8 mois à la cartographie et la volcanologie lors de nos étés de terrain dans cet extraordinaire région que sont les montagnes de San Juan. Je le remercie très chaleureusement, ainsi que sa femme Beverly, de m'avoir toujours accueilli et hébergé dans les meilleures conditions imaginables. Ces mois de terrain m'ont permis de vivre des moments hors du commun et resteront pour moi la vraie révélation de mon goût pour la géologie.

Je remercie Tim Druitt et Michel Pichavant d'avoir accepté de passer du temps sur mon travail et d'avoir su diriger mon attention sur des problèmes que je n'avais pas ou peu abordés.

Je suis reconnaissant aux personnes quio m'ont permis d'acquérir des données ou aider à améliorer ce travail de thèse: Felix Oberli (ETHZ ; géochronologie U/Pb), Giz Marriner and Matthew Thirlwall (RHBNC ; XRF), Nick Rodgers (Open University ; INAA), Robert Hinton (Edimbourg ; SIMS), Fabio Capponi (Genève ; XRF), Jean-Marie Boccard (Genève ; préparation échantillons et lames minces). Brad Singer (Genève, géochronologie $^{40}Ar/^{39}Ar$), Jacques Metzger (Genève ; graphisme)

Un grand merci à Bernard Evans, Georges Bergantz, Tim Druitt, et tous les participants du camp de terrain 1997 au Colorado (Charlie Bacon, Bill Bonnichsen, Chuck Chapin, Shan de Silva, Marty Godchaux, Chris Henry, Jan Lindsay, Jake Lowenstern, Curtis Manley, Mike McCurry, Bill McIntosh, Ren Thompson, Martin Streck) pour leurs précieux conseils.

J'ai beaucoup apprécié l'aide et le soutien du Prof. Lluis Fontboté tout au long de ces années d'assistanat et je le félicite pour sa gestion du département éclairée et toujours dirigée par un un soucis de justice.

Merci également à mes collègues post-doctorants Jenni Barclay, Laura Webb, Georges Morris et Andrea Marzoli pour leurs conseils et pour les bon moments passés ensemble lors des différent camps de terrain.

Merci infiniment à Christian Huber and Olivier Roche pour leur compagnie plus qu'agréable sur le terrain et pour leur soutien moral et scientifique pendant ces magnifiques mais longs étés dans ces forêts peuplées d'animaux insolites. Leur amitié depuis est pour moi la plus grande récompense de ma jeune carrière de géologue.

Grosses bises et poignées de main viriles, suivant leur arrangement chromosomique, à mes collègues de bureau et du 7ème, Thao Ton-That, Fleurice Parat, Alain Burgisser, Fidel Costa, Christian Huber, Yann Vincze, qui m'ont aidé plus qu'il n'y paraît tout au long de cette thèse. Chacun d'eux mériterait un paragraphe entier, mais le manque de place m'oblige à le garder pour moi. Ces paragraphes sont néanmoins disponibles pour les personnes concernées, sur demande de leur part...

Un hommage également vibrant à mes amis géologues, que je n'oublie bien évidemment pas, Benoît Piguet, Michel Meyer, Didier Morend, Massimo Massera, Alexis Carillat, Carol Nawratil, Claude-Alain Hasler, et mes collègues de licence et de diplôme, qui se reconnaîtront sous le vocable " Tassons et Tassonnettes ", qui m'ont permis de

passer une formation universitaire intense tout en étant divertissante.

J'aimerais m'excuser auprès des personnes qui vont lire assez assidûment cette thèse pour en découvrir les erreurs qui m'ont échappé, malgré les nombreuses relectures.

Pour finir, j'embrasse très fort ma famille, ma belle-famille, et ma tendre épouse, qui m'ont apporté, comme toujours, leur soutien inconditionnel. Les corrections ne se faisant pas en une nuit, il s'est passé beaucoup de choses depuis la soutenance. Je dédie donc cette thèse à notre merveille en formation, et à sa mère, je rajouterai: «Tu esti dragostea vieti mele»...